Development of pixel detector for ATLAS Inner Tracker(ITK) upgrade at HL-LHC and Searching for the Standard Model Higgs boson decay into b-quark pair with ATLAS experiment

Tasneem Saleem

université PARIS-SACLAY

NNT : 2019SACLS071

Thèse de doctorat

UNIVERSITÉ PARIS SUD
Comprendre le monde, construire l'avenir

Development of pixel detector for ATLAS Inner Tracker (ITk) upgrade at HL-LHC and Searching for the Standard Model Higgs boson decay into b-quark pair with ATLAS experiment

Thèse de doctorat de l'Université Paris-Saclay
préparée à l'Université Paris-Sud

Ecole doctorale n°576 Particules, Hadrons, Énergie, Noyau, Instrumentation, Imagerie, Cosmos et Simulation (PHENIICS)
Spécialité de doctorat : Physique des particules

Thèse présentée et soutenue à Orsay, le 08/01/2019, par

TASNEEM SALEEM

Composition du Jury :

M. Achille Stocchi Professeur, (Université Paris Sud/LAL)	Président du jury
Mme. Anna Macchiolo Directeur de recherche, (CERN/MPI)	Rapporteur
M. Giovanni Marchiori Chargé de recherche, (CNRS/LPNHE)	Rapporteur
M. Marco Meschini Directeur de recherche, (CERN/INFN)	Examinateur
M. Abdenour Lounis Maitre de conférence universitaire, (Université Paris Sud/LAL)	Directeur de thèse
M. Luc Poggioli Directeur de recherche, (CNRS/LAL)	Co-directeur de thèse
M. Ahmed Bassalat Maître assistant (Université Nationale An-Najah)	Invité

université PARIS-SACLAY | ÉCOLE DOCTORALE PHENIICS

Titre :Développement d'un détecteur de pixels pour la mise à niveau d'ATLAS Inner Tracker (ITk) au HL-LHC et recherche du modèle standard désintégration du boson de Higgs en paire de b-quark avec l'expérience ATLAS.

Mots clés : Mise à niveau ATLAS ITk au HL-LHC, Dommages par rayonnement, Boson de Higgs, b-quark, Fond multi-jet.

Résumé : ATLAS est l'une des deux principales expériences du LHC dans le but d'étudier les propriétés microscopiques de la matière afin de répondre aux questions les plus fondamentales de la physique des particules. Après les réalisations accomplies lors de la première prise de données, le potentiel de nouvelles découvertes et de mesures précises au LHC est étendu en repoussant les limites en matière d'énergie dans le centre de masse et de luminosité grâce à trois mises à niveau de l'accélérateur aboutissant au LHC à haute luminosité (HL-LHC). Pour tirer pleinement parti de l'augmentation de la luminosité, deux mises à niveau principales du détecteur interne ATLAS sont prévues. La première mise à niveau était déjà achevée au début de l'année 2015 avec l'insertion de l'IBL, une quatrième couche de pixels située à seulement 3,2 cm de la ligne de faisceau. Dans la deuxième mise à niveau majeure, prévue pour 2024, le détecteur interne complet sera remplacé par un tout nouveau dispositif de suivi interne entièrement constitué de dispositifs en silicium pour faire face à la forte densité de particules et à l'environnement de rayonnement intense du HL-LHC, qui pendant son fonctionnement période fournira 3000 fb^{-1}, près de dix fois la luminosité intégrée du programme complet du LHC. Cette thèse aborde l'étude de nouveaux détecteurs de pixels de bord actifs n + -in-p en développant deux nouvelles méthodes d'analyse du profil du dopage pour étudier les effets des dommages d'irradiation sur les performances des détecteurs de pixels. Ces méthodes sont la méthode d'imagerie 3D sims et la méthode TLM. La simulation TCAD a été utilisée pour simuler les profils de dopage, le comportement électrique et les dommages dus au rayonnement. La validation des modèles de simulation avec les données a été effectuée. De plus, la caractérisation de la salle blanche ainsi que la mesure sur un faisceau de test ont été effectuées pour tester les différentes conceptions de détecteurs. Dans la deuxième partie de la thèse, je discute de l'observation de la désintégration du boson de Higgs en une paire de quarks b à l'aide des données collectées par ATLAS lors du Run 2 du LHC à une énergie de 13 TeV dans le centre de masse et une luminosité intégrée de 79.8 fb^{-1}. J'ai contribué à l'analyse où le boson de Higgs est produit en association avec un boson de jauge W ou Z. L'analyse VH(bb) ne considérant pas les leptons tau, j'ai réalisé une étude estimant l'impact de leur utilisation sur l'analyse. De plus, pour l'analyse VH(bb), j'ai travaillé sur l'estimation de fond multi-jets dans le canal à 1 lepton en utilisant la méthode d'analyse dijet-masse.

Title : Development of pixel detector for ATLAS Inner Tracker (ITk) upgrade at HL-LHC and Searching for the Standard Model Higgs boson decay into b-quark pair with ATLAS experiment.

Keywords : ATLAS ITk Upgrade to HL-LHC, Radiation Damage, Higgs Boson, b-quark, Multi-Jet background.

Abstract : ATLAS is one of the two main experiments at LHC with the purpose of investigating the microscopic properties of matter to address the most fundamental questions of particle physics. After the achievements made during the first years of running, the potential reach for new discoveries and precise measurements at LHC is being extended by pushing further the center-of-mass energy and luminosity frontiers through three upgrades of the accelerator culminating in the High Luminosity LHC (HL-LHC). To fully profit from the increased luminosity, two main upgrades of the ATLAS inner detector are planned. The first upgrade was already completed at the beginning of 2015 with the insertion of the IBL, a fourth pixel layer located at just 3.2 cm from the beam line. In the second major upgrade, foreseen for 2024, the full inner detector will be replaced by a completely new inner tracker fully made of silicon devices to cope with the high particle density and the intense radiation environment at the HL-LHC, which during its operational period will deliver 3000 fb^{-1}, almost ten times the integrated luminosity of the full LHC program. This thesis addresses the study of new n+-in-p active edge pixel detectors by developing two novel doping profile analysis methods to study the radiation damage effects on the pixel detectors performance. These methods are the 3D sims imaging method and the TLM Method. TCAD simulation has been used to simulate the doping profiles, the electrical behavior and the radiation damage. Validating the simulation models with data have been done. Moreover, clean-room characterization, as well as testbeam measurement have been performed to test the different detector designs. In the second part of the thesis, I discuss the observation of the decay of the standard model Higgs boson into a pair of b-quarks using the data collected by ATLAS during the LHC Run2 at center-of-mass energy 13 TeV and an integrated luminosity 79.8 fb^{-1} of a proton-proton collision. I contributed to the analysis where the Higgs boson is produced in association with a W or Z boson. The VH(bb) analysis does not consider the tau leptons, I realized a study estimating the impact of their use on the analysis. In addition, for the VH(bb) analysis I have worked on the multi-jet background estimation in the 1-lepton channel using the dijet-mass analysis method.

Université Paris-Saclay
Espace Technologique / Immeuble Discovery
Route de l'Orme aux Merisiers RD 128 / 91190 Saint-Aubin, France

"Nothing is as important as passion.
No matter what you want to do with your life, be passionate.
Follow your passion, figure out what it is you love and discover who you really are!
People with great passion can make the impossible happen.
Follow your passion and it will lead you to your goal."

Dedication

To the memory of my beloved mother, Asma. Her support, encouragement, and constant love have sustained me throughout my life.

To who will always have a piece of my heart, to your smile which brightens up my days...
To my lovely children Abdelrahman and Asma. You have made me stronger, better and more fulfilled than I could have ever imagined.
I love you with all my heart.

To all the heroes who paid their lives in the defense of the land of beloved Palestine.
To the city that I was born in her heart, and accompanied me in my heart wherever I went, for you O flower of cities, O Jerusalem.

À la mémoire de ma mère bien-aimée, Asma. Son soutien, ses encouragements et son amour constant m'ont soutenue tout ma vie.

À toi qui aura toujours un morceau de mon coeur, à ton sourire qui illumine mes jours...
À mes adorables enfants, Abdelrahman et Asma, qui m'ont rendue meilleur, plus fort et plus épanoui que je n'aurais pu l'imaginer.
Je vous aime de tout mon cœur.

À tous les héros qui ont payé leur vie pour la défense de la terre de la Palestine bien-aimée.
À la ville où je suis né dans son cœur et qui m'a accompagné dans mon coeur partout où je suis allé, pour toi, fleur des cités, ô Jérusalem.

Acknowledgments

"Anything that makes you smile, keep it secret."

This thesis has been kept on track and been successfully completed with the support and encouragement of numerous people including my well wishers, my family and friends, and my colleagues. Therefore, at the end of my thesis, it is my greatest pleasure to offer my sincere gratitude to them all. Thanks for all those people who made this thesis possible and an unforgettable experience for me.

The start of this thesis was with you Marie-Helen Schune, when you in the first place welcomed me as a master student in NPAC. Thanks for believing in me and expressing your admiration of all what I am doing each time we meet.

Foremost, I would like to express my sincere gratitude to my supervisor Abdenour Lounis, firstly for providing me an opportunity to join the ATLAS groupd as intern. This has opened the door for me to enter in the great particle physics world. Your continuous support, your patience, motivation, enthusiasm, and immense knowledge and your guidance have helped me in all the time of research and writing of this thesis. Abdenour, throughout my thesis, by engaging me in new ideas and giving me the chance to take the initiative in many occasions have strengthened my personal skills as an independent researcher as well as enhanced my abilities to have critical thinking to draw a right conclusions. Your encouragement to attend various conferences and several meeting was of great importance to enhancing me to do more and more. I could not have imagined having a better advisor! A long all the way, your door was always opened for me and you have shown me how a good scientist (and humane!) should be. Without your precious support it would not be possible to conduct this research. Additionally, I would like to thank my co-supervisor, Luc Poggioli, for revising the physics part of this thesis. My deepest appreciation goes to Jean-François Grivaz, who completely followed up with me for every single contribution to the second part of my thesis dedicated for physics analysis in the bb decay channel. Without your wisdom, patience and your brilliant ideas, this would not be possible within the time constraint.

I am deeply grateful to Ahmed Bassalat who introduced me to Abdenour and the ATLAS group at LAL. It was the best idea ever! Moreover, since the beginning when I moved to France, your support, encouragement, advice, and suggestions are invaluable. Thanks for all the fruitful discussions and constructive opinions each time I needed it since I was in the Master. I have learned many things from you, that added a lot to my professional experience and my personality.

I would like to offer my special thanks to Achille Stocchi (Director of LAL), who always cares to know what I was doing and how I was proceeding. Your encour-

agement has motivated me to overcome many difficulties. Your actions and efforts, as a director of LAL, in cooperation with Ahmed, to empower many Palestinian students in various ways and give them the chance to be enrolled in the high energy physics domain is greatly appreciated. I am so proud to be a member of such a lab that is based on the principle of respect for the other. I would like also to show my greatest appreciation to you for being my thesis jury president.

I would also like to acknowledge all the committee members of this thesis for generously offering their time, support, guidance and good will throughout the preparation and review of this document . Special thanks to Anna Macchiolo and Giovanni Marchiori, I am gratefully indebted to both of you for taking time to read this thesis and and give your very valuable comments, and also for the several questions which incented me to widen my research from various perspectives.

I would like to convey my warmest gratitude to all my colleagues from the Pixel-LAL group including former and current members. Special mention to Ahmed, Clara, Evangelous, Dmytro, Dimitris, Jimmy. Thanks for all the discussions throughout my thesis, I have learned a lot from each of you. Special thanks to our technician Stephane Torchet who was always available and ready! Merci Stephane! A very special gratitude goes to the members of the ITk group and RD50 collaboration. I would like to thank the testbeam team and its organisers for being cooperative to share their experience during testbeam campaigns. For all the discussions on testbeam reconstruction and the student time at CERN, I am very thankful to Natascha, Audrey and Julien.

I gratefully acknowledge M. François Jomard (GEMAC laboratory at the University Saint-Quentin-en-Yvelines at Versailles) for his cooperation in developing the new SIMS Imaging method. I would also like to thank all experts from IEF laboratory at Orsay who were involved in the development of the TLM method through kindly sharing their experience and recommendations on the different skills needed for this research project. Without their participation, this contribution could not have been successfully conducted.

My warmest gratitude to all my colleagues from VH(bb)-LAL group for all the discussions and meetings we held. Special thanks for you Yanhui, who were so kind to share his experience in the VH(bb) analysis and framework with me. That helped me to get involved in the analysis within a shorter time. I thank also all the members of the VH(bb) group at CERN and the CxAOD production team, for the stimulating discussions and for the sleepless nights we were working together before deadlines to finish the production in time.

I want to thank everyone in the ATLAS-LAL group, it was fantastic to have the opportunity to do my thesis within your group and great sharing laboratory daily life with all of you during the last three years. I thank you all with a special mention of Nicolas Morange, David Rousseau, Laurent Serin, Laurent Duflot, Marumi

Kado for your tips and recommendation. Thanks, Lydia and Louis for the encouragement. Each time I see you give positive energy, especially during the weekend! Special thanks for you David Delgove for all the fruitful discussions and programming tricks you shared with me. Thanks for all of you who participated in the rehearsals and giving me feedback and suggestions, thanks for your time! Thanks also to my labmate students at LAL for all the good times we shared togather at lunch, the several student breakfast and student seminars, especially Steven, Baptiste, Christophe, Delphine and all the new students. Grand Merci pour tout les membres de Service personnel de LAL et service mission pour votre aide concernant les procedures administratives. Mention spéciale de Sylvie, Isabelle, Catherine, et Dominique (merci pour tout les posters que vous avez imprimé!)

Super merci pour mon amie, Brigitte Adde, qui a toujours voulu savoir ce que je faisais et comment je procédais. Je suis reconnaissant pour ton amour, ta sollicitude et ton soutien moral. Tous les moments agréables que nous avons partagés à différentes occasions me manqueront. Merci de ta patience et de ta façon de me corriger chaque fois que je fais une erreur en français. J'espére qu'il n'y a pas d'erreur dans cette phrase!

And last but by no means least, I would like to thank my family, my brothers, and my sisters, especially my oldest brother Bara, for supporting me spiritually throughout the writing of my thesis and my life in general. Without so much love from your side, this achievement would not be possible.

Finally, thanks for every one who participate in the success of this work even with just a smile!!

Tasneem Saleem
Paris in December 2018

Abstract

Following the successful discovery of the Higgs boson in 2012, and in order to maximise the discovery potential at the LHC and the capability for precision measurements, a new phase with a high luminosity upgrade of the LHC is foreseen for 2026. The HL-LHC will be operating at the maximum center-of-mass energy of 14 TeV and an increased instantaneous peak luminosity up to 7 times the design value of $10^{34} cm^{-2} s^{-1}$, which corresponds to approximately 200 inelastic proton-proton collisions per beam crossing (five times the current value). In order to maintain and improve the ATLAS detector performance, and to cope better with luminosity well beyond the design, ATLAS experiment will replace existing radiation-damaged inner detector with an all-silicon tracking system, the ITk. In the context of the ITk requirement for the high luminosity upgrade, new silicon sensors are currently under development. One of the candidates for silicon pixel sensors is the n-in-p active edge planar pixel sensors. These active edge sensors are promising candidates to instrument the inner layers of the new ATLAS pixel detector for HL-LHC, thanks to its radiation tolerant properties and the increased fraction of active area due to a distance as low as 50 μm between the last pixel implants and the active edge.

The first part of this thesis addresses the study of these new active edge pixel detectors by developing two novel doping profile analysis methods to study the radiation damage effects on the pixel detectors performance. These methods are the 3D-SIMS imaging method and the TLM Method. Moreover, TCAD simulation has been used to simulate the doping profiles, the electrical behavior, and radiation damage. Validating the simulation models with data have been done. Moreover, clean-room characterization, as well as testbeam measurement have been performed to test the different detector designs.

The second part of the thesis discusses the observation of the standard model Higgs boson decay into b-quark pair using the data collected by ATLAS during the LHC Run2 at center-of-mass energy 13 TeV and an integrated luminosity 79.8 fb^{-1} of a proton-proton collision. In the VH(bb) production mode, no sub-channel that considers the tau leptons in the final state exists. This work will present a feasibility study to verify the gain of using the taus in the analysis. Among the background processes for the VH(bb) signal, the QCD multi-jet background provide no real leptonic signatures, but still have the potential to contribute as a non-negligible background component. Due to difficulties encountered in modelling this background using Monte Carlo methods, data driven approaches are used instead. In this thesis, the estimation of the multi-jet background, in particular, in the 1-lepton channel using the dijet-mass analysis method is studied.

Keywords: Atlas, ITk, HL-LHC upgrade, Planar pixel silicon detector, Active edges pixel technology, SIMS, TLM, TCAD, Radiation damage, Testbeam, Standard Model Higgs, VH associated production, bottom-quark, tau leptons, multi-jet background.

Contents

1 Introduction **1**

2 The Large Hadron Collider and the ATLAS experiment **5**

2.1 The Large Hadron Collider Accelerator at CERN 6

2.2 The ATLAS Experiment at the Large Hadron Collider 12

2.2.1 Physics Goal of ATLAS 13

2.2.2 The layout of the ATLAS detector 14

2.2.3 Inner detector 14

2.2.3.1 Pixel detector 17

2.2.3.2 SemiConductor tracker (SCT) 18

2.2.3.3 Transition Radiation Tracker (TRT) 18

2.2.4 Calorimeters 19

2.2.4.1 Electromagnetic (EM) calorimeter 19

2.2.4.2 Hadronic calorimeter 20

2.2.5 Muon spectrometer 21

2.2.6 The trigger and data-acquisition system 21

2.3 Objects reconstruction and particle identification with ATLAS detector: Run-2 25

2.3.1 Tracks 26

2.3.2 Primary vertex 27

2.3.3 Tracks and vertex reconstruction performances 29

2.3.4 Electrons 31

2.3.5 Muons 31

2.3.6 Jets . . . 32
2.3.7 b-tagging . . . 33
2.3.8 Missing Transverse Energy . . . 35

I Development of pixel detector for ATLAS Inner Tracker (ITk) upgrade at HL-LHC **37**

3 Towards the High-Luminosity LHC **39**

3.1 Motivation . . . 39
3.2 LHC and ATLAS upgrade plans . . . 40
3.2.1 ATLAS performance at the HL-LHC . . . 42
3.2.2 The ATLAS physics at the HL-LHC . . . 43
3.3 Improvements during the first long shutdown, LS-1 . . . 44
3.3.1 The ATLAS Pixel Detector upgrade - Phase-0: IBL, 2013-2015 44
3.3.2 Tracking performance of the ATLAS Inner Detector with IBL in Run-2 . . . 46
3.4 ATLAS Detector upgrades for increasing luminosities, Phase-I: 2019-2020 . . . 46
3.5 Major detector upgrades for HL-LHC, Phase-II: 2024-2026 . . . 47
3.5.1 The ATLAS inner tracker upgrade - ITk . . . 48

4 Silicon particle detectors: Theoretical background **51**

4.1 Working principles of silicon pixel sensors . . . 52
4.2 Fundamentals of Silicon detectors . . . 53
4.2.1 Doping . . . 53
4.2.2 The pn-junction . . . 54
4.3 Radiation-Matter Interactions . . . 59

4.3.1 Interactions of charged particles 60
4.3.2 Photon interactions 63
4.3.3 Interaction of Hadrons 65
4.3.4 Interactions of neutral particles 65
4.4 Crystal defects from irradiation and their implications 65
4.4.1 Surface defects 65
4.4.2 Bulk defects 67
4.4.3 Defect annealing 72

5 The ATLAS Pixel Detector 75

5.1 Pixel detector in particle physics 76
5.1.1 Hybrid planar pixel detector 76
5.1.2 Pixel sensors Fabrication Process 77
5.2 The actual ATLAS pixel detector 80
5.2.1 Planar pixel technology 81
5.2.2 3D pixel techonlogy 84
5.3 The ITk pixel detector for HL-LHC Phase-II 85
5.3.1 Requirement of Planar pixel sensor technologies for HL-LHC upgrade 87
5.3.2 Other options for pixel sensor technologies for the upgrade . . 88
5.4 R&D study to improve the future ATLAS pixel sensor design 89
5.4.1 Active edge technology 90
5.4.2 Sensor electrical characterization 92
5.4.3 Results 95
5.4.4 Conclusions 98

6 Innovative methods for silicon pixel detector doping profile analysis 101

6.1 Secondary Ion Mass Spectroscopy Method (SIMS) 102

6.1.1 SIMS Instrumentation 103

6.1.2 SIMS data quantification 105

6.2 3D Doping Profile Measurement Using SIMS Imaging Method 109

6.3 TCAD Simulation models 110

6.3.1 Simulation tools to accelerate innovation 110

6.3.2 Frameworks and available algorithms 111

6.3.3 Meshing strategy 113

6.4 Experimental validation of TCAD simulation via SIMS method . . . 114

6.4.1 Comparison of doping profile measurements with TCAD simulations 114

6.5 Radiation damage in active edge pixel sensors 118

6.6 TLM method to study irradiation effect on active doping profile in pixel detectors 121

6.6.1 Motivation 121

6.6.2 Overview of the active dopant in semiconductor 122

6.6.3 Transmission Line Matrix (TLM) Method 124

6.6.4 TLM samples geometry and layout 126

6.6.5 TLM measurement 128

6.6.6 Experimental procedure 132

6.6.7 Results 133

6.6.8 Cross-check of TLM results 137

6.6.9 Conclusion 138

7 Testbeam Characterization 141

7.1 Testbeam facilities . . . 142
7.1.1 DESY . . . 142
7.1.2 Super Proton Synchrotron (SpS), CERN . . . 142
7.2 Testbeam Setup . . . 143
7.2.1 The EUDET telescopes for particle tracking . . . 144
7.2.2 Cooling . . . 146
7.2.3 Mounting devices . . . 147
7.2.4 Data acquisition software . . . 147
7.2.5 Online data monitoring . . . 148
7.3 Testbeam data analysis chain . . . 148
7.3.1 Track reconstruction . . . 149
7.3.2 Reconstructed Data analysis . . . 151
7.3.2.1 Cluster size . . . 151
7.3.2.2 Residuals and Spatial resolution . . . 152
7.3.2.3 Hit efficiency . . . 153
7.4 CERN Testbeam Results . . . 154
7.4.0.4 Systematic uncertainty . . . 157

8 Conclusion and Outlook I **161**

II Search for the Higgs boson in the $b\bar{b}$ decay channel with the ATLAS experiment **165**

9 Standard Model Higgs observation in ATLAS **167**

9.1 The Standard Model of Particle Physics . . . 167
9.1.1 Elementary particles in SM . . . 168

9.1.2 Interaction and force carriers of SM . . . 170
9.2 Spontaneous symmetry breaking and electroweak theory . . . 171
9.2.1 The BEH mechanism . . . 172
9.3 Higgs boson production and decay predictions at the LHC . . . 175
9.3.1 Higgs production mechanisms . . . 175
9.3.2 Higgs boson decay . . . 178
9.3.2.1 Bosonic decay modes . . . 179
9.3.2.2 The fermionic decay channels . . . 180
9.3.3 VH$\rightarrow b\bar{b}$ Channel . . . 181
9.4 LHC Higgs results . . . 185

10 Search for standard model Higgs boson decay into b-quark pair in the VH($b\bar{b}$) mode 189

10.1 Introduction . . . 190
10.2 Data and simulated event samples . . . 193
10.3 Object and event selection . . . 196
10.3.1 Analysis specific object definition . . . 196
10.3.2 Trigger selection . . . 200
10.3.3 Event selection and categorization . . . 201
10.3.4 Additional selections for dijet-mass analysis . . . 205
10.3.5 Analysis regions . . . 206
10.4 Systematic Uncertainties . . . 207
10.4.1 Experimental uncertainties . . . 207
10.4.2 Uncertainties on the MC modelling of signal and backgrounds 208
10.4.2.1 Signal uncertainties . . . 209
10.4.2.2 Background uncertainties . . . 210

10.4.3 Uncertainties of the multi-jet background . . . 213
10.5 Statistical Analysis . . . 214
10.5.1 Multivariate analysis . . . 215
10.5.2 Dijet-mass analysis . . . 216
10.5.3 Diboson analysis . . . 218
10.6 Results . . . 218
10.6.1 Results of the Multivariate analysis . . . 218
10.6.2 Results of the dijet-mass analysis . . . 219
10.6.3 Results of the diboson analysis . . . 225
10.7 Results of combinations . . . 225
10.7.1 Run-1 and Run-2 combination for VH,H$\to b\bar{b}$ . . . 225
10.7.2 Observation of H$\to b\bar{b}$ decays: combination of all production modes . . . 225
10.7.3 Observation of VH production: combination of all decay modes 228

11 Feasibility study of using taus in VH(bb) analysis 231
11.1 Motivation . . . 231
11.2 Methodology of the feasibility study . . . 232
11.2.1 Event Samples . . . 232
11.2.2 Analysis chain . . . 233
11.2.3 CxAOD Framework . . . 234
11.3 Tau identification and selection . . . 235
11.4 Z($\tau\tau$)H(bb) channel . . . 238
11.4.1 The hadronic channel, $\tau_{had}\tau_{had}$ . . . 239
11.4.1.1 Event selection criteria . . . 239
11.4.1.2 Results . . . 242

11.4.2 The semi-leptonic channel, $\tau_{lep}\tau_{had}$ . . . 243
11.4.2.1 Event selection criteria . . . 243
11.4.2.2 Results . . . 244
11.4.3 Optimizing the p_T^Z cut in the semi-leptonic channel . . . 247
11.5 W($\tau\nu$)H(bb) channel . . . 248
11.6 Conclusion . . . 249

12 Multi-jet background estimation in the 1-lepton channel 251
12.1 Template method . . . 252
12.2 Defining control region for the multi-jet template . . . 252
12.3 1-lepton channel: MVA analysis . . . 253
12.3.1 Shape uncertainties . . . 260
12.3.2 Normalisation uncertainties . . . 261
12.4 1-lepton channel: dijet-mass analysis . . . 263
12.4.1 Systematics uncertainties . . . 269
12.5 Multi-jet estimation in the 0- and 2-lepton channel . . . 270
12.5.1 0-lepton channel . . . 270
12.5.2 2-lepton channel . . . 272

13 Conclusion II 273

List of Figures 277

List of Tables 295

Bibliography 301

Chapter 1

Introduction

We look into the sky and see the entire history of the universe in front of our eyes. We question its origin, its destiny and what it is made of. How the universe was created? what is it made of? how much of space do we know? what holds the world together? These are a few questions that puzzled scientists over the centuries and many efforts have been made to understand the laws of nature. Nowadays, the scientists at CERN, the largest laboratory of particle physics in the world, seeking and finding answers to questions about the universe.

The Large Hadron Collider (LHC) at CERN accelerates and collides proton bunches at unprecedented energies, with the highest instantaneous luminosities achieved in hadron colliders so far. The proton-proton collisions provide access to an extended kinematic regime, which is probed by two multi-purpose experiments, ATLAS and CMS, able to test Standard Model (SM) predictions for elementary particles and their interactions, and to explore new physics scenarios beyond the SM (BSM). The search for the smallest building blocks of matter has been crowned by the recently discovered Higgs boson. However, all the discoveries of tiny structures could not be made without the parallel development of accelerators and particle detectors.

This thesis is divided into two complementary parts: the **first part** is devoted to the development of novel pixel detector for ATLAS Inner Tracker (ITk) upgrade at HL-LHC to maintain and improve the detector performance as well as to insure high performance tracking efficiency in the harsh environment of the HL-LHC.

Chapter 2: The LHC accelerator and some fundamental concepts of accelerator physics are introduced. A detailed description of the actual ATLAS detector with its several sub-detectors are presented. The object identification and reconstruction with the ATLAS detector, for all the main objects are summarized.

Chapter 3: The motivations and plans for the HL-LHC upgrade of the accelerator and of the ATLAS detector are presented. The experimental challenges and requirements for the three upgrade phases are discussed.

Chapter 4: The working principle of silicon-based detectors, principles of how

particles interact with matter, along with damages induced in the silicon sensors after irradiation are explained.

Chapter 5: Overview of the pixel detector in particle physics with a focus on the ATLAS pixel detector is presented. Detailed description of the actual pixel detector and the requirement for the ITk upgrade is given. Section 5.4, presents my contribution to one of the R&D activities, to study the performance of all the design variations of the novel active edge pixel sensors.

Chapter 6: Two innovative methods, that have been developed to study the doping profile in the silicon pixel detectors, are presented. The new 3D-SIMS doping profile technique is described in section 6.2. A comparison of measured and simulated doping profile, for the validation of simulation, is presented in section 6.4. In section 6.5, radiation defects have been simulated to investigate the electrical characterization before and after irradiation. Simulated leakage current as a function of voltage are compared to data. Section 6.6 presents a study of irradiation effect on active doping profile in pixel detectors using the TLM method, used for the first time in High Energy Phyiscs (HEP) domain.

Chapter 7: The various results from the CERN testbeam measurement of active edge pixel module to investigate the module hit efficiency is presented. Active and slim edge designs are compared.

Chapter 8: A summary of the main results obtained in the first part of the thesis is given, including an outlook on the possible outcome and future objectives of the presented research.

The **second part** is dedicated to the search for the Higgs boson in the $b\bar{b}$ decay channel with the ATLAS experiment.

Chapter 9: A brief overview of the SM and Higgs mechanism is presented, including description of the Higgs production and decay mechanisms. A summary of the latest LHC results in the Higgs sector is given.

Chapter 10: The analysis searching for the decay of the SM Higgs boson to a pair of bottom-quarks, in association with the production of a vector boson, VH(bb), using 79.8 fb^{-1} of data recorded by ATLAS during 2015-2017 is discussed.

Chapter 11: My contribution to estimate the impact of using the tau leptons in the VH(bb) analysis is presented. The motivation, the procedure, the selection criteria and the results from this feasibility study are discussed.

Chapter 12: Overview of the multi-jet estimation in the VH(bb) analysis. My contribution to the estimation of multi-jet background in the 1-lepton channel is presented.

Chapter 13: Outlines the general conclusions of the work presented in second part of this thesis.

Chapter 2

The Large Hadron Collider and the ATLAS experiment

Contents

2.1 The Large Hadron Collider Accelerator at CERN 6
2.2 The ATLAS Experiment at the Large Hadron Collider . . . 12
2.2.1 Physics Goal of ATLAS 13
2.2.2 The layout of the ATLAS detector 14
2.2.3 Inner detector 14
2.2.4 Calorimeters 19
2.2.5 Muon spectrometer 21
2.2.6 The trigger and data-acquisition system 21
2.3 Objects reconstruction and particle identification with ATLAS detector: Run-2 25
2.3.1 Tracks 26
2.3.2 Primary vertex 27
2.3.3 Tracks and vertex reconstruction performances 29
2.3.4 Electrons 31
2.3.5 Muons 31
2.3.6 Jets 32
2.3.7 b-tagging 33
2.3.8 Missing Transverse Energy 35

Le Conseil Européen pour la Recherche Nucléaire (European Organisation for Nuclear Research) (CERN), located in Geneva, Switzerland, was founded in 1954. CERN's first operational accelerator was the Synchrocyclotron, built in 1957, that provided 33 years of service. The Proton Synchrotron (PS) started up in 1959 and the Super Proton Synchrotron (SPS) in 1976. Both are still in use today. In 1989 the Large Electron-Positron Collider (LEP) started operation. After eleven successful years it was shut down in 2000 to make place in the same tunnel for the LHC, a proton-proton collider inaugurated in 2008. After initial low energy tests, when the data-taking began in 2010 the LHC replaced the Tevatron as the world's

most powerful particle accelerator. This Chapter is dedicated to the introduction to the LHC complex, with its accelerator systems, and a brief overview of the current ATLAS detector.

2.1 The Large Hadron Collider Accelerator at CERN

The Large Hadron Collider (LHC) is a two ring hadron accelerator installed in a 26.7 km circular tunnel that sits between the Jura mountains in France and Lake Léman in Geneva, Switzerland. The tunnel was originally constructed in the late 1980s for the Large Electron Positron (LEP) accelerator. LEP was decommissioned in 2000 and LHC civil works commenced in 1998, and its installation was finished in 2008. The tunnel has 8 straight sections and 8 curved sections and lies at a depth between 45 m and 170 m underground.

The LHC is capable of accelerating and colliding hadrons, namely protons, and heavy ions. The injection of protons and heavy ions into the LHC is done by the previously existing infrastructure: the Linear Accelerators Linac2 (protons) and Linac3 (heavy ions), Booster, the Proton Synchrotron (PS) and the Super Proton Synchrotron (SPS). They perform the pre-acceleration of the particles that are injected into the LHC ring.

As a proton-proton collider, the LHC was designed for a centre-of-mass energy of 14 TeV which is achieved from a 450 GeV beam injected from the Super Proton Synchrotron (SPS). Unlike the particle-antiparticle colliders, the LHC must have two separate rings for the counter rotating beams. Due to the lack of space in the LEP tunnel, the LHC had to use the two-in-one superconducting magnet design[1]. The LHC relies on the superconducting dipoles to steer the beams and keep them on the required trajectory. The magnetic field of the dipoles are generated by passing 12 kA through niobium-titanium cables which become super-conductive at 10 K. The use of super-fluid helium, as a coolant, brings the temperature of the magnets further down to 1.9 K. The 1232 dipole magnets make up to 80% of the LHC circumference. The 392 quadrupole magnets on the other hand, are used to focus the beams just before the interaction points in order to maximise the rate of collisions. For the other sections, as shown in Figure 2.1 , one straight section is used for the Radio Frequency (RF) cavities, one for the beam dump, two for cleaning the beam halo 1 and the other four are used by the detectors as interaction points.

The LHC depends on (RF) cavities to increase the energy of the two beams, only 16 RF cavities in total are used, eight for each beam. At the other sections, the LHC uses superconducting magnets to steer and focus the beam. To achieve precision measurements of interesting physics events (events with a cross section in the order of pico-barn, such as the Higgs production), the collider must operate with a high luminosity.

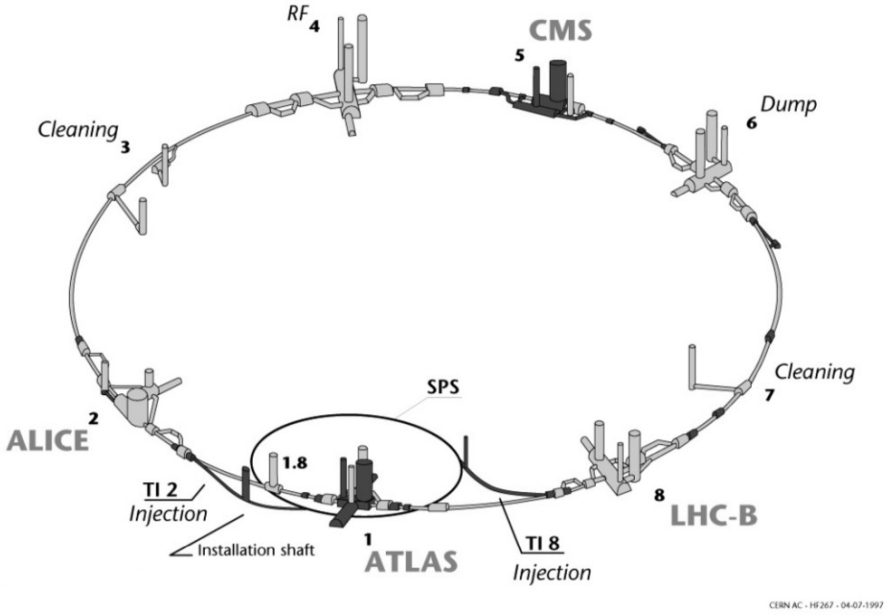

Figure 2.1: The LHC Layout

The instantaneous **luminosity** $\mathcal{L}_0$ determines the number of events per cm^2 per second for a certain process. For a specific number of bunches, N_b , and particles per bunch in each beam, n_i, the instantaneous luminosity is given as:

$$\mathcal{L}_0 = \frac{r}{4\pi}\frac{N_b f n_1 n2}{\sigma_x \sigma_y} \tag{2.1}$$

where f is the revolution frequency, and σ_i are the transverse beam dimensions in the x- and y-axis. The reduction factor, r, accounts for a non-zero crossing angle and the length of the bunch which is assumed to be equal in each beam. It is also assumed that the beams have a gaussian profile and equal velocities. For the LHC, the reduction factor is about 0.8. The interaction rate, R, for a given physics process can be determined from the instantaneous luminosity and the cross-section for that process, σ by,

$$R = \mathcal{L}_0 \sigma \tag{2.2}$$

If we integrate the instantaneous luminosity with respect to time, we get the integrated luminosity, L, which is given in units of cm^{-2}.

$$L = \int \mathcal{L}_0 \, dt \tag{2.3}$$

By using 2808 bunches of 10^{11} protons with a 25 ns spacing, the LHC can achieve an instantaneous peak luminosity of $10^{34} cm^{-2} s^{-1}$.

The cumulative luminosity delivered by the LHC and recorded by ATLAS for the 2015, 2016, 2017 and 2018 data-taking periods at $\sqrt{s}$= 13 TeV are shown in Figure 2.2 . The ATLAS data-taking efficiencies are generally above 90%.

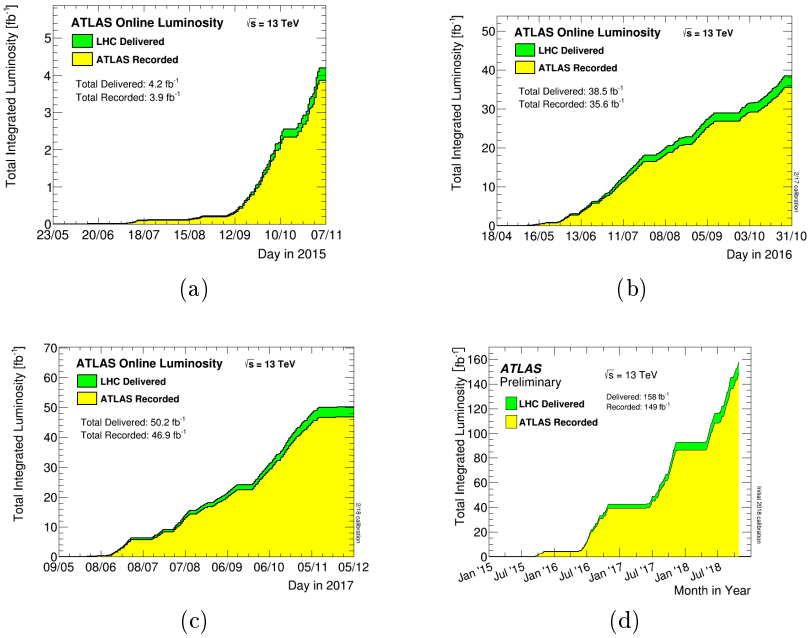

Figure 2.2: Cumulative luminosity versus time delivered by LHC (green) and recorded by ATLAS (yellow) during stable beams for pp collisions at $\sqrt{s}$= 13 TeV for the year of 2015 (a), 2016 (b), 2017 (c) and 2018 (d).[2]

By the end of the 2016 proton physics running period, the peak instantaneous luminosity reached $1 \times 10^{34} cm^{-2} s^{-1}$ with 2220 bunches per beam. The main beam and machine parameters that allowed reaching such luminosities are presented in Table 2.1.

The whole CERN accelerator complex, shown in Figure 2.3, comprises not only the LHC ring, but also the experiments, injectors and other non-LHC experiments. The six LHC experiments, of which four are depicted in the figure, are:

- *A Toroidal LHC Apparatus* (ATLAS): it is one of the two large general-purpose experiments at the LHC, located at intersection point IP1. It is used to study a wide range of physics, including the search for the Higgs boson, extra dimensions, super-symmetry and particles that could make up dark matter.

Parameter	Design	2012	2016	2017
beam energy [TeV]	7	4	6.5	6.5
bunch spacing [ns]	25	50	25	25
β_* CMS/ATLAS [cm]	55	60	40	40(33)
crossing angle [μ rad]	285	290	370/280	300
bunch population N [10^{11} ppb]	1.15	1.65	1.1	1.2
normalized emittance ε [μm]	3.75	2.5	2.2	2.2
number of bunches per ring k	2808	1374	2220	2556
peak luminosity $\mathcal{L}$ [$10^{34} cm^{-2} s^{-1}$]	1	0.75	1.4	1.7
peak average event pile-up μ	≈ 20	≈ 35	≈ 50	≈ 55
peak stored energy [MJ]	360	145	270	320

Table 2.1: Beam and machine parameters for collisions in 2012, 2016 and 2017 (projected) Compared to the design.[3]

- *Compact Muon Solenoid* (CMS): it is the other large general-purpose experiment together with ATLAS, located at intersection point IP5.

- *A Large Ion Collider Experiment* (ALICE): it is a specialized detector to study heavy ion collisions, which at the LHC are lead-lead (Pb-Pb) and proton-lead (p-Pb). The experiment is located at the intersection point IP2.

- *Large Hadron Collider beauty* (LHCb): located at intersection point IP8, it is a specialized B-physics experiment, that measures the parameters of CP violation in the interactions of b-hadrons (heavy particles containing a bottom quark).

- *Large Hadron Collider forward* (LHCf): it is a special-purpose experiment for astroparticle physics, designed to study the particles generated in the "forward" region of collisions, those almost directly in line with the colliding proton beams. It shares the interaction point IP1 with ATLAS.

- *TOTal Elastic and diffractive cross section Measurement* (TOTEM): it shares intersection point IP5 with CMS and has multiple detectors spread over 440 metres. Its purpose is to measure the structure and effective size of the proton, as well as precisely measure the cross section of proton-proton interactions.

The luminosity integrated by ATLAS and CMS during the 2016 proton physics run reached 40 fb^{-1} while the LHCb and ALICE experiments integrated 1.9 fb^{-1} and 13 pb^{-1}, respectively. The integrated luminosity exceeded the target of 25 fb^{-1} in the high luminosity experiments thanks to a higher peak luminosity and to a much improved availability of 48% as compared to around 33% in the earlier LHC runs. The cryogenic system of the LHC achieved a system availability above 98% [3]. The total integrated luminosity and data quality in the years 2015-2017 at 13

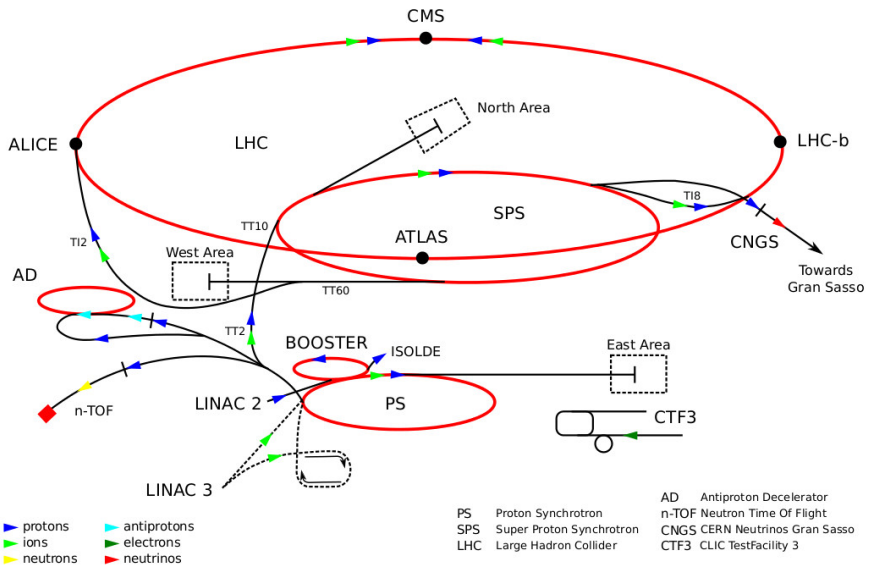

Figure 2.3: The CERN Accelerator Complex showing all experiments around the LHC.

TeV centre-of-mass energy is presented in Figure 2.4. The evolution in the delivered Luminosity versus time over the years 2011-2018 is also shown in Figure 2.5.

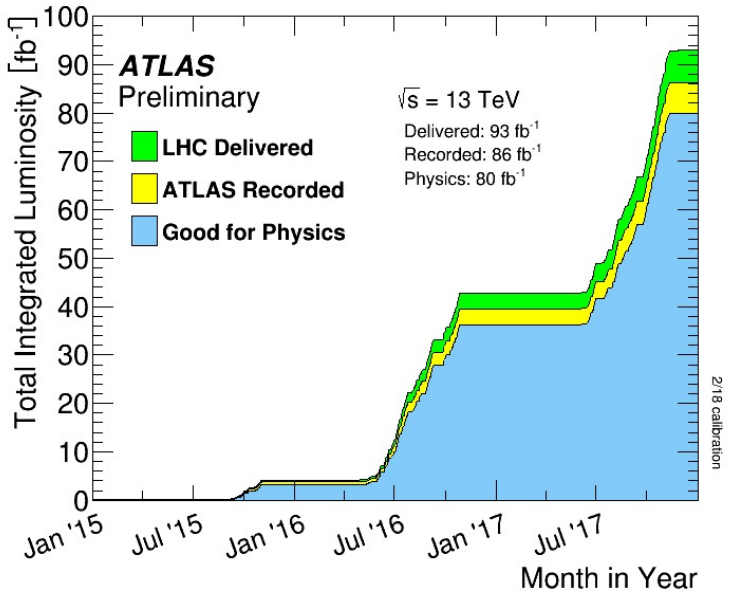

Figure 2.4: Cumulative luminosity versus time delivered to ATLAS (green), recorded by ATLAS (yellow), and certified to be good quality data (blue) during stable beams for pp collisions at 13 TeV centre-of-mass energy in 2015-2017.

In addition to the p-p collisions, one month a year, the LHC also collides heavy

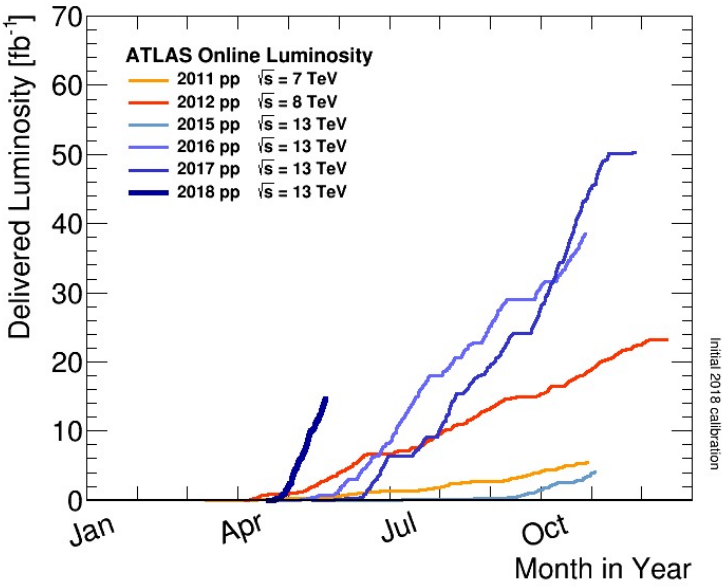

Figure 2.5: Cumulative luminosity versus day delivered to ATLAS during stable beams and for high energy p-p collisions over the years 2011-2018

ions, in particular lead nuclei, at a beam energy of 5.5 TeV and a design luminosity of 10^{27} $cm^{-2}s^{-1}$ [4][5]. ALICE uses this beam that provides an extreme energy density which can be used to study the properties of strongly interacting matter. This includes the possibility of creating a phase of matter known as the quark gluon plasma. The plasma can be studied to understand the phenomena of quark-confinement. ATLAS and CMS also take advantage of the ion beam and study the full range of observables which characterize the hot and dense collisions of the heavy lead ions.

For a given collider luminosity, $\mathcal{L}$, the mean number of interactions per crossing (called **"pile-up"**), μ, is given by:

$$\mu = \frac{\mathcal{L}\sigma}{n_b f} \tag{2.4}$$

where n_b is the number of colliding bunches and f is the bunch crossing frequency, σ is the total inelastic cross section for pp collisions.

Pile-up events are mainly soft interactions which considered as background to the hard interaction interested by the analysis. The level of pile-up effects also the physics objects measurement used in the analysis, the high pile-up worsen the resolution with which we can reconstruct hard-scattering events. The mean number of interactions per bunch crossing for the 2015, 2016 and 2017 datasets are presents

in Figure 2.6. The $< \mu >$ in 2015 data-taking was 13.4, increased to 25.1 and 37.8 in 2016 and 2017 data-taking due to the increased instantaneous luminosities, the total $< \mu >$ for the three years data-taking is 31.9.

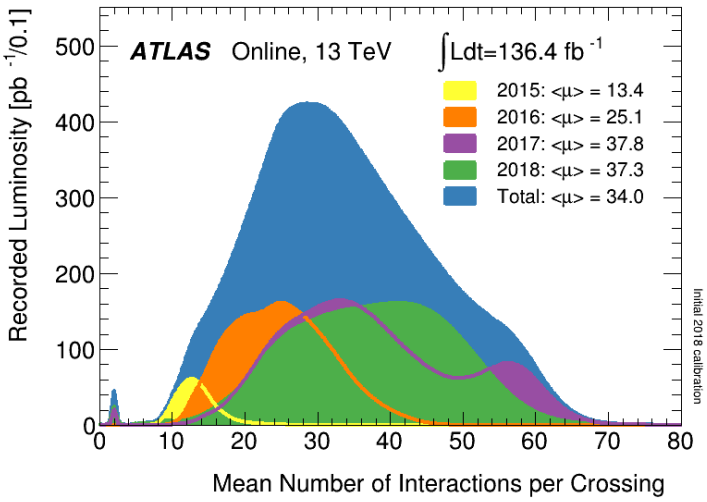

Figure 2.6: Mean number of interactions per bunch crossing for the 2015, 2016 and 2017 ATLAS pp datasets [6].

2.2 The ATLAS Experiment at the Large Hadron Collider

ATLAS (A Toroidal LHC Apparatus) is a particle physics detector designed to take full advantage of the physics potential of the LHC. It is a multi-purpose detector designed to primarily probe proton-proton collisions. ATLAS is designed to make precision measurements in an environment of high interaction rates and radiation doses. The design is highly granular to cope with the high particle fluxes arising from multiple interactions and overlapping events. While providing a large pseudorapidity acceptance and an almost full azimuthal angle coverage, ATLAS has been designed to achieve the following requirements:

- High efficiency in track reconstruction which provides good charged particle momentum resolution.
- Electromagnetic calorimetry to provide electron and photon identification, energy measurements and missing transverse energy measurements.
- Hadronic calorimetry to provide accurate jet and missing transverse energy measurements.

- Good muon identification and momentum measurements for high p_T muons.
- Efficient triggering with a low p_T threshold.
- High resolution at the inner tracker to allow precise measurement of the impact parameter.

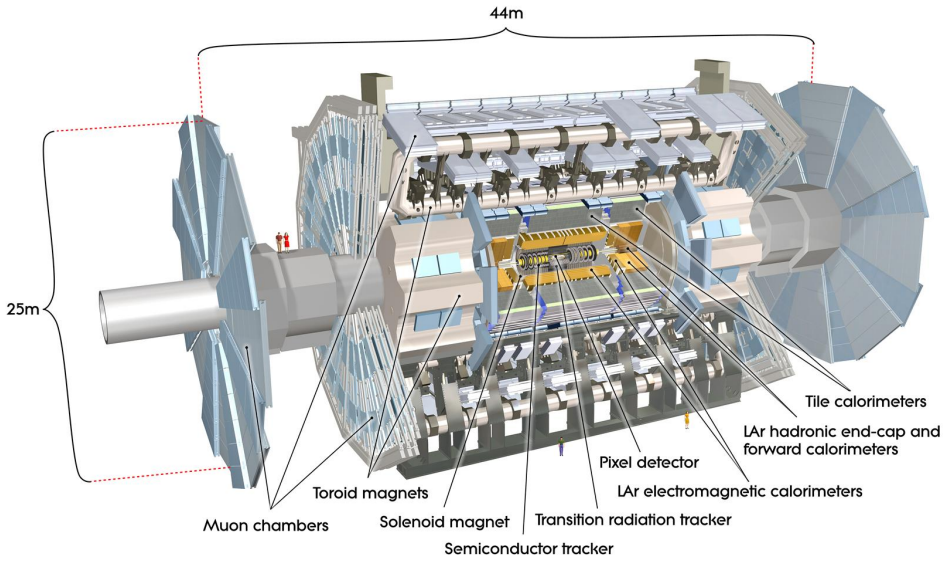

Figure 2.7: Cut-away view of the ATLAS detector.

2.2.1 Physics Goal of ATLAS

The ATLAS detector's design was mostly driven by the search of the SM Higgs boson and other possible extensions at the TeV scale. The discovery of the Higgs boson in 2012 [7][8] with a mass of $125.5 \pm 0.2 GeV/c^2$ [9]has crowned the efforts and the numerous instrumental challenges. In the next years, one has now to measure the properties of the Higgs boson as precisely as possible. Particularly, to provide precise measurement of its mass, width and decay branching fractions, in a variety of channels ($ZZ, \gamma\gamma, WW, b\bar{b}, \tau^+\tau^-$).

The detector must be able to identify and reconstruct many decay modes. For instance, in the $H \rightarrow \gamma\gamma$ case the photons are identified by having high energy deposits in the calorimeter without a preceding track. A constraint on the mass comes from the origin of the two photons and so it is important to know from which primary vertex the photons originated from, which requires high granularity tracking.

In addition, the detector must be able to search for physics beyond the SM. The SM is very successful in describing most of nature's particles and forces with great precision. However, it doesn't explain aspects of physics such as the matter-antimatter asymmetry of the universe, dark matter and gravity. A detector is therefore required that has the broadest sensitivity to the many possible extensions of the SM. In particular, it must be as hermetic as possible, to be highly granular and with linear response up to very high energies.

2.2.2 The layout of the ATLAS detector

Standing at 44 m long with a height of 25 m, the ATLAS detector is the largest particle detector at CERN. It is situated near the CERN main campus and is placed in a cavern 93 m underground. The ATLAS detector uses special cylindrical coordinate system with the notations (r, ϕ, θ). The Interaction Point (IP) is the origin of this coordinate system, r is the transverse radius from the beam pipe, ϕ is the rotational angle in the transverse plane and θ is the polar angle with respect to beam axis. The pseudo-rapidity η is defined as:

$$\eta = \ln\left(tan(\frac{\theta}{2})\right) \tag{2.5}$$

Pseudo-rapidity differences are invariant under boosts along the beam axis. This is particularly of importance with hadron collisions, as it is often the case that one of the colliding quarks or gluons may have a lot more momentum than the other, so the particles produced come out near one end of the detector. When the detected particles are plotted against η , they are effectively shifted to the center of the collision, where the particles come out symmetrically distributed, thus simplifying the analysis.

The ATLAS detector covers at maximum the region $|\eta| < 4.9$[10]. It is made of a central region "barrel" (concentric cylinders surround the beam line) and the region on the sides "end-caps" (disks on the two ends of the barrel). Within these regions, there are 4 sub-detectors. From the IP outwards, there is the inner detector (comprising three different layers Pixel, SemiConductor tracker (SCT), Transition Radiation Tracker (TRT)), the electromagnetic calorimeter, the hadronic calorimeter and finally the muon spectrometer. This can be seen in Figure 2.7.

2.2.3 Inner detector

The Inner Detector (ID), shown in Figure 2.8 aims to measure precisely the point of origin and trajectory of charged particles in the 2 T magnetic field of the central

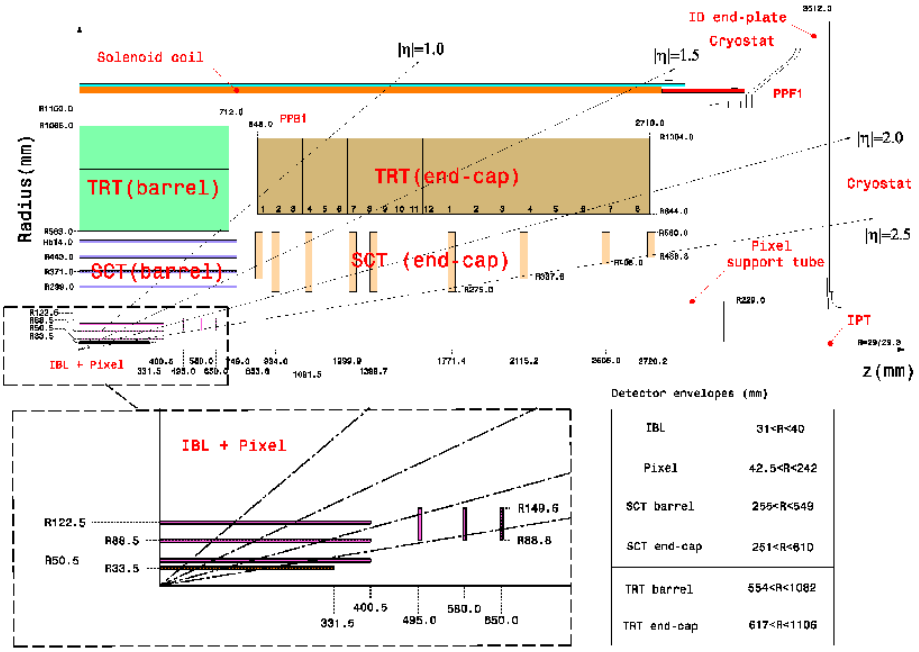

Figure 2.8: The layout of the current ATLAS inner tracking detector, including the additional IBL detector layer.

solenoid. This is achieved by combining very precise measurements from silicon detectors with the continuous tracking of gaseous detectors resulting in excellent pattern recognition and precise momentum measurements. The detector is as thin as possible, to minimise particle interactions before the calorimeter system. To better match the topology of the tracks emerging from the LHC proton-proton collisions, the ID is separated in a barrel part (measuring particles with $|\eta| < 1.2$) and two end-caps (covering the range $1.2 < |\eta| < 2.5$). The barrel region is made of concentric cylinders around the beam axis and the two end-cap regions are made of disks perpendicular to the beam axis. Different technologies are used at different radii to optimise the cost to performance ratio. The innermost layers, immediately surrounding the beam pipe and up to 15 cm, comprise the Pixel detector, that uses hybrid silicon pixel sensors for unambiguous pattern recognition, high accuracy and maximal radiation resistance. The intermediate region (radii from 30 to 60 cm) is covered by the SemiConductor Tracker (SCT), that uses microstrip detectors to provide excellent space resolution over a large area. The outer part (radii from 60 to 95 cm) is made of a large number of small diameter proportional drift tubes (straws) which provide good space resolution in the track bending plane and greatly contribute to pattern recognition with multiple measurements. This detector has also transition radiation detection capability (which helps in electron identification) and hence is called the Transition Radiation Tracker (TRT). The layout of the ID is shown in Figure 2.9 together with its dimensions. More details of the barrel part

are also shown in Figure 2.10.

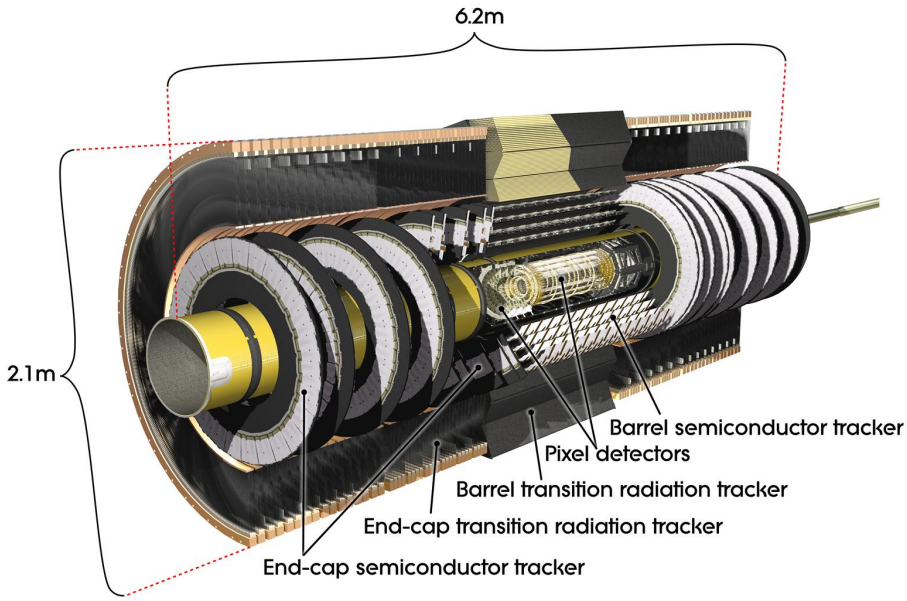

Figure 2.9: View of the Inner Detector, which consists of a set of precision silicon tracking detectors (Pixel and SCT) extending up to a radius of 60 cm surrounded by the TRT gaseous detector.

The typical spatial precision in the bending plane of tracks is of order 15 μm in the silicon part and 150 μm in the TRT. The ID was designed to perform efficient pattern recognition of all particle tracks with transverse momentum above 0.3 GeV up to a luminosity of $10^{34} cm^{-2} s^{-1}$, i.e. up to $\approx$ 25 simultaneous proton-proton interactions. The detector in fact works efficiently with more than 50 simultaneous collisions. Actually, despite the specifications, the current ID has demonstrated to sustain up to 60 interactions per crossing (the current pileup). Both the radius of curvature of the tracks and their extrapolation to the interaction vertex are measured with high precision. This results in a momentum resolution $\Delta p_T/p_T$ of $\approx$ 1% at 20 GeV and better than 50% at 1 TeV (important to measure high-mass particles) and transverse impact parameter resolution better than 20 μm (important for the tagging of the short lived heavy quarks and leptons which come from a displaced or "secondary" vertex). The choice of different detector technologies was driven by the role that each part plays in the measurements. A consequence of these choices is that the silicon part must operate below 0 in a dry nitrogen environment to limit radiation damage, while the TRT works at room temperature with specialised gases.

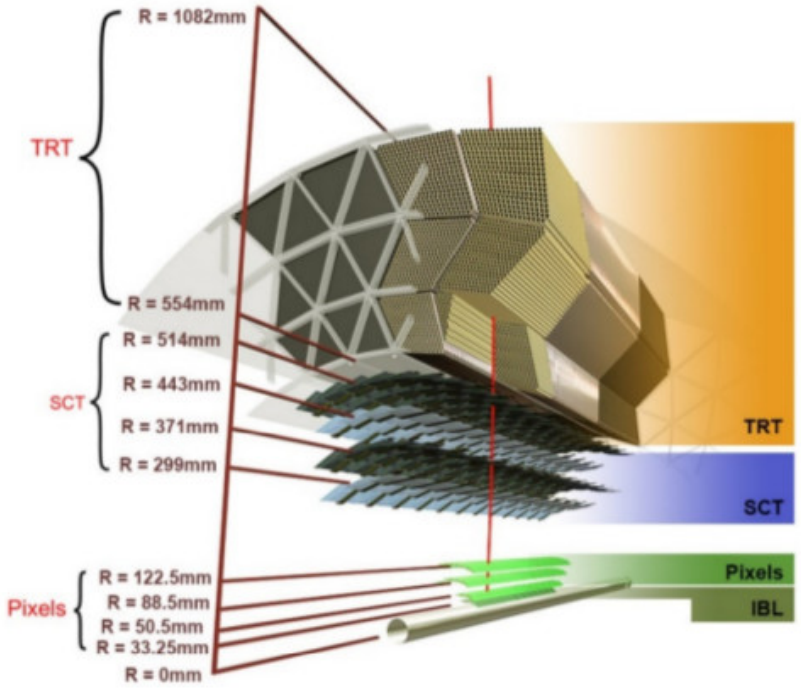

Figure 2.10: Layout of the ATLAS inner detector

2.2.3.1 Pixel detector

The Pixel detector is crucial for the precise extrapolation of the tracks to the pp collision point or to secondary vertices. It was initially made of three barrel layers (at radii 5, 9.8 and 12.2 cm) and three disks (of 8.9 cm inner radius and 15.0 cm outer radius) per side. Each layer is a mosaic of identical modules arranged so as to cover the sensitive surface without any acceptance loss. Each module is built with one sensor and sixteen readout chips, and has a $6.04 \times 1.64\ cm^2$ active area. The $1.7\ m^2$ surface of the Pixel detector is covered with 1744 modules given a total of 80 million individual pixels. Each pixel is a reversely polarised diode of $50 \times 400\ \mu m^2$ in which a current pulse is released by ionisation on the passage of a charged particle. The pixel is created by a n^+ implant on a n-doped silicon substrate. This arrangement allows partially depleted operation after type inversion due to radiation damage, should this be needed at the end of the detector lifetime. Every pixel is directly connected to its readout chain through high density bump-bonding. The passage of a particle is recorded if the current pulse exceeds an adjustable threshold. The pixel efficiency is above 99% and its time resolution is below 25 ns, as needed to unambiguously associate the pixel hits with a given LHC beam-beam interaction.

During the shutdown of the CERN LHC in 2013-2014, an additional pixel barrel layer was installed between the Pixel detector described above and a new, smaller

radius beam pipe. This new pixel layer, the Insertable B-Layer (IBL), has a radius of 33.5 mm, covers up to $|\eta|$=2.7 and improves the robustness and performance of the tracking system at high luminosity by providing an additional space point. The IBL retains the excellent secondary vertex reconstruction efficiency in the presence of high pile-up (> 50 primary vertices). In addition, the IBL improves the impact parameter resolution by a factor of two for low transverse momentum tracks. Smaller pixels (50×250 μm^2), better front-end electronics, realised in 130 nm gate length technology, and minimisation of passive material, with the adoption of CO_2 evaporative cooling and Al power supply cables, are the most important improvements realised in this additional pixel layer.

2.2.3.2 SemiConductor tracker (SCT)

The SCT is crucial for the precise momentum measurement. It consists of 4088 modules, 2112 located over four equally spaced barrel layers and 1976 over eighteen disks (nine per side). The total number of silicon strips is about 6 million. Nearly all the modules are made up of four strip sensors. Two are daisy-chained together to make effectively 12 cm long strips. The two pairs are mounted back to back on a thermally conductive pyrolytic graphite baseboard, with a 40 mrad angle between the strips on opposite sides to give a measurement in the second coordinate. The strips are wire-bonded to a double-sided readout hybrid. The sensors are single-sided p-in-n microstrip detectors, implanted on 285 μm thick high resistivity silicon wafers. Each sensor has 768 AC-coupled readout strips resulting in 1536 readout channels per module. Modules are all the same in the barrel and feature an 80 μm pitch. Four different shapes at different radial distances, with pitch ranging from 57 to 90 μm, are instead needed to match the end-cap geometry. (The end-caps also have some shorter two-sensor modules.) The strip pitch was chosen to optimise two-track separation and to provide an occupancy below 1.0% at full luminosity. The 40 mrad angle is chosen to minimise the number of ghost hits (accidental additional strip pairings) and to keep a longitudinal resolution well below a millimeter. The fast front-end electronics associate all hits to a unique bunch crossing. The only information stored is a 1 if the signal is above a threshold which is adjustable channel by channel. Data are read out through an optical link as soon as a trigger is received. To increase fault tolerance, a redundancy scheme is implemented to reroute signals in case a single chip or a readout link stops functioning.

2.2.3.3 Transition Radiation Tracker (TRT)

The main role of the TRT is to find track trails and eventually identify them as due to electrons. It does not cover the full pseudorapidity acceptance but ends at $|\eta| \approx 2.0$. The TRT is made up of 372,032 straws with 4 mm inner diameter filled with a

Xe-rich gas mixture. The straw diameter comes as a compromise between speed of response, number of ionisation clusters, and operational stability. The length of the straws is different if they are used in the barrel (144 cm) or in the endcap (37 cm), but all other characteristics are the same. The polypropylene transition radiation (TR) material interspersed in the TRT results in a converted X-ray in about 20% (30%) of the barrel (end-cap) straws for a high momentum electron. As the energy loss by ionisation is typically 2 keV (versus the 5 to 15 keV of the TR photons), the TR signal can easily be discriminated using double threshold electronics. The readout requires recording the drift time with a 1 ns precision, corresponding to 130 μm drift length. Gas proportional detectors (like the TRT) require careful monitoring of the amplification factor in the gas mixture. This factor depends on the electric field, the temperature and the gas mixture. All those parameters need to be continuously checked to avoid gain variations exceeding 20%.

2.2.4 Calorimeters

Calorimeters absorb and measure the energies of charged and neutral particles. Calorimeters are usually composed of absorbing high density layers (such as Lead) interleaved with active layers (such as liquid-argon). Electromagnetic calorimeters measure the absorbed energy as particles lose energy when they interact with charged particles in matter, while the hadronic calorimeter sample the energy of hadrons as they interact with the atomic nuclei. The energy measurement is usually localised which means the position of the particle can also be measured. They are also responsible for measuring the direction of the jets and the missing transverse momentum. By studying the shower profile, particle identification becomes possible and can also be involved in the event selection.

ATLAS has two types of calorimeters, the liquid-Argon Electromagnetic (EM) calorimeter and the hadronic calorimeter. The EM calorimeter surrounds the inner detector in the barrel region and is responsible for identifying and measuring the energies of electrons and photons. The hadronic calorimeter surrounds the EM calorimeter and is used to measure the energies of both charged and neutral hadrons. The hadronic calorimeter has a coarser granularity which is acceptable for jet reconstruction. Both calorimeters also have end-caps in the forward regions. The ATLAS calorimeters are shown in Figure 2.11.

2.2.4.1 Electromagnetic (EM) calorimeter

The EM calorimeter is a sampling calorimeter. It uses interleaved Lead and liquid-Argon in a radial accordion geometry where the Lead acts as an absorber and the liquid-Argon as the sampling material. The EM calorimeter has one barrel and two end-caps covering the pseudo-rapidity region $|\eta| < 3.2$[11] and has $\sim$ 170,000 readout

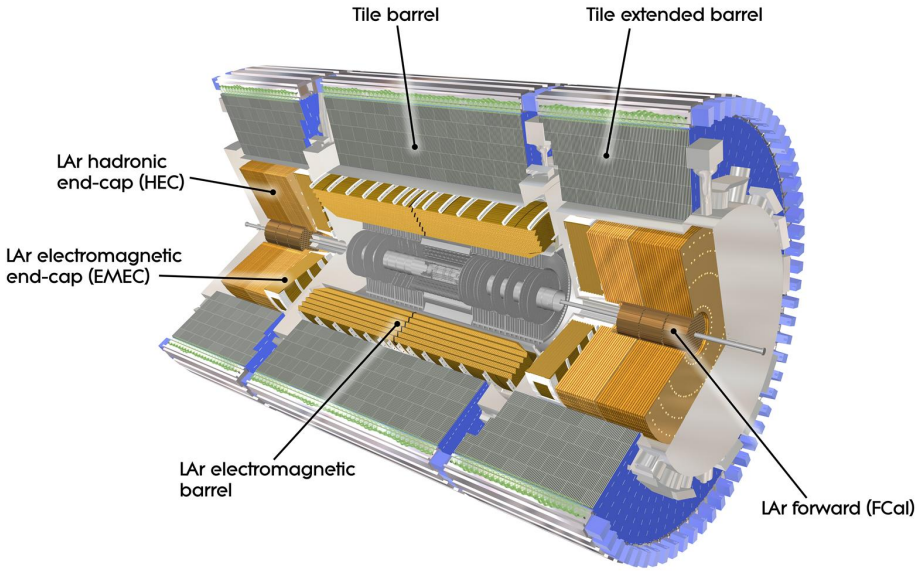

Figure 2.11: The ATLAS calorimeters. Image courtesy of the ATLAS Experiment at CERN, http://atlas.ch.

channels. The barrel is split into two identical halves separated by a gap of 6 mm at z = 0 and is also segmented into three longitudinal sections. The total thickness of the EM calorimeter in the barrel region is $24X_0$[1] and $26X_0$ in the end-caps (The radiation length of the inner detector is about $2.8X_0$). Thus, electromagnetic showers may start to appear in the inner detector and hence a 'pre-sampler' segment is required in the barrel region to allow energy measurement corrections.

2.2.4.2 Hadronic calorimeter

The layer surrounding the EM calorimeter is the hadronic calorimeter. The hadronic calorimeter has two components giving coverage in the region $|\eta| < 4.9$[12]. The first are tiles of steel inter-leaved with scintillators and the second is the liquid-Argon sampling calorimeter similar to the one used in the EM calorimeter. The thickness of the hadronic calorimeter corresponds to 11λ[2] which is enough to minimise the punch-through[3] to the Muon Spectrometer. The tile calorimeter occupies the central

[1] X_0 is the radiation length. It is a characteristic of the material and relates to the amount of energy lost in the material (mostly due to electromagnetic interaction), as high-energy particles travel through it.

[2] λ is the nuclear interaction length and it is the mean path length required to reduce the numbers of relativistic charged particles by the factor 1/e, as they travel through the material. X_0 is not used here as the presence of the stronger hadronic interaction is dominant.

[3] When stray particles are not absorbed at the calorimeters and reach the muon spectrometer.

and two extended barrels while the liquid-Argon occupies the end-caps and forward sections, providing better radiation tolerance. This feature is particularly beneficial for the forward calorimeter as it experiences the highest amounts of radiation and it acts as a good radiation barrier for the muon spectrometer.

2.2.5 Muon spectrometer

The spectrometer measures the deflection of muon tracks in large air-core toroidal magnets. The muon spectrometer is designed to offer triggering information and momentum measurements at a wide range of pseudorapidity and azimuth angles. The muon spectrometer is the largest component in the ATLAS detector. The measurements are achieved using the muon chambers that are placed between the eight superconducting toroidal magnets. The muon chambers all have the same underlying principle of having drift tubes with a thin wire held at high voltages in a tube filled with a gas mixture. When a particle crosses the tube the gas is ionized and an electric current is produced. The Monitored Drift Tubes (MDT) cover the range $|\eta| < 1.05$ and are used in both the barrel and end-caps. They consist of 30 mm Aluminium tubes with a thin central wire. The spatial resolution is around 80 μm. Within every MDT barrel layer a Resistive Plate Chamber (RPC) is placed. This chamber employs two plates with a gas filling the gap providing a spatial resolution of 10 mm. The Cathode Strip Chambers (CSC) are multi-wire proportional chambers that are placed in the innermost end-cap ring, closest to the beam pipe covering the region $2 < |\eta| < 2.7$. The CSC provides two coordinates, one read out from the cathode strips with a spatial resolution of 60 μm and the other through the anode wires (orthogonal to the cathode strips) with a resolution of 5 mm. Finally, the trigger signal is provided by the Thin Gap Chambers (TGC) along with a second coordinate measurement in the end-cap region. The TGCs are very similar to the CSC but have a faster drift velocity. The TGC resolution is about 2 mm to 7 mm and cover the range $1 < |\eta| < 2.7$[13].

2.2.6 The trigger and data-acquisition system

The trigger is responsible for identifying very quickly which bunch crossings contain potentially interesting physics, based on distinctive features, or signatures, such as electrons, muons or photons emerging with high momentum transverse to the beam directions. The data-acquisition (DAQ) system is responsible for collecting the data that are read out from the detectors, putting them into a coherent format and structure, and transporting them, for the selected events, to permanent storage that is provided by the offline computing system and infrastructure. Once stored, they are made available for further processing and analysis in ATLAS Institutes worldwide.

In practice, the trigger and DAQ components are intertwined as illustrated in Figure 2.12. The trigger selection is performed in steps, first using a system of custom electronics processors to reduce the event rate (i.e. the rate of bunch crossings to be recorded) to less than 100 kHz - already a massive reduction compared to the interaction rate of $\approx$ 2 GHz. The data for events that are retained after the first stage of selection, which is called the first-level trigger, are transferred to the DAQ system. The subsequent online selection, called the high-level trigger (HLT), is performed using a large number of rack-based commercial computers that can access the data selectively, guided by the results of the first-level trigger. High-speed commercial networks support data movement, and data storage and staging possibilities exist at various points in the system (in the readout systems connected to the detector electronics, within the HLT processors, and at the output towards the offline computing system).

Requirement

Due to the large number of bunch crossings and the fact that only a small number of events contain interesting physics, a triggering system is required to select and permanently store the events of interest. The triggering system faces the following challenges:

- The bunch crossing rate of 25 ns is a very short time to make a decision on whether to keep or discard the event. It takes longer than 25 ns for a particle travelling at the speed of light to go through the entire detector.
- The $\sim$25 interaction pile-up (for a $10^{34} cm^{-2} s^{-1}$ peak luminosity[14]) increases the volume and complicates the task.
- Only 100 interactions can be recorded from the 1 billion interactions every second (25 interactions $\times$ 40 million bunch crossings every second at a luminosity of $10^{34} cm^{-2} s^{-1}$).

System design

The ATLAS trigger is a three level triggering system, where each level refines the decisions made by the previous one. The triggering system must have a high rejection rate to reduce the 40 million events per second to only 100 events per second while maintaining high efficiency as not to compromise rare physics events.

The data flow of the triggering system is as follows. The main input for the triggering system comes from the calorimeters and muon spectrometer. The Level-I trigger processes this information to identify particles with high transverse momentum (p_T), and/or large missing transverse momentum (E_T^{miss}) and filters the data accordingly. The Level-I trigger then moves the selected events to Read Out Buffers

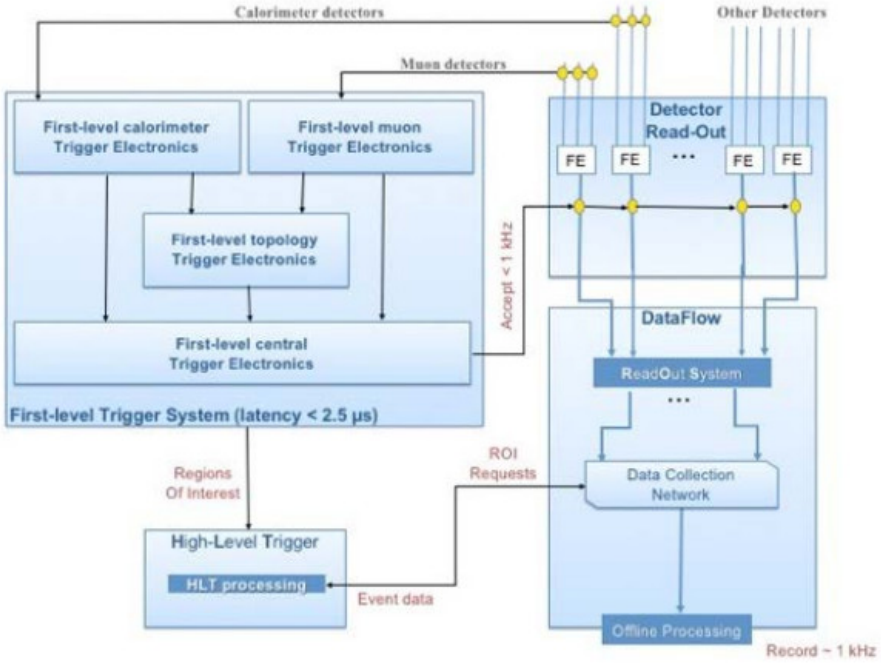

Figure 2.12: Diagram of principal components of the Trigger/DAQ system and interconnections.

(ROB) at a rate $<$ 100 kHz. The data is kept at the ROBs until a decision is made by the Level-II trigger. The Level-II trigger, which uses Region-of-Interest (RoI) information to make its decision, moves the data from the ROB to the full event buffer. This process is known as *Event Building*, because the event data are fragmented at the ROBs and they are joined up together for the Event Filter. At this level, the data rate is reduced to 1 kHz. The *Event Filter* will finally perform offline code algorithms and further filter the events taking the rate down to 200 - 400 Hz.

Level-I triggering system

The Level-I trigger decision relies on the input from the calorimeters and muon spectrometer. The muon spectrometer is used to identify high p_T muons and the calorimeters can identify high p_T electrons, photons, jets and taus decaying into hadrons. The physical size of the muon spectrometer alone implies a time-of-flight interval longer than the 25 ns bunch crossing interval. Also, the pulse shape of the calorimeter signal can extend over a number of bunch crossings. Due to these factors among others, the pipelines were designed to hold a hundred bunch crossing giving the readout electronics a latency of 2.5 μs.

The Level-I trigger also prepares RoI data to help with the selection process at the Level-II trigger. The RoI data includes locations of candidate muons, electrons, photons, jets and hadrons.

High level triggering system

The Level-II trigger and the Event filter define the high level trigger. Both of which are built using PC farms, the Level-II trigger provides a high rejection with limited algorithms and modest computing power. While the Event filter requires extensive computing power with high precision algorithms for a further rejection. As opposed to the fixed latency of the Level-I trigger, the latency of the Level-II trigger is variable and it ranges between 1 ms and 10 ms. The Level-II trigger employs optimized trigger selection algorithms that processes only a fraction of the event data, typically ∼2%. The RoI supplied by the Level-I trigger is the input for these algorithms. This enables the Level-II trigger to request only data from the ROBs holding the interesting features. In addition, the use of the RoI reduces the volume of data to be moved to and analysed in the Level-II trigger system. The Level-II trigger uses many processors from the farm to process the data and can treat several events concurrently.

For the selected events from the Level-II trigger, the event builder creates full events from the fragmented events held at the ROBs. The Event filter receives the selected full events and uses a single processor to implement complicated selection algorithms, which can take up to one second to complete.

The trigger and DAQ system as implemented at the start of Run-1 contained some novel features, such as the ROI mechanism in the first stages of the HLT processing, and the use of offline software in the later stages. At that time, the HLT was composed of two separate computer systems, the second-level trigger and the event filter, merged for Run-2 starting in 2015. Other changes for Run-2 included the addition of a topology processor in the first-level trigger, that could combine signatures, e.g. considering the angular separation between pairs of electrons, along with simple multiplicity requirements already available in Run-1.

With up to about 60 interactions per bunch crossing, the events are intrinsically very complex. It is therefore essential to associate detector activity with the correct bunch crossing, and for the first-level trigger to uniquely identify the bunch crossings containing physics of interest. Otherwise one would need to aggregate the activity over two or more bunch crossings, further complicating the picture. The first-level trigger must start processing a new event every 25 ns, and it must make a decision every 25 ns. However, allowing for propagation delays on cables and fibers $\approx$ 100 m long each way (corresponding to a transmission time of 500 ns) from the detector to the electronics systems and back, as well as processing and data movement within the trigger system, there is a latency of about 2.5 μs. A technique called pipelined processing is used whereby the calculations are broken down into steps that can be completed within 25 ns. In each step, data from different parts of the detector may be processed in parallel. The information pertaining to a given event moves along the processing pipeline, one step every 25 ns, with the final step giving the result

Figure 2.13: Racks of the first-level calorimeter trigger system installed close to the detector.

of the selection; i.e. to discard the event or to retain it for further examination in the HLT. Pending the first-level trigger decision, the information from all bunch crossings is retained in the detector electronics that is mounted on or close to the detector. In many cases, the information (either digital data or analogue signals) is retained, at least logically, in a pipeline memory; i.e. in a first-in-first-out memory.

The great challenges of implementing the first-level trigger can be illustrated taking the example of the calorimeter trigger. On-detector analogue electronics sum the calorimeter signals from 200,000 cells to 7000 trigger towers that are then digitised with 10-bits precision every 25 ns. This corresponds to 7 $\times 10^4$ bits at 4 $\times 10^7$ Hz, i.e. 2.8 $\times 10^{12}$ bits per second. A relevant comparison when ATLAS was being designed in the late 1990s, before the advent of smart phones and broadband home internet access, was the equivalent number of telephone calls, counting $\approx$10 kbps per voice call. Using this analogy, the calorimeter trigger alone required transferring data equivalent to $\approx$ 300 million phone calls into a system that occupies just a few electronic racks (see Figure 2.13).

2.3 Objects reconstruction and particle identification with ATLAS detector: Run-2

The ATLAS sub-detectors can measure energy and momentum. Stable particles that travel a measurable distance in the ATLAS systems can also be identified. The

following summarizes the techniques employed to identify and reconstruct electrons, photons, muons and jets.

2.3.1 Tracks

Tracks are reconstructed from the pixel and SCT detectors [15]. The first step of the track reconstruction [16] is the reconstruction of clusters based on a dedicated algorithm. This algorithm is based on the deposited energy in the pixel SCT, and TRT detectors. The clusterization begins with the deposition of enough energy deposition in one pixel, and usually include multiple adjacent pixels. After the clusterization, primary-tracks are reconstructed with an iterative track-finding algorithm using information of the SCT. A pattern-recognition is used, allowing various combinatorial track candidates. This step is followed by an ambiguity-solver that assigns an individually track score to each candidate. The track score is based on simple measures of the track quality, such as the χ^2 of the track fit, and missing hit in the detector after the fit (hole). The algorithm suppresses the large number of tracks with incorrect assigned clusters. Shared clusters and clusters used in multiple tracks candidates are limited. Clusters can be shared by a maximum of two tracks. A cluster is removed from a track candidate if it decreases the number of shared clusters. The track is then scored again and returns to the order list of remaining candidates. The flow of track candidates through the ambiguity-solver is summarized in Figure 2.14. The requirements for tracks candidates are the following:

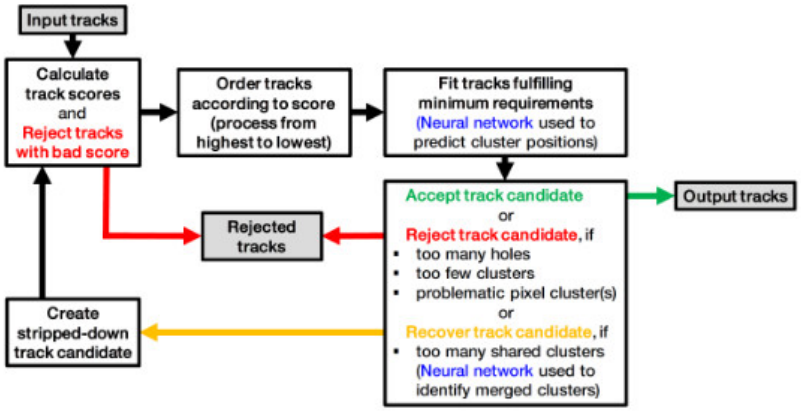

Figure 2.14: Sketch of the flow of tracks through the ambiguity solver. [16]

- $p_T > 400$ MeV,

- $|\eta| < 2.5$,

- minimum 7 of pixels and SCT hits (12 are expected),

- maximum of either one shared pixel cluster or two shared SCT clusters on the same layer,

- no more than two holes in the combined pixel SCT detector,

- no more than one hole in the pixel detector,

- $\left|d_0^{BL}\right| < 2.0mm$,

- $\left|z_0^{BL} sin\theta\right| < 3.0mm$,

where d_0^{BL} is the transverse impact parameter calculated with respect to the measured beam-line position, and z_0^{BL} is the longitudinal difference along the beam line between the point where d_0^{BL} is measured and the primary vertex, θ is the polar angle of the track. The following selections are added for the tight selection of tracks:

- minimum of 9 SCT hits if $|\eta| \leq 1.65$,

- minimum of 11 SCT hits if $|\eta| > 1.65$,

- either one IBL or next-to-innermost-pixel-layer hit,

- no pixel hole,

The performance of track reconstruction in jets can be estimated using a sample of dijets MC events. The reconstruction efficiency of charged-primary-particle as a function of the angular distance of the particle to the jet axis is shown in Figure 2.15. The efficiency is calculated for different p_T ranges. All charged particles studied are required to be created before the IBL. The efficiency is minimum at the center of the jet where track density is maximum, and increases at higher ΔR where density decreases. The track reconstruction efficiency decreases with jet p_T due to an increasing tracks density matched to the jet axis as shown in Figure 2.16 in the regions $|\eta| < 1.2$ and $|\eta| > 1.2$.

2.3.2 Primary vertex

The primary vertex corresponds to the hard scattering point. It is reconstructed from tracks with an iterative vertex finding algorithm [17] [18]. The z-position of reconstructed tracks is used as vertex seed. An iterative fit using the goodness of χ^2 is applied to test the compatibility of tracks with the vertex. Tracks displayed by more than 7 σ are removed from the list, and used to seed new vertices. The iterative procedure is repeated until no additional vertices can be found. Vertices are required to contain at least two tracks. The increasing number of fake tracks in high pile-up environment increases the probability to reconstruct a fake vertex.

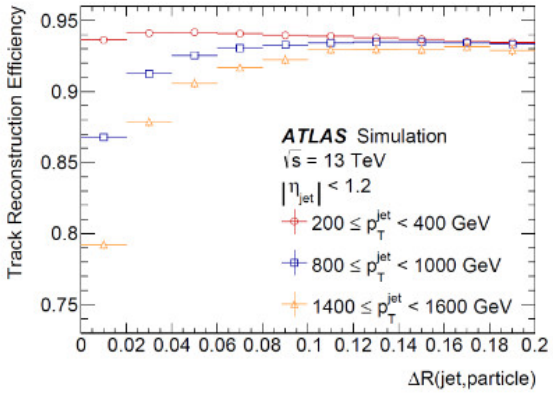

Figure 2.15: The efficiency to reconstruct charged primary particles in jets with $|\eta| < 1.2$ as a function of the angular distance of the particle from the jet axis for various jet p_T for simulated dijet MC events.[16]

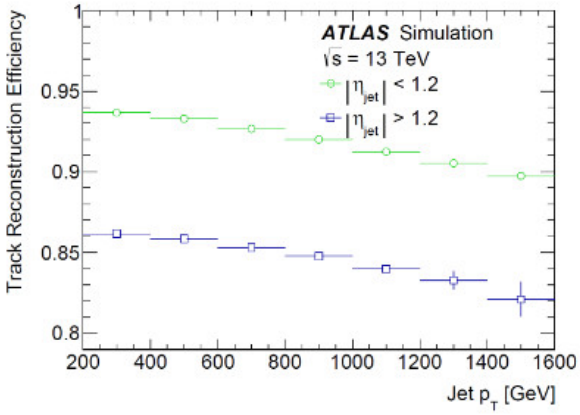

Figure 2.16: The track reconstruction efficiency is compared for charged primary particles in jets with $|\eta| < 1.2$ ($|\eta| > 1.2$) for the entire jet-p_T range as a function of the jet p_T for simulated dijet MC events.[16]

Primary vertices are difficult to reconstruct due to the high number of vertices in the collisions. The number of reconstructed vertices as a function of the average number of interactions per bunch crossing is shown in Figure 2.17.

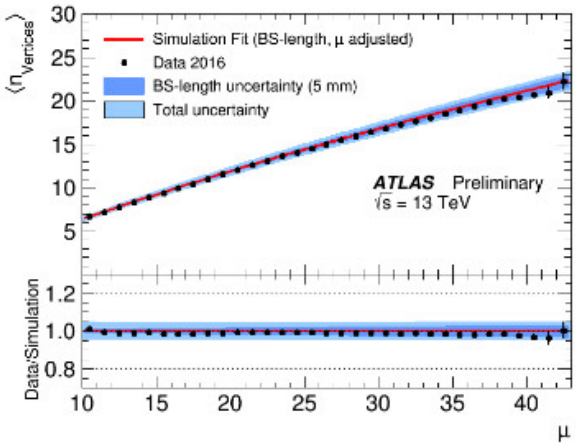

Figure 2.17: Distribution of the average number of reconstructed vertices as a function of μ. The curve represents the result of a fit to the simulation, while dots correspond to the 2016 data.[19]

2.3.3 Tracks and vertex reconstruction performances

Figure 2.18 shows the primary track reconstruction efficiency parametrized in two-dimensional bins of p_T and η. This quantity, ε_{trk} is determined from the simulation and defined as:

$$\varepsilon_{trk}(p_T, \eta) = \frac{N_{rec}^{matched}(p_T, \eta)}{N_{gen}(p_T, \eta)} \tag{2.6}$$

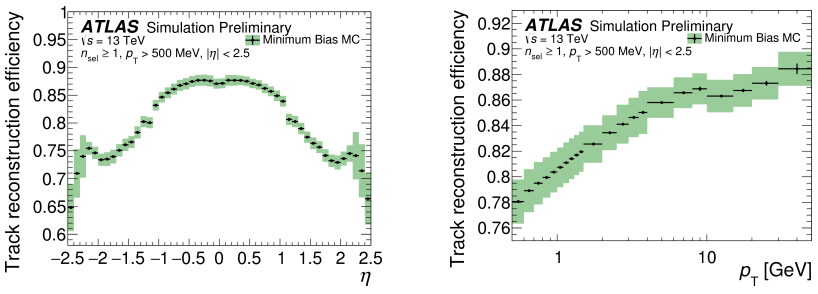

(a) (b)

Figure 2.18: The track reconstruction efficiency as a function of η (a) and p_T (b).[20]

where p_T and η are generated particle properties, $N_{rec}^{matched}(p_T, \eta)$ is the number of reconstructed tracks matched to a generated charged particle and $N_{gen}(p_T, \eta)$ is the number of generated charged particles in that bin.

The track reconstruction efficiency, Figure 2.18(a) is lower in the region $|\eta| > 1$ due to particles passing through more material in that region. The slight increase in efficiency at $|\eta| \approx 2.2$ is due to the particles passing through an increasing number of layers in the ID end-cap.

As mentioned earlier in this chapter, a new layer in the pixel detector, the IBL was inserted. Figure 2.19 shows the improvement of the transverse impact parameter resolution ($\sigma(d_0)$) between the 2012 data and the 2015. We see the clear gain thanks to the IBL usage.

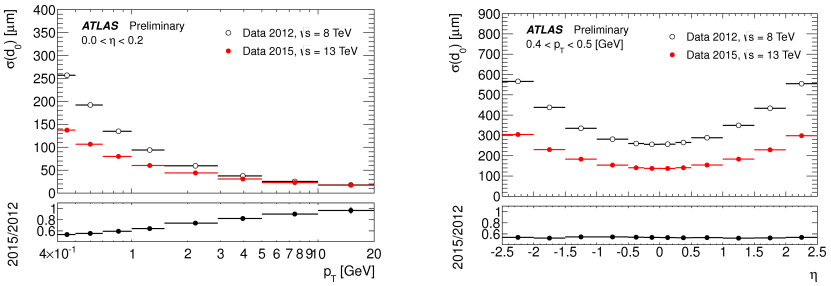

(a) (b)

Figure 2.19: The transverse impact parameter resolution in 2015 (with IBL) and 2012 (without IBL) as function of p_T (a) and η (b).[21]

In a high pile-up scenario the detector occupancy increases and this affects the number of reconstructed tracks without corresponding primary or secondary particles, called fake tracks. The dependence of the number of reconstructed tracks as a function of the number of interaction per beam crossing is shown in Figure 2.20.

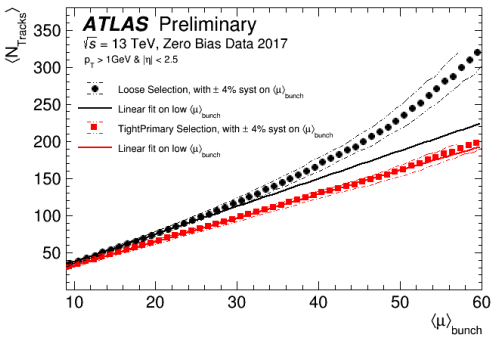

Figure 2.20: Average number of reconstructed tracks in the ATLAS Inner Detector as a function of μ for the Loose and TightPrimary track selections[22].

The vertex reconstruction efficiency is determined from data by taking the ratio between events with a reconstructed vertex and events with at least two reconstructed tracks. Concerning the dependence of the vertex reconstruction on pile-up conditions, as the number of interaction per bunch crossing increase, the fraction of fake tracks increase. This implies the degradation of the vertex reconstruction efficiency at high value of $< \mu >$.

2.3.4 Electrons

The identification and reconstruction of electrons can be performed with a combination of sub-detectors in the pseudo-rapidity range $|\eta| < 2.5$, and with calorimeter information in the forward pseudo-rapidity range.

As a charged particle traverses the different media in the TRT, alternating between the gaseous tubes and the radiator material between them, transition radiation will be emitted. The electron, with a larger characteristic Lorentz factor than charged hadrons, will emit more photons and consequently the number of TRT hits above a certain threshold can be used as a discrimination variable. Electrons originating from photon conversions can be rejected by requiring that their tracks have a hit on the b-layer.

The EM calorimeter will collect most of electron's energy. Due to its longitudinal and lateral granularity, it is also able to determine the impact point. The energy deposits in the barrel are selected by identifying clusters of energy with associated tracks in the ID. In contrast, the identification of a photon cluster requires that there is no track matching. An EM cluster is built by grouping cells within a fixed-size window, positioned in the local maxima of transverse energy. The four-momentum of the reconstructed electron is computed with the energy information from the EM cluster and the η, ϕ coordinates from the matched track.

Combining shower shape variables, track and track-cluster matching quality, TRT information, hits on the b-layer, and other variables, electrons can be identified with increasing degrees of purity, and corresponding increasing rejection factors against photon pair production and hadronic jets. The absolute energy scale of electrons can be measured in ATLAS with an uncertainty at the sub-percent level [23].

2.3.5 Muons

Muons, as minimum ionizing particles, typically traverse the ID and the calorimeters without great loss of energy, and their transverse momentum and charge sign can be measured by the muon spectrometer and the ID, covering a region with $|\eta| < 2.5$ .To a lesser extent,to recover acceptance losses,the calorimeter can also

be used to identify and reconstruct muons. The highest muon purity is achieved by combining tracking information measured independently in the ID and in the muon spectrometer, defining "combined" muons. When such information is not available, other types of muons can be defined, albeit with lower purity: "stand-alone", with tracking information from the muon spectrometer; "segment-tagged", in cases where the ID information can be combined with hits in the first chambers of the muon spectrometer; and "calorimeter-tagged", combing ID and a calorimeter energy deposit.

The muon momentum scale for combined muons in the range $5 \leq p_T \leq 100$ GeV is extremely well measured in ATLAS, with an uncertainty not larger than 0.2%, and a relative resolution of 2-4%[24]. High-p_T muons are subject to relative momentum resolutions of up to 10%.

Muon quality working points (tight, medium, loose) have been defined with decreasing reconstruction efficiency. Quality cuts mainly involve tracks parameters : number of hits in each sub-detector, impact parameter, . . .

2.3.6 Jets

Hadronic showers created in the electromagnetic and hadronic calorimeters can be clustered into structures referred to as jets. In addition to calorimeter clusters, other objects with a four-momentum representation, such as tracks, can be used as detector-level inputs to jet clustering algorithms.

Calorimeter jets are built from energy depositions in the hadronic and electromagnetic calorimeters. An incoming particle will deposit energy in the calorimeter cells, longitudinally and laterally with respect to its direction of motion. According to the total energy deposited in each cell and the overall expected noise, a seed cell is found and an iterative procedure adds the neighbouring cells if their energy is above a certain threshold. The resulting three-dimensional set of cells is referred to as a topological cluster (or topo-cluster) [25], and is classified as hadronic or electromagnetic depending on their shape, longitudinal and lateral depth and energy density. The total energy is measured by assuming the electromagnetic interaction as its origin, corresponding to the so-called EM scale, and can be calibrated to the hadronic scale through a process known as local cluster weighting [26], based on single pion interactions. This approach corrects for the calorimeter's different response to EM and hadronic showers.

Non-collision backgrounds affect the quality and purity of calorimeter signals. Their contamination is removed through jet quality criteria, so that the jets from the hard scatter can be distinguished. A variety of phenomena can give origin to these false signals, e.g. calorimeter noise, proton collisions with residual gas in

the beam pipe or cosmic ray muons, and an event containing any of these effects is discarded. Tracks can also be used as input to jet algorithms, defining the so-called track jets. Similarly to the jet quality criteria applied on the calorimeter signals, tracks are selected based on the number of ID hits, transverse momentum and impact parameters, to minimize the inclusion of tracks which do not originate from the primary vertex. A useful quantity known as Jet Vertex Fraction (JVF) can be used to reject jets originating from pile-up events [27]. JVF quantifies the fraction of the scalar summed p_T of the tracks in the jet that originate from the primary vertex. With the 2012 dataset, the JVF cut was optimized to efficiently select typically more than 90% of the jets originating from the primary vertex, figure which varies with the number of reconstructed vertices, and resulting in a pile-up rejection close to 100% [28].

Jets must further pass quality criteria and undergo a calibration procedure. The details of these procedure for Run-2 data are presented in [29]. Further studies with jets allows to identify, in some limit, whether the originating parton is a b quark. The Run-1 and -2 performances are described respectively in [30] and [31]. This allows improvements in signal efficiency and background rejections of many topologies such the ones involving top quarks in the final state.

2.3.7 b-tagging

Hadrons that contain b or c-quarks can be distinguished from hadrons composed of lighter quarks by their relatively long lifetimes and by their leptonic decay signatures. This is especially true for B hadrons, which have lifetimes of the order of 1.5 ps. When produced with enough transverse momentum (at least $\approx$ 20 GeV), their average flight length will be of a few mm, usually decaying before reaching the Inner Detector. Such features can be explored to develop techniques to identify jets that contain B hadrons.

The key inputs to the b-tagging algorithms developed in ATLAS are the charged particle tracks reconstructed in the Inner Detector, which are spatially matched to calorimeter jets with a p_T-dependent condition. Variables related to the impact parameter of the tracks, to the reconstructed secondary vertex where the decay occurs, and to the reconstruction of the topological decay chain [32] are used to discriminate between heavy flavour and light jets (see Figure 2.21). One of the most sophisticated algorithms, the MV1 tagger, implements a neural network that combines track, secondary vertex and decay chain information, taking correlations between the variables into account [33]. An alternative to MV1 is the MV1c tagger, which is trained specifically against a charm jet background and therefore achieves a higher discrimination between b and c originated jets.

The performance of a b-tagging algorithm can be characterized by its efficiency

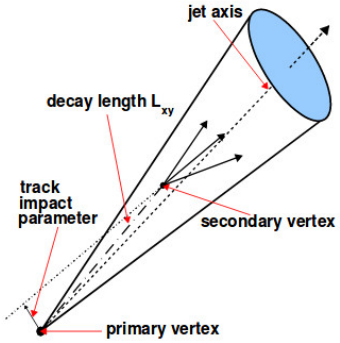

Figure 2.21: Schematic view of a B hadron decay inside a jet. [34].

to tag jets that originate from b-quarks and the corresponding rejection rates for c and light jets. The MV1 tagger is implemented by selecting an efficiency working point, typically 70%, which translates into charm and light mis-tagging rates of ≈20 % and ≈1 %, respectively. The light-jet rejection as a function of the b-tagging efficiency is shown in Figure 2.22. The b-tagging efficiencies measured in Monte-Carlo simulation as a function of the jet transverse momentum are calibrated to the values observed in data. The efficiencies for tagging b-jets, c-jets and light jets are measured in $t\bar{t}$ events, D^{*+} events and inclusive jet samples, respectively [33] [35]. The systematic uncertainties impacting the measurements on b-jets cover jet p_T values between 20 and 300 GeV and are of the order of 2% in the intermediate p_T range, being considerably larger at higher and lower values of p_T.

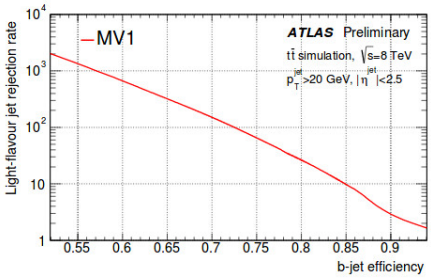

Figure 2.22: Light-flavor rejection (defined as the inverse of the mis-tagging rate) as a function of b-tagging efficiency for the MV1 algorithm, as measured in simulated $t\bar{t}$ jets. [33].

The identification of isolated b-jets in a moderated p_T range is well understood. However, the performance of these techniques worsens in dense environment such as boosted H→ $b\bar{b}$ decays, where the jets can overlap and their tracks can become very collimated. Due to the additional activity surrounding a given jet, track-jet matching, for example, becomes more ambiguous. Dedicated b-tagging trained specifically to handle high occupancy environment are currently being validated for

ATLAS [36][34], and will certainly be of use in a future boosted VH($b\bar{b}$) analysis.

b-tagging algorithms identify jets with B hadron content, but provide no information on the number of such hadrons in the jet.

2.3.8 Missing Transverse Energy

Stable and non-interacting particles, such as neutrinos, will escape the ATLAS volume undetected. Before the collision, the momentum of the incoming partons is essentially limited to the z direction. Due to conservation of momentum, a vectorial sum of all the calorimeter energy depositions can therefore be used to infer the transverse energy of escaping particles. E_T^{miss} is calculated as the negative of the vector sum of all reconstructed objects in the event (after calibration) and any remaining unmatched calorimeter deposits and tracks. Other sources of missing transverse energy are detector inefficiencies and resolution, which lead to mis-measurement of the true transverse energy of the event objects.

Part I

Development of pixel detector for ATLAS Inner Tracker (ITk) upgrade at HL-LHC

Chapter 3

Towards the High-Luminosity LHC

Contents

3.1 Motivation 39
3.2 LHC and ATLAS upgrade plans 40
3.2.1 ATLAS performance at the HL-LHC 42
3.2.2 The ATLAS physics at the HL-LHC 43
3.3 Improvements during the first long shutdown, LS-1 44
3.3.1 The ATLAS Pixel Detector upgrade - Phase-0: IBL, 2013-2015 44
3.3.2 Tracking performance of the ATLAS Inner Detector with IBL in Run-2 46
3.4 ATLAS Detector upgrades for increasing luminosities, Phase-I: 2019-2020 46
3.5 Major detector upgrades for HL-LHC, Phase-II: 2024-2026 47
3.5.1 The ATLAS inner tracker upgrade - ITk 48

The High-Luminosity Large Hadron Collider (HL-LHC) will begin collisions in the middle of 2026. The changes to the proton-proton collider will increase the average number of interactions per bunch crossings to up to five times the current value. This requires a new design for the current detectors to withstand the harsh conditions of the HL-LHC, such that they are able to exploit the new physics frontiers the HL-LHC might bring. One of the major changes to the new ATLAS detector, the so called ATLAS Upgrade, is the all-silicon inner detector. The new inner detector consists of a pixel and a strip detector. Both of these, will have new and improved sensor designs, readout electronics and powering schemes.

3.1 Motivation

Following the successful discovery of the Higgs boson-like particle announced on July 4th in 2012 with a mass at about 125 GeV, and in order to maximise the discovery

potential at the LHC, a new phase with a high luminosity upgrade of the LHC is foreseen for 2026 [37]. The most important LHC parameters for the ATLAS physics programme are the collision energy and the integrated luminosity. Increasing either or both of these increases the rate of rare processes which ATLAS explores. The pile-up events will increase to 200 from the current value of around 30-50. An upgrade programme of the LHC and its injectors is in place in order to increase both the energy and the luminosity, employing the periodic 2-3 year long LHC shutdowns. The full capability will come with the so-called high-luminosity LHC, HL-LHC, operation, which will be operated at the maximum center-of-mass energy of 14 TeV and an increased instantaneous peak luminosity up to $7\times10^{34}\ cm^{-2}s^{-1}$ and accumulate an integrated luminosity up to 4000 fb^{-1}, at least ten times the originally planned integrated luminosity, see Figure 3.1. ATLAS likewise uses the long shutdowns to consolidate and upgrade the detector in order to maintain and improve its performance, to replace radiation-damaged or aged components, and to cope better with luminosity well beyond the design. The capability of ATLAS to search for heavier particles and rarer physics processes, and to make higher precision measurements of the Higgs boson and other Standard Model particles, is substantially improved by these upgrades.

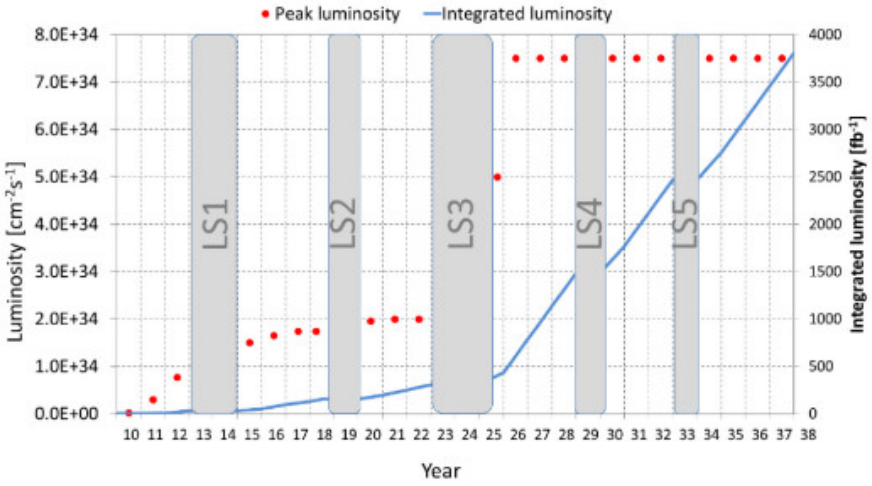

Figure 3.1: Forecast for peak luminosity (red dots) and integrated luminosity (blue line) in the HL-LHC era, for the case of ultimate HL-LHC parameters. Note that for the sake of simplicity there is no learning curve for luminosity after LS3.[38]

3.2 LHC and ATLAS upgrade plans

The long-term schedule for LHC operation is outlined in Figure 3.2. The path towards HL-LHC, can be divided into three steps from the year 2011 until 2025: named Run-1 (2011-2013), Run-2 (2015-2018), Run-3 (2021-2023) and Run-4 (from

2026 onwards). At the point of writing, the LHC is in its Run-2 phase, in which it is operated with a bunch-crossing time of 25 ns. In Run-3, the current center-of-mass energy of 13 TeV will be increased to its nominal energy of 14 TeV. The running times are separated by long shutdowns for accelerator and detector maintenance. The *first long shutdown* ("LS-1") took place in 2013-2014. For the LHC, LS-1 was used to reinforce the superconducting interconnects between the magnets and to consolidate the protection systems, allowing the collision energy to be raised safely from 8 TeV in 2012 to 13 TeV in 2015-2018 ("Run-2"). For ATLAS, the major upgrade during LS-1 was the installation of a fourth pixel detector layer closer to the collision point than the original pixel layers, and with better position resolution. Before LS-1 the LHC had reached about 80% of the design luminosity, but was able more than to double it in Run-2, thanks to ingenious use of both the LHC injectors and the LHC.

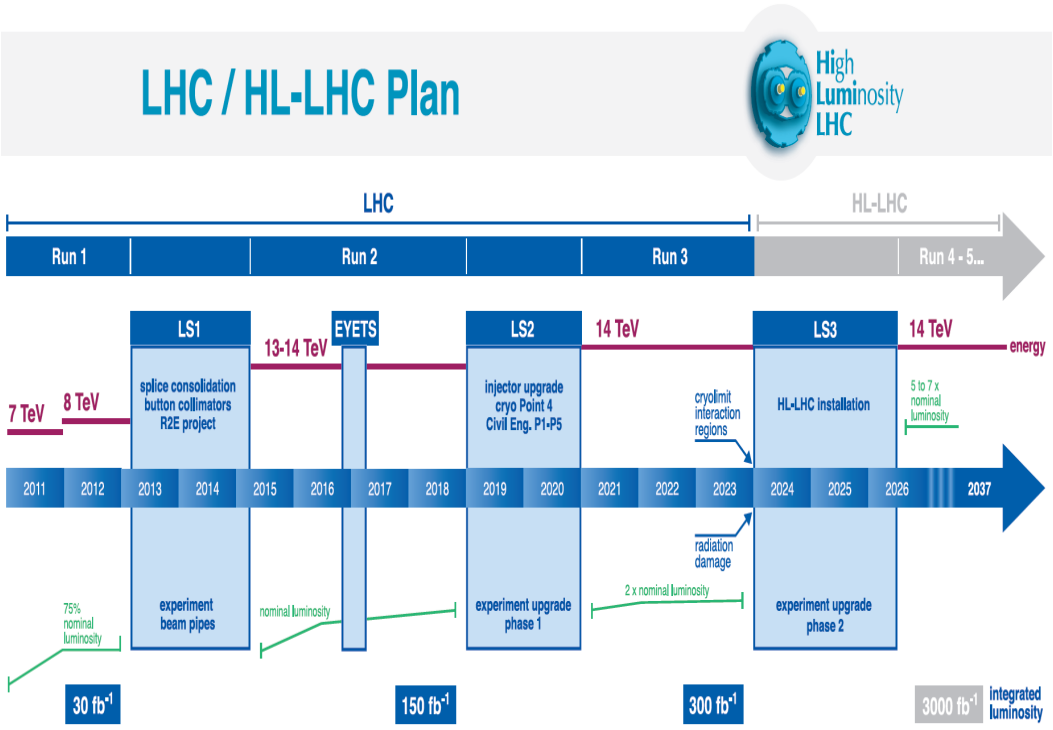

Figure 3.2: Plan for LHC operation towards the upgrade for the High-Luminosity LHC.

The *second long shutdown*, LS-2, is scheduled for 2019-2020. It will be used to increase the brightness of the beam delivered by the injectors to the LHC by increasing both the number of protons and their density. The maximum luminosity in the LHC will still be limited to about twice the original design due to cooling limitations in beam-focussing magnets located close to the experiment. However, these upgrades will allow the LHC to run at the same luminosity for long periods (hours) through a process called luminosity levelling, so increasing the data accumulated

per day. It is also an important milestone towards preparing for HL-LHC collision rates. In LS-2, ATLAS will make a major upgrade to its trigger system to increase its selectivity. The inner part of the endcap muon detector is also being replaced, to provide increased trigger capabilities at the expected HL-LHC particle fluxes.

The *third long shutdown*, LS-3, is scheduled for 2024-2026 and aims to complete the HL-LHC and detector upgrades. This is a major upgrade for the LHC where the magnets near ATLAS will be replaced to provide a stronger focussing of the beams, giving higher luminosities. In addition, the protection and beam dump systems will be upgraded to handle larger proton intensities. These upgrades will potentially allow luminosities up to twenty times the LHC design, but it is foreseen that the luminosity will be levelled at 5 to 7.5 times the design luminosity to provide better conditions. All of the inner tracker will be replaced during this shutdown, to increase the detector granularity to handle the higher pile-up and to increase the radiation hardness. The readout electronics and data acquisition system of almost all systems will also be replaced to cope with the much higher trigger and data rates. The trigger system in turn will be upgraded and expanded to facilitate more advanced algorithms needed for high pile-up. With these upgrades, it is expected that ATLAS will accumulate up to six times more integrated luminosity per year than in the best year so far (2017).

3.2.1 ATLAS performance at the HL-LHC

Reconstructing what happens in a collision at the HL-LHC in order to make physics measurements will be challenging due to the very high pile-up. At the ultimate luminosity, 7.5 times the design, an average of 200 proton-proton collisions are expected each time the bunches cross, i.e. every 25 ns. At most one of the 200 collisions will produce particles of interest for the vast majority of the physics programme: the rest effectively add noise and confusion. One powerful handle on the pile-up is the separation of collisions along the beam-line. The collisions in any single bunch crossing will be spread out over a distance of more than 10 cm, with an average separation between neighbouring collisions of around 1 mm. The upgraded inner tracker will be able to reconstruct the path of charged particles much more precisely than that over a large part of its angular acceptance, and so can remove charged tracks coming from pile-up. The calorimeters, used to detect uncharged neutral particles and measure the energy of photons, electrons and jets, have little capability on their own to reduce pile-up, but much can be gained by careful use of tracking information together with calorimeter energy deposits.

The expected performance of the upgraded detector to reconstruct, identify and measure different particles and jets in HL-LHC conditions has been studied in some depth. In many cases, performance can be obtained which is almost as good as, or even better than, the original detector at design luminosity. For example, the

charged particle momentum will be measured almost a factor of two more precisely, and the efficiency to identify jets which contain B-hadrons (so-called b-jets) improves, in both cases due to the better tracker granularity. The upgraded tracker also allows the identification of b-jets over a wider angular range. For quantities which rely mostly on the calorimeter information such as photon energy or the missing transverse energy, a degradation of up to a factor two due to pile-up may be seen.

3.2.2 The ATLAS physics at the HL-LHC

The discovery of the Higgs boson, H, with a mass of 125 GeV, by ATLAS and CMS opened a new chapter in physics at the TeV energy scale. The consistency, so far, of the measured properties of this new object with Standard Model (SM) predictions suggests that this is the last missing piece of the SM. Moreover, no observation of physics beyond the SM has yet been found. This has weakened the case for theories beyond the SM at the TeV scale. However puzzling observations, some astrophysical, indicate that the SM is not the final theory describing particles and forces, but may be a low-energy "effective" theory contained in some larger, as yet unknown, framework. Physics beyond-the-SM must come in at some higher energy scale that might be directly accessible at the LHC, or that may produce deviations from SM predictions when performing high-precision measurements at the LHC or elsewhere. A balanced strategy of direct searches for new physics, and high-precision measurements, is key to testing the SM at the energy scale offered by the HL-LHC.

Among the research topics that the HL-LHC will provide a unique opportunity to be probed and the very large luminosities are crucial to measure well are:

- rare decays of the Higgs boson, such as H$\rightarrow \mu^+\mu^-$. This decay is of great importance as it probes the Higgs boson coupling to second generation leptons.

- the Higgs potential - which affects how the Higgs boson interacts with other (identical) Higgs bosons, its "self-coupling" - represents a key test of the Standard Model description of the electroweak symmetry breaking mechanism.

- As well as exploring the Standard Model, including the Higgs sector, with its sensitivity to beyond-SM physics, the HL-LHC also increases the opportunities to discover directly new particles and new phenomena, ranging from modified Higgs sectors, to searches for dark matter candidates and for new resonances.

3.3 Improvements during the first long shutdown, LS-1

The first upgrades to ATLAS were made during LS-1 (2013-2015), together with a broad programme of maintenance and consolidation of detector systems. The most significant upgrade was the installation of a new innermost pixel sensor layer allowing improved tagging of b- and c-flavoured hadrons and tau leptons. A further important change was to the architecture of the High-Level Trigger (HLT): a three- level trigger system was used in Run-1, but the second-level and event filter stages were merged during LS-1 to give a two-level system (known as the first-level, "Level-1", trigger and HLT). Activities aimed at consolidating and improving the reliability of the detector included: improvements to the Inner Detector readout, refurbishing calorimeter power supplies and electronics, installing new muon chambers in the barrel-endcap transition region and in the feet of the detector, installing an improved luminometer LUCID; and additional improvements to the first- and high-level triggers. The combination of several of these improvements enabled the maximum first-level trigger rate to be increased from 75 to 100 kHz.

3.3.1 The ATLAS Pixel Detector upgrade - Phase-0: IBL, 2013-2015

The original plan for the Pixel Detector, well before the start of LHC data-taking, was to extract and replace the inner layer, located at approximately 5 cm from the beam-line, after a few years of running. However, after a detailed study in 2008, this strategy was changed in favour of an ambitious but appealing proposal: namely to insert a new, additional, innermost layer inside the existing Pixel Detector, reducing the beam pipe diameter. This new layer is known as the "IBL" (Insertable B-Layer), and was adopted as a Phase-0 upgrade project in 2009. The primary physics driver was to enhance the lifetime tagging of b-flavoured hadrons. The IBL project proceeded rapidly, given the short time before LS-1, and included the new beam pipe and its interface as well as many parallel activities for construction, integration, and finally installation.

The IBL upgrade project was possible thanks to the reduction of the inner diameter of the central beam pipe from 58 to 47 mm, with a wall thickness of 0.8 mm. The new beam pipe has a beryllium section 7.1 m long, positioned symmetrically around the interaction point. At the ends, aluminium flanges 10 cm long are welded on, to connect to the next beam-pipe sections. The IBL provides a new, high precision, track measurement close to the interaction point, improving the track extrapolation back to the interaction vertex. This is particularly important for low-momentum particles, where multiple scattering effects are more important. In addition a smaller pixel pitch of the IBL (250 μm) in the direction parallel to the beam axis improves the resolution of the vertex position in the longitudinal direction, across the full

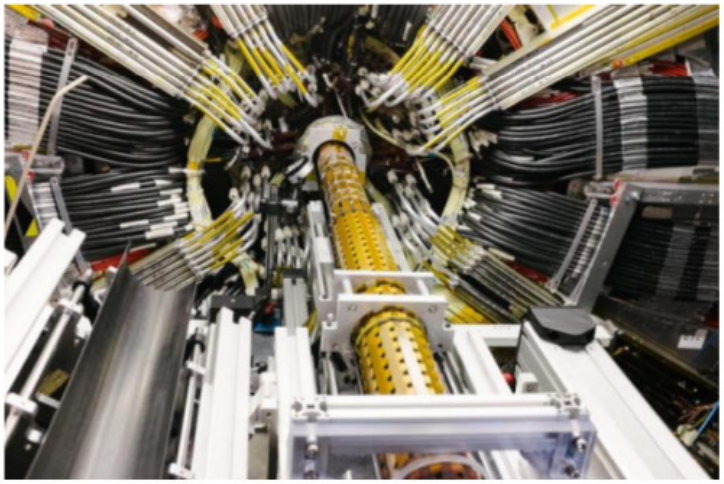

Figure 3.3: Insertion of IBL, together with the beam pipe, inside the pixel inner support tube.

transverse-momentum spectrum. Moreover, the IBL sensors are thinner than that of the original pixel sensors in ATLAS. The thickness was reduced from 250 μm to 200 μm. In addition the inactive area at the edge of the sensor was reduced to 200 μm in the IBL sensors.

The IBL is a relatively small detector with a little less than 0.2 m^2 of silicon sensors supported on 14 staves surrounding the beam pipe at an average radius of 3.3 cm from the beam axis. The instrumented length is 64 cm. The IBL was designed so that extraction and insertion is possible without removing the other layers of the Pixel Detector. The radial envelope is less than 10 mm between the beam pipe and the inner support tube of the Pixel Detector, within a 7 m-long enclosure. The staves and services are supported along an inner positioning tube, providing an independent mechanical support and a sealed volume with respect to the beam pipe.

The design, prototyping, production and integration phases took place on a relatively short time scale of approximately four years. This was possible thanks to a good connection between R&D groups and industrial partners while iterating on the fabrication techniques to comply with the targeted quality assurance [39]. Some novel technologies and ideas were adopted to build the detector in a different way than the original Pixel Detector. For instance a new front-end readout electronics chip, the FEI4, was implemented in industry-standard 130 nm CMOS technology, and is able to cope with higher occupancy while having lower noise and better radiation hardness. Its active area is almost 4.6 times that of the original pixel readout chip. This large area, in combination with the thin silicon layers for front-end and sensor, was a real challenge for the fine-pitch bump bonding.

After extensive qualification tests, excellent performance was obtained for two sensor technologies: planar, and 3D, silicon. For the latter, the production yield was not reliably established, and in order to gain experience also for future upgrades, it was decided to build a stave with mixed sensor flavours. The IBL staves were built with 12 planar double-chip modules located in the central region covering the range $|\eta| < 2.5$, while four 3D single-chip modules are mounted at the ends, extending the coverage at up to $|\eta| <= 3$.

The complete IBL detector was installed into ATLAS in spring 2014 (see Figure 3.3). Many technical challenges were dealt with during construction and installation, providing valuable experience toward the tracker upgrade for the HL-LHC.

3.3.2 Tracking performance of the ATLAS Inner Detector with IBL in Run-2

The tracking performance of the ATLAS Inner Detector has been significantly improved since the insertion of the IBL, as demonstrated in a large multiplicity of measurements. The impact parameter resolution is improved nearly by a factor of two. This is in good agreement with the expected impact parameter resolution improvement from the simulations prior to the IBL construction [40]. Figure 3.4 shows the impact parameter resolution in the longitudinal direction (along the beam) as a function of the transverse momentum of the tracks [41]. The impact parameter resolution of the Run-1 data, without IBL, and of the Run-2 data, with IBL, are shown. The improvement is a result of adding a new point measurement at the very small radius of IBL and with higher precision, due to a decreased pixel size (250 μm) in the longitudinal direction with respect to the three Pixel Detector layers (400 μm).

3.4 ATLAS Detector upgrades for increasing luminosities, Phase-I: 2019-2020

Phase-I upgrade (2019-2020) prepares for an instantaneous luminosity of $2 - 3 \times 10^{34}\ cm^{-2}s^{-1}$. The outstanding luminosity delivery of the LHC means that peak collision rates above LHC design were already achieved in 2017, and have become routine. Correspondingly high levels of pile-up, $\mu = 55$ up to twice the design level, are also being delivered. The discovery of the 125 GeV Higgs boson, and, at the time of writing, no higher-mass new states, pushes strongly to maintain relatively low transverse momentum inclusive triggers. While no upgrade is planned for the current ATLAS ID, a series of upgrade operations is underway, mainly for installation in LS-2, to provide additional selectivity in the trigger. This is being done through: improvements at the first-level trigger via new electronics for the calorimeter trigger

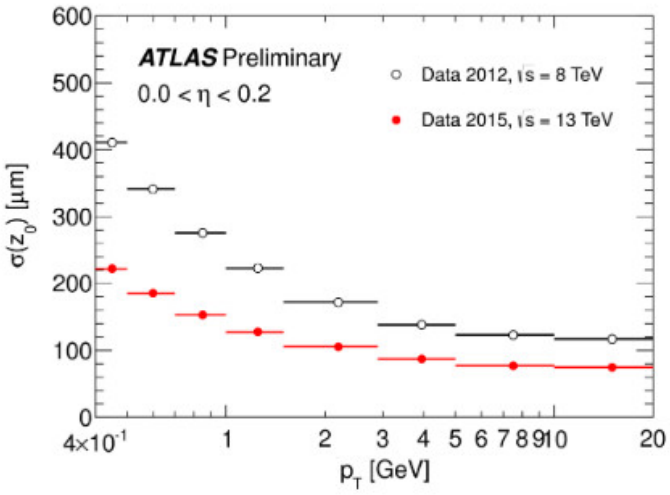

Figure 3.4: Unfolded longitudinal impact parameter resolution measured from data in 2015, at $\sqrt{s}$ 13 T eV , with the Inner Detector including the IBL, as a function of p_T compared to that measured from data in 2012, at $\sqrt{s}$ 8TeV . The data in 2015 is collected with a minimum bias trigger. The data in 2012 is derived from a mixture of jet, tau and missing E_T triggers [41]

chain; the introduction of a hardware track-finding processor FTK at the input to the High-Level Trigger; a new detector system - the New Small Wheel - for forward muon triggering; and the use of geometric properties in whole-event information ("topological triggering"). In addition, some barrel muon chambers located in the barrel-endcap transition region will be replaced, to incorporate new trigger chambers

3.5 Major detector upgrades for HL-LHC, Phase-II: 2024-2026

The largest changes to the ATLAS detector come with the Phase-II upgrade, preparing the detectors for the challenging environment during the HL-LHC period. The HL-LHC will operate at an instantaneous peak luminosity up to $7.5\times10^{34}\ cm^{-2}s^{-1}$ for a total integrated luminosity of 3000 to 4000 fb^{-1}. As a consequence, the detectors will have to handle higher particle densities leading to higher occupancies in the detector components and higher radiation levels. The number of pile-up events per collision will increase up to 200. The primary detector challenges in such an environment are to maintain the excellent performance, in particular the vertex and track reconstruction, lepton identification and heavy flavour tagging. These will be addressed via three major detector upgrades: a complete replacement of the inner tracking system; new radiation tolerant readout electronics using state-of-the-art 65nm CMOS technologies for the tracking, upgrade the calorimeter and muon detector systems; and an upgraded Trigger and Data Acquisition (TDAQ) architecture

that will cope with the increasing rates. These upgrades are necessary to offset the effects of high rates and radiation damages imposed by the HL-LHC environment and are designed to exploit fully the physics potential of the LHC. All upgrades have to fit to existing geometrical envelopes and reuse as far as possible the existing ATLAS infrastructure, to reduce cost.

3.5.1 The ATLAS inner tracker upgrade - ITk

The ATLAS inner tracking system plays an essential role in the reconstruction and identification of leptons, photons, hadronic decays and in the tagging of b-jets. The key role of the tracking detector in the physics programme becomes even more pronounced during the high-luminosity phase. The current tracking detector has been designed for ten years of operation at a peak luminosity of $10^{34}\ cm^{-2}s^{-1}$ with 25 pile-up events per 25 ns bunch crossing, a first-level trigger rate of 100 kHz, and a radiation tolerance equivalent to an integrated luminosity of 700 fb^{-1} for the SCT, and 850 fb^{-1} for the inserted IBL. For an optimal tracking performance up to 4000 fb^{-1}, new, much more radiation-tolerant, sensing elements and readout electronics are required. Due to a factor four higher track density the granularity of the tracking detector has to be increased, to $50 \times 50\ \mu m^2$ to keep the occupancies no more than 1%. The design of the layout of the new tracking detector has been a large effort over several years.

The new tracking detector ("ITk") consists of an all-silicon active-element detector with pixel sensors at the inner radii around the beam pipe, surrounded by strip sensors. The Strip Detector has four barrel layers and six endcap petal-design disks, both equipped with modules on both surfaces of the layers, each with a small stereo angle to add z(R) resolution, respectively. The Strip Detector, covering $|\eta| < 2.7$, surrounds a five-layer Pixel Detector extending the coverage to $|\eta| < 4$ to provide also measurements for particles at a shallow angle to the beam. In addition, and due to the harsh radiation environment expected, the inner two layers of the Pixel Detector, which will be exposed to the largest radiation fluences, equivalent to $2-3 \times 10^{16}$ 1 MeV n_{eq}/cm^2 , see Figure 3.5, will be replaceable. The maximum 1 MeV neutron equivalent fluences for the different parts of the pixel detector are predicted to be in the range $1.3 \times 10^{16}\ cm^{-2}$ for the innermost layer and $1 \times 10^{15}\ cm^{-2}$ for the outermost layer. The layout has been arranged to maximize the length of the trajectory of the particles inside the solenoid, providing a total of 13 hits for $|\eta| < 2.6$.

The layout of the ITk Pixel Detector, shown in Figure 3.6 is based on a short barrel part followed by inclined modules to cover the intermediate $|\eta|$-region. The high-$|\eta|$ region is instead covered by rings perpendicular to the beam direction. This arrangement covers the pseudo-rapidity region of $|\eta| < 4$. The baseline concept for all layers is to use 3D and hybrid planar pixel modules comprising two parts: a

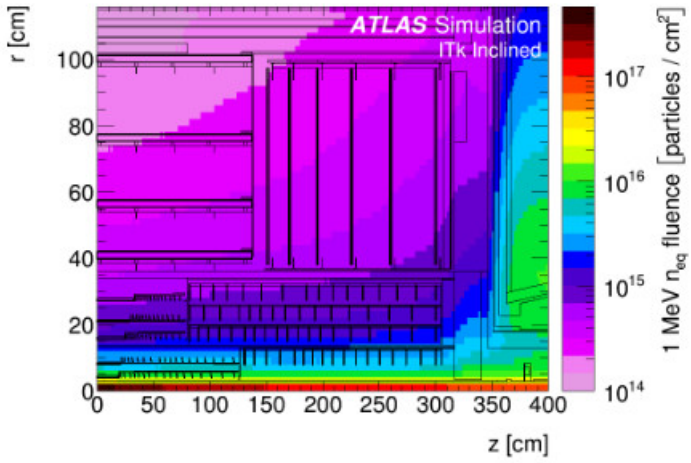

Figure 3.5: The fluence and dose distributions for the ITk (including the strip and pixel detector) layout in 1 MeV neutron equivalent flux using FLUKA [42] simulation. [43]

high resistivity silicon sensor and a front-end read-out chip fabricated in CMOS technology. The two parts are joined using the high-density flip-chip connection technique with solder bumps or indium bumps called "bump-bonding". This assembly is then glued on a flex circuit providing the connections to the read-out and power distribution systems.

The foreseen pixel sensor technologies are developed to withstand the harsh HL-LHC radiation environment and to meet expected industrial production capabilities. Different types of pixel sensors, with different level of radiation tolerance, will be used in the different parts of the detector: 3D sensors and thin (100 μm) planar sensors in the inner section, 150 μm planar sensors in the outer three layers and pixel end-caps, all to be bump-bonded to radiation-tolerant front-end electronics designed in 65 nm chip CMOS technology. The outer barrel layer may employ CMOS monolithic sensors if this technology is proven early enough.

In 3D pixel sensors, the charge collecting electrodes are columns etched into the sensor volume and oriented perpendicularly to the sensor surface. 3D sensors are intrinsically more radiation tolerant than planar sensors due to shorter drift distances and the feasibility of successfully using this technology in an LHC experiment was shown with the IBL. Planar pixel sensors were already used for the current Pixel Detector and further developed for use in the HL-LHC environment. While n-in-n technology was used for the current detector, the planar sensors will be using thin edge n-in-p technology featuring an increased radiation tolerance and the simplification of the production process. An advantage of the n-in-p technology is single-sided processing and reduced handling complexity.

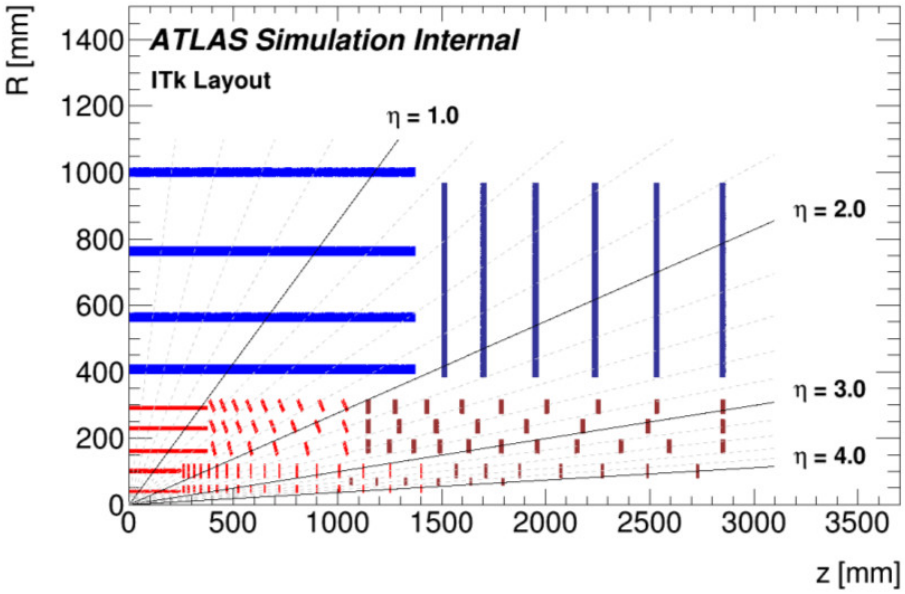

Figure 3.6: Schematic layout of the ITk for the HL-LHC phase of ATLAS. Here only one quadrant and only active detector elements are shown. The horizontal axis is the axis along the beam line with zero being the interaction point. The vertical axis is the radius measured from the IP.

A common effort between ATLAS and CMS has begun in 2013 to build a radiation-hardened front-end chip for the new Phase-II pixel detectors. The same front-end chip is used throughout the entire Pixel Detector. It will be implemented in 65 nm CMOS technology, which has the gate density large enough to define and implement all the building blocks needed for an HL-LHC pixel detector with 40 000 pixel cells per cm^2 . The chip size will be 20×19.2 mm^2 , and the pixel cell size 50×50 μm^2. More details about readout electronics for the upgrade Phase-II can be found in chapter 5.

The production of the ITk Detector is scheduled to take place over three years starting in 2020. Installation and commissioning is planned in 2025 to be ready for the HL-LHC start-up in 2026.

Chapter 4

Silicon particle detectors: Theoretical background

Contents

4.1 Working principles of silicon pixel sensors 52
4.2 Fundamentals of Silicon detectors 53
4.2.1 Doping 53
4.2.2 The pn-junction 54
4.3 Radiation-Matter Interactions 59
4.3.1 Interactions of charged particles 60
4.3.2 Photon interactions 63
4.3.3 Interaction of Hadrons 65
4.3.4 Interactions of neutral particles 65
4.4 Crystal defects from irradiation and their implications . . . 65
4.4.1 Surface defects 65
4.4.2 Bulk defects 67
4.4.3 Defect annealing 72

Since the invention of pixel sensors [44] and CMOS sensors [45] patterned semiconductor sensors have been used in many applications in science and industry. For particle detectors in high energy physics semiconductor pixel sensors with a high granularity are mostly used as tracking detectors reconstructing the trajectories of charged particles passing through the sensors.

The signal generation in semiconductor sensors is based on free charge carriers drifting in an electric field. As opposed to gaseous ionization chambers the active volume in which the charges are generated is a semiconductor whose surfaces are structured by photo lithographic processes. This allows for much smaller readout cells and hence a better resolution reaching for example less than 15 μm in the R-ϕ direction of the present ATLAS pixel detector [46]. Details about the working principles of semiconductor sensors are introduced in Section 4.1 with an emphasis on n-in-p sensors, being the main sensor type investigated in this work.

At high luminosity hadron colliders, especially at the LHC and its proposed luminosity upgrades to the HL-LHC, semiconductor sensors are exposed to intense high energy particle fluences. Next to the high signal rates which demand enormous data transport and processing capabilities the vast amount of secondary particles also introduces defects in the semiconductor crystals leading to a deterioration of the sensor performance. The different defects and their implications are presented in Section 4.4.

4.1 Working principles of silicon pixel sensors

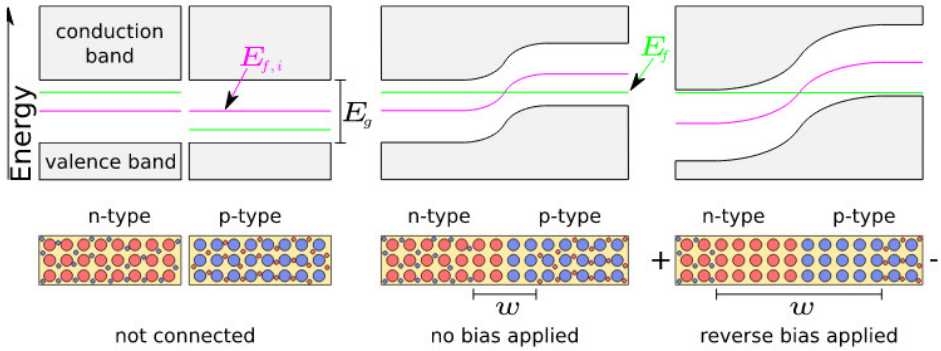

Figure 4.1: Working principle of the pn-junction. The upper images show the energy band structure in the n- and p-type silicon. The lower images visualize the acceptors, donors, electrons, and holes (large blue, large red, small blue, and small red circles, respectively) in the doped silicon materials. The width of the depletion zone is denoted by w.

While for single atoms electrons are confined to discrete energy levels, in condensed matter the electron wave functions of many atoms overlap, leading to continuous but possibly separated energy bands of phase-space states. The uppermost completely filled band is referred to as valence band while the lowest partially or not occupied band is called conduction band (see left side of Figure 4.1). The probability f_e that a phase-space state of energy E is occupied by an electron can be described by the Fermi-Dirac statistics [47]:

$$f_e(E) = \frac{1}{e^{(E-E_f)/kT} + 1} \tag{4.1}$$

Here k is the Boltzmann constant and E_f is the Fermi energy at which

$$f_e(E) = \frac{1}{2} \tag{4.2}$$

The temperature T determines the width in energy of the transition region between $f_e(E) \approx 0$ and $f_e(E) \approx 1$ Depending on the band gap E_g between the valence and conduction band and the position of E_f, condensed matter can be classified into insulators, conductors, and semiconductors. The latter are defined as having a band gap of $0eV < E_g \leq 3eV$ which contains E_f. Hence, at $T \to 0K$ all phase-space states in the valence band are occupied, whereas the conduction band is empty. Since no electron in the valence band can change to a state with a different momentum, a current is not possible.

The energy supplied by ionizing particles can lift electrons from the valence band into the conduction band, where they can move through the crystal. In a semiconductor sensor, these free charge carriers are propagated towards attached readout electronics in an electric field, created by applying different potentials at opposing sensor surfaces. This induces a time dependent current $I_e(t)$ in the electronics that forms part of the measured signal. At the same time the empty phase-space state in the valence band can be occupied by a neighbouring valence electron. Hence, the empty space, usually interpreted as a positively charged particle called hole, is - compared to the electrons - propagating in the opposite direction and generates an additional hole current $I_h(t)$ [1].

Silicon is the most prominent example of all semiconductor detector materials and it is used for the sensors relevant for the presented work. On average for each 3.6 eV energy lost or 12.5 nm travelled in silicon a Minimum Ionizing Particle (MIP) lifts an electron from the valence band into the conduction band, i.e. creates an electron-hole pair. This leads to an average collectable charge corresponding to 8000 electrons (8 ke) per 100 μm of sensor thickness. However, intrinsic silicon is not suitable as a sensor material, since at usual working temperatures many electrons occupy phase-space states in the conduction band and would cause a large current in the electric field. This leakage current would be far larger than the current induced by the electron-hole pairs created by penetrating MIPs. To reduce the leakage current and to create a sensor volume with very few free charge carriers, the rectifying properties of a junction between two extrinsic silicon materials is exploited.

4.2 Fundamentals of Silicon detectors

4.2.1 Doping

The lattice of a certain type of semiconductor has a specific density of electrons per unit area. Taking an intrinsic group IV semiconductor such as silicon as an example

[1] The Hall effect in semiconductors shows, that the concept of positively charged holes is more than a simple trick to ease the mathematical description of semiconductors. It is rather a consequence of the quantum mechanical properties of electrons in a crystal lattice (e.g. [48])

and adding an impurity from group V such as phosphorus, an excess of electrons are produced due to the extra electron provided by the dopant. This results in a lower proportion of holes. These are denoted as majority carriers and minority carriers respectively. The resulting semiconductor is known as n-type, shown in Figure 4.2. This type of dopant is called a donor. An excess of holes due to an impurity from a group III atom results in a p-type semiconductor, shown in Figure 4.2. An extremely large concentration of the impurity is denoted with a '+', thus a semiconductor with a very high density of group III impurities is called p^+-type. This dopant type is called an acceptor and a common acceptor for silicon is boron.

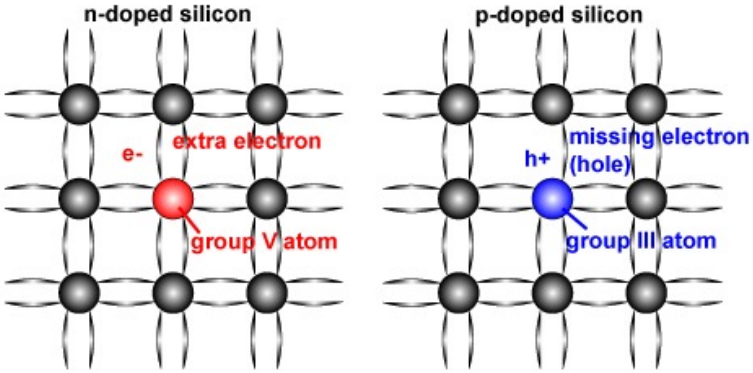

Figure 4.2: Representation of an impurity occupying the site of a silicon atom in the lattice. The donor (left) donates an extra electron, creating an n-type semiconductor. The acceptor (right) reduces the density of electrons creating a p-type semiconductor. The missing electron is illustrated by a missing bond line.

4.2.2 The pn-junction

A junction is formed when doped semiconductors of p-type and n-type are brought into contact with each other. Diffusion of carriers across the junction exposes fixed ionic charge, which results in an electric field (built-in) which prevents further diffusion. The density of free carriers is greatly reduced in the region close to the junction and this is known as the *depletion zone*, illustrated in Figure 4.3(a). Fixed positively charged donor ions are created in the n-region, while fixed negatively charged acceptor ions are created in the p-region, resulting in the so-called *space charge region*.

When an electric potential is applied, a small current is produced due to the net migration of the electrons and holes. If the positive terminal is connected to the p-type (and hence the negative is connected to the n-type) this is known as *forward bias* and results in a smaller depletion zone (Figure 4.3b). The opposite, where the positive terminal is connected to the n-type, is known as *reverse bias* (Figure 4.3c). In this case the depletion zone is extended. If the reverse bias voltage is great enough,

the depletion zone extends all the way to the edge of the semiconductor. This is called full depletion. If the voltage continues to increase, avalanche breakdown will eventually occur.

The Fermi energy E_f is changed from the intrinsic value $E_{f,i}$ and moves closer towards the valence band or the conduction band for p- and n-type silicon, respectively. Joining these two silicon types the majority charge carriers recombine at the pn-junction between them until the Fermi energy is equal throughout the crystal (middle section of Figure 4.1).

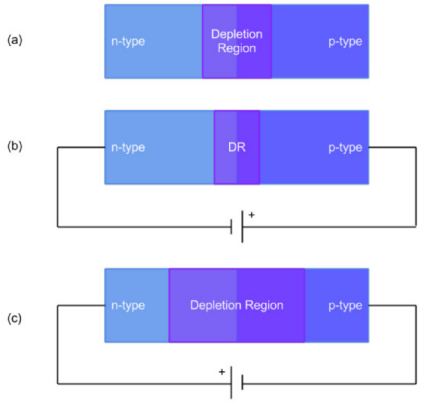

Figure 4.3: Representation of the relative depletion regions for (a) an unbiased pn-junction, (b) a forward biased semiconductor and (c) a reverse biased semiconductor.

The potential inside the p-n junction can be expressed by the Poisson equation:

$$\Delta\phi = \frac{\rho}{\varepsilon_{Si}\varepsilon_0} = \frac{e_0}{\varepsilon_{Si}\varepsilon_0}(N_A - N_D) \quad \text{with} \quad \rho = e_0(N_A - N_D) \tag{4.3}$$

with ϕ representing the electrostatic potential, $\varepsilon_{Si} = 11.75$ the dielectric constant of silicon and $\varepsilon_0 = 8.85 \times 10^{-12} F/m$ the vacuum permittivity. The term ρ represents the charge density, expressed by the elementary charge e_0 and N_A and N_D , the carrier acceptor and donor concentrations in the respective regions.

The space charge region causes an electrical field counteracting the diffusion of charge carriers until a difference of the electrical potential is reached, which prevents further diffusion of the charge carriers. This built-in potential can be expressed as:

$$\phi_{bi} = k_B T \ln\left(\frac{n_{0,n} \cdot p_{0,p}}{n_i^2}\right) \approx kT \ln\left(\frac{N_D N_A}{n_i^2}\right) \tag{4.4}$$

where $n_{0,n}$ represents the electron concentration in the n-type, $p_{0,p}$ the hole concentration in the p-type and n_i the intrinsic concentration. The corresponding built-in voltage can then be written as

$$U_{bi} = \frac{\phi_{bi}}{q} = \frac{k_B T}{q} \ln(\frac{N_D N_A}{n_i^2}) \tag{4.5}$$

where q is the charge. Typical built-in voltages are in a range between 0.5 V and 1 V. The width w of the depletion zone can be increased by an externally applied reverse bias voltage $U = U_{p-type} - U_{n-type} < 0$ over the pn-junction (right side of Figure 4.1):

$$w(U) = \sqrt{\frac{2\varepsilon_{Si}\varepsilon_0(N_A + N_D)}{qN_A N_D}(U_{bi} - U)} \tag{4.6}$$

Here q is the elementary charge, N_A and N_D are the concentrations of acceptor atoms in the p-type and donor atoms in the n-type silicon and ε_{Si}, ε_0 are the permittivity for silicon and the vacuum. The built-in voltage U_{bi} is generated by the ionized donor and acceptor atoms and determines the width of the depletion zone when no external voltage is applied. Ideally within the depletion zone no free charge carriers are present and hence, a current only flows when additional electron-hole pairs are created by ionization. The built in voltage distribution within the pn junction in thermal equilibrium is shown in Figure 4.4.

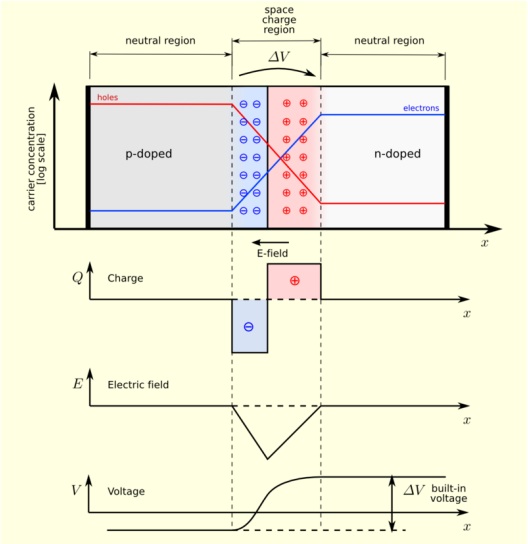

Figure 4.4: A p-n junction in thermal equilibrium with zero-bias voltage applied. Under the junction, plots for the charge density, the electric field, and the voltage are reported. (The log concentration curves should actually be smoother, like the voltage.) [49]

However, small leakage currents can be measured also under reverse bias, since the thermal generation rate of carriers at finite temperatures is not zero, and charge carriers diffuse from the undepleted volume into the depletion zone. The expected leakage current for a given T can be written as:

$$I_{leak}(T) = I_{leak}(T_{ref})\frac{T^2}{T_{ref}^2}\exp\left(\frac{-E_g}{2k_B}\left[\frac{1}{T} - \frac{1}{T_{ref}}\right]\right) \tag{4.7}$$

with $I_{leak}(T_{ref})$ is the current measured at T_{ref} . According to this formula, the leakage current approximately doubles every 7 K. This relation also holds for devices irradiated to high fluences. It shows, that cooling is imperative to reduce the leakage current to an acceptable level.

The voltage U_{fd} needed to deplete the full detector thickness $d = w(U_{fd})$ is naturally referred to as full depletion voltage. The depletion voltage is mainly dependent on the bulk thickness d and the bulk resistivity ρ and can be expressed as:

$$U_{fd} = \frac{d^2}{2\rho\mu_e\varepsilon_{Si}\varepsilon_0} = \frac{N_{eff}d^2}{2\varepsilon_{Si}\varepsilon_0} \tag{4.8}$$

where $N_{eff} = N_D - N_A = \frac{1}{\rho\mu_e}$.

To collect the full charge generated by ionizing particles in the sensor volume, it is needed to apply a bias voltage of $U \geq U_{fd}$. Depending on the silicon material properties, for example after heavy irradiation, U_{fd} can reach several thousands of Volts for a typical 250 μm thick sensor, since the effective doping concentration strongly increases. Such high voltages can exceed the maximum operating voltage of the sensors above which the pn-junction will show a junction break-down. A junction break-down is characterized by a strong increase of the leakage current by several orders of magnitude rendering the pn-junction unusable for particle detection. Three effects are responsible for break-downs:

- **Thermal instability** As the power dissipation increases for higher voltages the device heats up. This leads to an increased thermal generation rate of free charge carriers and hence a higher leakage current. Larger currents again cause a higher power dissipation resulting in a positive feedback situation and quickly evolving towards very high currents.

- **Tunnelling** As higher bias voltages are applied the band structure is more and more deformed until the valence band energy of the p-type silicon is far above the lowest energy of the conduction band of the n-type silicon. The potential barrier of forbidden states between them decreases and consequently the chance for band-to-band tunnelling strongly increases.

Parameter	$1.75 \times 10^5 \leq \mathcal{E}/(V/cm) \leq 4.0 \times 10^5$	$4.0 \times 10^5 \leq \mathcal{E}/(V/cm) \leq 6.0 \times 10^5$
$\alpha_{\infty e}[10^6/cm]$	0.703	0.703
$b_e[10^6 V/cm]$	1.231	1.231
$\alpha_{\infty h}[10^6/cm]$	1.582	0.671
$b_h[10^6 V/cm]$	2.036	1.693

Table 4.1: Parameters for the multiplication rate, defined in Equation 4.9, in high electric fields as listed in [56].

- **Avalanche multiplication** If the electric field at the pn-junction reaches very high values, the free charge carriers are strongly accelerated. Above a critical field strength the energy gained by a charge carrier between two scattering interactions is enough to create more charge carriers by ionization. The latter generate further electron-hole pairs and so on, leading to an avalanche of charge carriers.

The avalanche process is the most important breakdown mechanism, imposing an upper limit on the reverse bias for most sensors. However, this mechanism can also be used in a controlled way to amplify the signal within the sensor itself. This approach is followed with the so called avalanche photo-diodes and silicon photo-multipliers [50].

A parametrization of the multiplication rate (ionization rate) $\alpha(\mathcal{E})$, i.e. the number of newly created electron-hole pairs per drift length, is formulated in [51] and depends on the electric field $\mathcal{E}$:

$$\alpha_{e,h}(\mathcal{E}) = \alpha_{\infty e,h} e^{-b_{e,h}/|\mathcal{E}|} \tag{4.9}$$

with $\alpha_{\infty e,h}$ and $b_{e,h}$ the ionization coefficient. $\alpha_{\infty e,h}$ is the maximum number of carriers that can be generated per unit distance at very high electrical fields. The corresponding parameters for electrons (e) and holes (h) can be found in Table 4.1

Signal in pixel detectors

As described before electrons and holes generated by ionizing particles passing through the depleted volume are separated by the electric field within the sensor and induce a signal current in one or more nearby readout channels. Depending on the signal sizes in the individual readout channels the position of the particle penetration is reconstructed. The signal current $I_{je,h}(t)$ induced in a pixel channel j from a number $N_{e,h}$ of charge carriers generated in the sensor at a single position $x_{e,h}(0)$ is described by Ramo's theorem [52]:

$$I_{je,h}(t) = \pm q N_{e,h}(t) v_{dr_{e,h}}(x_{e,h}(t)) \mathcal{E}_{w,j}(x_{e,h}(t)) \tag{4.10}$$

Parameter	parameterization	at $T = 294$ K
$\mu_e[cm^2/Vs]$	$1.51 \times 10^9.(T/[K])^{-2.42}$	1605.4
$\mu_h[cm^2/Vs]$	$1.31 \times 10^8.(T/[K])^{-2.2}$	486.3
$v_{sat_e}[cm/s]$	$1.53 \times 10^9.(T/[K])^{-0.87}$	1.09×10^7
$v_{sat_h}[cm/s]$	$1.62 \times 10^8.(T/[K])^{-0.52}$	0.84×10^7
β_e	$2.57 \times 10^{-2}.(T/[K])^{0.66}$	1.09
β_h	$0.46.(T/[K])^{0.17}$	1.21

Table 4.2: Parameters for the drift velocity relation in silicon.

Here, $\mathcal{E}_{w,j}(x_{e,h}(t))$ is the weighting field for the j-th pixel channel, and $v_{dr_{e,h}}$ is the drift velocity of the charge carriers. The weighting field solely depends on the sensor and implant geometry and is calculated by applying a unit potential to channel j while leaving all others at 0 V . The drift velocities depend on the electric field $\mathcal{E}$, the mobilities $\mu_{e,h}$ of electrons and holes and their trajectories $x_{e,h}(t)$:

$$\begin{aligned} v_{dr_e}(x_e(t)) &= -\mu_e \mathcal{E}(x_e(t)) \\ v_{dr_h}(x_h(t)) &= \quad \mu_h \mathcal{E}(x_h(t)) \end{aligned} \tag{4.11}$$

This linear relation is valid for fields small enough that the velocity change due to acceleration by the electric field is small with respect to the thermal velocity. For higher electric fields a saturation of the drift velocities is measured. A common interpolation between the linear relation and the saturation velocity is given in [53] and reads:

$$v_{dr_{e,h}}(x_{e,h}(t)) = \frac{\mu_{e,h}\mathcal{E}(x_e(t))}{(1 + (\frac{\mu_{e,h}\mathcal{E}(x_e(t))}{v_{sat_{e,h}}})^{\beta})^{\frac{1}{\beta}}} \tag{4.12}$$

The parameters to be used in Equation 4.12 are given in Table 4.2.

4.3 Radiation-Matter Interactions

There are various methods in which particles interact within matter depending on their mass, charge and momentum. Brief descriptions of interactions of charged particles, photons and heavy neutral particles with matter will be presented in this section.

4.3.1 Interactions of charged particles

Charged particles interact mostly with electrons and loose energy through different mechanisms:

- Ionization and excitation of atoms encountered along the path

- Bremsstrahlung

- Cherenkov Radiation

- Transition Radiation

In addition, charged particles undergo multiple scattering that produces a series of small deviations from the path that increases its effective length.

► **Energy Loss by Ionization**

A charged particle in matter looses energy by ionization and excitation of the atoms along the path, transferring energy to the atomic electrons. The key parameter is the maximum amount of energy transferred in a single collision. The energy loss is different for heavy particles and electrons/positrons, due to their mass, that must be compared with the mass of target electrons. The energy loss per unit length of heavy charged particles, or stopping power, is described by the Bethe-Bloch equation. The Bethe-Bloch formula (eq. 4.13) describes the energy loss as a function of distance for heavy charged particles. It can also be thought of as the stopping distance for a particle travelling with a relativistic velocity, β, in a particular material with an atomic number, Z.

$$-\langle\frac{dE}{dx}\rangle = Kz^2\frac{Z}{A}\frac{1}{\beta^2}[\frac{1}{2}ln\frac{2m_ec^2\beta^2\gamma 2T_{max}}{I^2} - \beta^2 - \frac{\delta(\beta\gamma)}{2}] \tag{4.13}$$

The Bethe formula above is only valid for the range $0.1 < \beta\gamma < 10^4$ [54] and the definitions of the variables are in Table 4.3. Figure 4.5 shows the stopping power for positive muons in copper as a function of the muon momentum.

During the interaction of the charged particle with the medium, there will be fluctuations in the energy loss, whose properties depend on the thickness of the absorber material. The Bethe-Bloch equation describes only the average energy loss of particles. The distribution of the energy loss is a Gaussian with thick absorbers, due to the large number of collisions, but becomes asymmetrical in thin absorbers, where it is described by the Landau distribution [56] [57]. The Bethe dE/dx and most probable energy per unit thickness $\delta p/x$ in silicon are shown as a function of muon energy in Figure 4.6.

In addition, the straggling function (i.e. defined as the probability that the ionizing process during the passage of a fast charged particle through matter

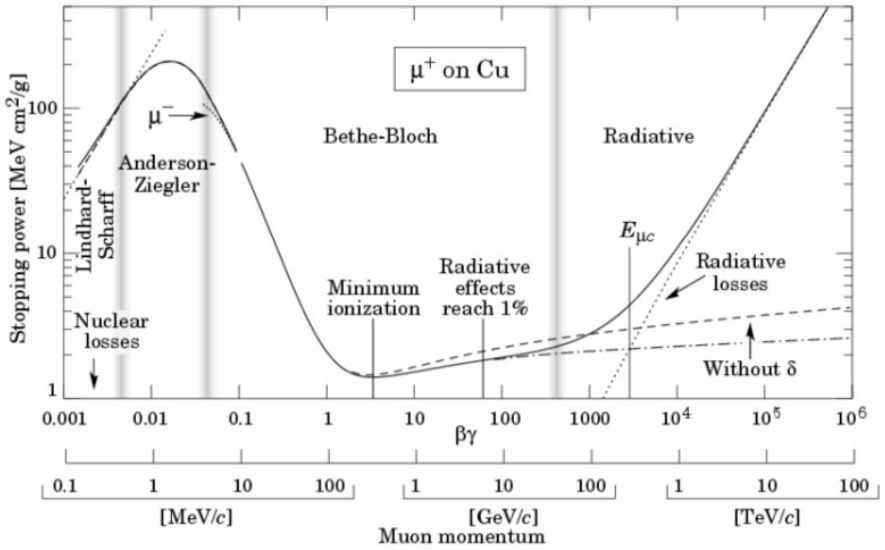

Figure 4.5: The stopping power for positive muons in copper as a function of the muon momentum [54]. The solid line is the total stopping power of the muon. [55]

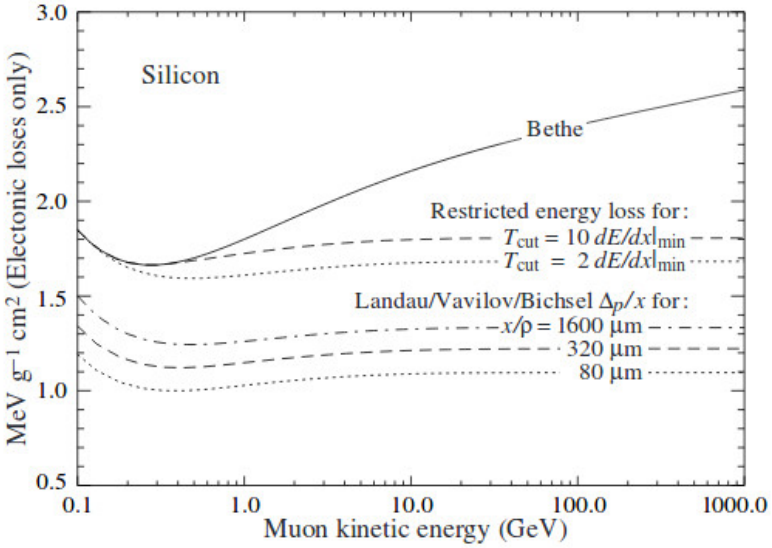

Figure 4.6: The Bethe dE/dx and the Landau most probable energy per unit thickness $\delta p/x$ in silicon. Minimum ionization ($dE/dx|_{min}$) is 1.664 MeV $g^{-1}cm^2$. Radiative losses are excluded. The incident particles are muons.[55]

Symbol	Definition	Units or Value
E	Incident particle energy γMc^2	MeV
T	Kinetic energy	MeV
$m_e c^2$	Electron mass $\times c^2$	0.510 998 918(44) MeV
r_e	Classical electron radius $e^2/4\pi\varepsilon_0 m_e c^2$	2.817 940 325(28) fm
N_A	Avogadro's number	$6.0221415(10)\text{x}10^{23} mol^{-1}$
z	Charge number of the incident particle	
Z	Atomic number of absorber	
A	Atomic mass of absorber	$g.mol^{-1}$
K/A	$4\pi N_A r_e^2 m_e^2/A$	0.307075 $MeV.g^{-1}.cm^2$ for A = 1 $g.mol^{-1}$
I	Mean excitation energy	eV
$\delta(\beta\gamma)$	Density effect correction to ionization energy loss	

Table 4.3: Definition and units/values of the variables used in Bethe-Bloch formula, Equation 4.13.

results in a large fluctuations of the energy loss (δ)) for 500 MeV pions incident on several silicon detector thicknesses are shown in Figure 4.7. The most probable energy loss, scaled to the mean loss at minimum ionization, is shown in Figure 4.8.

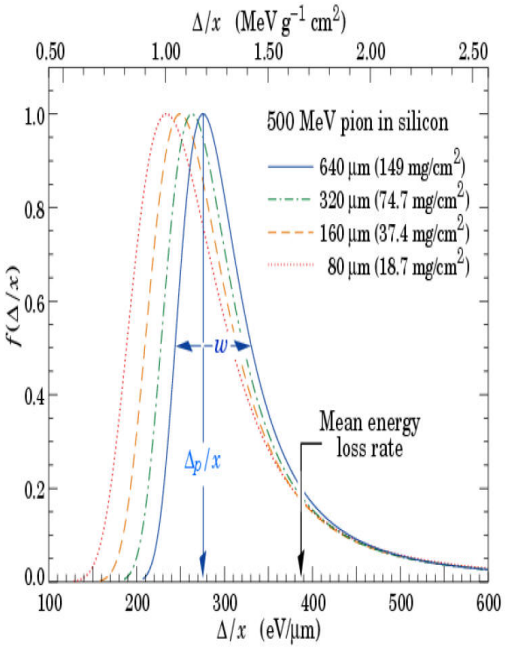

Figure 4.7: Straggling functions in silicon for 500 MeV pions, normalized to unity at the most probable value. The width w is the full width at half maximum. [55]

- **Bremsstrahlung** A charged particle in a medium will loose energy not only by ionization, by also by interaction with the Coulomb field of the nuclei of the material. When decelerated in the nuclear field, the particle will loose energy by emitting photons in the bremsstrahlung process. The radiation loss by bremsstrahlung is characterized by the radiation length X_0, the mean distance required to reduce the particle energy to a fraction 1/e of the initial

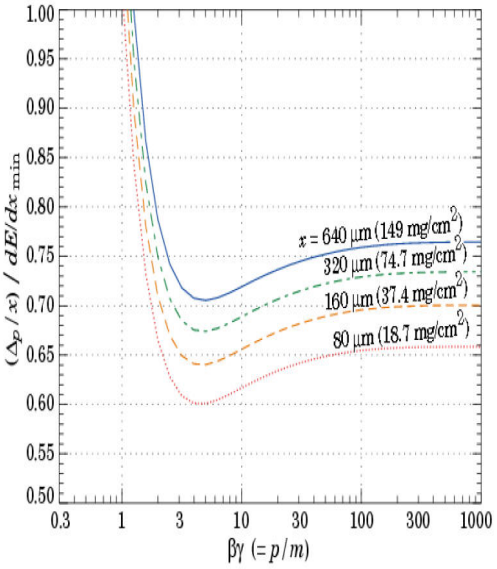

Figure 4.8: Most probable energy loss in silicon δp per unit thickness (x) , scaled to the mean loss of a minimum ionizing particle, 388 eV/μm (1.66 MeV $g^{-1}cm^2$)[55].

value. For Silicon the radiation length, X_0, equals to 21.82 $g.cm^{-2}$. The energy loss by bremsstrahlung is proportional to the particle energy, while the energy loss by ionization is proportional to the logarithm of energy: the bremsstrahlung will be the dominant source of losses at high energies.

- **Cherenkov Radiation** The Cherenkov radiation is emitted when a charged particle travels in a medium at a speed larger than the light speed in the medium. The velocity of light in a medium with index of refraction n is c/n. The energy loss by Cherenkov radiation is much smaller than the loss by ionization. However, its detection is the signature that the incident particle velocity is above the threshold.

- **Transition Radiation** The transition radiation is an effect related to the polarization of the medium produced by the passage of a charged particle. When a charge in relativistic motion crosses the boundary between two media with different dielectric properties, photon emission occurs.

4.3.2 Photon interactions

The three main processes for interactions of photons with matter are via the photoelectric effect, Compton scattering and pair production, each illustrated in Figure 4.9 (a), (b) and (c) respectively and described below.

Photoelectric effect

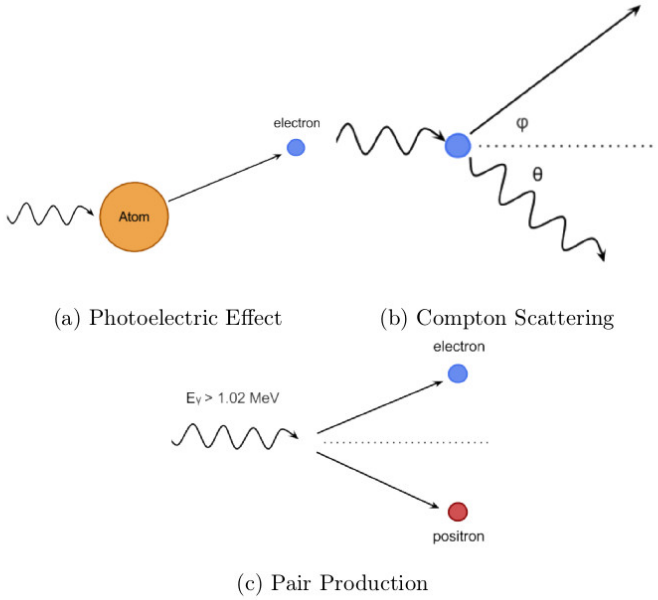

(a) Photoelectric Effect (b) Compton Scattering

(c) Pair Production

Figure 4.9: Illustrations of the three major photon interactions with matter.

When the energy of a photon is greater than the binding energy of an electron to an atom, the photon can be absorbed by the atom causing the release of the electron. The remaining atom is ionised until a free electron is captured. The energy of the emitted electron, E_{e^-} , is given by

$$E_{e^-} = h\nu - E_b \tag{4.14}$$

where $h\nu$ is the energy of the photon and E_b is the binding energy of the electron to the atom.

Compton Scattering Compton scattering occurs when a photon hits an atomic electron, transferring some of its energy and causing the electron to move off at an angle ϕ. The photon is scattered at an angle θ with a reduced energy. This effect was first observed by Arthur H. Compton in 1923 [58].

Pair production

The creation of an electron-positron pair can occur when a photon has an energy of greater than the combined rest mass of the two new particles. Any extra photon energy is equally divided between the two particles as kinetic energy. After a short period of time, the positron will annihilate with an electron in the bulk of the material producing two photons with energy of 511 keV.

4.3.3 Interaction of Hadrons

Hadrons interact with matter through strong interactions, in addition to the electromagnetic ones. The majority of process belonging to this class involve inelastic scattering events that produce additional hadronic particles. An high energy hadron, a proton or a nucleus, will experience a nuclear interaction after one interaction length λ_{int}, while loosing only a small energy by ionization. The interaction length λ_{int} of Silicon is 108.4 $g.cm^{-2}$. The interaction length plays, for hadron reactions, the same role of the radiation length for electromagnetic interactions.

4.3.4 Interactions of neutral particles

Neutral particles, as the name suggests, carry no charge and therefore do not interact via the electromagnetic interaction. Neutrons interact with the nucleus of an atom within matter and can travel centimeters before such an interaction occurs. During an interaction, the neutron can lose all of its energy, or some energy with a large change in direction. Secondary particles from an interaction are either those displaced from the atomic nuclei, or products of neutron-induced nuclear reaction [59].

4.4 Crystal defects from irradiation and their implications

Next to the ionizing energy loss caused by interactions with the valence electrons, particles penetrating the sensors are also subject to non ionizing energy loss through scattering off the lattice atoms. Both effects are taking place not only in the silicon bulk but also in the SiO_2 , used to electrically passivate the sensor surface. Surface and bulk defects have to be considered separately since the impact of the defects on the device performance, as well as the time scales of the defect formation, are very different.

4.4.1 Surface defects

To electrically passivate the surface of silicon sensors a layer of several 100 nm of SiO_2 is grown onto the silicon wafers in a high temperature oxygen atmosphere. Through this layer two kinds of crystal defects are introduced in the sensor surface region:

- **Defects within the volume of the SiO_2 layer:** Due to the growing process,

the crystal lattice of the SiO_2 has many imperfections, which are mostly positively charged. The most important defects are tri-valent silicon (positively charged), non-bridging oxygen (negatively charged), and interstitial oxygen (positively charged). As the defects worsen the quality of the SiO_2 layer, annealing techniques are used to passivate the defects during the sensor production. This is done by the diffusion of H^+ and OH^- ions into the oxide to pair-up with and neutralize the defect charges [60].

- **Defects at the interface between the silicon and the SiO_2:** As the lattices of silicon and SiO_2 are not identical there are unpaired, positively charged dangling bonds at the interface plane forming the interface defects. Also for these defects a controlled annealing with H^+ ions diffused into the silicon is used to passivate the dangling bonds by forming neutral Si - H bonds [61].

Surface damage is caused by ionising radiation such as photons, X-rays and charged particles and occurs in the $Si - SiO_2$ interface. Radiation penetrating the sensors, reactivates the passivated defects in the SiO_2 volume and the interface plane. Radiation-generated electrons will diffuse out of the oxide layer, while holes, with their much smaller mobility, will remain there, creating a positive charge region attracting electrons to the $Si - SiO_2$ interface and influencing the electric field in this area between the pixel implants. Consequently, to achieve, that the sensor performance is not influenced by surface damage, the changes in the electric field need to be taken into account in the sensor design.

Implications of surface defects

Both kinds of surface defects after irradiation lead to a positive charge density of the sensor surface which attracts electrons from the silicon bulk. This leads to a partial compensation of the p-type doping between the pixel implants and consequently to a reduction of the isolation capability. For a homogeneous p-spray implant the lower doping concentration results in a decreased electric field, while for a p-stop isolation the electric field is increased due to the overcompensation of the acceptors in the p-type bulk [62] In the moderated p-spray option, during irradiation the location of the highest field region can move from the transition between pixel and moderated p-implants towards the transition between moderated and not moderated p-implant during irradiation. Since both, the defects in the SiO_2 layer as well as those in the interface plane, are only reactivated, their amount is limited to the initial number of defects generated during the sensor production. As a consequence, a saturation of the number of surface defects is expected.

4.4.2 Bulk defects

Strong head on collisions of high energetic particles with silicon atoms can lead to atom displacements if the energy transferred is larger than about 25 eV [63]. These primary knock-on atoms (PKA) can either come to rest at a close-by interstitial position to form a Frenkel pair together with the vacant lattice site, or trigger further displacements, i.e. point-like crystal defects, along their trajectory if their energy is sufficient. As the scattering cross section increases with decreasing particle energy, an increased scattering rate and energy loss can develop at the end of the trajectories leading to a dense volume of defects called terminal cluster or cluster defect, see Figure 4.10 [64].

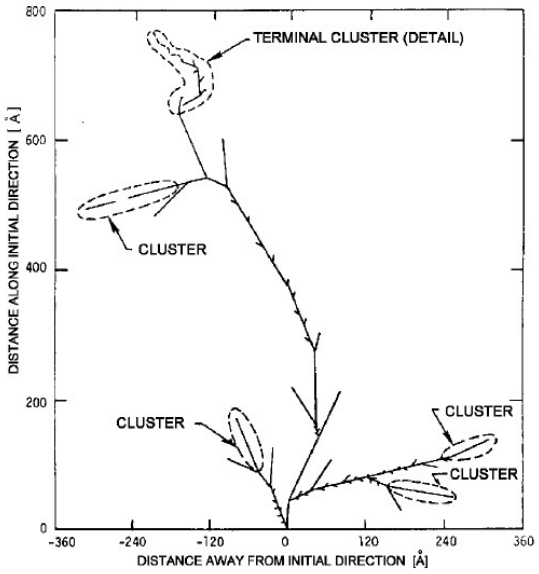

Figure 4.10: Monte Carlo simulation of the interaction of a PKA with an initial energy of 50 keV in silicon. The PKA initially travels in the vertical direction upwards, starting from the origin. At the ends of the trajectories of the displaced atoms, clusters of defects are generated [63].

Next to the above mentioned displacement of the PKA also atoms other then silicon can be introduced at lattice positions or in-between those, forming point defects. These impurity defects are usually enclosed during the production or processing of the silicon material. Naturally, the deliberate n- and p-type doping atoms also constitute this kind of impurities. In general, three types of point defects can be differentiated: interstitials, substitutionals, and vacancies. Figure 4.11 shows a classification of different point defects in silicon sensors. Furthermore, combinations of these are classified as they reveal additional properties [65].

Implications of bulk defects

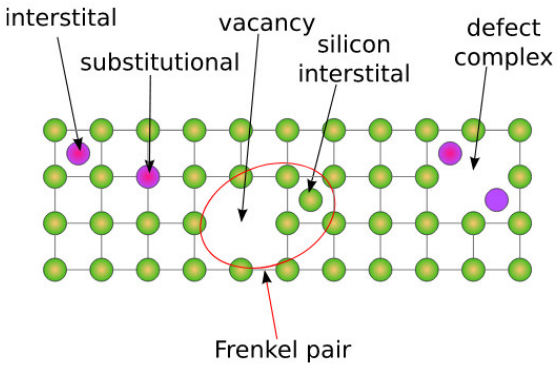

Figure 4.11: Schematic representation of some point defects in a square lattice. Silicon atoms are shown in green, other atoms in purple.

In general, any defects in the silicon crystal disturbing the periodicity can lead to additional energy levels in the band gap region. These energy levels act as donors or acceptors, hence constitute an effective doping, and thereby change the properties of the semiconductor sensor. In the following the effects from bulk defects are briefly discussed:

- **Generation**: Especially defects close to the middle of the band gap lead to increased thermal generation rates as the band gap can be overcome by two smaller steps in energy. The closer the defects to the mid-gap position the higher is the generation rate. This leads to large leakage currents in the devices proportional to the received irradiation fluence.
- **Recombination**: Some lattice defects can capture charge carriers of both polarities at the same time, leading to an increased recombination of electrons and holes after irradiation. The free carrier lifetime and drift length are reduced and hence the signal size decreases. This effect depends on the density of these recombination center defects, their energy levels, and the capture cross-sections for both carrier types.
- **Trapping**: Especially shallow defect levels close to one of the bands can temporarily trap charges after an effective trapping time $\tau_{eff_{e,h}}$. After large irradiation doses $\tau_{eff_{e,h}}$ decreases and many charges are trapped within the readout time window of the readout electronics, which leads to an exponential reduction of the signal size. The effective trapping time is inversely proportional to the received equivalent fluence, as a result, after fluences as expected at the HL-LHC, charge trapping is the dominating effect for reduced charge collection efficiencies (CCEs).
- **Scattering**: Radiation induced defects can act as scattering centers which reduce the mobility of electrons and holes. Hence, for the same voltages applied,

the drift velocity of the charge carriers is lower, reducing the induced signal current.

- **Change of effective doping concentration**: Most bulk defects in irradiated silicon exhibit acceptor like behaviour and compensate the donors present in the sensors. Hence, the effective doping concentration $N_{eff} = N_D - N_A$ decreases. The change of the effective doping concentration as a function of the equivalent fluence Φ_{eq} can be parametrized as an exponential reduction of donors and a linear introduction of acceptors. For n-type silicon the radiation induced decrease of the effective doping concentration can lead to a full compensation of donors and a space charge sign inversion (SCSI) into a p-type bulk. For the present ATLAS n-in-n pixel sensors this already happened in the early operation phase at around 3×10^{13} n_{eq}/cm^2

  After the SCSI the depletion zone develops from the front n-implant like in an n-in-p sensor, while before, it develops from the back side p-implant.

  For a detector of depth, d, the depletion voltage, V_{dep} , is related to the effective doping concentration by,

$$|V_{dep}| = (\frac{q_0}{2\varepsilon\varepsilon_0})|N_{eff}|d^2 \tag{4.15}$$

  It is foreseen that the V_{dep} in the current the ATLAS pixel b-layer reach 600 V at the end of Run-3. For the envisaged HL-LHC the V_{dep}, for a 150 μ m thick planar silicon sensor will reach several kV . Therefore, the sensors will have to be operated partly depleted, since the needed power supplies and cooling infrastructure are not in place. This leads to a decrease of the signal size

- **Poole-Frenkel effect** after high irradiation doses the effectiveness of thermal carrier creation is enhanced in high electric field regions [66]. This is known as the Poole-Frenkel effect and is a source for additional leakage current.

All the different displacement-defects introduced above are created by the Non-Ionizing Energy Loss (NEIL) of penetrating particles. However, the amount of damage varies widely with the type of incident particles and their energy. Low energy protons for example mainly interact by Coulomb interactions with the electrons and nuclei. Low energy neutrons only interact by elastic scattering with the lattice nuclei. For energies above several MeV for both, protons and neutrons, nuclear interactions begin to be the dominating effects for energy loss. The NIEL scaling hypothesis correlates the amount of displacement-damage to the incident particle type and energy. The NIEL scaling hypothesis is used to scale the radiation damage to the equivalent damage of 1 MeV neutrons to allow for comparisons of irradiations at the various irradiation facilities. Figure 4.12 shows the calculated damage functions for protons, neutrons, pions, and electrons over a wide range of energies.

Summary of Consequences of defects on silicon detector performance:

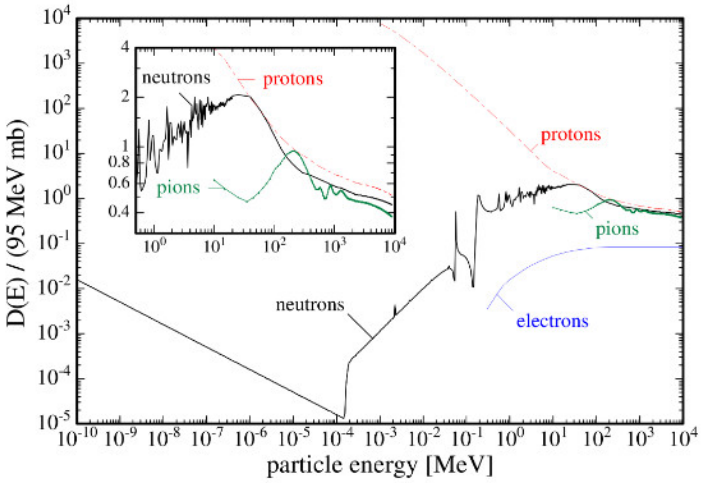

Figure 4.12: The calculated damage functions for protons, neutrons, pions, and electrons over a wide range of energies. The normalization of the ordinate to 95 MeV mb represents the damage equivalent to 1 MeV neutrons [67].

As explained before, two kind of radiation damage are important in the case of silicon sensors : Bulk damage caused by Non Ionizing Energy Loss (NEIL) and Surface damages caused by ionizing energy loss. Effects caused by particles interacting with the sensor's material lead to specific changes in the sensors operation conditions and electrical characteristics.

Exposure of planar pixel sensor to NEIL from protons, pions and neutrons modify its electrical properties in the following ways:

Effect on the depletion voltage: Due to the fact, that a change in the effective doping concentration after irradiation has an impact on the depletion voltage, as shown in Equation 4.15, radiation in p-type material induces an increase of N_{eff} and consequently increases the voltage needed to be applied for fully depleting the sensor. This altering of the effective doping concentration results what we called type inversion. As a result, in the n-type material, the depletion voltage first drops and then increases after type inversion. Instead, in the p-type material, the depletion voltage always increases with fluence. This effect is illustrated in Figure 4.13 for a 300 μm silicon detector of n-type at various fluence levels.

Effect on the leakage current: The increase in leakage current is material type independent and is generally proportional to the radiation dose, Φ_{eq} , and the total depleted sensor volume, V as shown in the following,

$$\Delta I = \alpha \Phi_{eq} V \tag{4.16}$$

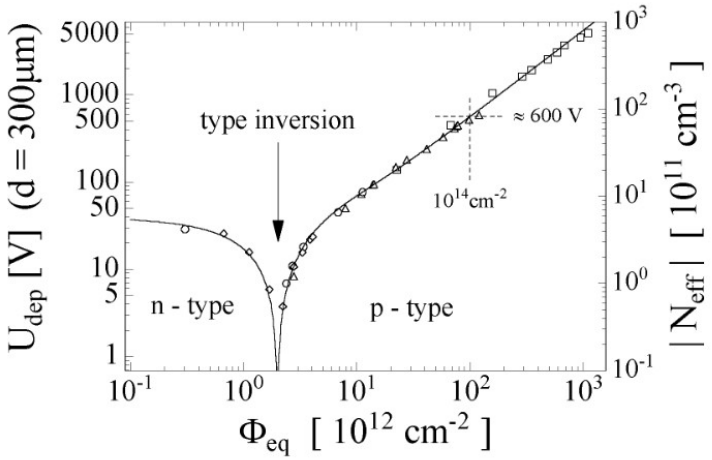

Figure 4.13: Relationship between the depletion voltage, U_{dep} , (left) and effective doping, N_{eff} , (right) as a function of the fluence for a 300 μm silicon detector [68].

where α is the current related damage constant. Radiation-induced defects increases the sensor current when interstitials or vacancies in the energy levels close to the band gap are generated. Electrons from the new energy levels are then able to be excited into the conduction band. For detector operation, an increased leakage current after irradiation result in increased noise and thus the signal to noise ratio decreases significantly. Furthermore, the leakage currents lead to a larger power dissipation. This needs to be compensated, if possible, by more powerful cooling systems, that may introduce additional inactive material into the detector system.

Effect on the charge collection efficiency: the presence of defects caused by radiation leads to reduced charge collection efficiency (CCE), which is defined as the ratio of the collected charge after irradiation to the full collected charge before irradiation. Loss of collected charge occurs due to charge trapping of the charge carriers after high irradiation within the defects in the silicon lattice sites. This lost charge does not contribute to the total collected charge from the particle and results in a reduction of the CCE. It becomes especially relevant after an exposure to irradiation fluences above 10^{15} $n_{eq}cm^{-2}$. The inefficiencies in charge collection significantly contribute to inefficiencies in particle detection in the tracking devices at the fluence levels expected at the HL-LHC.

On the other hand, surface damages lead to unwanted parasitic leakage path in the sensor and increase the crosstalk. This is due to the presence of electron layer at the interface. The positive charge collects at the oxide layer resulting in an increase in the positive surface charge. These effects are more serious in MOS devices and is not normally a problem in bulk silicon detectors.

4.4.3 Defect annealing

Not all defects generated by NIEL are stationary and permanent. Some are mobile even at room temperature and interact with other defects in the silicon material. These interactions are in generally referred to as annealing and are often classified into beneficial and reverse annealing (Figure 4.14) as they lead to a decrease or increase of the effective doping concentration. The annealing mechanisms can roughly be classified into three categories [69]:

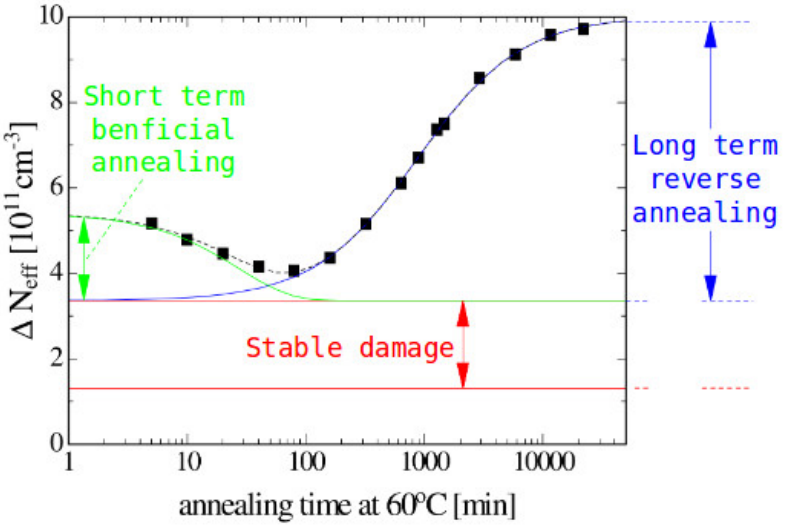

Figure 4.14: Measured change of the effective doping concentration as a function of the time during controlled annealing at 60 °C with fitted contributions of short term beneficial annealing, long term reverse annealing, and stable damage [65].

- **Migration**: the mobility of some defects strongly depends on the temperature as they are loosely bound to certain lattice positions. Above a certain activation energy which can be supplied by thermal excitations, these defects become quasi free and start to migrate until they are trapped by deep potential sinks from other crystal defects or the temperature is decreased again.

- **Complex formation**: the migrating defects can form new complexes. These can either result in larger stable defects like the formation of a double vacancy or result in defect recombination e.g. of Frenkel pairs. In the latter case the lattice locally returns into its undisturbed state recovering from the crystal damage.

- **Dissociation**: larger complex of defects can dissociate into smaller defects if the energy supplied is above a corresponding dissociation energy. After

this, the complex defect acts as separated defects usually showing different properties.

In all cases of defect annealing a certain activation energy needs to be supplied usually via thermal excitations. Depending on the activation energy for each annealing process an annealing temperature can be defined as described in [65]. With knowledge of the annealing temperature and corresponding annealing times it is possible to perform a controlled beneficial annealing of some of the bulk defects. Because permanently damaging reverse annealing processes dominate after long exposure to high temperatures (Figure 4.14) the annealing parameters have to be chosen carefully.

Chapter 5

The ATLAS Pixel Detector

Contents

5.1 Pixel detector in particle physics 76

5.1.1 Hybrid planar pixel detector 76

5.1.2 Pixel sensors Fabrication Process 77

5.2 The actual ATLAS pixel detector 80

5.2.1 Planar pixel technology 81

5.2.2 3D pixel techonlogy 84

5.3 The ITk pixel detector for HL-LHC Phase-II 85

5.3.1 Requirement of Planar pixel sensor technologies for HL-LHC upgrade 87

5.3.2 Other options for pixel sensor technologies for the upgrade . 88

5.4 R&D study to improve the future ATLAS pixel sensor design 89

5.4.1 Active edge technology 90

5.4.2 Sensor electrical characterization 92

5.4.3 Results 95

5.4.4 Conclusions 98

The ATLAS pixel detector is the innermost sub-system immediately outside the LHC beam pipe. Formerly built as a three-layer detector, the present ATLAS pixel detector was upgraded with a fourth layer, the Insertable B-Layer (IBL), located closest to the interaction point. This chapter should help to understand the basic concepts which are necessary to understand the design, functionality and operation of the ATLAS pixel sensors. The first section gives a brief introduction to role of pixel detector in HEP. It is followed by introducing the hybrid planar pixel sensor technology and explaining the entire process flow for the production of n^+-in-p silicon pixel sensors. The second part of the chapter focuses on description of the layout of the current ATLAS pixel sensors and modules as well as the future ATLAS pixel detector for the ATLAS Phase-II at HL-LHC.

5.1 Pixel detector in particle physics

Silicon-based detector have been used for the last 60 years as an efficient mean to detect the presence of charged particles. Gold contact barrier, then p-n junction diodes were used between 1955 and 1965 as an efficient small size spectroscopic sensor to measure the ionizing energy deposition of β particles in silicon. The first HEP experiments to make a wide use of silicon as a tracking detector were CERN's NA11 and NA32 [70]. The strip sensors used in their tracking system showed the possibility of large scale usage of these sensors in tracking applications in HEP.

Over the last 30 years solid state detectors have gained an important role with their excellent tracking capabilities for high energy physics experiments. In a regime of high particle multiplicity at hadron colliders, segmented semiconductor devices are a suitable technology for position sensitive detection, while keeping low cell occupancy. In the volume closest to the interaction point, pixel detectors are normally used thanks to their finer segmentation. The pixel cells define the granularity of the detector and provide a two-coordinate position sensitivity for the point of incidence together with a fast timing. From the particle trajectories, the basic properties of the traversing charged particle, like momentum and point of origin, can be evaluated. Up to now the pixel detectors at LHC have been built with a hybrid technology, where the sensing element (sensor) and the matching readout chip are processed independently and then connected. In this way the material and processes aree individually optimised. This approach makes it possible to achieve fast enough readout and radiation hardness to cope with the LHC environment.

5.1.1 Hybrid planar pixel detector

Hybrid detectors are particularly beneficial in the LHC and the HL-LHC environment, given the fact, that they allow for a separate optimization of the sensing and readout elements against radiation effects. A hybrid pixel detector is composed of a sensitive volume, the sensor, and a readout chip for processing the signal produced in the sensor. The fine segmentation results in good position resolution of the tracking devices. With solder bumps of diameter around 20-30 μm , which are deposited on each readout cell, a mechanical and electrical connection to the sensor cells is established. The interconnection method is known as flip chipping . For the deposition of the bump balls, an under bump metallisation (UBM) made of different metal alloys, depending on the production, is grown on the contact pads of both the readout chip and sensor side. On the UBMs on the chip side, bump balls are grown by electroplating with solder and shaped into spheres by a re-flow process. They create the electrical connection between readout chip and sensor. To prevent from oxidation or diffusion of the bump balls into the UBM, gold is added in some productions on top of the UBM. The pixel cell size is defined by the size of the

readout cell of the chip. For the currently implemented pixel sensors in the ATLAS detector, the pixel cells are 50×250 $\mu m^2$and 50×400 μm^2 . A schematics view of one pixel cell in a hybrid pixel detector is shown in Figure 5.1

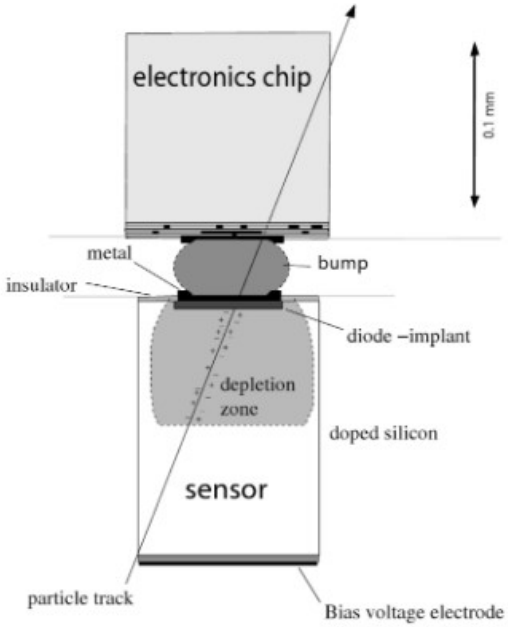

Figure 5.1: Schematic view of a pixel cell in a hybrid pixel detector. This detector is composed of a sensor and a readout chip interconnected via a bump ball in between the under bump metallizations on chip and sensor side [71].

5.1.2 Pixel sensors Fabrication Process

Pixel sensors, initially introduced as planar pixel sensors [72], are composed of a lightly doped bulk material with highly doped implants on the sensor front (n^+) and backside (p^+) in the case of n^+-in-n and n^+-in-p planar sensors. The highly doped implants on the opposite sides with the lightly doped silicon bulk in between are characteristic for planar sensors. The sensor is produced in such a way, that first the entire silicon surface of the wafer is polished by removing all natural oxide layers and then accurately thermally oxidised. As the next step, photoresist is deposited on the sensor surface and the front side is exposed to a mask to create openings in the photoresist in correspondence of the n^+ implants. The implanted ions are annealed to activate the dopants. Afterwards, silicon nitride and Low Temperature Oxide (LTO) are deposited onto the front side of the wafer and etched away in a successive way in selected areas over the n^+ implants to allow for contacts of the implants through these isolation layers. Afterwards, a layer of aluminium is deposited over the pixel implants, to which it is contacted through the openings in the silicon oxide and nitride. As a last step, the sensor front side is protected with

a passivation layer, left open in the area, where the contact to the chip bumps must be established [71].

Inter-pixel isolation

Electrons accumulate in these inter-pixel regions, being attracted by the fixed positive charge of the SiO_2 layer, especially after irradiation. This increases the amount of negative charge up to the n^+ pixel implantations and causes conducting n-channels between them, resulting in a creation of shorts on the sensor surface. To insulate the n^+ pixel implantations, a low dose Boron implantation is performed between the n^+ implants, leading to the creation of positive fixed charges, that compensate the electron layer. Three different solutions are presently available: p-stop, homogenous p-spray and moderated p-spray. In the solution of isolation by the p-stop method, a mask is used to create a p^+ layer in the central area between two implants, requiring an additional photolitographic step. Next to the drawback in terms of cost due to an additional production step, it can be difficult to allocate space for the p^+ stop line for the small distances in between the pixels cells. The p-spray method prevents from these drawbacks with a homogenous low dose p-spray in between the pixel implants. However, the homogenous p-spray leads to a creation of high electric field regions between the p-doped silicon and the pixels. To prevent this problem, the doping concentration of the p-spray in the region close to the pixels can be reduced, the so-called moderated p-spray method. This method is currently employed in the ATLAS pixel detector.

Pixel sensor design

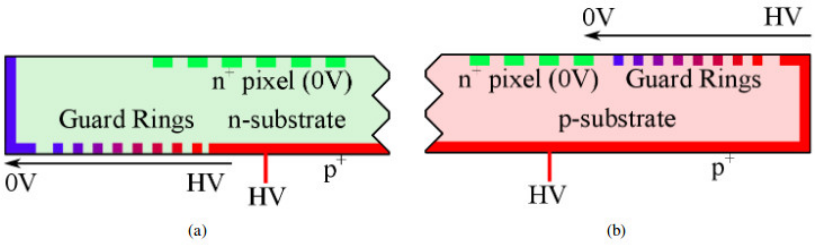

Figure 5.2: (a) n^+-in-n sensor design with an n-type bulk and n^+ implants. The guard rings are located on the backside. (b) n^+-in-p sensor design with a p-type bulk and n^+ implants [73]. The guard rings are on the topside.

The sensor are either built on an n-type or p-type material. In high energy physics either the n^+-in-n or n^+-in-p technologies are employed for pixel sensors. This is due to the fact, that n^+ implants act as the collecting electrode for electrons, generated in the bulk, in reverse bias mode. Electrons have a higher mobility compared to holes, resulting in a lower probability for the electrons to be trapped after irradiation. The n^+-in-n technology is presently used in the ATLAS pixel detector, while the n^+-in-p technology is foreseen to be implemented in the future ATLAS pixel detector. The

layouts of both technologies are displayed in Figure 5.2. One difference of the two technologies concerning the design is, that in the n^+-in-n planar sensor technology the main junction is at the backside of the sensor, while in the n^+-in-p planar sensor technology the main junction is located at the front side of the sensor. Consequently, the depletion in the different sensor types start at either the backside or the front side of the sensor. After irradiation of an n^+-in-n sensor, type inversion changes the n-type bulk to a p-type bulk. The p-n junction moves to the front side and the depletion starts from the front side. Given the fact, that the main junction is on the backside, n^+-in-n sensors need the guard ring structure, explained later on in this section, to be implemented there, thus requiring a complete double-sided processing.

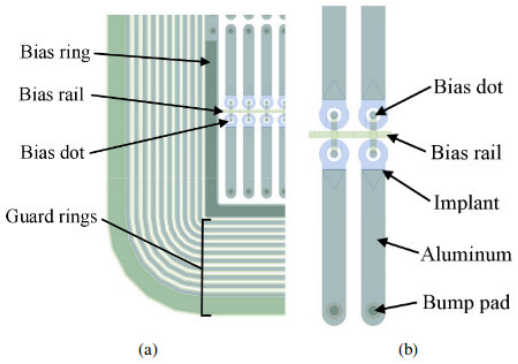

Figure 5.3: Layout of a pixel sensor: (a) cut-out of a sensor corner with GRs in the periphery of the active area of the sensor, (b) cut-out of four pixels from the active area of the sensor. A bias rail runs in between the short side of the pixels. It is situated on the same side as the bias dots, implemented either in an opening of the pixel implant (as shown in the figure) or in close proximity. Such design is called standard single punch-through design. On the other side of the pixel cell the bump pad for the interconnection to the readout channels is located [74].

Guard ring structure

Guard ring (GR) structures are needed to achieve a smooth potential drop from the active area at ground to the region, where the high voltage potential is applied. In n^+-in-p sensors the GRs are implemented on the front side, where the main junction is located. Increasing the number of GRs in the same area leads to smaller potential steps between them and to a reduction of the electric field. The innermost GR is grounded for biasing purposes of the entire sensor and is therefore called bias ring (BR). Through the BR the electrical properties of sensors are tested before interconnection to readout chip. With this, rare damages are identified by increased leakage currents. The BR is connected to a bias rail , which runs between every second pixel column passing close to the pixel implants. The pixel implant itself derives its potential from the bias rail through a circular implant, the bias dot, which is located either in an opening of the pixel implant itself or in close proximity. The bias dots are always designed to be on the opposite side of the bump bond pads. An example of the sensor surface layout with pixel implants and their biasing structure

is shown in Figure 5.3.

To obtain an induction effect between different potentials, either in the area where the GRs are situated, or in the active area with the pixel implants, the so-called punch-through effect [74] is used. With the punch-through effect the potential of the outer GRs decreases gradually from the ground potential of the innermost one, down to the value of the outermost one, that is very close to the negative high voltage applied at the backside. From the BR, the ground potential is transmitted to the connected bias rail and bias dots. The pixel implants are then lifted through the punch-through effect to a potential close to ground, but still negative. The potential difference between the bias dot and the pixel implant increases with the high voltage applied to the backside. This is due to the fact, that the silicon bulk between the two parts acts like a dynamic resistance.

5.2 The actual ATLAS pixel detector

The present pixel detector is made of 1456 modules, distributed in the three outer layers, named L_1 , L_2 and L_3 , at radii of $L_1 = 50.5$ mm, $L_2 = 88.5$ mm and $L_3 = 122.5$ mm. Additional 288 modules are located at the three disks at the forward and backward direction of the detector [75]. It was designed for an instantaneous luminosity of $10^{34} cm^{-2} s^{-1}$. Since during ATLAS Run 2 and Run 3, the luminosity is expected to increase up to a value twice the nominal one, resulting in a higher number of pile-up events, a fourth pixel layer was built to retain the performance of the pixel detector. The additional IBL layer implementing a new readout chip and two new sensor technologies (planar and 3D), is located at a distance of 33.0 mm from the beam pipe. The 4-layer system of the pixel detector and the radial position of the barrel layers are illustrated in Figure 5.4. With the insertion of the IBL and, hence, the addition of a further space point, the tracking performance was improved.

The IBL is constructed of fourteen local support and cooling structures (staves), which are loaded with 20 hybrid pixel detector modules each. Two types of modules are used for IBL, planar double chip modules and 3D single chip modules. Both module types are read-out using the FE-I4 readout chip. The FE-I4 holds a pixel matrix organized in 80 columns and 336 rows. The planar modules consist of a single silicon sensor produced at CiS, Erfurt, Germany, which is connected to two FE-I4 chips. The 3D silicon modules make use of 3D silicon sensors for the first time in large scale in a collider experiment, which were produced by FBK, Trento, Italy and CNM, Barcelona, Spain, and are read-out by single FE-I4 chips. The IBL 3D sensors are a double readout-column design with 50 μm pitch between the vertical readout-electrodes. Twelve planar modules are placed in the central region of each stave and four+four 3D modules are loaded at each extremity, as indicated in Figure

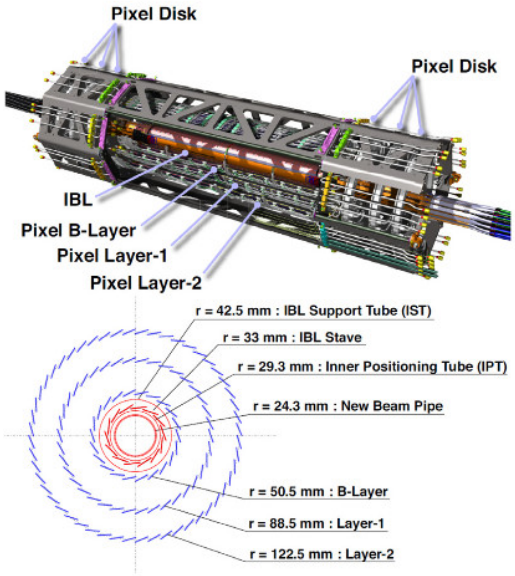

Figure 5.4: Schematic view of the ATLAS 4-Layer Pixel Detector for Run-2[76].

5.5.

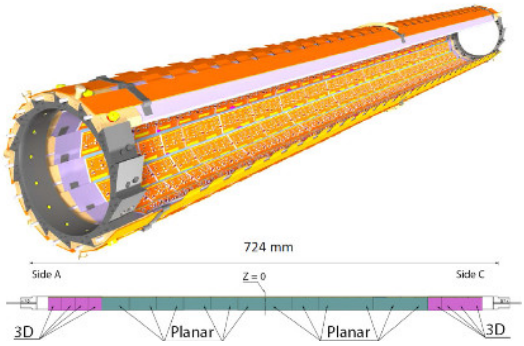

Figure 5.5: Top: 3D rendering of the IBL detector with its 14 staves (some staves removed to make the module side of staves visible). Bottom: Sketch of the loading scheme of the different module types on the IBL staves.

5.2.1 Planar pixel technology

The n^+-in-n planar sensor technology is the sensor technology implemented in the ATLAS pixel detector. The FE-I3 front-end chip [77] pixel sensors of the three outer layers consist of a 250 μm thick n-doped bulk, while the upgraded pixel sensors of the IBL consist of a thinner 200 μm thick bulk. The front side of the sensor is highly doped with n^+ implants, defining the size of the pixel cell with the size of

the n^+ implants. The isolation of the pixel implants is achieved with moderated p-spray, where a higher p-spray dose is implanted in the center area between two pixels through an opening of the nitride layer. The backside has a uniform p^+ implant and forms, together with the patterned n^+ implant on the front side, parallel electrodes. This is the key feature of the planar sensor technology for the present ATLAS module. The present ATLAS module is illustrated in Figure 5.6.

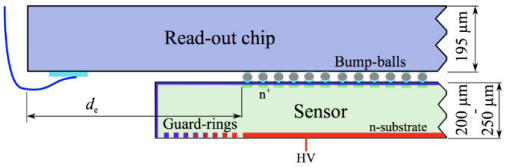

Figure 5.6: The present ATLAS module displaying a sensor in the thickness range from 200 μm (FE-I4 sensor) to 250 μm (FE-I3 sensor)[78].

The outer three original layers of the ATLAS pixel detector are instrumented with ATLAS FE-I3 readout chips, interconnected to the n^+-in-n planar sensors. The sensor has a pixel cell size of 50×400 μm^2 organised in a 328×144 pixel matrix plus additional slightly larger pixels in the outer 16 columns with a cell size of 50 ×600 μm^2. The sensor is manufactured in such a way, that it can be interconnected to a total of 16 readout chips. With this, it makes up an active sensor area of 16.4 ×60.4 mm^2. While in case of the IBL, the modules are composed of a sensor interconnected to FE-I4 readout chips. The sensors are designed to be interconnected to two readout chips with an active sensor area of 16.8 ×40.9 mm^2 with two columns at the edge and two columns in the middle of the double chip employing longer pixel cells of 50 ×500 μm^2. To be compatible with the FE-I4 readout chip, the pixel pitch of the FE-I4 sensor is reduced to 250 μm in the beam direction, to achieve a lower hit occupancy per pixel together with a better resolution in the beam direction.

The main difference between the two sensor designs (FE-I3 and FE-I4), shown in Figure 5.7, lies in the number of implemented GRs on the sensor backside, where the GRs control the potential drop from the high voltage applied in the area within the innermost GR on the backside, to the ground potential at the edges and the front side. The FE-I3 sensor hosts 22 GRs. This results in a dead area of 1.1 mm. Instead in the FE-I4 sensor, the inactive region was decreased to 200 μm in the column direction and to 450 μm in the row direction by reducing the number of GRs to 13 and by partially shifting the rings, situated on the backside, underneath the outermost n^+ implants, situated on the front side. Consequently, the inactive area is smaller in the FE-I4 sensor. The two sensor design are shown in Figure 5.8.

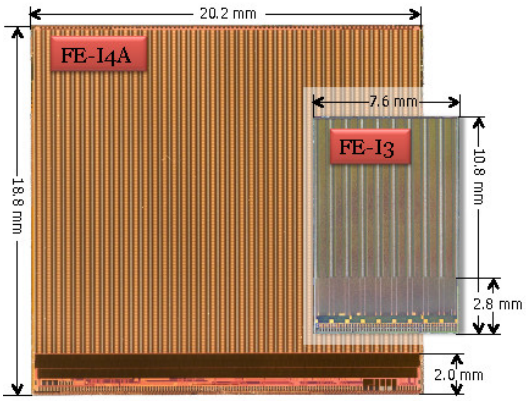

Figure 5.7: The FE-I4 readout chip for IBL with the to-scale FE-I3 readout chip used in ATLAS for comparison to[79].

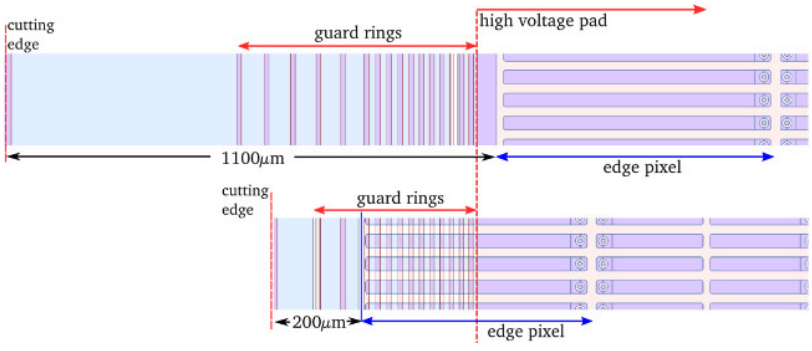

Figure 5.8: (top) the current ATLAS sensor design and (bottom) the IBL sensor design [80].

5.2.2 3D pixel techonlogy

As mentioned before, for the IBL construction, a new pixel technology has been used. This is the 3D pixel sensor. The 3D silicon detectors are intrinsically more radiation tolerant than other available sensor technologies. In the planar sensor technology the minimum distance between the two electrodes is limited by the minimal achievable thickness of the sensor. This distance in the 3D sensor technology is decoupled from the device thickness and can be chosen to be significantly smaller than the thickness of the standard planar sensors. As the drifting distance of the generated electron/hole pairs in the bulk is reduced, this leads to less charge trapping from radiation induced defects and lower operational voltages, which, in turn, translates into lower power dissipation after irradiation. . The IBL 3D sensor design is accomplished by inserting electrodes perpendicular to the sensor surface into the p-type bulk. The p-type substrate is chosen to prevent the bulk from type inversion after high irradiation fluences. The electrodes are produced by etching narrow columns into the bulk substrate using Deep Reactive Ion Etching (DRIE) [81] and subsequently n^+ and p^+ doped, where in a single pixel cell two n^+ columns are surrounded by six p^+ columns in total. An electric field is generated between oppositely doped neighbouring columns, as depicted in Figures 5.9(b). The spacing between the n^+ columns defines the pixel cell size, while the spacing between the oppositely doped columns defines the charge collection distance. This first generation of 3D pixel sensors implemented in the IBL with a charge collection distance of 67 μm and a sensor thickness of 230 μm demonstrated a radiation tolerance of at least up to $5{\times}10^{15}$ $n_{eq}cm^{-2}$. The 3D modules of the IBL employ the FE-I4 pixel cell size of $50{\times}250$ μm^2 which are produced by two silicon processing facilities: Centre Nacional de Microelectronica (CNM) [82] and Fondazione Bruno Kessler (FBK) [83], see Figure 5.10. About 25% of the IBL modules are produced with the 3D sensor technology, populating the outer parts of the staves.

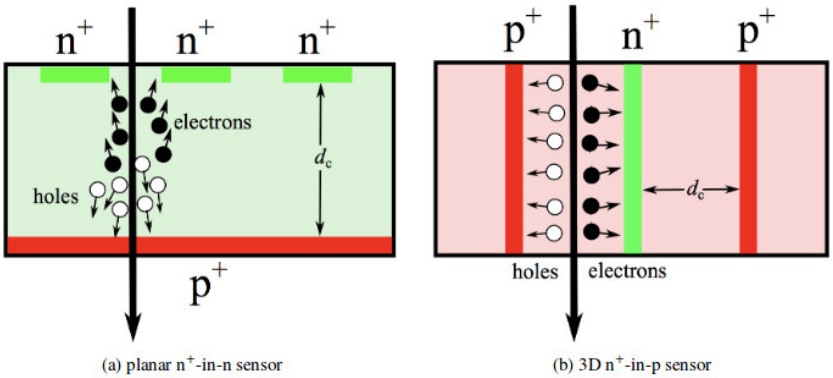

Figure 5.9: The two sensor technologies: (a) planar n^+-in-n and (b) 3D n^+-in-p sensors. The n^+ electrodes are illustrated in green, while the p^+ electrode are coloured red. In the IBL, the charge collection distance d_c is 200 μm for the planar sensors and 67 μm for the 3D sensors [74].

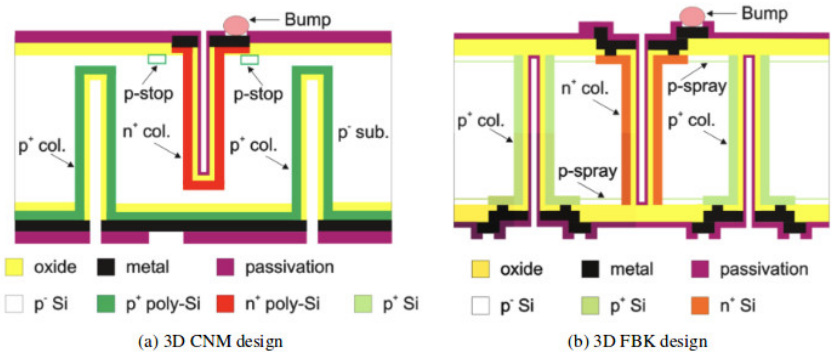

Figure 5.10: Schematics of the two 3D sensor options presently operational in the ATLAS IBL. The 3D sensor (a) with columns, etched partially through the bulk (CNM design) and (b) with full-through columns (FBK design). Both sensors are processed double-sided. [80]

With its decoupled electrode spacing, 3D sensors are advantagous in terms of lower depletion voltages compared to the planar sensors, especially after high irradiation fluence. The resulting lower operational bias voltage leads to a decreased power dissipation. The main disadvantage is the low production yield of 60% calculated on 50 wafers [84] produced for the IBL, caused by the complex 3D sensor fabrication.

5.3 The ITk pixel detector for HL-LHC Phase-II

For the upcoming challenges posed by the HL-LHC especially for the innermost layers of the pixel detector, the currently implemented pixel technologies will not be capable to maintain their tracking and b-tagging performance. Consequently, the present pixel detector will be replaced using modules with upgraded sensor technologies. This will reduce the material budget and consequently the multiple scattering within the tracking devices. The total pixel detector surface foreseen to be approximately 14 m^2 , will be almost 10 times larger compared to the current pixel detector employing a total surface of 1.73 m^2 [43]. The detector will employ modules with decreased sensor thicknesses, as well as finer pixel cell granularity. The new modules are designed to be able to withstand a radiation fluence in the order of 10^{16} $n_{eq}cm^{-2}$.

The future ATLAS pixel detector will consist of five barrel layers at radii of 39 mm, 99 mm, 160 mm, 220 mm and 279 mm for the five successive layers L_0 to L_4. Due to the harsh radiation environment over the full HL-LHC run period, the ITk detector will be built in such a way, that it will be possible to replace the two innermost pixel layers after around half its lifetime. In this scenario, the highest fluence in L_0 is expected to be 1.4×10^{16} $n_{eq}cm^{-2}$ and 3-4 $\times10^{15}$ $n_{eq}cm^{-2}$ in L_1 . The fluence in the outer layers is expected to be at maximum 3 $\times10^{15}$ $n_{eq}cm^{-2}$

[43]. An inclined layout option, with a pseudo-rapidity coverage up to $|\eta| = 4$, is foreseen. A schematic of the pixel detector layout, designed to avoid long clusters and reduce the occupancy as well as the material crossed by charges particles, is shown in Figure 5.11. The 3D sensors are the baseline in the innermost layer and planar sensors in the four outermost layers. The planar sensors will be based on a thinner bulk of 100 μm in layer 1 (L_1) and of 150 μm in layer 2 to layer 4 (L_2 -L_4). In the innermost layer (L_0) single and quad chip modules with single 3D sensors are foreseen. Instead, the remaining barrel layers will hold quad chip modules employing the planar sensor technology based on thin n^+-in-p planar pixel sensors. For a potential cost reduction, CMOS active devices are a promising candidate to instrument the large area of the fifth barrel layer. Close to the interaction point, a small pixel cell size and slim edge sensors are essential to cope with the increased particle density and to avoid a large fraction of inactive sensor area.

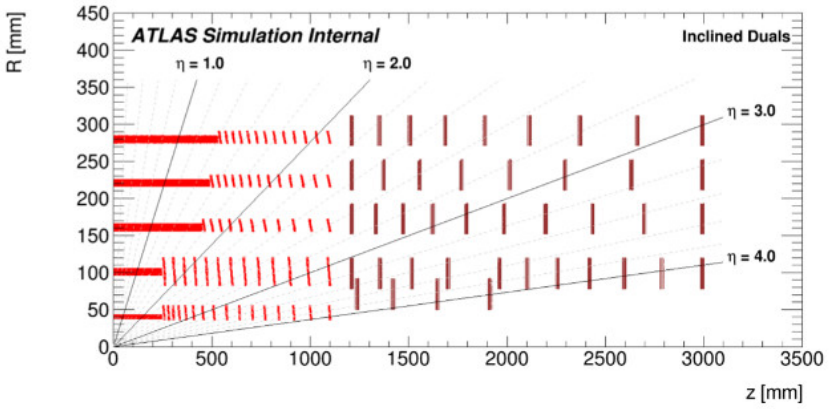

Figure 5.11: A possible schematic layout of the pixel detector for Phase-II. It represents the inclined layout with a pseudo-rapidity coverage up to $|\eta| = 4$. The horizontal axis is parallel to the beam line, while the vertical axis is the radius from the center of the beam line, point zero in the diagram. Only the active detector elements of the first quadrant are shown. [43].

In hybrid pixel modules not only sensors have to withstand the upcoming challenges, therefore a new readout chip, the RD53A readout chip, was developed. The RD53A ATLAS readout chip is implemented in the 65 nm CMOS technology and developed by the RD53 Collaboration [85] to sustain three main challenges: radiation tolerance (at least up to a total dose of 500 MRad), high hit rate capabilities and stable low threshold operation. The RD53A readout chip will be compatible with both 50×50 μm^2 and 25 ×100 μm^2 sensor cell sizes and stable low threshold operation. The chip cell size is chosen to be 50 ×50 μm^2 with a larger number of readout channels with respect to the present readout chip in order to maintain the present level of occupancy at the high particle multiplicity of the HL-LHC. Table 5.1, summarize the design parameter for the RD53A chip compared to the two predecessor, FE-I3 and FE-I4 readout chips.

	First Chip in ATLAS FE-I3	IBL chip-Phase-I FE-I4	ITk chipe-Phase-II RD53A
Pixel size [μm^2]	50×400	50×250	25×100 and 50×50(**)
Number of Pixel	2880	26880	76800
Readout rate [Mb/s]	40	320	1000-4000
Radiation hard [Mrad]	100	200	500
CMOS technology	250 nm	130 nm	65 nm

Table 5.1: Summary of the RD53A chip specification, that will be used in Phase-II upgrade for the ITk, in comparison with the previous readout: the FE-I3 and the FE-I4.[86]. (**) Note that for the RD53A chip, the chip grid is 50×50 μm^2 but the compatible sensors are either 25×100 μm^2 or 50×50 μm^2.

5.3.1 Requirement of Planar pixel sensor technologies for HL-LHC upgrade

Planar pixel sensors are the baseline for Layer 1 to Layer 4 for the ITk Pixel Detector. The following explains briefly the different technologies that are recommended for the ITk requirement:

- The ***n^+-in-p planar technology*** Due to its simplified process flow with a single-sided processing, it represents a cost-effective option with respect to the double-sided processed n-in-n planar sensors currently implemented in the ATLAS pixel detector. Moreover, the p bulk is known for it radiation hardness properties as it is non-inverting material compared to the n bulk sensors.

- Use of ***thinner sensors***. The active thickness of the sensors in the different layers need to be adjusted depending on the irradiation fluence they are exposed to, taking into account the requirement of maintaining high hit efficiency and low power consumption after high irradiation fluences. High hit efficiency can be achieved by reducing the sensor thickness that results in a shorter collection time and hence in a lower probability for the charge to be trapped, while drifting to the electrodes. Thin sensors reduce the power dissipation due to the fact that the thinner devices need smaller operational bias voltage. Therefore, Planar sensors with 150 μm thickness are chosen to instrument L_2-L_4 of the ITk, while for L_1 100 μm thick sensors are necessary to meet the requirements on the power dissipation.

- Thin planar pixels can also be further processed to obtain activated vertical sides that allow for an extension of the depleted region up to the edges. ***Slim and Active edges*** are example of such technology. The active edge is obtained by the extension of the backside implantation to the sensor edge. With this process, the electric field shape get smoother at the edges with respect to standard sensors without side activation which helps to decrease the number of GRs needed and consequently to increase the active area. This is important, given the fact, that in the ITk, sensors with slim edges of below 250 μm are required especially in the innermost region close to the interaction point, to allow for minimal inactive areas at the peripheries of the module for high tracking efficiency.

- Increase sensor granularity to maintain the performance of the pixel detector at high particle densities (high pileup) at HL-LHC. The pixel cell size of the sensors is designed to be 50×50 μm^2 or 25×100 μm^2. The ***reduced pixel cell size*** (which is compatible to the RD53A chip size) will have the further benefit of a better position resolution in the ITk

- Regarding the ***GR structure***, for n^+-in-p, the GR region will be implemented with the n^+ pixel implants on the front side of the sensor. Since this side is interconnected to the readout chip, the ground potential of the readout chip is transferred to the pixel implants. Sparks can occur between the readout chip and the sensor edge due to fact that the GR situated at the sensor edge and being on a potential different to ground. To avoid this problem, and different to the n^+-in-n sensor technology, the module needs a further isolation layer between sensor and chip. Possible explored solutions using BCB, , which is a Benzocyclobutene deposition either on sensor or readout chip before interconnection or Parylene coating, performed at module level, to ensure operation at high bias voltages.

- In addition to the GR structure, an additional implementation of punch-through structures (p-t structures) can be used. It allows for grounding all pixel implants of the sensor to measure the leakage currents. Studies have shown that the p-t structures induce a decrease of the collected charge in the area, where they are implemented, especially after irradiation. An alternative bias grid, created with a temporary layer, is investigated for the future sensor productions. The temporary layer is used for shorting all pixels to measure the leakage currents before interconnection and removed before further processing and interconnection to the readout chip.

5.3.2 Other options for pixel sensor technologies for the upgrade

Along with the n^+-in-p planar pixel modules, the 3D sensor technology as well as the Complementary Metal-Oide-Semiconductor (CMOS) monolithic sensors are foreseen to instrument the future ATLAS pixel detector.

The ITk Pixel Detector requires very particular developments of the ***3D sensor technology***: smaller pixel sizes, thinner active areas and extreme radiation tolerance. Due to the deficiencies exhibited by the planar pixel modules in a high radiation environment of around 10^{16} $n_{eq}cm^{-2}$, i.e. the higher operational voltage and the resulting higher power dissipation, the 3D sensor technology is chosen as the baseline for the innermost layer, L_0. For the ITk detector, productions of 3D devices is foreseen with a pixel sizes of 25×100 μm^2 and 50×50 μm^2 with the inter-electrode spacing, currently 67 μm, will decreased to 28 μm or 35 μm , depending on the pixel cell size chosen [87]. This also further enhance their radiation hardness. Hit reconstruction efficiencies greater than 97% with an associated power dissipation of about

10 mW cm^{-2} have been demonstrated for 3D devices with 50×50 μm^2 pixel geometries irradiated with 24 GeV protons up to 1.4×10^{16} $n_{eq}cm^{-2}$ [88]. Furthermore, specific productions of 3D sensors compatible with the first ITk prototype front-end chip (RD53A), at the time of writing, have been, or are being, completed at CNM (Barcelona), FBK (Italy) and Sintef (Norway). Despite the known drawback of the 3D sensors, the relatively small area to be covered in the innermost layer is not overmuch affected by the lower yield and high production costs of 3D sensors.

A different approach to planar sensor fabrication is the use of ***CMOS*** technologies, see Figure 5.12 The CMOS technology is based on the approach, that pixel sensor and readout chip are integrated into one unit, often called Monolothic, in contrast to hybrid pixel modules.

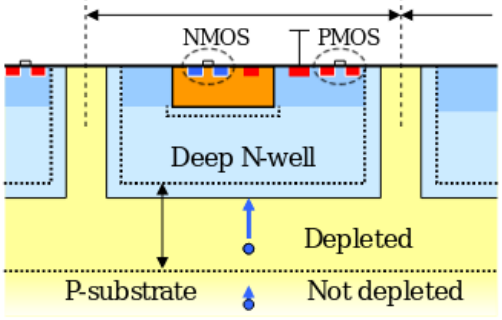

Figure 5.12: schematic of a HV-CMOS pixel. A CMOS consists of an NMOS and a PMOS. The NMOS is embedded in a shallow p-well inside the deep n-well while the PMOS is located inside the deep n-well in the p-substrate [89].

In the context of the ITk upgrade, the hybrid pixel modules are unrivaled in terms of rate and radiation tolerance. Therefore, the CMOS technology is an option only for L_4 , an area with low occupancy and low irradiation level in the ITk. The benefit to chase the CMOS technology is to further minimize the cost.

5.4 R&D study to improve the future ATLAS pixel sensor design

Nowadays, there are many proposed novel pixel sensor technology, but to have a proven technology that match all the requirement for the HL-LHC upgrade, we need to perform many tests to validate the performance of the new sensor design. The R&D activities contribute to the design optimization of future ATLAS pixel sensors, through testing of prototypes of novel sensor technology, that is playing a key role in the fundamental understanding and optimization of the performance of the developed prototypes. This can be achieved through detailed characterization,

modelling and simulation, including the effect of radiation exposure to the levels expected at future hadron colliders. But before the devices can be irradiated, first they need to be characterised to determine how well they function. In this section, a performance study of novel n^+-in-p, planar, thin, active edge detectors pixel detectors fabricated by Advacam foundry [90].

5.4.1 Active edge technology

Large-area hybrid silicon detectors are widely used in high energy experiments [91]. It is usual to dedicate a sizeable zone on the sensor border to host a safety region. this normally includes a set of bias and guard ring implants surrounding the effective sensitive region. The safety region turns out to act as an area with low or poor efficiency for signal collection. It is known that guard rings (GR) are structures that gradually ensure a smooth decrease voltage towards the cutting edge and protect the active area from electrical breakdowns. In the case of ATLAS-FEI3 sensor, an inactive region of 1100 μm is used to host 16 GR and Bias Grid (BG) of 600 μm width plus a safety margin of 500 μm, giving a total sensor surface sensitivity of only 74% [92][93]. Thus solutions have to be brought to minimize the charge loss at the edges to improve the total charge collection efficiency. Traditionally, the solution provided is to combine several layers of tracking information using large arrays of silicon sensors stacked and overlapped in turbo fan mechanical shape. Such approach impacts badly the tracking pattern recognition performance due to the complex mechanical layouts and additional overhead of material budget of the support structures and services.

An alternative novel approach in sensor design tends to reduce inactive or dead regions zones, by sensor side doping processes further beyond edge termination structures and cut region [94].The process involves a Deep Reactive Ion Etching (DRIE) to form a trench surrounding the active pixels and a side implantation with the same dopants as the one with which the backside layer is implanted. The backside implantation is extended to the sensor borders and acts as an active edge. The edgeless sensors used here are commercial products fabricated by VTT [95] which were transferred to its spin-off company "Advacam" in a CERN multi-project wafer run.

The sensors under study are n-in-p planar pixels with a size of 5×5 mm^2. The pixels are organized in 23 columns and 96 rows. The pixel cell dimension has been reduced to 25×200 μm^2. Three sensor thickness have been produced, namely 50, 100 and 150 μm. The backside implantation is extended to the side edge. Two edge options of 50 μm width and 100 μm width have been implemented in the design. A brief schematic of the process is presented in Figure 5.13.

As shown in Figure 5.14 , for the edge configurations, four alternative structures

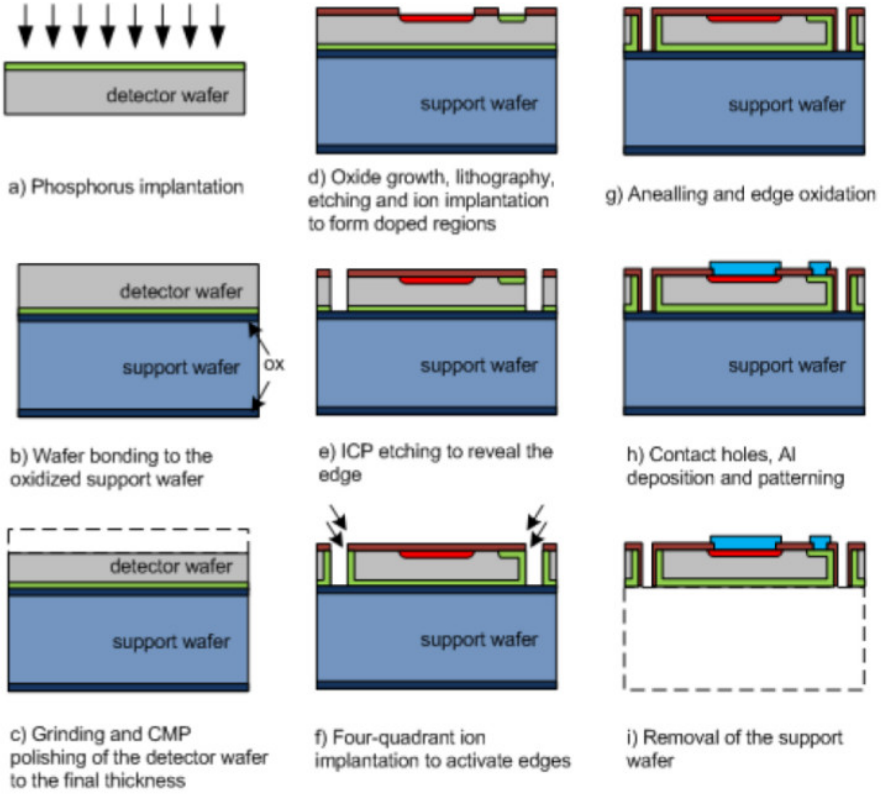

Figure 5.13: A brief representation of the active edge process flow applied on n-in-p detector fabrication [94].

Edge Desgin	No BR - No GR	BR - No GR	No BR - GR	BR - GR
Guard Ring Width	-	-	16 μm	16 μm
Bias Rail Width	-	37 μm	-	37 μm
Bias Rail - Guard Ring distance	-	-	-	5 μm
Last pixel distance	47 μm	16 μm	6 μm	16 μm
Distance to sensor edge	47 μm	25 μm	25 μm	25 μm
Total inactive region	47 μm	78 μm	57 μm	100 μm
% of inactive region	3.8 %	6.2 %	4.6 %	8 %

Table 5.2: Summary of the geometrical characteristics of the four active edge sensor designs.

were designed. The first device has no GR nor Bias Rail (BR), the second option has one floating GR only and no BR, the third option has only one BR and no GR and finally the last option has one GR and one BR. A summary of all design characteristics is presented in Table 5.2. Four samples of each design were included per wafer, resulting in a total of sixteen active edge sensors. Taking into account the three different thicknesses as well as the wafer multiplicity, 70 sensors were delivered.

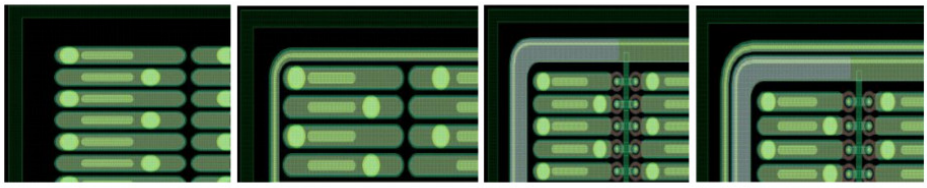

Figure 5.14: The four design variations of the active edge production. From left to right: no Guard Ring - no Bias Rail design, no Bias Rail - one Guard Ring design, no Guard Ring - one Bias Rail design and one Guard Ring - one Bias Rail design.

As mentioned before, the active edge sensors studied here are fabricated by Advacam. However, there are other active edge sensors fabricated by FBK and have been investigated in a study found in [96].

5.4.2 Sensor electrical characterization

In the normal work-flow for HEP silicon sensors, after design and production of sensors, electrical characterization is the final phase of sensor testing before interconnection with a readout electronics ASIC. Electrical characterization can reduce to two essential measurements:

- **Current measurement vs. Bias Voltage (IV):** the IV-measurement allows to define the level of leakage current and the break down voltage. The leakage current is the amount of charges per second generated by a fully depleted detector when no external excitation is provided. Since for silicon detectors the interest is to increase sensitivity of the signal created by charged

particles passing through, leakage current is always required to be the smallest possible. Since this corresponds to the number of electron-hole pairs intrinsically produced by the detector, if it is significant it will introduces noise to readout electronics. As a result, distinguishing signal induced by low energetic particles from the background is rendered more difficult. The breakdown voltage corresponds to the potential value for which the electrical field within the detector becomes so high that the structure operates in avalanche mode. In such a regime no energy linearity can be achieved and if the field increases, the sensor will adapt a resistive behaviour. In an irradiated sensor, defects are introduced and the performance decreases. To recover efficiency, higher operational voltage is applied. Therefore, it has to be assured that even after heavy irradiation with an increased biasing voltage, the breakdown value is sufficiently high to allow stable operation. Therefore, the breakdown voltage is also required to be as high as possible.

- **Capacitance measurement vs. Bias Voltage (CV):** the CV-measurement is performed to obtain the value depletion voltage. The depletion voltage is the reverse bias voltage, needed to be applied to the semiconductor silicon device to extend the mobile-free charge carrier zone to the full depth of the sensor. The capacitance C of the diode is inversely proportional to the depletion depth which itself is directly proportional to the square of the applied bias voltage V. In CV measurement, we measure $1/C^2$ vs V to determine the full depletion voltage. The capacitance of the diode decreases with increasing bias voltage until full depletion (V_{fd}) is reached and then remains constant. Graphically, V_{fd} has been determined for all diodes by plotting $1/C^2$ versus bias voltage and fitting lines to the two regions as shown in Figure 5.15. The intersection of the lines determines V_{fd}. The CV-measurements are carried out at three operational frequencies (30 kHz, 50 kHz, 100 kHz).

  For new sensor designs, we require the smallest depletion voltage, to have a large as possible operational range and also limit the dissipation power from high voltage power lines.

The electrical characterization of Advacam active edge sensors were performed in the LAL-clean-room with the use of a probe station shown in Figure 5.16. Sensor biasing is performed using a low impedance probe while current is measured through the copper conductive base chuck. Among the large variety of the Advacam structures received, three types of parameters have been investigated to take into account all the design variations: thickness (50 μm, 100 μm and 150 μm), edge design (BR-GR, GR-NoBR, BR-NoGR and NoGR-NoBR) and UBM variations (NiAu and Pt).

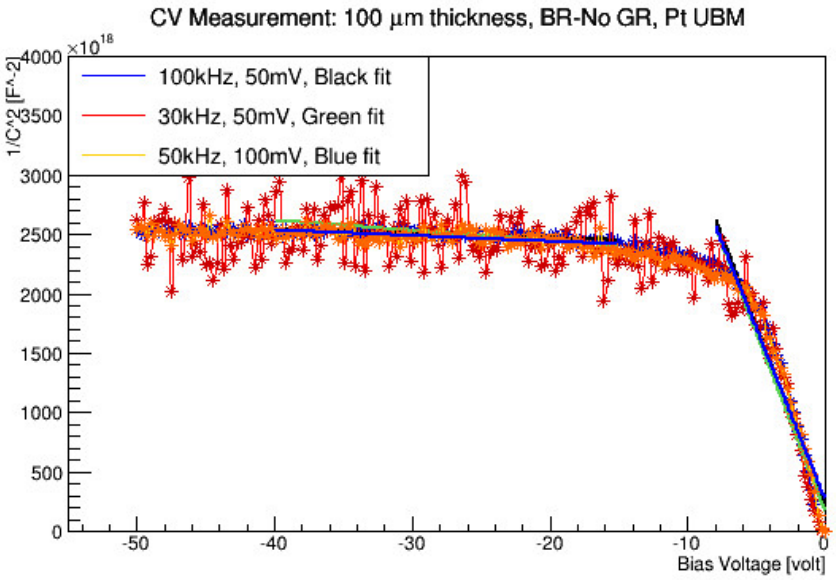

Figure 5.15: Measured $1/C^2$, where C is the capacitance, as a function of bias voltage for an Advacam active edge structure. CV-measurement is carried out at three operational frequencies (30 kHz, 50 kHz, 100 kHz). The three CV curves are fitted with linear function in two regions. The intersection of the lines determines $V_{fd} \approx 6$ V.

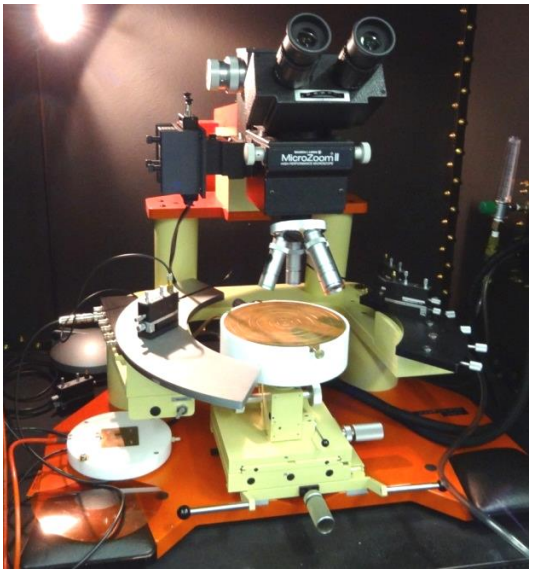

Figure 5.16: Probe station at LAL-clean-room used for the IV- and CV- measurements. The probe is attached to an optical microscope and a conductive copper chuck. The needle probe and high precision mechanical base is also visible at the left side of the picture.

5.4.3 Results

The results of testing the 70 Advacam active edge structures are shown in Figure 5.17 - Figure 5.21. The average breakdown voltage with the corresponding error is summarized in Table 5.3 and Table 5.4 for Pt UBM and NiAu UBM respectively. All structures show a low leakage current level in order of 10^{-8} A and a very low depletion voltage, less than 10 V.

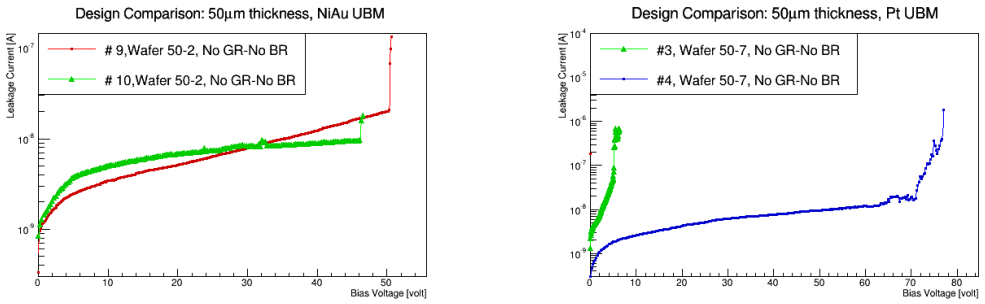

(a) (b)

Figure 5.17: IV-measurement for different design variations for all the structures with 50 μm thickness and NiAu UBM (a), Pt UBM (b). Semi-logarithmic scale is used.

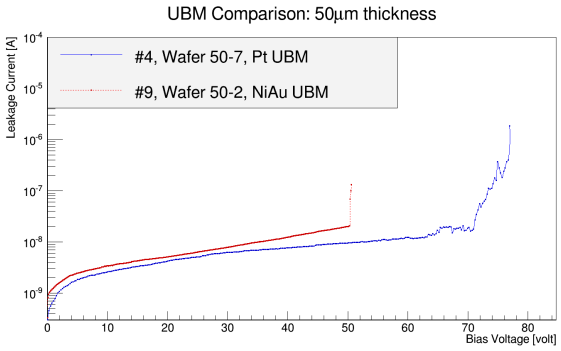

Figure 5.18: IV-measurement for the two UBM variations for all the structures with 50 μm thickness and NoGR-NoBR design. Semi-logarithmic scale is used.

Moreover, a chart summarizing the average breakdown voltage vs. thickness is shown in Figure 5.22. This figure shows that:

- The NiAu UBM has higher breakdown voltage than Pt UBM for all thicknesses except for the 50 μm, where it is nearly the same.

-The 100 μm sensors have the highest breakdown within all the thicknesses, about 130 V on average.

Similar comparison of average breakdown voltage vs. design for both UBM option

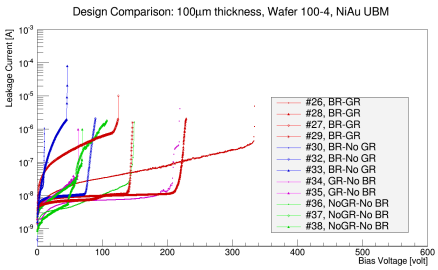

(a)

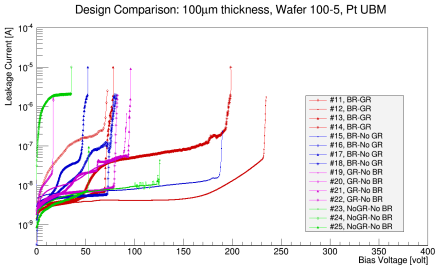

(b)

Figure 5.19: IV-measurement for different design variations for all structures with 100 μm thickness and NiAu UBM (a), Pt UBM (b). Semi-logarithmic scale is used.

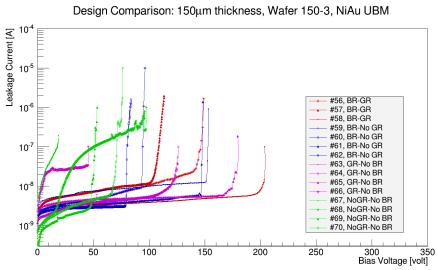

(a)

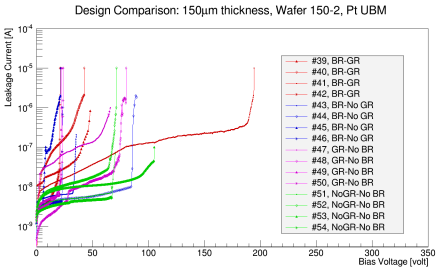

(b)

Figure 5.20: IV-measurement for different design variations for all structures with 150 μm thickness and NiAu UBM (a), Pt UBM (b). Semi-logarithmic scale is used.

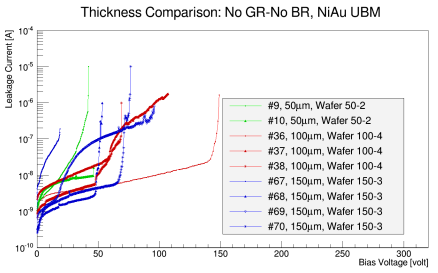

(a)

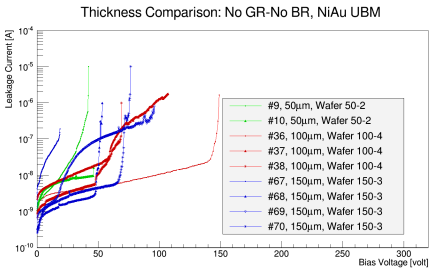

(b)

Figure 5.21: IV-measurement for different thickness variations for all structures with NoGR-NoBR design and NiAu UBM (a), Pt UBM (b). Semi-logarithmic scale is used.

	NoBR-NoGR	BR-NoGR	NoBR-GR	BR-GR
50 μm	47±30 V	-	-	-
100 μm	40±20 V	70±30 V	48±18 V	100±40 V
150 μm	52±9 V	28±16 V	32±15 V	50±40 V

Table 5.3: Average breakdown voltage for different design and thickness variations for all structures with Pt UBM.

	NoBR-NoGR	BR-NoGR	NoBR-GR	BR-GR
50 μm	44±2 V	-	-	-
100 μm	50±20 V	20±2 V	50±6 V	140±50 V
150 μm	41±17 V	80±18 V	70±30 V	100±20 V

Table 5.4: Average breakdown voltage for different designs and thickness variations for all structures with NiAu UBM.

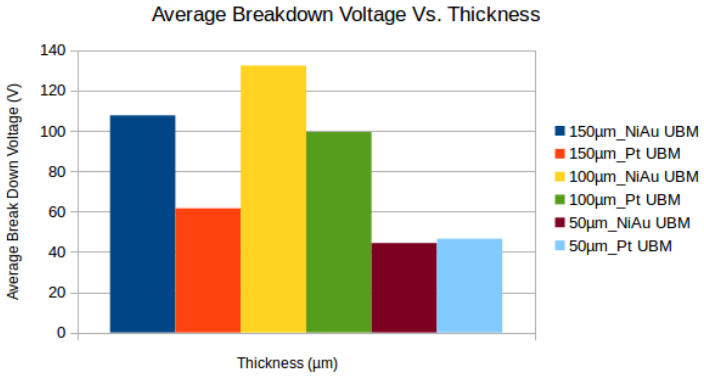

Figure 5.22: Average breakdown voltage for different wafer thickness, comparing NiAu UBM and Pt UBM.

is shown in Figure 5.23. From this figure, one can notice that:

- The BR-GR structure with NiAu UBM has the higher breakdown voltage with respect to all the other designs, around 185 V on average.

- The No GR-No BR structure shows a tiny difference between NiAu UBM and Pt UBM.

- The designs with at least one GR are more stable than the NoGR designs

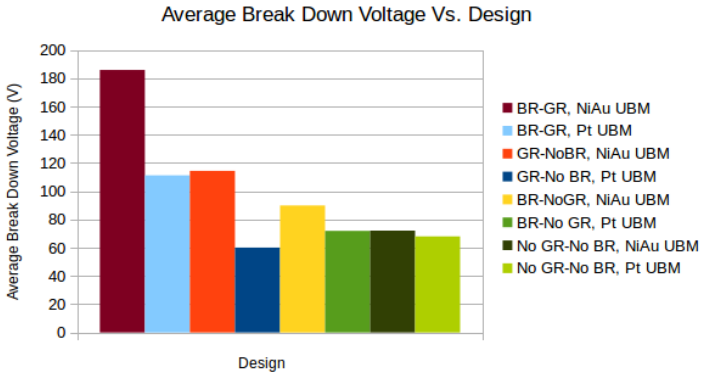

Figure 5.23: Average breakdown voltage for different design, comparing NiAu UBM and Pt UBM.

The average depletion voltage vs. thickness is presented in Figure 5.24. It is found that:

- The Pt UBM shows higher depletion voltage.

- The 100 μm and 150 μm thicknesses sensors have a depletion voltage around 10 V.

- The 50 μm thickness with NiAu UBM has a very low depletion of few Volts.

5.4.4 Conclusions

The performance study of the active edge sensors shows that:

- Considering the 70 Advacam sensors that have been received, the production yield is 90%. Yield here is defined as the ratio of the working sensors to the total number of sensors received.

- Concerning the thickness comparison:

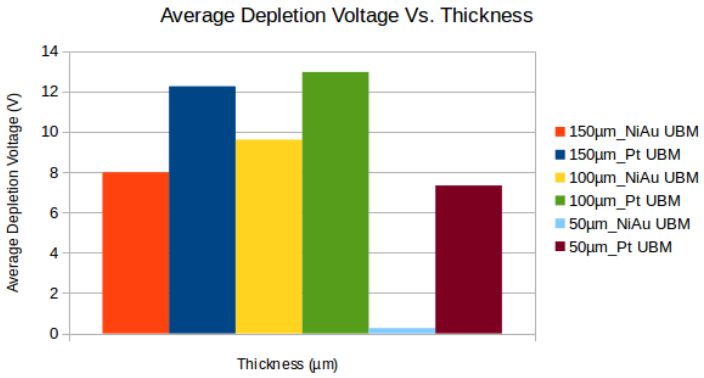

Figure 5.24: Average depletion voltage for different wafer thickness, comparing NiAu UBM and Pt UBM.

- The 50 μm samples with No GR-No BR, which is the only edge design received for this thickness category, is the only structure actually seems to work.

- The 100 μm samples have the higher depletion voltage.

- The 150 μm samples have a lower depletion voltage than the 100 μm.

► Concerning the design:

- For all thicknesses, the designs with at least one GR are more stable than the No GR designs.

- The No GR-No BR designs works in all thicknesses.

► Concerning the UBM:

- The NiAu UBM design presents higher breakdown voltages than Pt UBM for all thicknesses, except in the case of the 50 μm thickness, where there is a small difference in average. The different behaviour of the different UBM variations, investigated in this study, has been observed in similar studies within the collaboration. This need to be further studied in order to draw a conclusion.

Chapter 6

Innovative methods for silicon pixel detector doping profile analysis

Contents

6.1 Secondary Ion Mass Spectroscopy Method (SIMS) 102
6.1.1 SIMS Instrumentation 103
6.1.2 SIMS data quantification 105
6.2 3D Doping Profile Measurement Using SIMS Imaging Method 109
6.3 TCAD Simulation models 110
6.3.1 Simulation tools to accelerate innovation 110
6.3.2 Frameworks and available algorithms 111
6.3.3 Meshing strategy 113
6.4 Experimental validation of TCAD simulation via SIMS method 114
6.4.1 Comparison of doping profile measurements with TCAD simulations 114
6.5 Radiation damage in active edge pixel sensors 118
6.6 TLM method to study irradiation effect on active doping profile in pixel detectors 121
6.6.1 Motivation 121
6.6.2 Overview of the active dopant in semiconductor 122
6.6.3 Transmission Line Matrix (TLM) Method 124
6.6.4 TLM samples geometry and layout 126
6.6.5 TLM measurement 128
6.6.6 Experimental procedure 132
6.6.7 Results 133
6.6.8 Cross-check of TLM results 137
6.6.9 Conclusion 138

In this chapter, I introduce two novel technique for measuring silicon pixel detector doping profile. The first method, the Secondary Ion Mass Spectroscopy (SIMS) imaging method, is based on mass spectrometric technique that can provide element analysis of the scanned surface. This work aims to provide a high lateral resolution technique to study the doping profile at the pixel level inside the complex structure of the Advacam active edge detectors. Furthermore, in order to study the variation of active dopants before and after irradiation, the Transmission Line Matrix (TLM) method was developed and used for the first time in the HEP domain. In addition, the measured doping profile from previous methods was employed as an input to TCAD simulation. Simulation was tuned with the correct process parameters using the adequate physical model to study the radiation damage in Advacam active edge pixel structure.

6.1 Secondary Ion Mass Spectroscopy Method (SIMS)

The Secondary Ion Mass Spectroscopy (SIMS) method described in the following section is a destructive method and a very powerful tool, allowing to extract doping profiles of the different implant layers in silicon pixel detectors. This information is of vital importance in detector design as knowledge of the dopant profile distribution within the detector is required to complete the electrical characterization and to explain the operational behaviour. Moreover, depletion voltage, leakage current and breakdown boundaries are directly dependent on the concentration and shape of the dopant distribution within the substrate.

Beyond the pure scope of the testing, the doping profile measurements are also used to improve the simulations and therefore the design optimization. The final goal is to have a complete knowledge of the detector quality from fabrication to electrical characteristics and signal response through simulations. Before even a single wafer is produced, one needs to establish a library and calibrate the simulator framework prior to sensor design step. The acknowledged dependence of functional characteristics of a silicon detector from the doping profile distribution as well as the close relationship of the later with charge generation process, mandates detailed modelling of the implantation process. Using simulation tools, it is possible to approximate with great detail the fabrication processes. Nevertheless, deviation in both doping profile distributions and expected electrical characteristics from those generated by simulations, require further modelling and understanding.

6.1.1 SIMS Instrumentation

Secondary ion Mass Spectroscopy is an analytical technique allowing to characterize impurities in the surface and near surface ($\approx 10\mu m$) region with a nominal sensitivity of $10^{13} atoms/cm^3$. The method consists of sputtering an energetic primary ion beam (0.5-20 keV) on the sample surface and on subsequent analysis of produced ionized secondary particles by mass spectrometry. This allows multi-element detection with a depth resolution of 1 to 5 nm depending on abrasion seed and beam characteristics. Surface information about the probing region can also be obtained, since the affected area extends up to 150 $\times$150 μm^2 with respect to the sample surface. However, it is a destructive method, since removing material by sputtering leaves a crater in a sample, rendering impossible any further treatment on the affected region.

Determining the total dopant profile with SIMS is subjected to a number of constraints, primarily in relation with the stability, polarity and intrinsic characteristics of the primary ion beam. Boron, Phosphorus and Gallium are the most commonly used elements for doping in semiconductor industry. Probing each one of these analysts requires beam reconfiguration and is subject to different constraints for each case.

For the Phosphorus case, bombardment with the usual negative oxygen ion beam would only allow a concentration resolution of about $10^{18} atoms/cm^3$ [97]. At the same time, using an oxygen jet to deposit a secondary oxide on the sample surface in order to increase ionization yield would be problematic. The H_2O contamination induced from ambient humidity, would dramatically increase the SiH signal in the silicon substrate, degrading resolution beyond any usable limit. In contrast, one can take advantage of the high negative ionization yield exhibited under electropositive Cs^+ ion bombardment by replacing the oxygen ions in the primary beam with cesium. In such a setup, resolution limits of $10^{13} atoms/cm^3$ can be achieved for a thick silicon target.

In the case of non-conductive sample, no effective path is available for the incoming charge to be evacuated. As a result, the probed area will become positively charged, suppressing negative ion production yield. Furthermore, beam instabilities will be induced and secondary ion resolution will be degraded by the increase of the evacuation field. To neutralize the charging effect and stabilize the surface potential at the necessary (close to the ground) value, introduction of an additional negative charge, in the form of low energy electron beam, is necessary at the sample vicinity [98]. A correct adjustment of the charge compensation mechanism is required at the early steps of the measurement serving as guideline for subsequent corrections. In the case of negative secondary ions, partial charge compensation is achieved by the secondary beam itself, rendering the effect less significant.

While an electro-positive element was used for Phosphorus analysis, in the Boron case, electronegative Oxygen ions are exploited to produce a B^+ secondary beam. Since in any case the primary ion bean is positively charged while the electronegative nature of oxygen will create positively charged Boron secondary ions, the charge compensation mechanism described in the previous paragraph becomes significantly important in Boron analysis. No self-stabilization mechanism by using secondary ions exists in this case and if no action is taken, produced ions are scattered and their energy altered. In this case, the introduction of the negative electron beam is important to re-stabilize the potential on the sample surface.

To achieve an initial reference potential needed to correctly calibrate the charge compensation mechanism, a non-insulating metal layer is deposited on all samples where a silicon dioxide layer precedes the substrate. Using palladium or gold plasma enhanced chemical vapour deposition a reduced thickness (≈ 50 nm) surface metal film is deposited on top of the SiO_2 layer. To develop an accurate understanding of the compensation mechanism, in several samples with superficial oxide layers SIMS measurements were also conducted after chemically etching any process induced regions. Results were subsequently compared with the ones obtained when no etching is performed and necessary adjustments were made. Individual series of measurements were performed to determine the interface of each layer (palladium/gold, oxide and silicon) and the relevant ion velocities in order to have an exact depth extrapolation.

An additional limitation of the technique is the maximum probing depth achievable under normal conditions. Although a uniform beam exposure to the target surface is performed, beam non-uniformities as well as non-crystalline surface structures can result in exposure to ion beam under various angles. Furthermore, as the measurement progresses and the induced crater deepens, ion reflection on the sidewalls degrade beam stability and introduce collisions at a wide variety of angles and energies. The effect is more prominent in polycrystalline materials since no uniform refraction plane exists. Combination of non-perpendicular surface collisions with crater side-wall reflections roughen the surface at the bottom of the crater preventing a continuously uniform sputtering. While at the initial stages the effect is not significant, the more the measurement progresses and the target surface becomes non-uniformed, the phenomenon is self-amplified due to the variation of primary ion incidence angle. At extreme cases the end of the crater becomes "dark"-non reflective for secondary ions - while, the resolution and the precision degrades with respect to depth. To treat this effect, all depth measurements were limited to a maximum depth of 4 μm, well below the expected 10 μm limit value of maximum penetration depth [99].

6.1.2 SIMS data quantification

For elemental analysis, such as SIMS, the first question is "what elements are present in the sample?" and the second is "How much?" and to answer these two questions, we do concentration quantification and depth quantification, which will be explained in the following section.

Concentration Quantification During SIMS measurements, secondary ion intensity of elements of interest is recorded using an electron multiplier, in the form of an electron induced current. In order for these values to be converted to actual element concentrations, a multiplication factor is needed, known as the Relative Sensitivity Factor (RSF). Since ionization yield depends on probed element, matrix composition, ion beam nature and measurement conditions, special reference samples of nominal concentrations have to be used in each series of measurements to calibrate the results and calculate the RSF. Those samples need to be of the same matrix (i.e. silicon substrate in this study) and to contain the same element of interest ((i.e. Boron or Phosphorus implant in this study) as the ones been analysed. Consequently, to quantify for example phosphorous concentration in silicon, an accurately phosphorous doped silicon calibration target is measured at the same conditions as the probed sample. Then corresponding multiplication factor is extracted.

To avoid depth imprecision in the determination of the reference profile, measured ion intensity (S_M for the matrix and S_i for the element of interest) is integrated along the total elapsed measuring time. The average intensity is calculated for the matrix (I_M) and the element of interest I_i by dividing the signal integral with the total duration of the measurement (see equations 6.1 and 6.2).The latter, is defined as being the time interval between the first and last recorded data point of the corresponding element, thus accounting for any time differences due to magnetic field adjustments.

$$I_M = \frac{\int_0^{T_M} S_M dt}{T_M} \tag{6.1}$$

$$I_i = \frac{\int_0^{T_i} S_i dt}{T_i} \tag{6.2}$$

The average implant concentration (C_i) is computed by dividing the known implanted dose with the crater depth, created by the ion beam during the measurement (equation 6.3).

$$C_i = \frac{\text{Implanted dose (C)}}{\text{Crater depth (D)}} \tag{6.3}$$

Element	RSF Value (atom/cm^3)
Boron	$5.50 \times 10^{22} \pm 1.24 \times 10^{21}$
Phosphorus	$8.80 \times 10^{22} \pm 1.84 \times 10^{21}$

Table 6.1: Typical RSF values calculated in silicon sensors measurements.

Finally, the RSF is calculated by multiplying the average implant concentration with the ratio of the average secondary ion signal for the matrix over the secondary ion signal related to the element of interest (equation 6.5). Expected units of the final RSF factor are atoms/cm^3 since multiplied by detector counts should yield dopant concentration in the matrix.

$$RSF = C_i \frac{I_M}{I_i} \tag{6.4}$$

SIMS is not self-quantitative technique, i.e. to quantify the existence of an element, we need to have a secondary standard reference sample with pre-existing calibration of the element of interest. Since the matrix has to be the same in both the measured and reference samples, there is a limited amount of possible applications. In that sense, although we can quantify phosphorous concentration in silicon, it is impossible to accurately determine its density in the preceding silicon oxide or other layers on top of the substrate. Although dopant concentrations are always presented quantified in the entire region, a conservative approach has to be taken concerning measurements in any silicon oxide, nitride or passivation layers where silicon substrate approximation is made.

In table 6.1, the typical phosphorous and Boron in silicon RSF values are represented with their respective evaluated uncertainties for measurements conducted at the GEMaC facility of the university of Versailles.

Since for the estimation of the RSF the secondary ion intensity of the matrix element is taken into account, during measurement quantification we need to use not only the ions intensities of the analysed element but also that of the matrix. The concentration of the analysed element can then be derived in the following manner:

$$C_i = RSF \frac{S_i}{S_M} \tag{6.5}$$

where S_i and S_M are the ion intensities for the element and the matrix and C_i the final extracted concentration in atoms/cm^3 . Corresponding uncertainty is mostly dominated by limits on the precision of the RSF value which are mainly affected by the accuracy on the determination of the implantation dose on the reference sample. As a result, precision on the final concentration calculation is of the same order as

initial dose uncertainty on the calibration target for regions where the secondary ion signal is significant. A 2 % precision can be obtained for Phosphorus and Boron implanted silicon, assuming a uniform matrix.

Depth Quantification

Secondary ion intensity of probed elements is recorded as a function of time, generating a time profile. By measuring the depth of the SIMS crater created by the primary ion beam on the sample, time intervals can be converted to depth values. Assuming stable experimental conditions, mainly concerning the primary ion beam, a fixed abrasion speed is considered throughout the entire measurement. Once the crater depth is evaluated, it can be divided by the total exposure time to determine average abrasion speed. Depth can then be computed for each data point by multiplying the corresponding time value with the average speed.

Crater depths are measured using a mechanical fixed tip profilometer, calibrated to a precision of $\pm$ 5.3 nm. An average of three values is used per crater depth while total final uncertainty includes both statistical and systematic contributions. Concerning the thickness of the initial plasma deposited metal layer for ion beam stabilization, a sharp trench is created through surface scraping with a controlled load platinum tip. On silicon targets, surface layers are composed of silicon dioxide and/or silicon nitride with increased density that cannot be affected by the applied weight. It can be therefore safely be assumed that only the metal layer is removed and the trench corresponds to the thickness of the layer.

Although this method gives accurate results for homogeneous substrates, in case of multiple superimposed layers, the fixed speed approximation cannot be applied. Material sputtering and penetration depth depend on layer density and can vary substantially between different compounds. Abrasion speeds need to be determined for each layer separately through dedicated measurements. By starting on the top layer, the first measurement will stop exactly at the interface between the first and second matrix material. The subsequent measurement will again start on the surface but will stop at the interface between the second and third material and so on until the final layer is reached. At the end, there will be as many craters as layers, each one traversing all preceding deposits. Each layers thickness can then be estimated by measuring the corresponding crater's depth and subtracting the depth of the previous layer's crater. Using the consecutive obtained datasets, beam time on each layer is extrapolated by looking for point of abrupt change on secondary ion intensities (several orders of magnitude). Finally, using determined layer thickness and spent time in each one, a single penetration speed per compound is determined.

During actual conditions, multiple elements are monitored. To determine the transition point between consecutive layers, the first derivative of the secondary ion intensity is plotted for all elements. Because of the different extraction potential in each layer, Dirac-like peaks are expected to form in the derivative at the interface

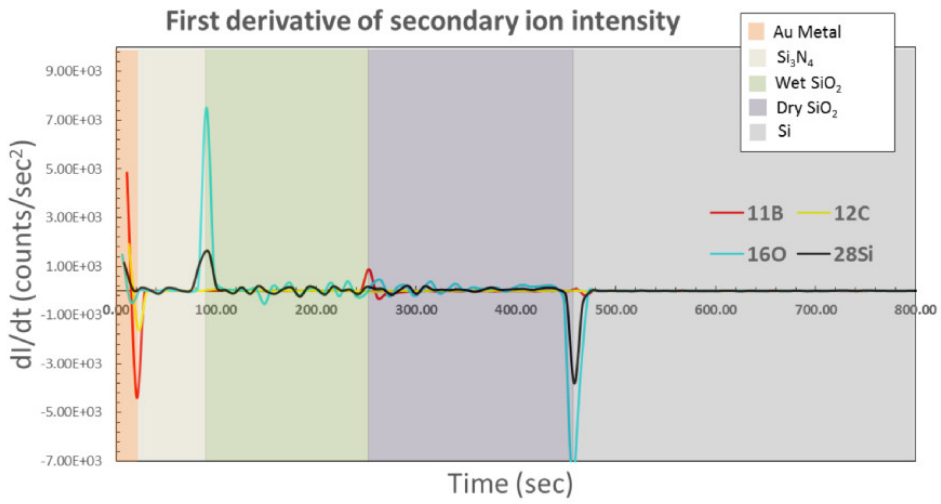

Figure 6.1: First order derivative of secondary ion intensity for all monitored elements on a typical silicon sensor sample. Abrupt changes are observed in layer interface regions which are marked with different shading colors. Oxygen and silicon curves are scaled to a factor of 10^{-2} and 10^{-5} respectively for representation purposes.

edge. For a perfectly separated interface layer and in measuring intervals infinitesimally close to zero, a perfect Dirac form is expected (Figure 6.1). Nevertheless, because of the time resolution limits as well as atomic layer mixing at the transition region, a narrow width Gaussian approximation can be applied. By applying a statistical fit at the transition point, the time position is defined as the position of the Gaussian distribution maximum for every monitored element. Using all available maxima, an average transition point is estimated while, standard deviation of the values convoluted with half of the time interval between two data points is considered as uncertainty.

After the definition of transition time between consecutive layers and the measurement of associated thicknesses, an average abrasion speed is computed for each region along with the corresponding uncertainty. In contrast with the RSF, which is globally fixed for a series of measurements concerning the same element, abrasion speeds are separately calculated for each profile, since they heavily depend on the primary ion beam configuration. Parameters like the primary ion current, beam acceleration potential and focusing configuration can impact the depth determination accuracy for each sample. A typical value of the the primary ion beam is about few nm/s. Although precise values are not of particular interest since they can vary significantly, their scale as well as the ratio of speeds between different layers is interesting.

Penetration speeds never exceed a few nm per second. Since silicon dioxide density is lower than that of the silicon itself, the expected abrasion speed is slightly in-

creased. For samples having undergone both wet and thermal SiO_2 growth, slightly different penetration speed values are determined. Because of the better quality of the dry oxidation process and the more regular structure of the produced layer, extraction potential is expected to be higher and beam penetration less efficient than in the wet SiO_2 region. Finally, silicon nitride layers most commonly used as passivation have similar densities and penetration efficiencies as wet silicon dioxide layers.

Final quantification is performed through multiplication of the penetration speed with each time point. When different layers are involved, the transition time is used to define layer change and the time in the new layer is calculated as the difference of the data point with respect to the average defined transition time. The time in which the layer was transversed is multiplied by the corresponding velocity and thicknesses of any previous layer as defined from crater measurements are added. In that way uncertainties can be kept under control, since preceding layer's speed and time estimations do not propagate to the following layer. In a four layer sample, a cumulated relative uncertainty of 4 % can be established for depth calculation, when combining uncertainties for all four regions.

6.2 3D Doping Profile Measurement Using SIMS Imaging Method

Over the decades, SIMS has been utilized to characterize a very wide range of materials. it has many applications in biology and chemistry to analyse organic materials, minerals and different microbiological tissues. In this thesis, and for the first time in High Energy Physics (HEP), we show that SIMS Imaging method can be very helpful in developing efficient design and fabrication techniques as well as building confidence level in simulation output that requires rigorous testing and evaluation of the final detector. SIMS Imaging is a novel method that can be used to extract 3D doping profiles of silicon pixel sensors for particle physics application.

SIMS Imaging is a special technique that gives us a unique combination of chemical and spatial information to identify the different components of the analysed surface. By scanning the samples surface and depth we can obtain three-dimensional dopant maps.

The surface sensitivity of SIMS limits analysis to two-dimensional images; however, it is possible to use the dynamic sputtering capabilities of the incoming ion beam to etch away part of the sample and reveal a lower layer (or slice) of the sample. Figure 6.2 shows a schematic of this where a sputter ion source is used to erode a layer of the sample followed by two-dimensional image analysis using the analysis ion beam. In this manner a series of separate layers can be etched and

then imaged. By reconstructing these serial 2D images it is possible to obtain a 3D representation of the sample, even the 3D reconstruction of the sample. This type of data reconstruction demonstrates the possibility for SIMS to be used to create a three dimensional maps of samples with sub-micron resolution.

Features of SIMS imaging method

- Can achieve higher lateral resolution up to 5 μm, which is mandatory to analysing small region of interest like the pixel region and the active edge region.

- High surface sensitivity at ppb level can be reached.

- Equivalent measuring time with standard 1D SIMS.

- Sample preparation is rather simple.

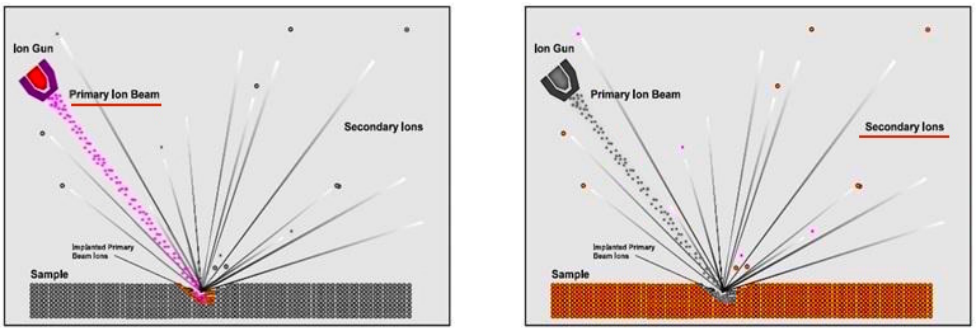

(a) (b)

Figure 6.2: Schematic of the SIMS sputter-then-image method to create separate two-dimensional images. A series of these 2D images can be reconstructed to create a 3D representation of the sample.

Lastly, the improved primary ion beams, advances in mass spectrometers, and increased sophistication of data processing methods suggest a very bright future for SIMS imaging to obtain 3D doping profile measurement for physics application.

6.3 TCAD Simulation models

6.3.1 Simulation tools to accelerate innovation

Technology Computer-Assisted Design (TCAD) refers to the use of computer simulations to develop and optimize semiconductor processing technologies and devices. Synopsys TCAD software solves fundamental, physical partial differential equations, such as diffusion and transport equations, to model the structural properties and

electrical behaviour of semiconductor devices. This deep physical approach gives TCAD simulation predictive accuracy for a broad range of technologies. Therefore, TCAD simulations are used to reduce the costly and time-consuming test wafer runs when developing and characterizing a new semiconductor device or technology.

Synopsys TCAD tools are used by all leading semiconductor companies throughout the technology development cycle. At the early stage of technology development, TCAD tools allow engineers to explore product design alternatives such as engineering the substrate to enhance channel mobility and meet performance goals even when experimental data is not readily available. During the process integration stage, Synopsys TCAD tools enable engineers to do simulation split runs such as Design of Experiment (DOE) to comprehensively characterize and optimize the process, which saves time and money by reducing experimental runs on real wafers. As the process is introduced into manufacturing, TCAD tools provide a mechanism for advanced process control during mass production, thereby improving parametric yield.

The TCAD simulation can be beneficial in many aspects:

- Explore new device structures to select viable process and device development pathways.

- Use TCAD to optimize process modules and integration by fully exploring the process parameter space while reducing the number of experimental wafers and development cycles.

- Apply TCAD to capture and analyse the impact of process variation on device performance, and to increase process capability, robustness and yield.

6.3.2 Frameworks and available algorithms

Many software are currently available in the form of TCAD packages, grouping several elements and algorithms from different fields. Two main derivations are available, SYNOPSYS Sentaurus [100] and SILVACO TCAD [101] frameworks, both grouping the main elements for Monte Carlo simulation, finite element solution algorithms, electrical field calculations, geometry generation and active domain simulations. The SYNOPSYS package, used in all simulation studies performed in this work, allows for a full 3D electrical field and process simulation through both Monte Carlo or analytical models, making it possible to probe efficiency and charge propagation in complex structures that cannot be represented in a two dimensional transverse plane. Two main kinds of simulations are possible:

Process simulation Most TCAD simulation software include a process simulation package that allows to simulate the fabrication process of silicon sensors. Since

production involves several steps, mainly dopant introduction on the substrate, an extensive knowledge of the technological process is needed. Lithographic masks and layer deposition techniques along with thermal diffusion and chemical reaction process are used. The main step to produce a realistic process simulation of a pn junction are as follow :

1. Initial oxidation for the development of a mask layer to be used as pattern for subsequent doping operations.

2. Photoresist layer on sensor front side.

3. Photolithography on sensor front side for implant segmentation.

4. Chemical etching of the oxide layer at specific regions.

5. Ion beam, Plasma or chemical implantation affecting only the areas not protected by the oxide layer.

5. Annealing of implanted ions for electrical activation where it is heated for sometime at very high temperature.

6. Aluminium layer on the implants on sensor front side to produce the electrical contacts to the implants

7. Passivation layer on sensor surface in between the implants to provide a good protection of the surface

The parameters of the process affecting the implant profile need to be known to create accurate representation of the device we wish to simulate. The process details we use in our simulation have been obtained through discussion with designers and manufacturer of silicon devices. Some parameters are however hard to determine from accessible data and are not disclosed by the manufacturer. These values can however be obtained through experimental methods as will be shown in the rest of this chapter.

Device simulation

Alternatively called Functional/electrical simulation, which is used to obtain electrical parameters of a geometry we built through process simulation. For a device simulation, the geometry to be simulated must be carefully chosen to avoid increasing the computational complexity of the problem to be solved. Boundary conditions must also be selected to represent the operation conditions of the device.

Charge propagation and diffusion is simulated inside the already defined sensor geometry though resolution of Maxwell's equations. They are additionally coupled to diffusion models and boundary conditions, defined by applied potential at fixed

points. To solve our set of differential equations we need to restrict ourselves to a solution in a bounded domain, the sensor. We must choose boundary conditions reflecting the properties of the system we want to simulate. There are three types of boundaries: the oxide-silicon interface, the electrode interface, and the periodicity boundary. The boundaries between silicon dioxide and silicon is a semiconductor/insulator boundary characterized by the presence of an accumulated charge layer at the interface. Metal-semiconductor surfaces are the boundaries between the silicon bulk and the metallic electrodes. This is usually an ohmic contact and the current is allowed to flow through them.

These two types of simulation can be interfaced and sequenced, feeding the result of a process simulation to the subsequent electrical model. Nevertheless, it is also possible to complete each phase independently of the other. In this approach, sensor geometry for a functional simulation can be hard-coded while, dopant distributions are provided as an external input. The most accurate result however can be obtained by interfacing the two stages such as final electrical characteristics are intransigently defined by the followed process steps. This is the adopted approach in this work and detailed process simulations are performed.

6.3.3 Meshing strategy

Uses our present knowledge of the partial differential equations describing charge carrier's motion and interactions with the crystal lattice in semiconductors, coupled to finite element method to simulate the electrical parameters of the device. Finite element method use a linearised version of the transport equation to describe the problem in terms of a linear system of equation that can be solved by linear algebra methods. To obtain a solution to the variables of the transport equations (n,p,V) in a arbitrary geometry, we must subdivide the surface or volume in rectangular, triangular, prismatic or pyramidal sub-elements small enough that the solution is locally polynomial in this domain. Within a finite element, the partial differential equations are approximated with a polynomial Φ. Once individual solutions are calculated for each cell, the solution to the equations can be expressed as:

$$V, p, n = \sum_{i}^{n} {\alpha_i}^{V,p,n} \Phi_i \tag{6.6}$$

Where i is the indice of an intersection of the sub-elements. The function Φ are usually chosen to be equal to 1 at element intersection i and 0 at all other surrounding intersection. And α is the multiplication factor. The sum of all sub-elements covering the simulation geometry is call the mesh, as seen in the example for a simple geometry in Figure 6.3.

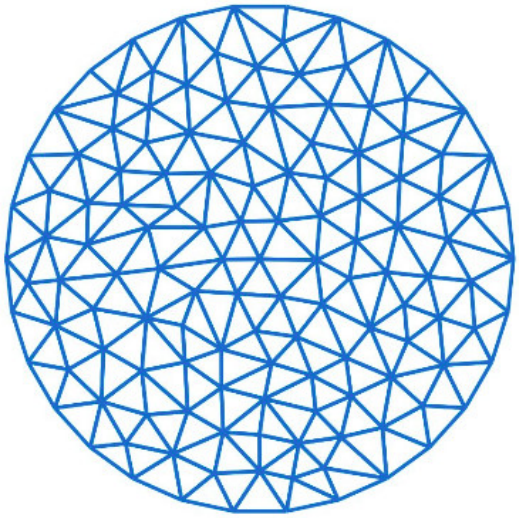

Figure 6.3: Meshing of a disc surface using triangular sub-elements.

6.4 Experimental validation of TCAD simulation via SIMS method

Accurate TCAD simulation can offer better understanding of the behaviour of the ATLAS existing and future pixel sensors. TCAD simulation models presented in the last chapter require the input of a large number of parameters (e.g. different layers, concentration (doping) profile for the different implanted regions, resistivity of the bulk, ..etc) to obtain quantitatively comparable results. Experimental measurement on test structure, prototypes and sensors can help to obtain the parameters needed to tune the simulation models and obtain quantitative results. In the following, the experimental work that was performed to calibrate the simulation models used in this work using Advacam active edge pixel sensors will be presented. All doping profile measurements introduced in this work were conducted in the laboratory of the GEMAC group (Group d'Etude de la Matiére Condensée) of the University Saint-Quentin-en-Yvelines at Versailles. The SIMS apparatus available at GEMAC facility is shown in Figure 6.4.

6.4.1 Comparison of doping profile measurements with TCAD simulations

TCAD simulation offers a good opportunity to better understand the electrical behaviour of the sensor. But to go further with the simulation (e.g. investigate the electrical behaviour of the detector), we need first to validate the simulation model

Figure 6.4: The CAMECA IMF 7F System where SIMS measurements were performed at GEMAC laboratory at the university Saint-Quentin-en-Yvelines at Versailles [102].

of the doping profile against experimental data. Moreover, TCAD simulation results such as leakage current and breakdown voltage are dependent on the doping profile of the structure. Knowing the doping profile of the different implant is therefore an important step to validate the simulation model and obtain accurate simulation.

As stated before, the simulation model used in this study is based on solving partial differential equations using finite element method [103]. Modelling of the semiconductor device consists of set of equations, derived from Maxwell law which links together electrostatics potential and carrier densities. Poisson's equation 6.7 relates variations in electric potential to carrier densities, whereas continuity equations 6.8 and 6.9 describe the way electron and hole densities evolve as a result of transport, generation and recombination processes. Carrier generation-recombination is based on Shockley-Read-Hall model [104].

$$-\nabla^2 V = \nabla.\vec{E} = \frac{\rho}{\varepsilon} \tag{6.7}$$

$$\frac{\partial p}{\partial t} = \nabla.D_h \nabla p + \nabla.(p\mu_h \vec{E}) + G_h - R_h \tag{6.8}$$

$$\frac{\partial n}{\partial t} = \nabla.D_e \nabla n + \nabla.(n\mu_e \vec{E}) + G_e - R_e \tag{6.9}$$

In the above equations, p and n are respectively the density of holes and electrons in $[\frac{1}{cm^3}]$, D in $[\frac{cm^2}{s}]$, their respective diffusion coefficient, μ the mobility of carriers in $[\frac{cm^2}{V/s}]$. G is the generation rate and R, the recombination rate, both in $[\frac{1}{cm^3/s}]$. The h and e subscript respectively design holes and electrons. ρ is the net charge density in $[\frac{C}{cm^3}]$, where C is the charge unit, Coulomb.

A validation of the simulator framework is needed before full exploitation of the

results. The methodology used in this work is to implement a set of basic n-in-p test structures, with a set of defined intrinsic process parameters in a specific wafer production. The implantation includes well known technological and process parameters tailored to our specifications. The ultimate motivation is to compare the measured doping profiles (using SIMS) with those obtained by TCAD simulation. The benefit of such method is meant not only to calibrate the modelling approach, for checking its reliability, but also allow us to extract a process library for future pixel design cases. This is a cost effective operation because for such approach no mask lithography is required.

Doping profile measurements using SIMS Imaging have been carried out for Advacam active edge detectors of 100 μm and 150 μm thickness. Both samples have Bias Rail (BR) and Guard Ring (GR) at the edge. Three different regions have been analysed: Centre Pixel region, Active Edge region and Backside. On the other hand, Synopsys TCAD simulation for different doping profiles regions have been performed. Several comparisons between measured doping profile versus TCAD simulation results are shown below.

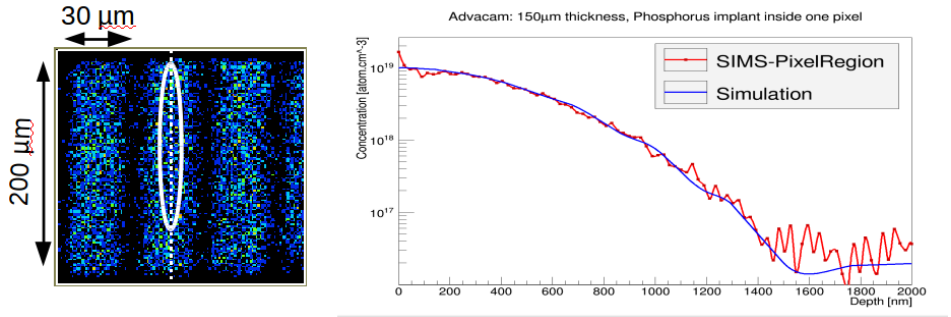

Figure 6.5: Doping profile map (left) and comparison of 1D doping profile from simulation (blue curve) and SIMS measurement (red curve) for Phosphorus implant in the pixel region (right).

Figure 6.5(left) shows a top view of the Phosphorus implant in a region that covers three pixels. In Figure 6.5(right) a 1D doping profile of Phosphorus implant obtained by simulation (blue curve) shows a good agreement with experimental result (red curve). Results shows peak concentration of $1{\times}10^{19}$ $atom/cm^3$ and a detection limit around $2{\times}10^{16}$ $atom/cm^3$. The implants extend to 1.5 μm in depth.

Figure 6.6(left) shows a top view of Phosphorus implant in the GR and BR region at the edge of the detector. A quite reasonable agreement between 1D doping profile of Phosphorus implant from simulation (blue curve) and experimental data (red curve) has been achieved, see Figure 6.6(right). Results shows a peak concentration of $\approx 1 \times 10^{19}$ $atom/cm^3$ and a detection limit around $2{\times}10^{16}$ $atom/cm^3$. The implant extends to nearly 1.5 μm inside the substrate.

Figure 6.7(left) shows a top view of Boron implant in the p-spray region in be-

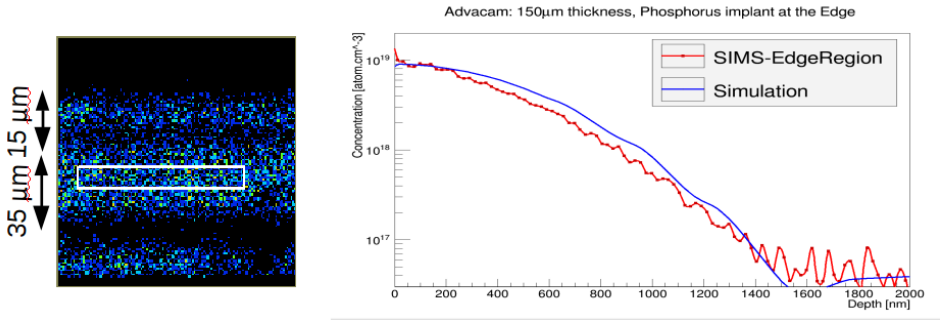

Figure 6.6: Doping profile map (left) and comparison of 1D doping profile from simulation (blue curve) and SIMS measurement (red curve) for Phosphorus implant in the Edge region (right).

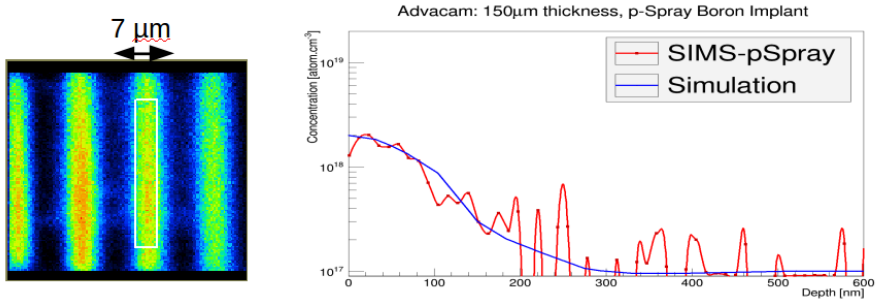

Figure 6.7: Doping profile map (left) and comparison of 1D doping profile from simulation (blue curve) and SIMS measurement (red curve) for Boron implant for p-spray (right).

tween pixel implants. The 1D Boron doping profile implant from simulation (blue curve) has been compared to experimental data (red curve). It shows a good agreement, see Figure 6.7(right). Peak concentration value around $2{\times}10^{18}$ $atom/cm^3$ and a detection limit of around $1{\times}10^{17}$ $atom/cm^3$ has been measured. The p-spray extends to 250 nm in depth inside the device.

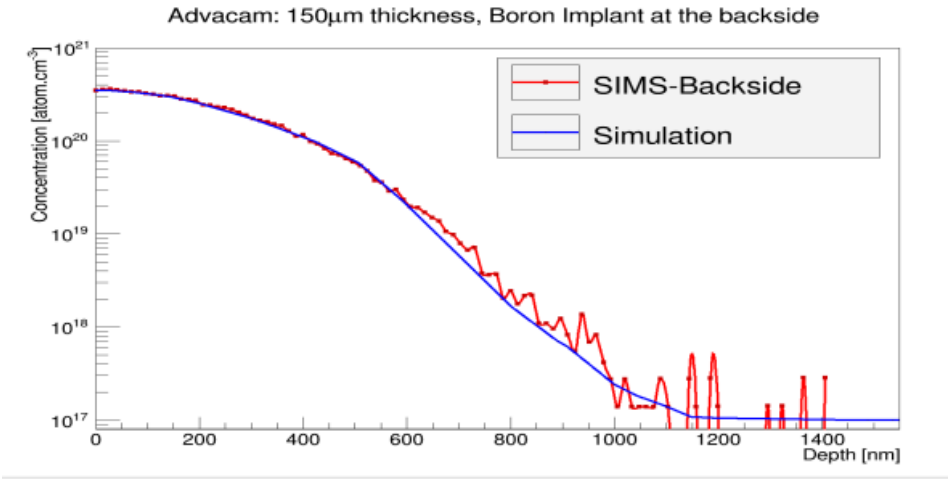

Figure 6.8: Doping profile map (left) and comparison of 1D doping profile from simulation (blue curve) and SIMS measurement (red curve) for Boron implant in active edge region (right).

Several trials have been performed to find the Boron doping profile in the active edge region. Unfortunately, no Boron was detected in the edge region. While sputtering the sample, the aluminium layer at the top of BR and GR was identified and a layer of silicon oxide was also found. Then silicon substrate has been reached without any significant trace of Boron. Consequently, to investigate the Boron doping distribution at the active edge region, SIMS Imaging measurement has been performed at the backside of the pixel sensor. A peak value of Boron concentration was found to be $3{\times}10^{20}$ $atom/cm^3$ with a detection limit around $1{\times}10^{17}$ $atom/cm^3$. Moreover, Boron region extends to about 1.2 μm inside the substrate. Figure 6.8 shows the comparison between modelled 1D doping profile of Boron implant (blue curve) and experimental results at the backside of the detector (red curve).

6.5 Radiation damage in active edge pixel sensors

After the validation step of our doping profile simulation using SIMS measurements, a 2D device simulation was performed to investigate the pixel sensor break-down. The layout structure of active edge detector has been simulated. The actual doping profiles have been exported to simulation. The overall simulated layout is shown in Figure 6.9 and Figure 6.10.

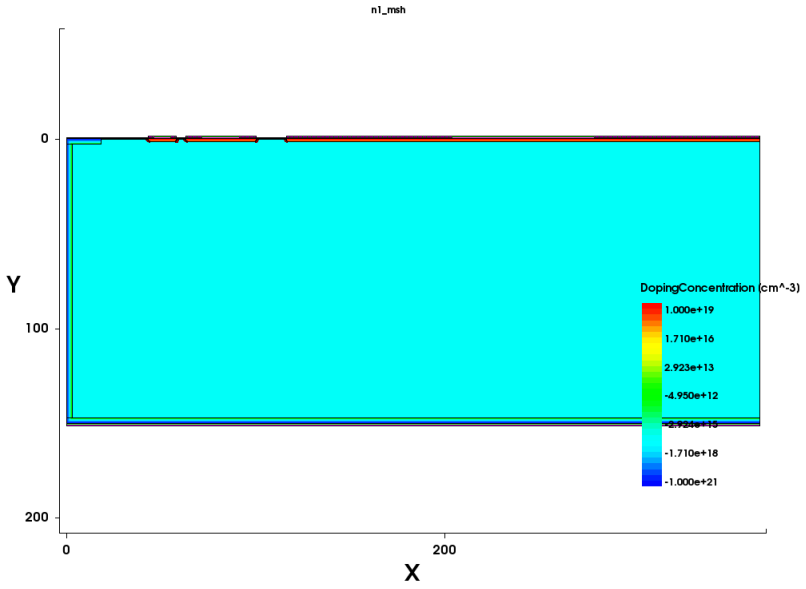

Figure 6.9: Overall view of the simulated n^+-in-p active edge pixel structure showing dopant concentration profile. Sensor geometrical size is $400\mu m$ in the x-direction and $150\mu m$ in the y-direction.

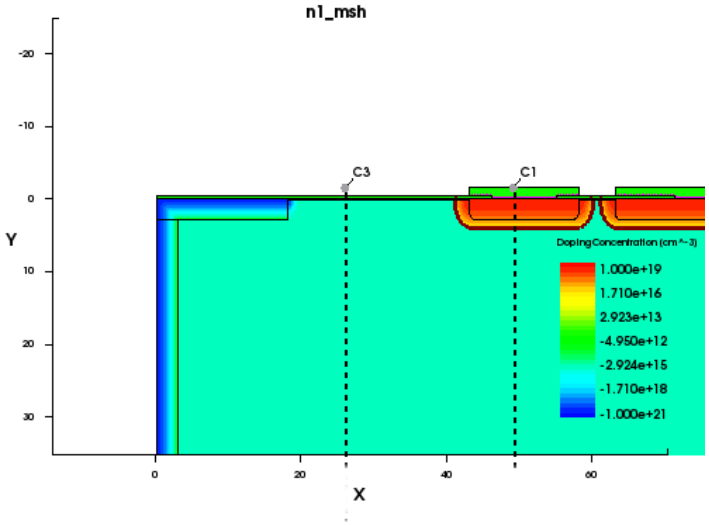

Figure 6.10: Doping profile map (left) and comparison of 1D doping profile from simulation (blue curve) and SIMS measurement (red curve) for Boron implant in active edge region (right).

Defect	E(eV)	$\sigma_e(cm^{-2})$	$\sigma_h(cm^{-2})$	η
Acceptor	$E_c - 0.42$	1.00×10^{-15}	1.00×10^{-14}	1.6
Acceptor	$E_c - 0.46$	7.00×10^{-15}	7.00×10^{-14}	0.9
Acceptor	$E_v - 0.36$	3.23×10^{-13}	3.23×10^{-14}	0.9

Table 6.2: The radiation damage model for P-type (up to 7×10^{15} n_{eq}/cm^2)

Defect	E(eV)	$\sigma_e(cm^{-2})$	$\sigma_h(cm^{-2})$	η
Acceptor	$E_c - 0.42$	1.00×10^{-15}	1.00×10^{-14}	1.6
Acceptor	$E_c - 0.46$	3.00×10^{-15}	3.00×10^{-14}	0.9
Acceptor	$E_v - 0.36$	3.23×10^{-13}	3.23×10^{-14}	0.9

Table 6.3: The radiation damage model for P-type (in the range $7\times10^{15} n/cm^2 - 2.2\times10^{16}$ n_{eq}/cm^2)

In this work, the radiation damage model used is based on three level traps, where irradiations generate two acceptor levels, near the mid band gap level and one donor level located far below, near the valence layer, as shown in Table ?? and Table ??, for p-type silicon detectors have been recently implemented in the TCAD simulation tool. These models are based on two acceptor and one donor levels, deeply located into the forbidden energy gap of the semiconductor. Based on these models, radiation damage was simulated in this study. The University of Perugia new radiation damage model [105][106], featuring both bulk and surface radiation damage effects has been proposed and validated through the comparison of simulations and experimental measurements. The model was approved as a predictive tool for investigating sensor behavior at different fluences up to 2×10^{16} n_{eq}/cm^2, temperatures, and bias voltages for the optimization of both 3D and planar silicon detectors for future HL-LHC HEP experiments.

Using the model above, IV-curves, namely leakage current as function of bias voltage) has been simulated for 150 μm sensor thickness for different fluences and shown in Figure 6.11. The breakdown voltage has increased from 150 V for unirradiated sensor to up 230 V for fluence of $2\times10^{16} neq/cm^2$. In general, one can notice that as the irradiation dose increases, both the leakage current and breakdown voltage increases too, as expected.

Simulated IV-curves have been validated for irradiated and non irradiated sensors. Data to simulation comparison for irradiated and non irradiated sensors are shown in Figure 6.12 and Figure 6.13, respectively. The breakdown voltage of non-irradiated sensor is about 150 V. The breakdown voltage estimated from simulation for the non irradiated sensor is compatible with the expectations from our clean-room characterization measured on a real sensor. A good agreement between data and simulation is observed also for the irradiated case, shown in Figure 6.12. The

breakdown voltage of irradiated sensor increases up to 225 V for 2x10^{16} n_{eq}/cm^2. The breakdown voltage increases about 50% for radiation dose of 2x10^{16} n_{eq}/cm^2 with respect ot the non irradiated sensor.

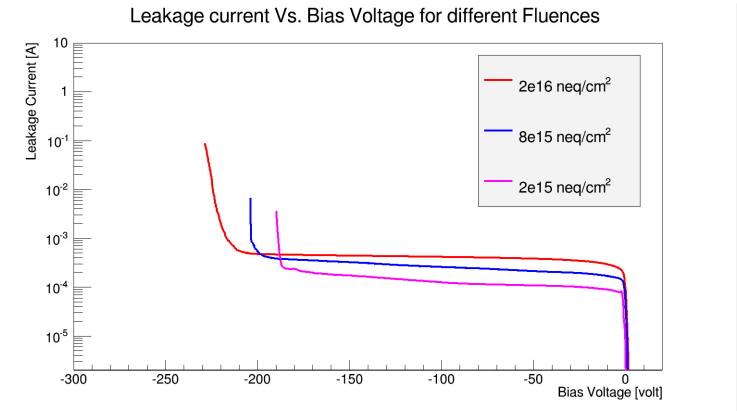

Figure 6.11: Simulated Leakage current as a function of Bias Voltage for different doses. As the irradiation dose increases the breakdown voltage increases up to 225 V for 2x10^{16} n_{eq}/cm^2.

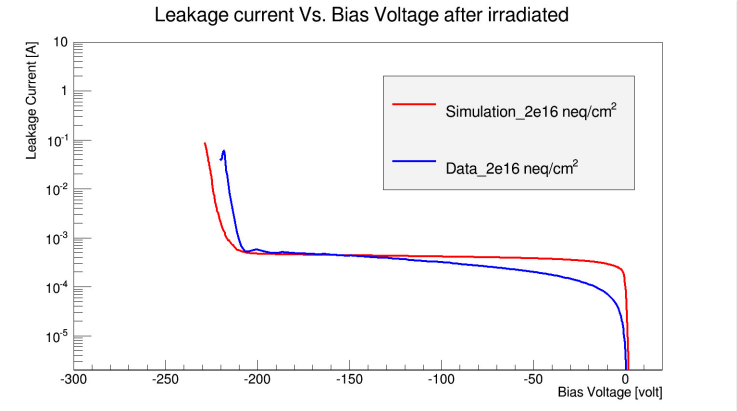

Figure 6.12: Leakage current as a function of Bias Voltage, with a comparison of simulation to data, after irradiation. The sensor is 150 μm thick and has a GR and BR at the edge. The breakdown of irradiated sensor increases up to 225 V for a fluence of 2x10^{16} n_{eq}/cm^2.

6.6 TLM method to study irradiation effect on active doping profile in pixel detectors

6.6.1 Motivation

In view of the LHC upgrade phases towards the HL-LHC, the ATLAS experiment plans to upgrade the current Inner Detector (ID) with an all-silicon tracker, the

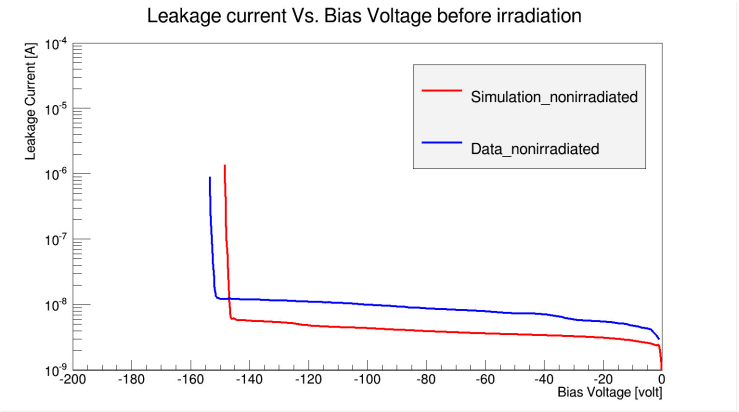

Figure 6.13: Leakage current as a function of Bias Voltage, with a comparison of simulation to data, before irradiation. The sensor is 150 μm thick and has a GR and BR at the edge. The breakdown of non-irradiated sensor is about 150 V.

ITk. As explained in details in Chapter 5 the ITk will be operated in an extremely intense radiation environment. In this context, the study of the radiation damages in silicon detectors after high radiation exposure is mandatory. The study of radiation damage in silicon detectors will give us some insight of changes in the active dopant concentration and how much electrically active carriers are lost after intense radiation exposure. Answering these questions will help us to understand if this loss of active carriers affect the performance of silicon detector used in high energy physics (HEP) experiments.

The work presented in this chapter addresses the variation on the active dopant profile before and after irradiation by developing a new method, the Transmission Line Matrix method (TLM). The TLM method enables us to see the change of electrically active dopant concentration after the irradiation and to compare the active doping profiles before and after irradiation. This study is mainly concerned to addressing the following questions: Does the active dopant concentration change after irradiation? How much electrically active carriers we lose?

6.6.2 Overview of the active dopant in semiconductor

Almost all of the basic semiconductor devices parameters are affected by the distribution of dopants in the device. Doping refers to the process of introducing impurity atoms into a semiconductor region in a controllable manner in order to define the electrical properties of this region. The doping with donors and acceptors allows to modify the electron and hole concentration in silicon in a very large range from 10^{13} cm^{-3} up to 10^{21} cm^{-3}. The carrier concentration can also be varied spatially quite accurately, a fact that is used to produce pn-junctions and built-in electric fields. All electronic and optical semiconductor devices incorporate dopants as a

crucial ingredient of their device structure.

Ion implantation is the primary technology to introduce doping atoms into a semiconductor wafer to form devices and integrated circuits [107][108]. This low-temperature process uses ionized dopants which are accelerated by electric fields to high energies and are shot into the wafer. The main reason in applying this technique is the precision with which the amount and position of the doping can be controlled. Dopant ions can be masked by any material which is thick enough to stop the implant as well as by existing device structures, which is referred to as self-aligned implants. After the implantation process the crystal structure of the semiconductor is damaged by the implanted particles and the dopants are electrically inactive, because in the majority of cases, they are not part of the crystal lattice. A subsequent thermal annealing process is required to activate the dopants and to eliminate the produced crystal damage.

As previously mentioned in Section 4.2, in processing of modern semiconductor devices, doping refers to the process of introducing impurity atoms into a semiconductor wafer by ion implantation. The purpose of semiconductor doping is to define the number and the type of free charges in a crystal region that can be moved by applying an external voltage. The electrical properties of a doped semiconductor can either be described by using the "bond" model or the "band" model. When a semiconductor is doped with impurities, the semiconductor becomes extrinsic and impurity energy levels are introduced. The bond model is used to show that a tetravalent silicon atom (group IV element) can be replaced either by a pentavalent Phosphorus atom (group V) or a trivalent Boron atom (group III). When Phosphorus is added to silicon, a Phosphorus atom with its five valence electrons forms covalent bonds with its four neighbouring silicon atoms. The fifth valence electron has a relatively small binding energy to its Phosphorus host atom and can become a conduction electron at moderate temperature. The Phosphorus atom is called a donor and a donor-doped material is referred to as an n-type semiconductor. Such a semiconductor has a defined surplus of electrons in the conduction band which are the majority carriers, while the holes in the valence band, being few in number, are the minority carriers. In a similar way, if a Boron atom with its three valence electrons replaces a silicon atom, an additional electron is "accepted" to form four covalent bonds around the Boron, and a hole carrier is thus created in the valence band. Boron is referred to as an acceptor impurity and doping with Boron forms a p-type semiconductor. The dopant impurities used in controlling the conductivity type of a semiconductor usually have very small ionization energies, and hence, these impurities are often referred to as shallow impurities.

Due to the electron-hole recombination process, not all dopant are electrically active! Therefore, the active dopant in semiconductor are the ones who contribute to the electric current flow when a potential difference is applied to the semiconductor. The major contribution to the electric current flow is negatively charged electrons

(e^-) in the n-type semiconductor and the positively charged holes (h^+) in the p-type. The majority charge carriers contribute to the electric current in n-type and p-type semiconductor are shown in Figure 6.14. As detailed in Section 4.4.2, after high irradiation exposure, and due the NIEL in silicon, the bulk defects increases the recombination rate. Hence, the density of free carriers as well as the density of the electrically active carriers are reduced.

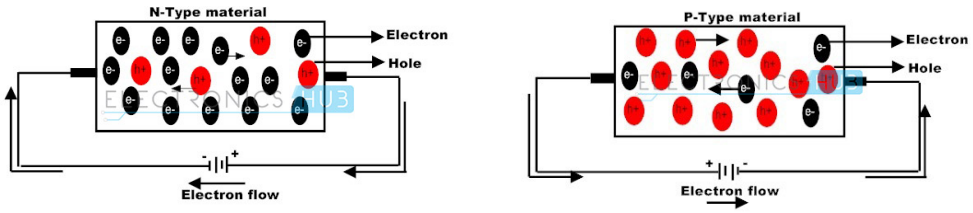

(a) (b)

Figure 6.14: The majority charge carriers contribute to the electric current in n-type and p-type semiconductor .

The loss of the active carriers in the bulk region due to radiation damages will lead to performance degradation of the silicon detector such as an increase in noise, a changing in material resistivity and a reduction in the amount of collected charge. All these effects result in a degradation in the device performance. Consequently, the study of the variation on the active dopant profile before and after irradiation is of great concern.

6.6.3 Transmission Line Matrix (TLM) Method

Stemmed from our interest in studying the active dopant profile for improving the performance of the silicon detector for HEP application, I have been working on developing a new innovative method to measure the active dopant concentration. This method is the Transmission Line Matrix Method, shortly, TLM [109]. In this section, I present the TLM method as a promising and ingenious technique, used for the first time in HEP domain, to the study of the irradiation effects on active doping profile.

TLM is a technique widely and often used in semiconductor physics and engineering to determine the contact resistance between a metal and a semiconductor[110]. TLM was originally proposed by Shockley [111]. TLM consists of resistance measurements performed on samples with a set of rectangular contacts and give access to contact and layer resistance and from this to the layer resistivity and the electrically active carrier concentration in silicon. In this study, the TLM method extrapolates from two point resistance measurement and is employed to measure the resistance of doped silicon layers at depths increasing incrementally in the implanted area.

The TLM test structure is based on the geometry shown in Figure 6.15. The TLM test structure consists of several electrodes that exhibit of the same geometry of length (L) and width (W)[112]. These aluminium contacts are separated by unequal spacing distance (d). This array of contacts with various spacing is formed on the top of a single rectangular doped region.

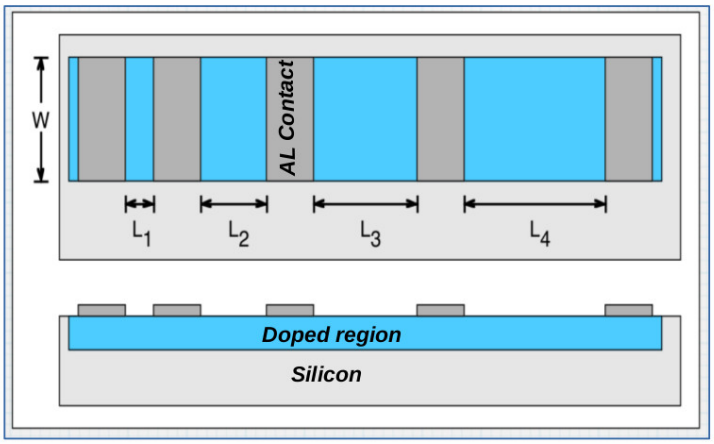

Figure 6.15: A transmission line method (TLM) test structure. The Blue regions is the doped silicon region. Dark gray region is the array of aluminium contacts which formed with various spacings over the doped region.

TLM basics

Let's consider a simple homogeneous rectangular semiconductor with resistivity ρ and thickness t with two contacts as shown in Figure 6.16. The total resistance $R_T = V/I$, measured by passing a current I through the sample and measuring the voltage across the two contacts. Assuming identical contact resistance for the two contacts in this test structure allows the total resistance to be written as:

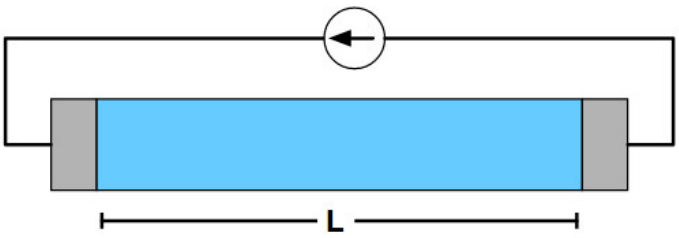

Figure 6.16: Top view of a two-terminal contact semiconductor structure.

$$R_T = R_{semi} + 2R_C + 2R_m \tag{6.10}$$

where the R_{semi} the usual semiconductor resistance, R_C is associated with the metal/semiconductor interface and R_m is the resistance due to the contact metal. The resistance of a single contact would be $R_m + R_C$. However, in most situations, the resistivity of the metal in the contact is so low that $R_C >> R_m$, and so R_m can be ignored.

The resistance R_{semi} of semiconductor is directly proportional to the semiconductor resistivity ρ by:

$$R_{semi} = \rho\frac{L}{A} = \rho\frac{L}{Wt} \tag{6.11}$$

where L is length in (cm) of the resistor the and A is the cross-section area in (cm^2). For a rectangular resistor, $A = W.t$ where W is the width and t is the thickness.

The dopant concentration N_D in the substrate is related to the resistivity ρ of doped silicon by:

$$N_D = \frac{1}{e\mu_e\rho} \tag{6.12}$$

where e is the elementary charge and μ is the charge carrier mobility.

For semiconductors doped through diffusion or surface peaked ion implantation with junction depth x_j, we define the sheet resistance R_s using the average resistivity $\overline{\rho} = 1/\overline{\sigma}$ of the material, where σ is the material conductivity:

$$R_s = \overline{\rho}/x_j = \frac{1}{\int_0 x_j\sigma(x)dx} \tag{6.13}$$

which in materials with majority-carrier properties can be approximated by (neglecting intrinsic charge carriers):

$$R_s = \frac{1}{\int_0 x_j\mu eN(x)dx} \tag{6.14}$$

Therefore, by using Ohm's law and measuring the resistance between the contacts, it is possible to find the resistivity of a sample's layer which leads to the active carriers dopant concentration in that layer.

6.6.4 TLM samples geometry and layout

In order to carry out the TLM measurement, samples with special geometry and layout have been designed. In the following, I give the description of the TLM test structure used for this study.

In this thesis, a total of four wafers with special geometry and with both Phosphorus and Boron implantation have been produced at CNM[1] manufacturer in the framework of the RD50 collaboration. A 525 μm thickness n-type (p-type) silicon wafers with electrical resistivity 1-12 $\Omega.cm$ (0.1-1.4 $\Omega.cm$) were used. Wafers fabrication process is done through following steps:

- Wafer Implantation to create the n-type and p-type doped region: doping is done using the ion implantation technique. A beam of dopant ion with energy 60 keV for the Boron implantation and 130 keV for Phosphorus implantation is used. The implantation dose used is either 1×10^{14} $atom/cm^2$ or 1×10^{15} $atom/cm^2$. Implantation was done through a 100 nm SiO_2 layer. Activation of the dopant is accomplished by thermal anneal of implant at 1000 °C for 180 min in N_2.

- Photoresist coating and opening using the mask: a photoresist layer is developed at the top of the doped silicon. The unwanted resist is washed away by the wet etching technique and opening are made through the photoresist using the mask show in Figure 6.17 to cross-link the polymer in the desired areas.

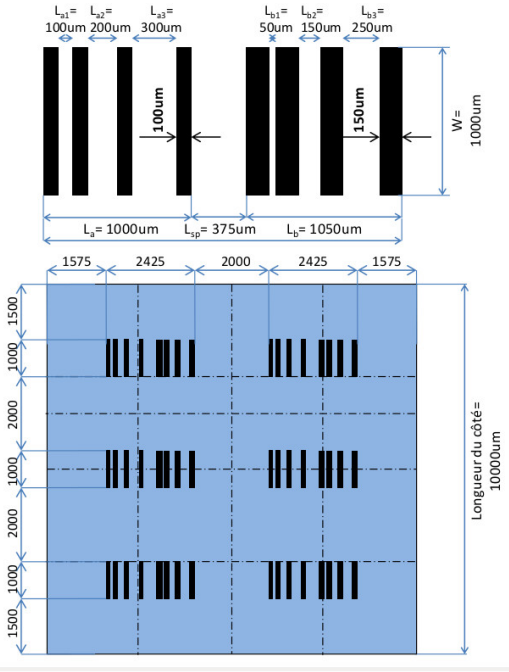

Figure 6.17: Mask used in the mask-based lithography with direct laser writing used produce the TLM test structure used in this study.

- Metallization to make the contacts: immediately after cleaning and wet etch-

[1]Centre Nacional de Microelectronic

Wafer #	Substrate type	Resistivity [$\Omega.cm$]	Implantation Ion	Implantation Energy [keV]	Implantation Dose [$atom/cm^2$]	Expected Peak Concentration
Wafer 1	p-type	0.1-1.4	Phosphorus	130	1×10^{14}	1.5×10^{18} $atom/cm^3$
Wafer 2	p-type	0.1-1.4	Phosphorus	130	1×10^{15}	1.5×10^{19} $atom/cm^3$
Wafer 3	n-type	1-12	Boron	60	1×10^{14}	1.3×10^{18} $atom/cm^3$
Wafer 4	n-type	1-12	Boron	60	1×10^{15}	1.3×10^{19} $atom/cm^3$

Table 6.4: Main characterization of the different wafers fabricated for this study.

ing BHF[2] 30-60s, a 300 nm layer of aluminium is deposited. A lift off of the undesired regions where the alumnium is on the top of the photoresist is done.

Figure 6.19 shows a brief process flow illustrating the fabrication of TLM test structure. A summary of the different wafer characterization is given in Table 6.4.

As shown in Figure 6.17, each TLM sample is designed as a 2×3 matrix of series of contacts, that have 6 sets of adjacent contacts with distance between the contacts increasing as you move down the columns. For for the two series of contacts in the first row, the separation distance between the two adjacent contact is increasing by 25 μm starting from 25 μm (between the first two contacts) and reach up to 275 μm (for the last two contacts). For the second and the third row, the spacing distance is incrementally increased by 30 μm and 40 μm respectively. An example of layout design of one of the contact series is shown in Figure 6.18.

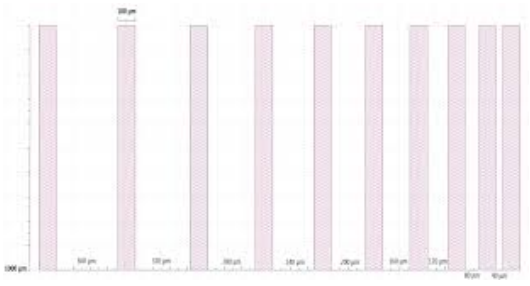

Figure 6.18: An example of the layout design of one of the contact series in the TLM test structure used in this study, taken from the GDS design file.

6.6.5 TLM measurement

To measure the active doping profile for a TLM test structure like that in Figure 6.15, we need to generalize the above result in equation 6.14 and measuring the resistance between adjacent contacts and repeat the measurement at different depths. By etching a small doped Si layer ($\approx$ 200 nm/measurement) then measuring the resistance at different depth, the resistivity depth profile can be found. Consequently

[2]BHF is the buffered hydrofluoric acid that is known to be used in the wet etching techniques

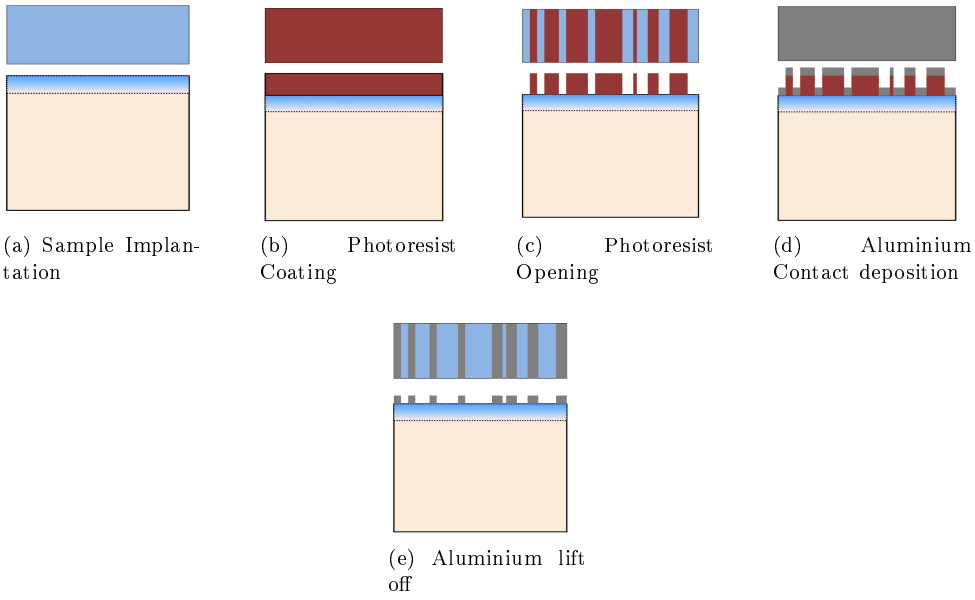

Figure 6.19: A brief process flow to fabricate the TLM test structure.

the active carrier concentration can be calculated. Illustration of the etching process for n-times of doped layers until reaching the substrate is shown in Figure 6.20

Probes are applied to pairs of contacts, and the resistance between them is measured by applying a voltage across the contacts and measuring the resulting current. The current flows from the first probe, into the metal contact, across the metal-semiconductor junction, through the sheet of semiconductor, across the metal-semiconductor junction again (except this time in the other direction), into the second contact, and from there into the second probe and into the external circuit to be measured by an ammeter. The resistance measured is a linear combination (sum) of the contact resistance of the first contact, the contact resistance of the second contact, and the sheet resistance of the semiconductor in-between the contacts.

Using the setup shown in Figure 6.21, the voltage applied and current measurements are made across the contacts with increasing distance between the contacts. Several such measurements are made between pairs of contacts that are separated by different distances. In this way, a plot of resistance versus contact separation can be obtained. Such a plot, shown in Figure 6.22 should be linear, with the slope of the line being the sheet resistance divided by the area between the contacts while the intercept of the line with the y-axis, being twice the value of the contact resistance as explained in section 6.6.3. Thus the sheet resistance as well as the contact resistance can be determined from this technique.

Since our interest in this study is to find the doping concentration as a function of

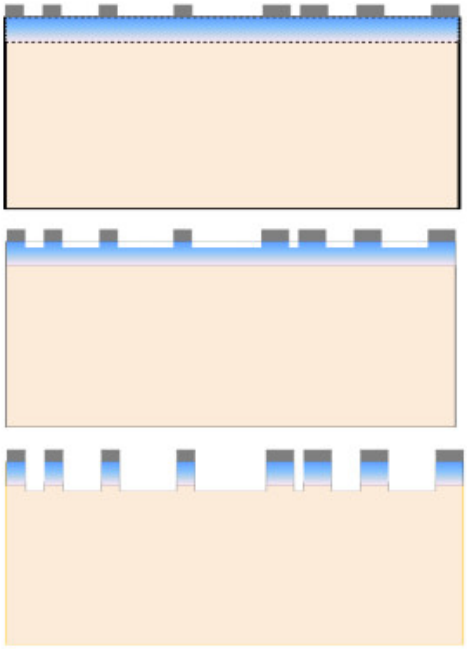

Figure 6.20: Schematic cross section of TLM sample illustrating the etching process for n-times of doped layers (blue region) until reaching the silicon substrate (beige region).

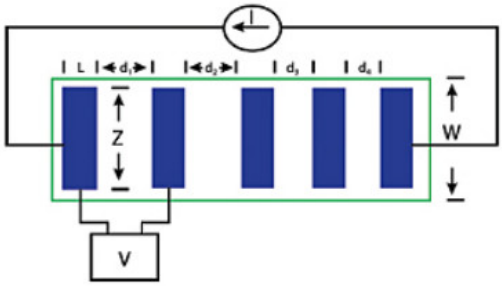

Figure 6.21: The TLM measurement allows assessing the magnitude of the resistance by applying a voltage across the contacts and measuring the resulting current.

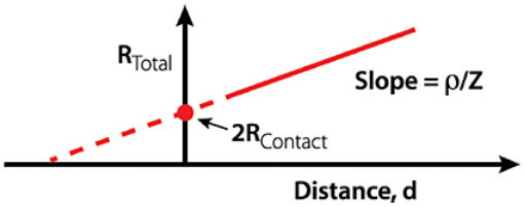

Figure 6.22: Resistance versus contact separation obtained from TLM measurement. Both the sheet resistance as well as the contact resistance can be determined using this technique.

the depth (i.e. doping profile measurement), then a resistance in depth measurement has to be performed. This is achieved by repeating the resistance measurement not only across each row between pairs of contacts but also in trenches obtained by etching a layer of doped silicon using the Reactive Ion Etching (RIE) [113] technique as shown in Figure 6.23. The RIE technique is a type of dry etching which has different characteristics than wet etching [114]. RIE uses chemically reactive plasma to remove material deposited on wafers. The plasma is generated under low pressure (vacuum) by an electromagnetic field. High-energy ions from the plasma attack the wafer surface and react with it. The RIE technique is well known for its a good compromise between resolution and selectivity among the other dry etching techniques.

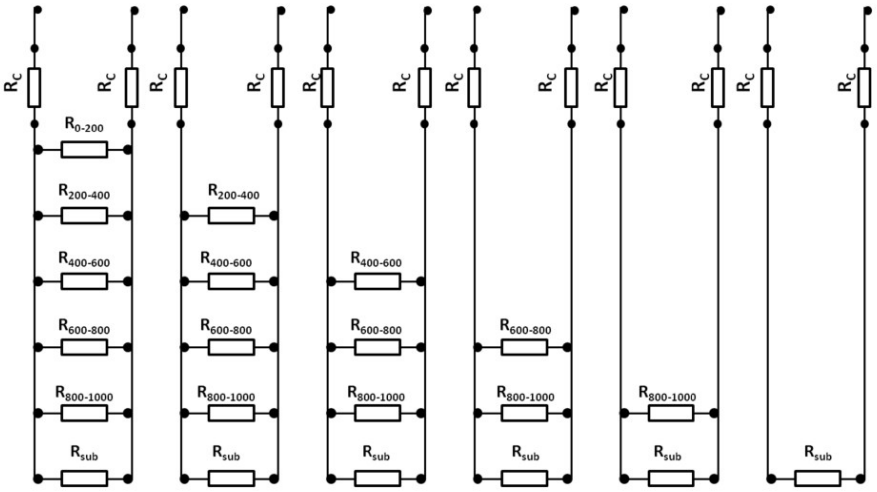

Figure 6.23: Resistance in-depth measurement used in this study. Repetitively, a small layer of implant is etched, using Reactive Ion Etching (RIE), and the resistance at different depths is measured until reaching the substrate.

After performing several etching, the variation of the thickness of the doped region (t) should be taken into account in the resistivity calculation. Equation 6.11 is not any more valid here, though it still can be used as an approximation in some cases where the precision is not a priority. But in our study, the variation of the active doping profile could be tiny, therefore, it is preferable to find the exact solution for the resistivity after etching.

The exact calculation of the resistivity is derived as follows. As can be seen from Figure 6.23, the resistivity of the substrate ρ_{sub}, at the last step of the etching, is simply written as:

$$\rho_{sub} = (R_{10} - 2R_C)\frac{Wt_{sub}}{L} \tag{6.15}$$

where L is the spacing distance between the contact, W is the contact length and t_{sub} is the thickness of the substrate after etching the dopant layer.

However, to calculate the resistivity in the previous layers, we need to take into account that these are resistances in parallel. Therefore, by having calculated the resistance for the last layer it is possible to calculate it for the previous ones. For example, the resistivity of the previous layer of thickness 100 nm, $\rho_9 = \rho_{900-1000}$, in Figure 6.23, which is the last etched layer before reaching the substrate would be:

$$\rho_9 = R_9 \frac{W t_9}{L} \tag{6.16}$$

But R_9 is not directly measured. The total resistance R_{Total} measured in each step is the equivalent resistance of three resistance: R_C, R_{sub}, and R_9.

$$R_{Total} = 2R_C + R_{sub}//R_9 = 2R_C + \frac{R_{sub}.R_9}{R_{sub} - R_9} \tag{6.17}$$

Solving equation 6.17 for R_9:

$$R_9 = \frac{R_{sub}.(R_{Total} - 2R_C)}{R_{sub} - (R_{Total} - 2R_C)} \tag{6.18}$$

and the layer resistivity ρ_9 is:

$$\rho_9 = \frac{R_{sub}.(R_{Total} - 2R_C)}{R_{sub} - (R_{Total} - 2R_C)} \frac{W t_9}{L} \tag{6.19}$$

In the same way, all the previous layers resistivity have been derived.

6.6.6 Experimental procedure

After the necessary cleaning of TLM samples with ethanol, a procedure of three main different operational steps were performed repetitively in the following order:

1. IV measurement: the measurement was performed using a two-point probe station shown in Figure 6.24(a). The two needle are placed on two adjacent contacts Figure 6.24(b). The voltage applied through one of the needle, in the range 0 - 0.5 V, and current is measured using the other needle. In the chosen voltage range, the linear behaviour of the device under test is assured and resistance between each pair of contacts is measured.

2. RIE etching: The "Advanced Vacuum-Vision 320" RIE machine, shown in Figure 6.25, has been used. The sample is placed inside the chamber shown in

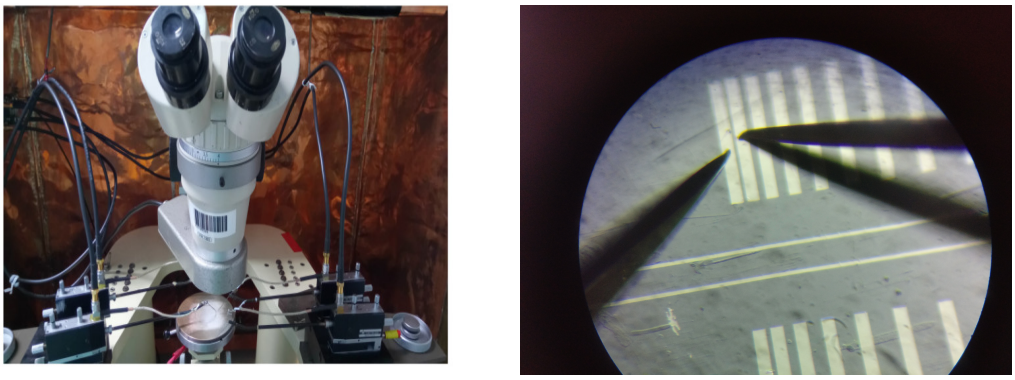

(a) (b)

Figure 6.24: (a) The two-point probe station used to measure the resistance using the TLM method. (b) Microscope view of needles placed on two adjacent contacts to perform the IV measurement.

Figure 6.26. The etching process of silicon is a Fluoride base process, where both CHF3 and SF6 gases were used. Pre-etching cleaning of the sample using a factory plasma with O_2 is done before each etching step. Plasma of density 10^9 cm^{-2} is generated under low pressure of order 10^{-6} Torr. Electrons from the gas are torn out (ionisation) and electrically accelerated up and down in the chamber. Some of them are deposited in the wafer while the rest is absorbed by the chamber walls and fed out to ground. The electrons deposited on the wafer surface generate a large negative charge (typically hundreds of volts). As a consequence, the ions are drifted towards the wafer since the plasma has a positive charge due to the higher concentration of positive ions and, therefore, a large potential difference is generated. Consequently, the ions interact with the doped silicon chemically and kinematically, knocking off a doped silicon layer. Etching is performed in a perpendicular direction inside the depth of the wafer, that's why the RIE etching technique is known as anisotropic etching.

3. Profilometer measurement: scanning the sample surface to measure the depth of the etched layer. Figure 6.27 shows an example of three profilometer measurements of an irradiated sample obtained after the first, second and third etching was performed.

This procedure (the three aforementioned measurements) is repeated ten times per sample in order to obtain the full profile of the active carriers concentration.

6.6.7 Results

In this section, the results of the TLM measurements for non-irradiated and irradiated samples is presented. In addition, a cross-check of the TLM measurement

Figure 6.25: The "Advanced Vacuum-Vision 320" RIE machine used in this study to etch the TLM samples.

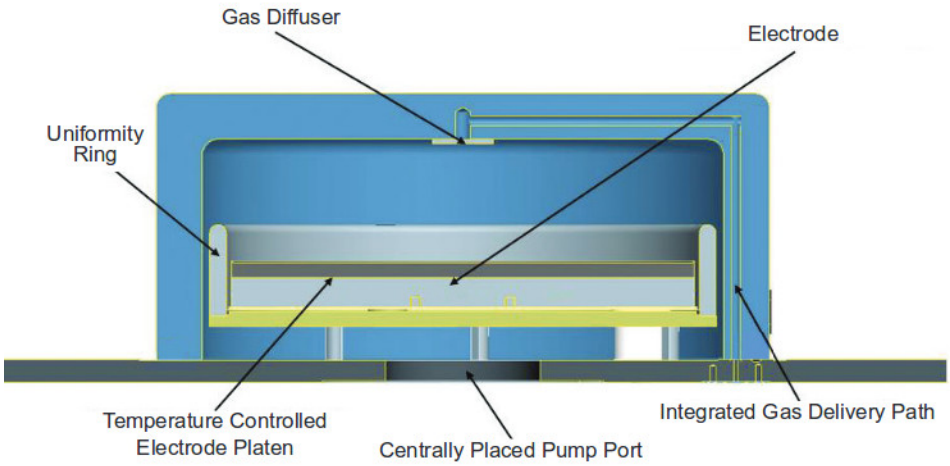

Figure 6.26: Cross section of the RIE chamber where the TLM samples were etched.

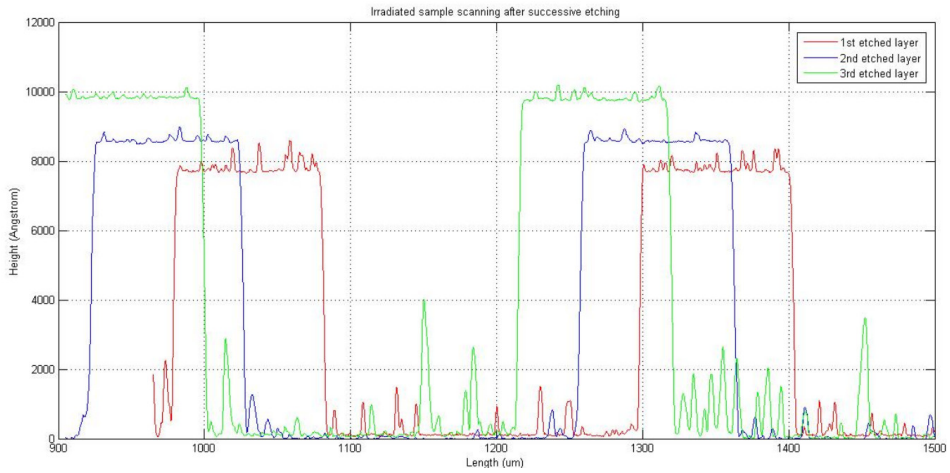

Figure 6.27: Three consecutive profilometer measurement of an irradiated sample obtained after the first, second and third etching was performed. A layer of thickness 200 nm is etched in each step.

obtained in this study with SIMS measurement is discussed. Measured doping profiles from TLM and SIMS measurements are compared to the simulated doping profiles.

Some of the measured IV curves of non irradiated Boron doped sample at different spacing between the contacts is shown in Figure 6.28. The measurements were performed by applying a bias voltage of 0.5 V. The expected linear behaviour of the IV curves is observed.

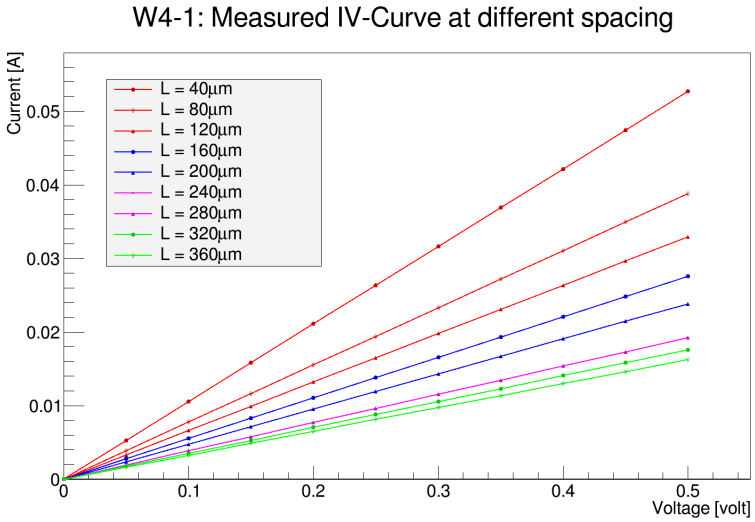

Figure 6.28: Measured Current as function of bias Voltage of a non irradiated Boron doped sample at different spacing between contacts.

Several samples from different wafers have been sent to be irradiated with different irradiation type (i.e. Protons, Neutrons and Gamma) and fluences (2×10^{15} n_{eq}/cm^2 and 2×10^{16} n_{eq}/cm^2). But due to time constraint, only the irradiated samples that were irradiated at Ljubljana irradiation facility [115] using neutrons, are used for this study.

Figure 6.29 compares the measured resistance as a function of contact spacing distance of before and after irradiation at four different etching steps. From this figure one can observe the expected behaviour of the resistance as the spacing distance increases. The resistance is directly proportional to the spacing distance as shown in equation 6.11. Moreover, one can notice that with more and more etching, the resistance increase. This is due to the fact that at deeper layers the dopant concentration decrease, and so less electrically active carriers are present, which induces a larger resistivity. This is demonstrated by the inversely proportional relation between carrier concentration and resistivity of semiconductor in equation 6.12. These observations confirm the reliability of our measurement. The resistivity of the doped silicon at different depth has been calculated using the equations derived in section 6.6.5.

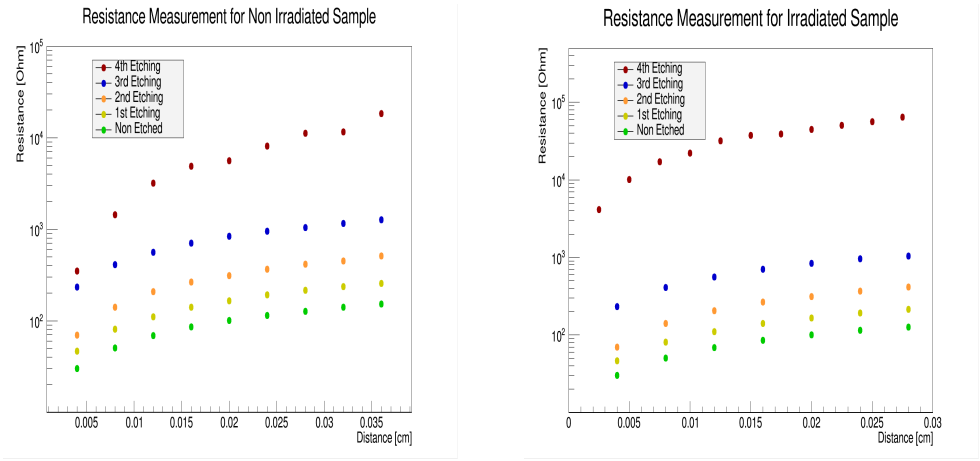

(a) (b)

Figure 6.29: Measured resistance as a function of contact spacing distance for non irradiated sample (a) as well as irradiated sample (b) at four different etching steps. The semi-logarithmic scale is used here.

Finally, the active carrier concentration for non irradiated and irradiated samples has been calculated directly using equation 6.12. Figure 6.30 shows the active carrier concentration as a function of depth for one non irradiated sample and two irradiated samples as measured using the TLM method. The irradiated samples were irradiated with neutrons at two irradiation dose: 2×10^{15} n_{eq}/cm^2 and 2×10^{16} n_{eq}/cm^2. In this plot, the measured peak concentration was found to be of order 10^{19} $atom/cm^3$ and it is in a good agreement with expected value provided by manufacturer, quoted

previously in Table 6.4. Moreover, the loss of active carriers due to interaction with the penetrating particles after irradiation is more visible at deeper layers. As it can be seen from Figure 6.30, the change of the doping profile, due to radiation damages, seems to start appearing at depth of 350-400 nm. At a depth ≈ 0.7 μm, the less irradiated sample shows a high level of noise and it was not possible to have further measurement. For the highest irradiated sample, instead, a saturation is observed. The interpretation is that all the doped silicon layers are removed and substrate concentration is reached. The loss of active carriers, at the deepest level measured for both samples, is around 95% for the less irradiated sample with respect to the non irradiated sample, while the loss for the most irradiated sample is 99.8%, caused by exposure to this high radiation dose.

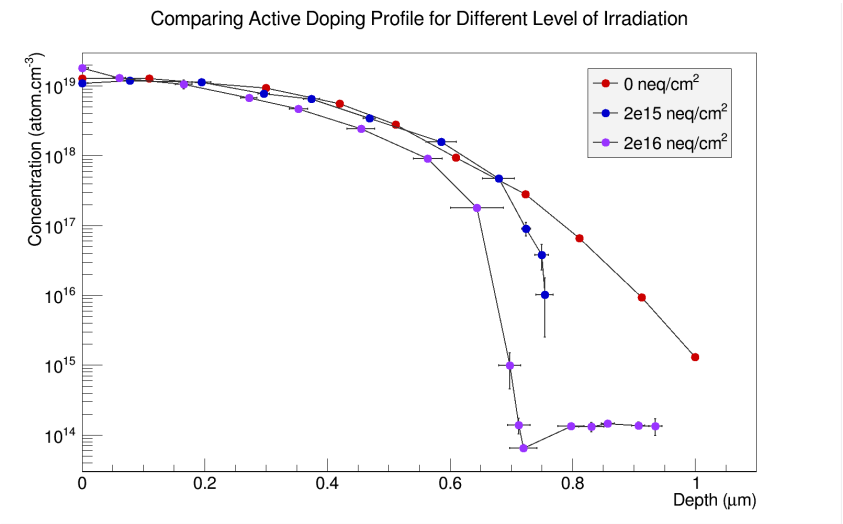

Figure 6.30: TLM measurement of the active carrier concentration as a function of depth for non irradiated sample (red curve) compared to two irradiated samples of 2×10^{15} n_{eq}/cm^2 (blue curve) 2×10^{16} n_{eq}/cm^2(Violet curve) neutrons irradiation fluences.

6.6.8 Cross-check of TLM results

The results herein obtained shows that TLM method is a promising method to measure the variation of active dopant concentration after irradiation. In order to prove that the TLM method is reliable, two cross-check have been performed. The first consist in using the SIMS method, previously introduced in section 6.1. The second check is a comparison of the TLM measurement with the doping profiles simulated using TCAD simulation, presented in section 6.3.

Figure 6.31 compares the TLM measurement with SIMS measurement (red curve) for non irradiated Boron doped sample. The discrepancy observed between the two measurements is explained by the fact that the SIMS technique measures the total

dopant concentration, contrarily, the TLM method is sensitive only to electrically active dopant.

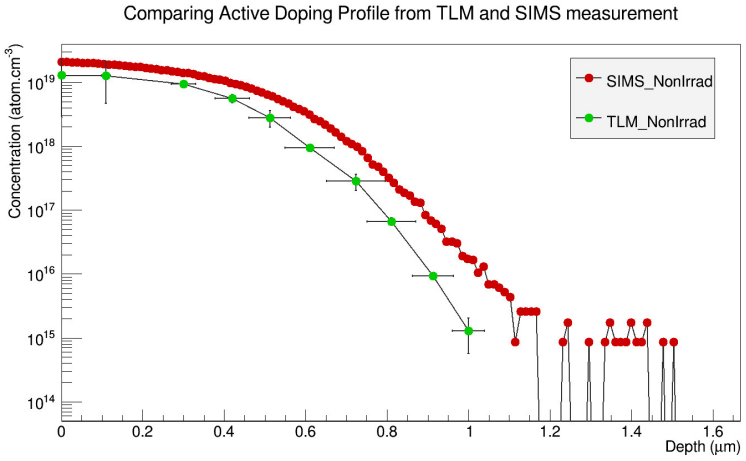

Figure 6.31: TLM measurement (green curve) compared to SIMS measurement (red curve) of the active carrier concentration as a function of depth for non irradiated sample.

A comparison of the doping profiles from the TLM measurement to simulated doping profile is displayed in Figure 6.32. Simulation has been performed for three different implantation energies: 240 keV, 130 keV and 60 keV. Among the three simulated doping profiles, good compatibility between the TLM measurement and the simulated 60 keV implantation dose is observed. This as well is in a good agreement with the production parameters shown in Table 6.4. Again, the divergence between the measurement and the simulation results is due to the fact that the simulation tools provide information about the total dopant concentration and not the electrically active dopant.

6.6.9 Conclusion

Understanding the structure of the silicon detectors, by measuring the doping profile, is important due to the fact that it can explain the operational behavior of the device, and can be a kind of quality assurance of the detector production where any failure in the fabrication process can be found. Moreover, the doping profile measurement can provide important inputs to simulation in order to get precise results. The total doping profile of a silicon detector can be measured with very high precision using the Secondary Ions Mass Spectrometry (SIMS) introduced in the previous sections. Though, unfortunately, the SIMS method measures only the total doping profiles.

This section is dedicated to introducing an alternative scanning technique based on the Transmission Line Matrix (TLM) method that can measure the electrically active doping profiles of silicon detectors. The preliminary results of the TLM

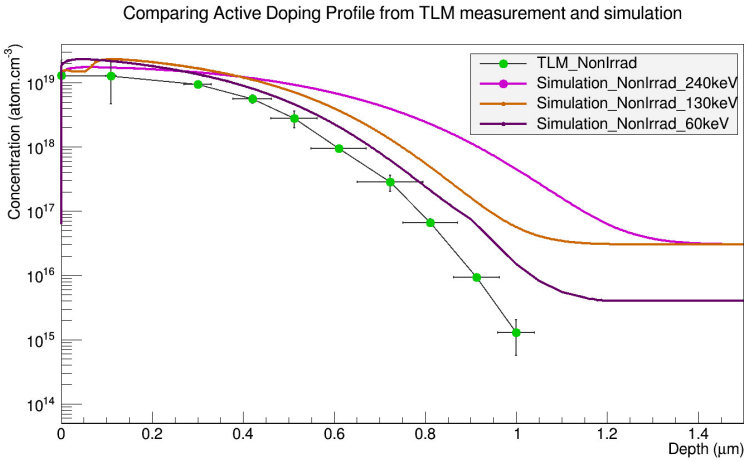

Figure 6.32: TLM measurement (green curve) of the active carrier concentration as a function of depth for non irradiated sample compared to simulated doping profile corresponding to three implantation energies: 240 keV, 130 keV and 60 keV. The sample provided by the manufacturer was implanted with a 60 keV.

measurement indicate that the concentration of active dopant are modified by irradiation. For a high irradiation dose, a loss in the active dopant concentration has been observed, of about 99% at 0.7 μm of depth . The TLM results have been validated using SIMS data and simulated doping profile using TCAD simulation tools. An overall very good agreement and constancy of the results have been shown. This study provides important information on the electrically active dopant distribution and concentration, which determine the properties of semiconductor devices and can be useful to tune the irradiation models to predict the behaviour of silicon pixel detector after irradiation. The different results obtained concerning the irradiation study using the TLM method were presented in a poster in the "12th Trento Workshop on Advanced Silicon Radiation Detector" in February 2017 in Itlay, and I got the **Best Poster Award** in this workshop.

Chapter 7

Testbeam Characterization

Contents

7.1 Testbeam facilities 142

7.1.1 DESY 142

7.1.2 Super Proton Synchrotron (SpS), CERN 142

7.2 Testbeam Setup 143

7.2.1 The EUDET telescopes for particle tracking 144

7.2.2 Cooling 146

7.2.3 Mounting devices 147

7.2.4 Data acquisition software 147

7.2.5 Online data monitoring 148

7.3 Testbeam data analysis chain 148

7.3.1 Track reconstruction 149

7.3.2 Reconstructed Data analysis 151

7.4 CERN Testbeam Results 154

New detectors are required to be tested in an environment similar to that which they will be exposed to within ATLAS to determine how well they function. A beam test, where the device is read out within a beam of particles, is preferable to using a radioactive source in a lab since the statistics will be much higher. The particle type and energy is usually well known within a beam test, however the exact position of a particle at any one time is difficult to determine. Therefore, a set of well understood detectors known as a telescope is used in beam test experiments to track the charged particles. These tracks can be reconstructed off-line to evaluate the efficiency and charge sharing performance of the devices under test for various parameters such as the tilt angle, threshold or bias voltage.

7.1 Testbeam facilities

7.1.1 DESY

Deutsches Elektronen-Synchrotron (DESY) is the German accelerator research centre located in Hamburg. The facility was the location of the Hadron-Elektron-Ring-Anlage (HERA) accelerator, which collided electrons or positrons with protons primarily to investigate the properties of the quarks within via deep inelastic scattering. These collisions took place in two main detectors, H1 and ZEUS, both built in 1997 and run until shutdown in 2007.

An illustration of the process of producing electrons (e^-) or positrons (e^+) at a specific energy for beam tests at DESY is shown in Figure 7.1 [116]. The DESY II synchrotron accelerates positrons or electrons and then a carbon fiber placed in the e^+ or e^- beam produces photons through bremsstrahlung radiation. These photons impact a metal plate which converts them to pairs of e^- /e^+ . A dipole magnet spreads the beam out as a function of the sign and energy. The desired beam energy within the range of 1-6 GeV/c is chosen with a collimator. The beam is subsequently directed into one of three beam areas. The rate of electrons or positrons is 1000 $s^{-1}cm^{-2}$. A photograph of beam area 21 at DESY is shown in Figure 7.2; the telescope and tested devices are to the left of center and the beam direction is from right to left.

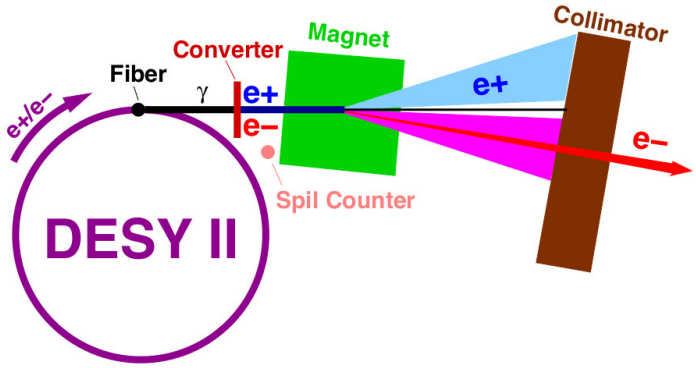

Figure 7.1: A diagram illustrating the process of producing an electron or positron beam for tests at DESY [115].

7.1.2 Super Proton Synchrotron (SpS), CERN

The Super Proton Synchrotron (SpS) at CERN is the final accelerator in the injection chain for the LHC and is primarily required to accelerate protons to 450 GeV.

Figure 7.2: Photograph of the DESY beam hall. The beam direction is from right to left.

However, the CERN-SpS provides a pion beam with an energy of either 120 GeV or 180 GeV, which allows for a minimization of the influence of the multiple scattering. In this thesis, all beam test measurements were performed with a 120 GeV particle beam. The particle beam is delivered to four beam lines used as beam test facilities. Every beam line contains magnets for bending and beam focusing. To obtain a pion beam, protons from the SpS are accelerated to 400 GeV and directed to one of the three available targets. The generated pions traverse a spectrometer magnet filter, where their momenta are adjusted. Subsequently, they are directed to the beam lines with a maximum number of $2{\times}10^8$ particles per spill. The spill length and repetition frequency depend on the number of facilities used in parallel. The SpS is able to offer a spill length of 4.8 s to 9.6 s and a repetition frequency every 14 s to 48 s. Due to the fact, that the CERN-SpS is serving multiple experiments, the beam is not continuously present. The planar pixel silicon detector tests used both beam lines H6 and H8.

There is a preference of having beam tests located at the SpS at CERN instead of at DESY. This is due to the higher level of multiple scattering of the positrons from DESY, which produces reconstructed results with a lower resolution.

7.2 Testbeam Setup

The common beam test setup for pixel silicon devices consists of a telescope, which is split into two arms with a central testing area in the middle. Two pairs of scintillators ($1 \times 2\ cm^2$), each pair at 90° to each other, are located in coincidence either side of the telescope to trigger on incident particles. Data are recorded during a window of 16 level 1 (lvl1) trigger counts, this is known as an event. These triggers are passed to a Trigger Logic Unit (TLU). This setup is illustrated in Figure 7.3. After a specific number of events, the data set is saved as a run. Runs are required to be big enough that sufficient statistics are collected, but low enough that the setup has not changed significantly over the time taken to record it. Furthermore, it is desirable to keep file sizes small and to save data frequently enough to safeguard against possible software crashes.

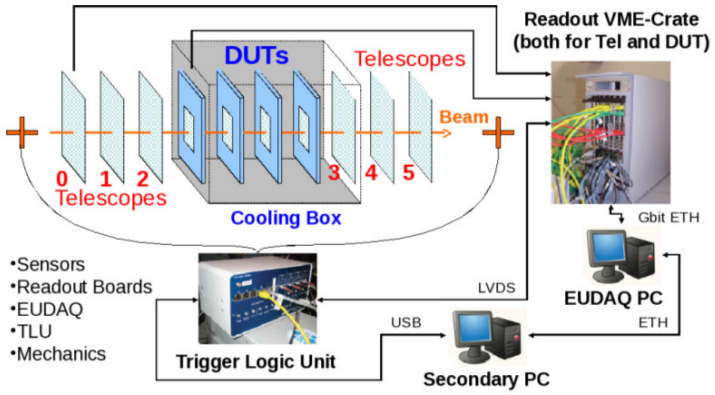

Figure 7.3: Illustration of a standard beam test setup [117].

The Devices Under Test (DUTs) are located in the central area and each are readout via a USBPix system. Several USBPix devices can be run simultaneously from a single computer running the data acquisition software, EUDAQ. At DESY, due to the increased amount of multiple scattering, normally only two devices are tested; at CERN up to four devices can be run at once and generally this number is limited by the size of the box that will be described later. For various reasons it is required to have a device that is well understood as part of the testing setup, known as a reference sensor. Since the telescope is read out at a rate of 112 μs in a rolling shutter mode and the DUTs are read out every 400 ns, the reference sensor is primarily there to determine if a hit on the DUT is registered as 'in time'. Another reason to have a reference sensor is to check that the data are sensible by comparing established plots, such as cluster size and TOT histograms, for the reference with previous results.

7.2.1 The EUDET telescopes for particle tracking

The purpose of a telescope is to use mature detectors that are well understood with a resolution better than the pixel pitch of the devices under test, to record hits from a particle track in a beam test environment. Using offline software to reconstruct the tracks from the telescope planes, studies of new detectors can be performed to understand various features such as efficiency and the sharing of charge between pixels.

The beam telescopes of the EUDET family are equipped with six fine-segmented MIMOSA26 [118] detectors, which feature the architecture of monolithic active pixel sensors (MAPS) with fast binary readout and integrated zero suppression [119]. The EUDET telescopes provide a precise reference track trajectory using its 3 planes of the MIMOSA26 sensors upstream the Device Under Test (DUT) and another 3

planes downstream the DUTs. In terms of readout of FE-I4 modules, the USBPix, as well as the RCE (Reconfigurable Cluster Element), are integrated in the telescope DAQ. In the front and back of the telescope four scintillators (two in the front, two in the back), with a total area close to the one of the MIMOSA26 pixel sensor, are placed to trigger the readout, when particles are crossing. The size of the MIMOSA26 chip is 13.7 mm $\times$ 21.5 mm and the sensor matrix is composed by 576$\times$1152 pixels of 18.4 μm pitch with a thickness of only 25 μm. A pixel pitch is defined to be the length from the center of one pixel cell to the center of the neighbouring one. Owing to this remarkably low thickness, the telescope allows for tracking of low energy particles with a reduced multiple scattering affecting the pointing resolution in a less relevant way.

For single pixel clusters, the sensor intrinsic resolution is estimated starting from the sensor pixel pitch. Using the term $p/\sqrt{12}$ [120] with p corresponding to the pixel pitch, an intrinsic resolution of 5.3 μm is reached by the telescope. Larger pixel clusters, obtained by lowering the threshold values of the MIMOSA26 chips, improves the intrinsic resolution. Doing so, each EUDET plane reaches up to 3.5 μm of spatial resolution in case of low energetic electrons and 2 μm for high energetic pions [121]. The possibility to integrate readout micro-circuitry on the sensor, which is given by monolithic sensors, results in a very low readout noise and in a powerful signal processing capability. An operation point, resulting in an efficiency of 99.5 $\pm$ 0.1% for a MIP at a fake rate of 10^{-4} per pixel, can be reached at room temperature [118]. With a MIMOSA26 integration time of 115.2 μs, the maximum possible rate is set to be 10 k hits per frame and second [119]. Due to the much smaller integration time of the FE-I4 readout chips, an FE-I4 module is included in the data taking as a reference device to select the tracks, which are in time with the DUT. A total number of seven EUDET-type beam telescopes was developed since 2009, of which AIDA and ACONITE are installed at CERN, owned by ATLAS, while DATURA and DURANTA are stationed at DESY.

An important feature of the telescope plane is the **pointing resolution** which defines the precision of the determination of a particle trajectory. The pointing resolution is a crucial property for telescope plans since the minimal achievable pointing resolution, the better spatial resolution (smaller than the pixel size) can be achieved. The pointing resolution is influenced by parameters, such as the number of the available tracking planes, as well as by physical effects such as the multiple scattering. The latter is more relevant for lower energetic particles. Charged particles are deflected, when traversing material between the very first and the last telescope plane. The particle deflection is dependent on the detector material, as well as the path length in the surrounding air.

In the case of measurements at the CERN-SpS, where 120 GeV pions are used, the effect of multiple scattering, due to Coloumb interactions with the nuclei of the traversed material, is negligible. Instead, the lower energetic electrons with a

maximum achievable energy of 6 GeV at DESY, are significantly affected by multiple scattering. Even though the multiple scattering is taken into account by the broken-line fit, introduced later on in this chapter, the material in between the telescope planes needs to be reduced.

7.2.2 Cooling

Due to the increase in leakage current from radiation damage, irradiated sensors should be operated in the dark and at low temperatures. A cooling box, placed at the centre of the two telescope arms in the beam test setup, is used to reduce the amount of light impacting on the sensors during data taking, to have a low material budget and provide insulation from external temperature changes. At CERN-SpS, the DUTs are mounted in a cooling box, developed and built at MPP, to ensure a stable temperature of 20°C, in case the devices are not irradiated, or a low temperature range of -30°C to -50°C to measure irradiated devices. The cooling box is made from aluminium and is connected to a chiller and a nitrogen source to allow for dry air. The Nitrogen gas is piped into the box to reduce condensation and ice forming on the sensors which could cause damage through short-circuiting or possibly through the expansion of ice on the delicate wire-bonding. An additional cooling box, designed at the University of Dortmund [122], is in use at CERN. The cooling box is made from foam and consists of two areas, which are separated from each other by an additional aluminium plate. The inner area is dedicated to the DUTs, while the outer area is used to place the dry ice close to the modules for cooling to temperatures down to about -50°C. The temperature is monitored during measurements using a temperature sensor inside the cooling box. The same type of cooling box is mounted at DESY. A photograph illustrating the cooling box design is in Figure 7.4.

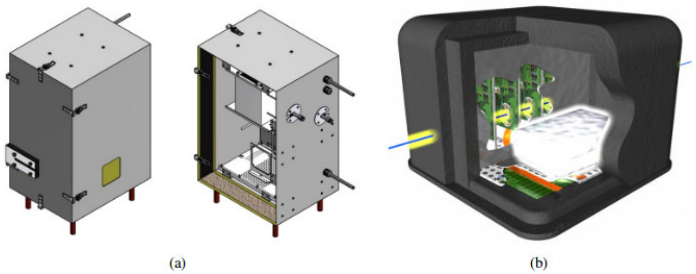

Figure 7.4: The cooling box, manufactured by MPP (a) which is situated at CERN, while the Dortmund cooling box (b) is used at CERN and DESY [122].

7.2.3 Mounting devices

A high-precision xy-table is used to move the DUT through the active area of the telescope. All devices being tested are mounted onto a L-shaped aluminium mount which, when screwed into the aluminium plate in the Dortmund cooling box, places the sensors normal to the beam and ideally overlapping in the x-y plane. The material choice allows to transfer heat away from the sensors thanks to the fact that the aluminium is also in contact with the dry ice. Kapton tape, which is electrically insulating and stable at low temperatures, is used cover the L-shaped mounts to prevent short-circuiting.

7.2.4 Data acquisition software

The software used for data acquisition is called EUDAQ [123], which is an operating system independent framework that uses processors to communicate between the various hardware devices. The graphical interface called Run Control, allows the user to interact with these processors. Data are output as a single RAW file and contains all the information from each telescope plane and DUT such as hit positions and time over threshold for individual events.

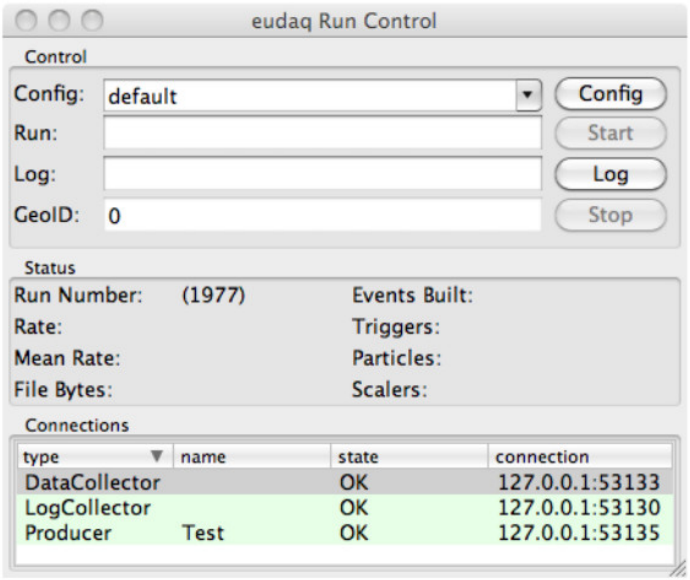

Figure 7.5: The EUDAQ control panel.

7.2.5 Online data monitoring

During data taking, it is useful to monitor certain plots in real time using a Data Quality Monitoring (DQM) programme. This is to ensure that the data for each run are not corrupted. Figure 7.6 shows an example of online data monitoring plots provided by the EUDET Telescope Online Monitor. For each DUT and telescope plane the two dimensional hitmaps for the raw and clustered data are available as well as the TOT and cluster size. A histogram of hot pixels gives an indication of how noisy the sensor is; masking noisy pixels or increasing the threshold could reduce problems with data analysis later. The Online Monitor also provides correlation plots.

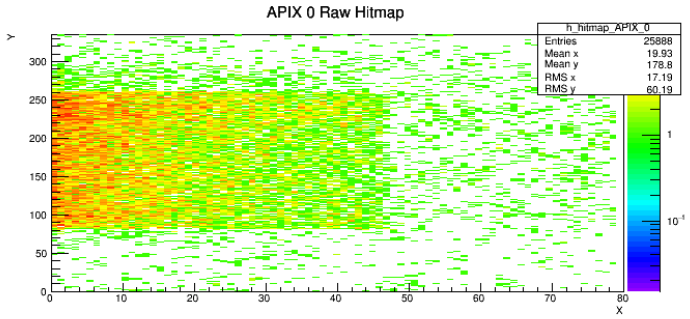

Figure 7.6: Example of EUDET Online Monitoring plots for a non-irradiated Active edge pixel detector. The colorbar in this plot indicate number of hits. As seen here, most of the particle hits are positioned at the edge of the module. The module was placed such that the beam hits the edge in order to study the edge efficiency in this case.

A two-dimensional plot of the position of a hit in x or y for one device compared to the hit position on the same axis for another is known as a ***correlation plot***. These are provided in the Online Monitor (see Figure 7.7), they indicate whether two sensors overlap in the beam and allow the shifter to check that one device has not fallen out of sync with the other. Ideally for two well aligned sensors of the same dimensions and rotation, the hits on the correlation plots will start at the bottom left corner at zero, and extend at a 45° angle to the top right. Hits due multiple scattering or those that are out of time will not be on this line. Straight lines in the horizontal or vertical direction are generally due to noisy or 'stuck' pixels.

7.3 Testbeam data analysis chain

Before the data from the beam test can be analysed, particle tracks through the setup must be reconstructed; this is performed with the **EUTelescope** software framework[124], and then reconstructed data is further reprocessed in **TBmon**[125]

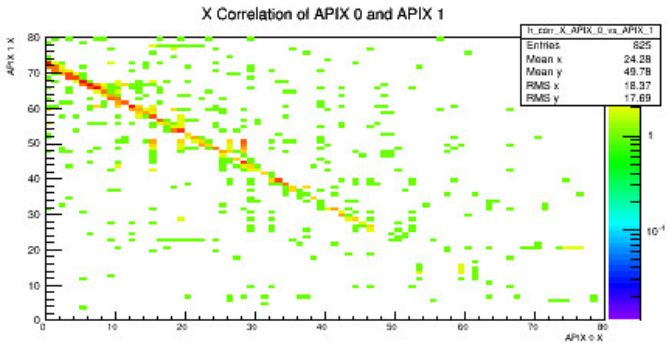

Figure 7.7: Example of EUDET Online Monitoring correlation plot for a non-irradiated active edge pixel detector with another DUT. The majority of the hits lie on the straight line start at the top left corner and extend to the bottom right corner. This indicates a negative correlation between the two modules. Hence, the fact that the two DUTs are not aligned. This is explained by the fact the two DUTs where mounted back-to-back.

analysis software framework.

7.3.1 Track reconstruction

The particle trajectory is reconstructed from raw hit positions on the telescope planes and the DUTs by a sequential algorithm of the EUTelescope software framework. EUTelescope is an offline reconstruction and data analysis programme using Marlin processors. EUTelescope requires a description of the position of each device in the telescope frame of reference, this is recorded in a GEAR file. In the GEAR file, the layout of the experiment is described, and the positions and sizes of each telescope and tested device in the setup is detailed. Further information such as pixel pitch, rotations using Euler angles, thickness and radiation length of each device is also entered by the user. A unique device ID is assigned to distinguish detectors.

The software takes the RAW data output from a beam test and, after a number of stages, produces fitted tracks in a three dimensional global reference frame as a .root file. These stages are conversion, clustering, hitmaker, alignment and tracking. Each stage is described in detail below.

Converter

As the first step, the events are defined from trigger information and hits in pixels, recorded with a time stamp, defined by the trigger logic unit (TLU), and converted into a EUTelescope internal data format. A hit is defined as a signal of a pixel above threshold. All noisy pixels are excluded before data taking. In case of further pixels

exceeding the firing frequency threshold of 1%, the pixels are removed from the subsequent data analysis and their position is stored into the noisy pixel database.

Clustering

In the second step, a sparse pixel clustering algorithm groups together all hit pixels in close proximity, calculating the coordinates of the formed clusters. There are many algorithms designed for clustering data, the two main ones used for track reconstruction are Cluster Weighted Centre and Cluster Charge Weighted Centre. In the Cluster Weighted Centre, the X and Y coordinates are averaged separately to give a value for the cluster centre. This algorithm is used for the telescope planes since only the location of the hit for each position in the cluster is known, therefore each hit has an equal weighting in determining the centre of the cluster position. Cluster Charge Weighted Centre is using the Time Over Threshold (TOT) information from the DUT as a weight, from which the 'centre of mass' for the cluster can be calculated.

Hitmaker

The third step, the Hitmaker, transforms the hits in the local coordinate system of each detector plane to a global reference frame, in which the z axis is parallel to the beam direction. The geometry of pixels in x and y position, as well as their rotation are taken into account. Based on these coordinates and the resulting correlations between the devices, a coarse pre-alignment is done with a precision of a few hundred *mu*m. With this, the pre-alignment corrects for any global misalignment and is used for the subsequent, crucial and next step, the alignment.

Alignment

In the second alignment iteration, an alignment processor tries to fit tracks through all telescope planes and DUTs in the set-up, taking into account the spatial resolutions of each device. The requirement of how many and which telescope planes and DUTs are taken into consideration for alignment is set in this step. The first telescope plane is always fixed in its orientation and position to allow for a fixed starting point of the particle trajectory. The selected tracks are gathered and passed to the MILLEPEDE-II algorithm [126] that minimizes the global χ^2 of the track residuals by trying all the possible combinations of hits. Tracks with $\chi^2 > 50$ are excluded from further track processing. In addition, the uncertainties of the fitted track parameters are minimized, while the constants of the alignment for each telescope plane and DUT are returned.

Track finder

After alignment, the final stage is to reconstruct the particle track though the setup. Track fit is s affected by false track candidates. Therefore, it is essential for

track reconstruction, that track fitting algorithms allow for autonomous filtering of false track candidates. To overcome these difficulties, the deterministic annealing fitter (DAF) [127], which is based on a Kalman filter [128], is used. The track reconstruction is completed by finally fitting the tracks with the track model of the general broken lines [129] including effect of the multiple scattering in the initial particle trajectory. The data is stored in ROOT files on a per run basis with the reconstructed tracks, as well as with information on the telescope planes and DUTs. These final output root files at the end of the reconstruction step are used as input files for TBMon analysis software.

7.3.2 Reconstructed Data analysis

A detailed analysis of the DUTs with their specific types of geometries is conducted using TBMon offline analysis software developed by the ATLAS pixel collaboration to study beam test data. TBMon reads in the .root file produced after the tracking stage of EUTelescope and allows the user to cluster the DUT data, fine-tune alignment and analyse the efficiency, charge sharing and other features of the sensor depending on the analysis class selected. In the following, the different analyses are summarised.

7.3.2.1 Cluster size

Charge is collected in multiple, neighbouring pixels when the particle track is at an inclination or when charge sharing occurs. These accumulation of hits in the sensor that are approximately close in space and time and assumed to be created by the same traversing particle is known as **Cluster**. **Cluster size** is defined as the number of hit pixels forming a cluster. while the length of the pixels, fired in the two detector coordinates, is referred to as **cluster width**. Although clustering is already performed in the reconstruction stage, this information is not stored in the .root file and so clustering must be performed again.

To distinguish between multiple clusters in the same event, a threshold of the signal in the pixels is set as well as a minimum distance between two clusters to be identified as originating from separate tracks. Both restrictions cut out possible noise, appearing at the same time as the actual hits, where the first hit pixel in time is defined as the **seed pixel**. The local point, where the particle crosses the sensor, is defined as the **geometrical center** of the pixel cell.

The cluster size is a function of the incidence angle and the length of the pixel cell side. In the first case, at perpendicular beam incidence, the average cluster size is between one and two. Two-hit clusters (i.e. the cluster size equal 2) means that either the particle enters the detector close to the edge between two pixels or with

an incidence angle slightly different than perpendicularly to the detector surface. This result into charge diffusion of the charge carriers which fires two pixel cells. Consequently, the higher incidence angle the particle enter the detector surface, the larger cluster size we get. Moreover, the cluster size is dependent on the length of the pixel cell side. In this case, the two-hit clusters are mostly originating from the short pixel side, where the adjacent pixels below and above the seed pixel have a higher probability to record a signal. An example of TBMon output cluster size plot is shown in Figure 7.8. The figure in the left shows a steady cluster size over time, indicating that the sensor has not tilted significantly during these runs. The figure on the right is an example of poorer set of runs. The statistics are lower and the alignment not perfect. This results in a greater spread in cluster sizes.

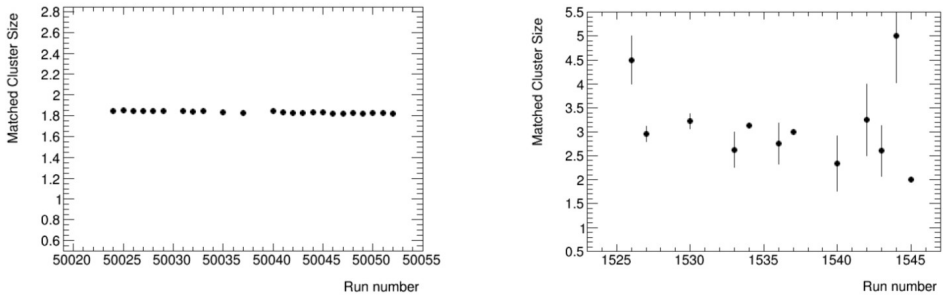

(a) (b)

Figure 7.8: An example of the output from the clusters vs run analysis class written for TBMon, showing the total matched cluster size for a sensor as a function of time (per run). (a) is an example of a good set of runs while (b) is an example of a set of runs with lower statistics and poorer alignment.

7.3.2.2 Residuals and Spatial resolution

The **spatial resolution** of a detector is defined as the width of the residual distributions. The **residual distribution** is obtained from the distance between the extrapolated track of the particle, traversing the telescope and DUTs, and the recorded position of the hit in the device. The residuals are calculated separately for x and y. The residual in x, Δx, is given by:

$$\Delta x = x_{track} - x_{hit} \tag{7.1}$$

and the residual in y is defined in similar way. In the ideal case of a uniform particle beam flux, box-shaped residuals with an RMS equals to the the **intrinsic spatial resolution** (σ_{int}). The intrinsic spatial resolution for an FE-I4 pixel cell of 50×250 μm^2 pixel size are calculated to be $\sigma_{int,x} \approx 72$ μm and $\sigma_{int,y} \approx 14$ μm.

But due to the charge sharing at the edge of the pixels, the shape of the residual distribution is a Gaussian distribution centred at zero with a base width approximately equal to the pixel pitch. However, this would be wider for results where there is increased multiple scattering, such as in the case of DESY testbeams.

Moreover, the measured spatial resolution (σ_{meas}) of the DUTs is influenced by the intrinsic resolution of the device, as well as by the pointing resolution (σ_{int}), associated to the telescope performance. The measured spatial resolution is given by

$$\sigma^2_{meas} = \sigma^2_{int} + \sigma^2_{point} \tag{7.2}$$

The spatial resolution in the short pixel direction shows a slightly higher discrepancy, due to the fact that multiple-hit clusters are more prone to occur in the short pixel direction, resulting in more charge sharing between the neighbouring pixel cells. In the case of perpendicular beam incidence, the one-hit clusters are dominate, and in this case, the obtained spatial resolution is comparable with the intrinsic spatial resolution.

7.3.2.3 Hit efficiency

When a particle beam traverse a DUT, a signal is recorded in the projected impact point of the track on the sensor. This recorded signal is called hit. Reconstructing the date from the testbeam, as explained in the previous section, results in what we call **reconstructed tracks** which are passing through a DUT. We say that a track is matching a hit if it is within a given maximum distance between the two.

The hit efficiency of the DUTs is defined as the ratio of the number of reconstructed tracks with matching hits in the DUT to the total number of reconstructed tracks passing through the DUT.

$$Efficieny = \frac{\#MatchedTracks}{\#TotalTracks} \tag{7.3}$$

The hit efficiency can be estimated for the entire module area, as well as within a pixel cell. Since the pointing resolution of the telescope is depending on to the energy of the particles traversing the telescope planes, the in-pixel efficiency maps obtained at CERN result in a better resolved distribution of the hit efficiency within the pixel cell.

In addition to previously introduced analysis that can be performed within the TBmon framework, one can investigate other analysis such as the one of the beam profile, charge collection efficiency and many others provided in the framework.

Edge Design	Thickness [μm]	Edge distance [μm]	edge structure	Pixel cell [μm^2]
Active edge	150 100 50	50	one GR,no p-t	50×250
Slim edge	150	100	one BR,external p-t BR+GR, standard p-t one BR,standard p-t	50×250
	100			
	50			

Table 7.1: Summary of the single chip modules from Advacam productions relevant for this thesis. [132]

7.4 CERN Testbeam Results

During the testbeam at SpS-CERN, the properties of n^+-in-p planar pixel modules with different sensor designs are investigated and compared. In the following, the sensor production and the performance of sensors in the testbeam will be presented with focusing on the tracking efficiency at perpendicular beam incidence. The presented results are obtained by measurement performed in collaboration with the MPI group, within the framework of the RD50 collaboration, the AIDA-2020 project [130] and the Inner Tracker (ITk) group of ATLAS [131], focusing on the requirements for the ATLAS pixel detector upgrade at HL-LHC.

The sensors under study were produced by Advacam. Two edge designs have been implemented in the Advacam production: the slim edge and the active edge design, each has a different distance (d_e) of the last pixel implant to the sensor edge. There are two variants of slim edge sensors with $d_e = 100\ \mu m$: the first one with a single BR, the second one with a BR together with one GR at floating potential. In both designs the single punch-through (p-t) design is implemented, as well as the common p-t design in case of the single BR design. The active edge design is characterized by $d_e = 50\ \mu m$ and employs only one GR at floating potential. No p-t structure is implemented in this design. Due to the non existent biasing structures, it is not possible to test the functionality of the pixel cells before interconnection. Moreover, after bump bonding the pixels are only grounded via the connection to the chip. A disconnected channel will cause a local modification of the electric field, which may lead to a lower breakdown voltage. On the other side the absence of the biasing rail avoids the efficiency loss after high irradiation doses, observed in the area where these structures are placed [74]. The four different sensor types are illustrated in Figure 7.9.

The different module characteristic, pertinent to the thesis, of the Advacam production are summarised in Table 7.1.

One of the most interesting properties of a tracking device in testbeam measurements is the hit efficiency of devices, when they are traversed by charged particles. The hit efficiency of modules from the Advacam productions is investigated in beam tests at the CERN-SpS facility. Thanks to the high resolution of the telescopes of

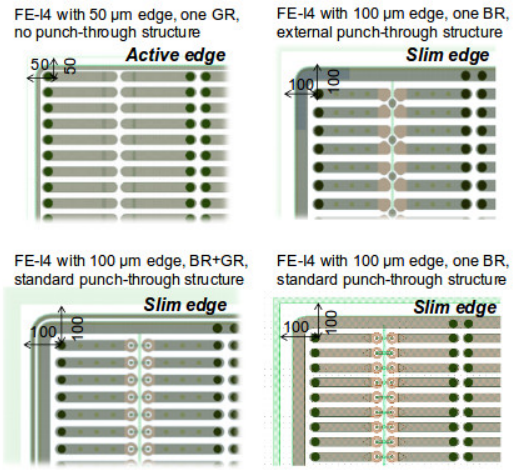

Figure 7.9: Four different sensor types of the Advacam SOI production: the active edge design with $d_e = 50\ \mu m$, one GR and no p-t structure (top left), the slim edge design with $d_e = 100\ \mu m$, one grounded BR and the common p-t structure (top right), the slim edge design with one BR and GR and the single p-t design (bottom left) and the slim edge design with only one BR and the single p-t structure (bottom right) [132].

the EUDET family, it is further possible to investigate the spatially resolved in-pixel hit efficiency, charge sharing properties and the performance of the sensor edge.

Un-irrdadiated Advacam modules with (150 μm and 100 μm) thicknesses were employed to perform an analysis of the hit efficiency at the periphery of the devices. The slim edge design with one BR and common p-t structure and the active edge design with one GR and no p-t structure were investigated. The layout of these two designs are shown in Figure 7.10. Different results for global efficiency, in-pixel efficiency as well as the edge efficient are shown in this section.

Comparison of the global hit efficiency map for these two designs before irradiation are shown in Figure 7.11. The active edge sensor achieved a global hit efficiency of 98.645 $\pm$ 0.005%. A hit efficiency of 98.558 $\pm$ 0.004% is reached for the slim edge sensor. Both designs shows a hit efficiency higher than 97%, which is the limit required for th ITK upgrade.

Figure 7.12 shows the in-pixel hit efficiency map, measured at CERN-SpS, before irradiation, of (top) a 150 μm active edge sensor and (bottom) a 100 μm slim edge sensor. The active edge design shows a uniform efficiency over all the pixel cell. The efficiency loss at the left edge of the pixel in the slim edge design is due to punch-through structure in the inter-pixel region.

Hit efficiency at the sensor edge

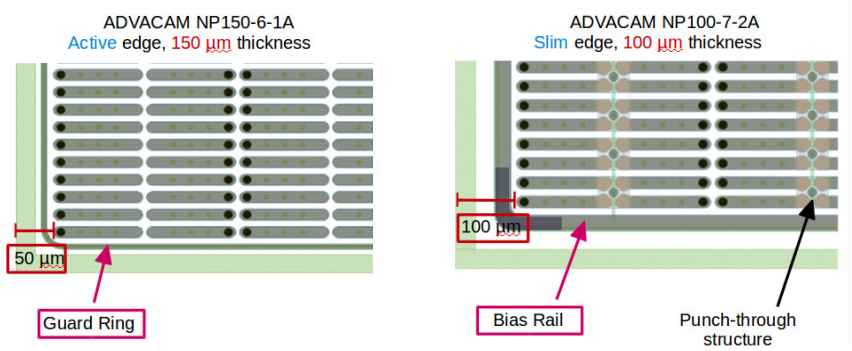

(a) (b)

Figure 7.10: Sensor design under study. (a) Active edge design of 150 μm thickness with GR edge structure. (b) Slim Edge design of 100 μm thickness with BR and punch-through edge design.

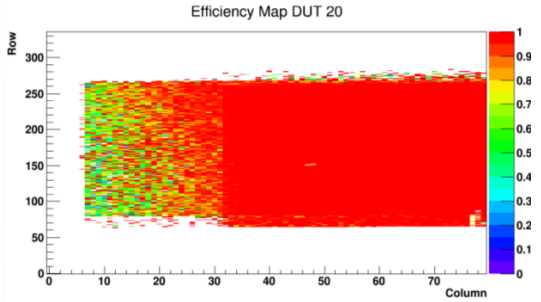

(a)

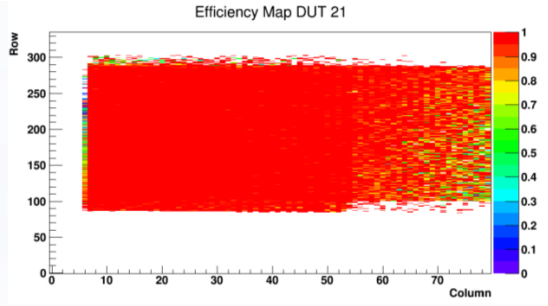

(b)

Figure 7.11: Comparison of the hit efficiency maps of active edge and slim edge modules. (a) Active edge design of 150 μm thickness with GR edge structure. (b) Slim Edge design of 100 μm thickness with BR and punch-through edge design. The modules were measured at a beam test at CERN-SpS.

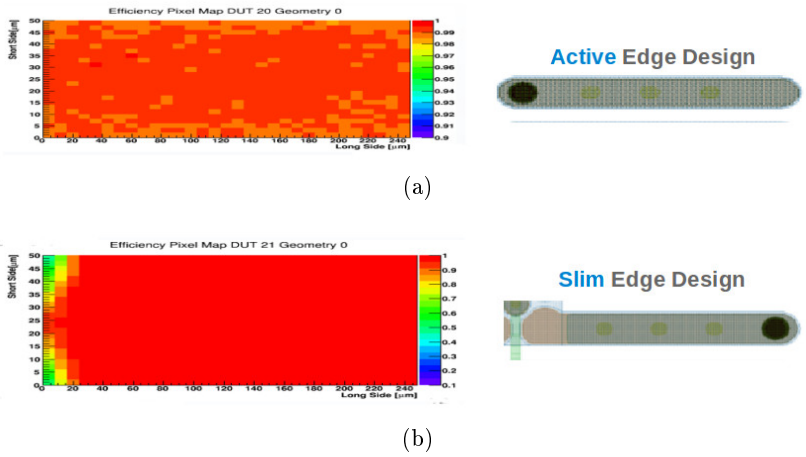

Figure 7.12: Comparison of the in-pixel hit efficiency maps of active edge and slim edge modules with a projection of the pixel cell in each design. Pixel cell size in both designs is 50×250 μm^2. (a) Active edge design of 150 μm thickness with GR edge structure. (b) Slim Edge design of 100 μm thickness with BR and punch-through edge design. The modules were measured at a beam test at CERN-SpS.

Due to the limited beam size and the high statistics required in this analysis, for each measurement the beam was centred on only one of the two edge pixel columns. The edge efficiency of the active edge module was measured before irradiation at CERN-SpS with consistent results. Despite the low statistics of events collected at the border of the sensor , this edge design was demonstrated to be sensitive up to the activated edge showing an average hit efficiency of 90% in the last 30 μm after the end of the last pixel implant. The edge efficiency as a function of the distance from the last pixel coloumn to the edge region is shown in Figure 7.14. This result shows that the edge region is efficient to higher than 97% up to 20 μm from last pixel.

Recent results, see ref. [132], showed that compared to the active edge design, the slim edge design shows an active region only up to the BR, which is 25 μm away from the last pixel implant.

A study of the performance of the two module after irradiation could not be included in this thesis due to lack of time that is needed to irradiate the modules and measure them in the testbeam.

7.4.0.4 Systematic uncertainty

An absolute systematic uncertainty of 0.3%, as estimated in ref [132], is associated to all hit efficiency measurements. Due to high statistics usually collected at beam tests, this systematic uncertainty is dominant.

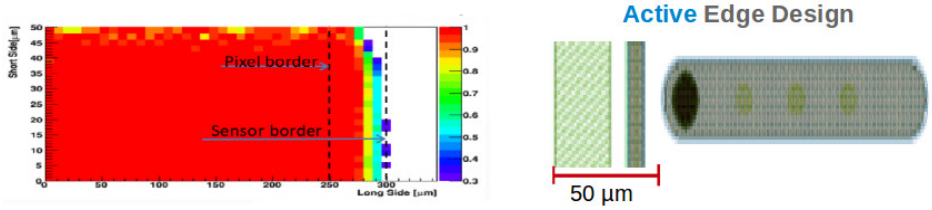

Figure 7.13: In-pixel hit efficiency map (left) at the edge of 150 μm thick sensor with 50 μm active edge module with a projection of the pixel cell (right). Pixel cell size is 50×250 μm^2. The module was measured at a beam test at CERN-SpS.

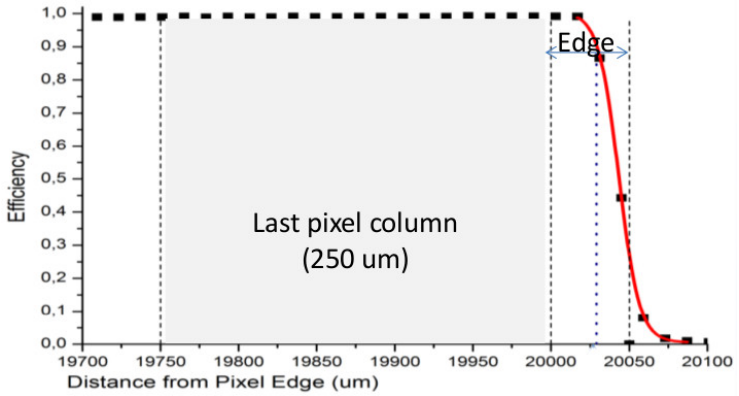

Figure 7.14: Hit efficiency at the edge of the 150 μm thick active edge module with the 50 μm edge distance. The module was measured at CERN-SpS. The pixel cell has an FE-I4 cell size of 50×250 μm^2 and the hit efficiency is evaluated as a function of the distance from the last pixel column to the edge region.

The systematic uncertainty is arising from three sources:

- The trajectory reconstruction,

- The subsequent DUT analysis,

- The fluctuations on the resulting efficiencies during the measurement time.

During track reconstruction, different track parameters can be used to reconstruct the tracks of different measurement set-ups. For the estimation of the uncertainties arising from the offline trajectory reconstruction, the resulting efficiencies should be compared for different values of the finder radius and χ^2. Using the finder radius, a track in the last track reconstruction step is reconstructed via a cone, that searches for hit points on every plane from a starting track candidate on the first hit plane of the telescope (plane 0). All hit points in the search area of the finder radius are included in the reconstruction analysis. It is found that the track parameters deviated by maximum 30% from the nominal values given by the EUTelescope software[132]. With this deviation, an efficiency variation of 0.06% is observed. No fluctuations in efficiency are observed for different χ^2 settings.

In a similar measurement, according to [132], an additional fluctuation in efficiency of 0.04% is observed during a running time of above 2 hours.

In the subsequent DUT analysis, efficiency fluctuations up to 0.5% are obtained [132] for track-hit matching values from 0.5 to 2 times the pixel cell size. To minimize the systematic uncertainty, the value of the track-hit matching in the DUT analysis is set to 1.5 times the pixel cell size of the device in each direction and not changed for different measurement set-ups. The total systematic uncertainty on all obtained hit efficiency values is calculated to be 0.3%. This value is well in agreement with previous estimations [133].

Chapter 8

Conclusion and Outlook I

The HL-LHC represent a powerful upgrade of the cern accelerator complex to explore the new high-energy physics frontiers. The ATLAS Inner Tracker (ITk) will replace the current ATLAS Inner Detector at the HL-LHC. The ITk will improve tracking performance compared to current ATLAS Inner Detector. In the first part of this thesis, I have shown my contribution to different R&D activities aiming to develop a new efficient active and slim edge planar pixel detectors for the ITk upgrade.

A novel planar module concept was presented to face the challenges imposed by the high luminosity upgrade of the LHC. This is based on n-in-p planar sensors relying on innovative aspects: thin sensors to ensure radiation hardness, active edges to maximize the sensitive area of the sensor. An extensive electrical characterization of the active edge sensors was performed with the aim of optimizing the fabrication process and identifying the best designs to fulfil the requirement of the ATLAS pixel detector at HL-LHC. Two essential measurement, IV- and CV- measurement, were performed to test a total of seventy active edge structure and to investigate the leakage current, breakdown and depletion voltage for the Advacam production. The yield production was found to be 90%. Different design variations have been studied, comparing structure with respect to their thickness, edge design and UBMs used. This study has shown that the sensor design with 100 μm thickness with at least one GR design is the most stable design among the various design variations. It was observed that the NiAu UBM designs present a higher breakdown voltages compared to Pt UBM designs.

Two innovative scanning methods, 3D-SIMS and TLM, for silicon pixel detector doping profile analysis were presented. The new 3D-SIMS imaging technique was developed to study the total doping profile at the pixel level inside the complex structure of the Advacam active edge detectors. By the high lateral resolution provided by this technique, it becomes possible to analyse small region of interest like the pixel cell and the active edge region. Using the 3D-SIMS technique, three different implanted regions have been analysed: center pixel region, active edge region, inter-pixel (p-spray) region and backside implant. Doping maps of these regions have been shown and 1D doping profile has been extracted. Moreover, doping profiles were simulated and a good agreement with measured doping profile

using SIMS Imaging is observed.

To investigate the radiation hardness of active edge sensors, a TCAD structure simulation was created using the exact doping concentrations from SIMS measurement. The simulation used to study the radiation damage effect based on three level traps model, the new Perugia model. By introducing traps inside the bulk region, the effect of the radiation damage on the leakage current and the breakdown voltage have been simulated. The breakdown voltage has been predicted to be increased about 50% for radiation dose of 2×10^{16} n_{eq}/cm^2. The simulated IV-curves for irradiated and non-irradiated sensors have been validated by comparing to data. Measured IV-curves are found to be compatible with those from simulation.

A novel TLM method was used to study the variation of active dopant concentration before and after irradiation. Preliminary results show that the concentration of active dopant are modified by irradiation. A loss of the active carriers after irradiation has been observed. This study of irradiation damage with TLM method provides important information on the electrically active dopant distribution and concentration, which determine the properties of semiconductor devices and can be useful to tune the irradiation models to predict the behaviour of silicon pixel detector after irradiation. These results were presented in the "12th Trento Workshop on Advanced Silicon Radiation Detector" in Itlay last year. The contribution was greatly appreciated by the conference committee that I am honored to have been chosen for the **Best Poster Award**.

The efficiency for the Advacam active edge detectors was investigated in testbeam. Results from CERN-SpS testbeam for two different edge design (Active and Slim) have been shown. Two modules have been studied. An active edge module with thickness 150 μm and 50 μm distance between the last pixel implant and the sensor edge and a slim edge module with 100 μm and 100 μm distance between the last pixel implant and the sensor edge. The active edge design achieved a global efficiency of 98.645±0.005% while the global efficiency reached 98.558±0.004% in the slim edge design, with an absolute systematic uncertainty of 0.3% is associated to all hit efficiency measurements. Uniform in-pixel efficiency has been observed in the active edge module. While, an efficiency loss at the edge of the pixel cell in the slim edge module has been found. The edge region in the active edge module is efficient to higher than 97% up to 20 μm from the last pixel column. These two sensors have been irradiated after I finished the work on the first part of the thesis and unfortunately the results after irradiation could not be included in the thesis.

During the last three years, I am grateful to have had the opportunity to attend and share my research, my work and and the different achievements I have accomplished, in many to national meetings (e.g. PHENIICS Ecole Doctoral Fest, the Physics ATLAS France (PAF) meeting and Journée de Rencontre des Jeunes Chercheurs (JRJC) meeting) and many other international conferences, on the top

of that the Trento conference, IEEE Conference and the Europeon School in High Energy Physics.

A paper including the results from the SIMS study and radiation damage modelling is published in 2016 IEEE (NSS/MIC/RTSD) conference proceeding, it can be found in ref.[134]. It has also been submitted to be published in NIM journal and the correction from reviewers is in process to be implemented and resubmitted again. A second publication including the results from the TLM method is planned soon.

Part II

Search for the Higgs boson in the $b\bar{b}$ decay channel with the ATLAS experiment

Chapter 9

Standard Model Higgs observation in ATLAS

Contents

9.1 The Standard Model of Particle Physics 167
9.1.1 Elementary particles in SM 168
9.1.2 Interaction and force carriers of SM 170
9.2 Spontaneous symmetry breaking and electroweak theory . 171
9.2.1 The BEH mechanism 172
9.3 Higgs boson production and decay predictions at the LHC 175
9.3.1 Higgs production mechanisms 175
9.3.2 Higgs boson decay 178
9.3.3 VH$\rightarrow b\bar{b}$ Channel 181
9.4 LHC Higgs results 185

In this chapter, I give a brief overview of the Standard Model (SM) of particle physics and the Higgs mechanism, following a short discussion of the SM Higgs boson phenomenology by discussing its main modes of production and decay. Particular emphasis is given to the VH associated production mode and the H$\rightarrow b\bar{b}$ decay channel, which is the subject of this research work.

9.1 The Standard Model of Particle Physics

During the twentieth century, major achievements in theoretical and experimental physics led to the development of Quantum Field Theories describing the Electromagnetic, Weak and Strong interactions. Together with Gravity, these are the forces governing all known fundamental particles. The unification of quantum electrodynamics (QED) and weak theory, by Glashow, Salam and Weinberg [135] [136] [137], laid the theoretical ground for the formulation of quantum chromodynamics (QCD) [138] [139] [140] [141]. The resulting SM of Particle Physics (SM), combining three of the four fundamental forces in nature, is a mathematical framework which has

provided numerous predictions confirmed by experimental observations. This model has proven to be extremely successful in describing experimental data over many decades. The Higgs boson is the most recent elementary particle discovered. It was predicted by the SM [142] in the '60 and discovered at CERN in 2012 [143] [144].

The SM describes three of the four fundamental forces of nature: electromagnetism, weak and the strong interactions. The behaviour of particles is described by the unification of quantum mechanics and special relativity in a theory called quantum field theory [145]. A theory of quantized fields relies on symmetry principles to consistently describe interactions. In other words, the invariance of the dynamical properties of a system under a continuous symmetry transformation translates into the conservation of a physical property, as stated by Noether's theorem [146]. The principle of energy conservation, for example, is in this way incorporated through the time translation symmetry.

Gauge theories are described by a Lagrangian that remains invariant under a continuous group of local [1] transformations. Different mathematical configurations of the fields will therefore result in equivalent observable physical states. A theory with predictive power must fulfil this requirement.

The SM is a gauge quantum field theory which is invariant under transformations governed by the $SU(3)_C \times SU(2)_L \times U(1)_Y$ groups. Here C refers to the colour charge , L refers to left-handed fields, and the U(1) charge is the hypercharge Y. This gauge symmetry include the symmetry group of strong interaction $SU(3)_C$ which is associated to the QCD sector of the Lagrangian and describes the interactions between colour-charged particles (quarks and gluons). The gauge group of electroweak interaction, the $SU(2)_L \times U(1)_Y$ symmetry, corresponds to the electroweak sector, with the weak isospin T_3 and weak hypercharge Y for the corresponding generators. This sector incorporates the interaction of the photon with electrically charged particles, as well as the $W^{\pm}$ weak couplings to left-handed particles and Z^0 couplings to right and left-handed particles. The gauge symmetry of the electromagnetic interaction $U(1)_{em}$ appears in the SM as a subgroup of $SU(2)_L \times U(1)_Y$.

9.1.1 Elementary particles in SM

The SM postulates that elementary particles are divided into two groups: gauge bosons and fermions, listed in Table 9.1, Table 9.2 and Table9.3, respectively. **Fermions** are the fundamental constituents of the matter. They have spin-1/2. They obey to the Fermi-Dirac statistics. An anti-particle is associated with each fermion, with the same mass and statistic rules, but opposite electric charge. Fermions are divided into two categories: leptons and quarks.

[1] Local transformations are dependent on the space-time coordinates of the system.

Boson	Interaction	Electric Charge (Q)	Mass (GeV)
gluon (g)	strong	0	0
photon (γ)	electromagnetic	0	0
$W^{\pm}$	weak	± 1	80.385 ± 0.015
Z^0	weak	0	91.1876 ± 0.0021

Table 9.1: Gauge bosons in the Standard Model. [148]

There are three families (generation) of **leptons** formed by three charged leptons (the electron (e), the muon (μ) and the tau (τ) leptons) and the associated neutral leptons, the neutrinos ($\nu_e, \nu_\mu$and ν_τ), as shown in Figure 9.1. The electron, muon and tau have the same electric charge but an increasing mass while neutrinos are electrically neutral and have a very small mass.

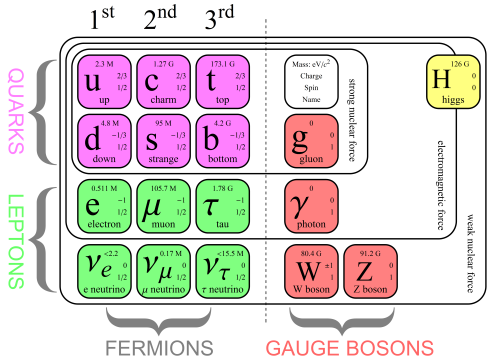

Figure 9.1: The Standard Model of particle physics, with quarks (purple), leptons (green), gauge bosons (red), and Higgs boson (yellow). The first, second, and third columns show the three generations of fermions, the fourth, fifth columns show the vector bosons, and the sixth columns shows the Higgs boson. The gluon is the vector boson of strong nuclear force, the photon is the vector boson of electromagnetism, and the Z and $W^{\pm}$ are the vector bosons of weak interaction. The Higgs boson is linked to the electroweak symmetry breaking. The mass, charge, spin and name of each particle is given in the Figure [147].

In a similar way to the leptons, **quarks** consists of a group of six particles related in pair (doublet), see Figure 9.1. The first generation of the quarks is composed of quark up and down, the second of charmed and strange quarks, and the third of bottom (or beauty) and top quarks. Quarks interact by strong nuclear force, and come in three different colours. They only mix together to form colourless objects. Quarks can not exist in a free state. They are confined to exist as a doublet (quark-antiquark pair forming a **meson**) or as a triplet (three quarks forming a **baryon**, which includes the neutrons and protons of ordinary matter). The bound state of quarks and anti-quarks, held together by the strong force, as mesons and baryons, belonging to a broader group called **Hadrons**. Therefore, hadrons are not elementary particles.

Looking in details at Figure 9.1, the two lightest and more stables particles belong

Leptons	Particle	Electric Charge (Q)	Mass (GeV)
1^{st} Generation	ν_e	0	$< 10^{-9}$
	e	-1	0.5×10^{-3}
2^{nd} Generation	ν_μ	0	$< 10^{-9}$
	μ	-1	106×10^{-3}
3^{rd} Generation	ν_τ	0	$< 10^{-9}$
	τ	-1	1.78

Table 9.2: The Standard Model leptons and corresponding electric charge and mass. The antiparticles are implicit, with opposite sign electric charges. Neutrino masses are larger than zero for at least two generations. [14]

Quarks	Particle	Electric Charge (Q)	Mass (GeV)
1^{st} Generation	u	+2/3	2×10^{-3}
	d	-1/3	5×10^{-3}
2^{nd} Generation	c	+2/3	1.28
	s	-1/3	95×10^{-3}
3^{rd} Generation	t	+2/3	173.3
	b	-1/3	4.18

Table 9.3: The Standard Model quarks and corresponding electric charge and mass. The antiparticles are implicit, with opposite sign electric charges.[14]

to the first generation, and the heaviest and short-lived particles belong to the second and third generations. The matter in the universe is made from particles of the first generation, while heaviest particles decay in the next more stable generations.

9.1.2 Interaction and force carriers of SM

There are four types of forces in nature: electromagnetic force, weak force, strong force and gravitational force. They work over different ranges and have different strengths. Gravity is the weakest but it has an infinite range. The electromagnetic force also has infinite range but it is many times stronger than gravity. The weak and strong forces are effective only over a very short range and dominate only at the level of subatomic particles. Despite its name, the weak force is much stronger than gravity but it is indeed the weakest of the other three. The strong force, as the name suggests, is the strongest of all four fundamental interactions.

The SM describes three of the four fundamental forces which result from an exchanged of force-carrier particles. These particles are of integer spin bosons, and are also known as **vector bosons**. These bosons exchanged can be seen as discrete amounts of energy transfers. The gauge bosons, responsible for mediating the interactions, are a consequence of the gauge invariance built into the model. Bosons obeys the Bose-Einstein statistics. Through an interaction, a boson is emitted by a

matter particle and then absorbed by another particle. Feynman diagrams (see example Figure 9.2) can be used to visualize these interactions. In these diagrams, the external lines are the real particles and at each vertex, the energy and momentum are conserved, and there is a coupling "g" which characterizes the different types of forces.

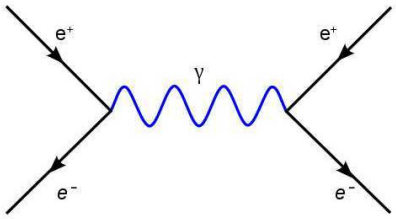

Figure 9.2: Feynman diagram example: Annihilation of an electron and a positron creating a photon which decays into a new electron positron pair.

Each fundamental force has its own corresponding boson. The **electromagnetic force** is carried by photons, the **weak interaction** is carried by Z and $W^{\pm}$ bosons, and the **strong interaction** is carried by gluons. The vector bosons are represented in Figure 9.1. The interactions described by the SM work over different ranges and have different strengths, they are shown in Table 9.4. The weak and strong forces are effective only over a very short range (the size of a proton) and dominate only at the level of subatomic particles. Despite its name, the weak force is much stronger than gravity but it is indeed the weakest of the other three. The strong force is, as the name implies, the strongest among all the four fundamental interactions. The electromagnetic and gravity forces have an infinite range but the electromagnetic force is many times stronger than gravity.

Interaction	Electromagnetic	Strong	Weak
Boson	Photon γ	Gluons g	$W^{\pm}, Z^0$
Mass [MeV]	(0)	(0)	(80-90 $\times 10^3$)
Intensity wrt strong	10^{-2}	1	10^{-13}
Range [m]	∞	$\approx 10^{-15}$	$\approx 10^{-15}$

Table 9.4: Interaction and force carriers of the Standard Model. Relative intensity with respect to the strong interaction is given at low energy.

9.2 Spontaneous symmetry breaking and electroweak theory

The introduction of gauge local transformations in the electroweak theory brings up new interaction mediator particles such as the photon and the two vector bosons, W

and Z, without giving them masses (consequence of Yang-Mills theory)[149]. However, the experimental observations have shown that the W and Z bosons have non zero mass, since the interaction has a limited range. The solutions of this issue was found by introducing the mechanism of "spontaneous symmetry breaking" (SSB) [150] [151]. The physicist and theoretician Peter Higgs has introduced (with Brout and Englert)[152] this mechanism to explain first specific phenomena in condensed matter physics, then it has been extended to build a renormalizable field theory of electro-weak interactions in a renormalizable Yang-Mills theory with massive bosons.

9.2.1 The BEH mechanism

An unbroken gauge symmetry $SU(3)_C \times SU(2)_L \times U(1)_Y$ would imply that gauge bosons are all massless, while a non-zero mass of W and Z bosons have been measured. The problem is fixed by introducing a single $SU(2)_L$ doublet scalar field Φ , causing the spontaneous breaking of $SU(2)_L \times U(1)_Y$ gauge symmetry via the **Higgs mechanism**.

$$\Phi = \begin{pmatrix} \Phi^+ \\ \Phi^0 \end{pmatrix} \tag{9.1}$$

Where Φ^+ and Φ^0 correspond to a charged and a neutral complex scalar field. The new term in the Lagrangian involving Φ is then given by:

$$\mathcal{L}_{Higgs} = |\mathcal{D}_\mu \Phi|^2 - V(\Phi) \tag{9.2}$$

Where the first term contains the kinetic and gauge-interaction terms, and the second term is the potential energy function. The gauge invariant potential V is given by:

$$V(\Phi) = -\mu^2 \Phi^\dagger \Phi + \lambda (\Phi^\dagger \Phi)^2 \tag{9.3}$$

Where μ and λ are free parameters. The Higgs term in the Lagrangian can then be expressed as:

$$\mathcal{L}_{Higgs} = |\mathcal{D}_\mu \Phi|^2 + \mu^2 \Phi^\dagger \Phi - \lambda (\Phi^\dagger \Phi)^2 \tag{9.4}$$

- If $\lambda < 0$, then V is unbounded and there is no stable vacuum state.

- If $-\mu^2$ and λ are both positives, the potential energy function has a minimum at $\Phi = 0$. In this case the symmetry is unbroken in the vacuum (Figure 9.3 on the left).

- If $-\mu^2$ is negative and λ is positive, the minimum is not 0 and the vacuum or minimum energy state is not invariant under $SU(2)_L \times U(1)_Y$ transformation: the gauge symmetry is spontaneously broken in the vacuum (Figure 9.3 on the right).

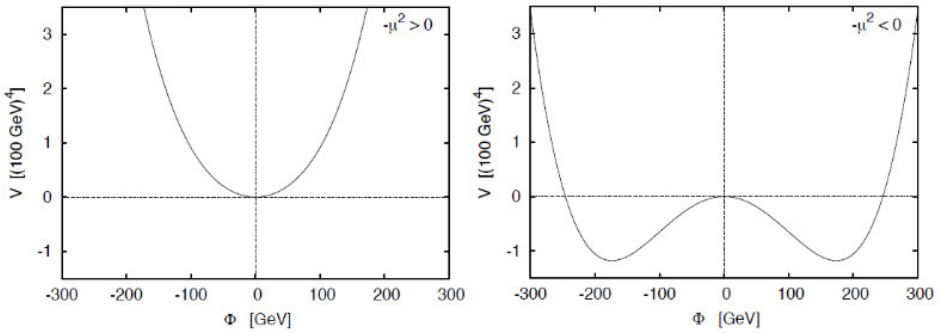

Figure 9.3: Shape of the Higgs potential for negative (a) and positive μ^2(b) [153].

The vacuum expectation value (VEV) is invariant by $SU(2)_L$ transformation, if Φ is excited it can be written as:

$$\Phi = \frac{1}{\sqrt{2}} \begin{pmatrix} 0 \\ \nu + h \end{pmatrix} \tag{9.5}$$

We can then examine the gauge-kinetic term acting on Φ:

$$\mathcal{D}_\mu = \partial_\mu - i\frac{g'}{2}B_\mu - i\frac{g}{2}W_\mu^a\sigma^a \tag{9.6}$$

Where g and g' are respectively the coupling constants of $SU(2)_L$ and $U(1)_Y$ interactions, W_μ^a, a = 1,2,3 correspond to the three gauge fields of the group $SU(2)_L$, B_μ to the gauge field of U(1), and σ^a to the Pauli matrices. Then it follows:

$$\mathcal{D}_\mu\Phi = \frac{1}{2} \begin{pmatrix} -\frac{i}{2}g(W_\mu^1 - iW_\mu^2)(\nu + h) \\ \partial_\mu h + \frac{i}{2}g'(W_\mu^3 - g'B_\mu)(\nu + h) \end{pmatrix} \tag{9.7}$$

by introducing the combinations corresponding to the charged W bosons,

$$W_\mu^\pm = (W_\mu^1 \pm iW_\mu^2)/\sqrt{2} \tag{9.8}$$

One can define the mass term of the W as:

$$M_W = \frac{g\nu}{2} \tag{9.9}$$

Since M_W have been directly measured as M_W= 80.370 ±0.019 [154], and g can be computed from the Fermi constant $\frac{G_F}{(\hbar c)^3} = \frac{\sqrt{2}}{8}\frac{\sqrt{g^2}}{m_W^2} = 1.1663787(6) \times 10^{-5} GeV^{-2}$ [155], one can determine that $\nu \approx$ 246 GeV. The field A_μ does not couple to the Higgs field, and thus does not acquire a mass through the Higgs mechanism. This state is then identified as the photon.

$$A_\mu = sin\theta_W W_\mu^3 + cos\theta_W B_\mu \tag{9.10}$$

The field Z_μ couples to the Higgs fields and thus receives a mass from the Higgs field and is identified to the Z boson:

$$Z_\mu = cos\theta_W W_\mu^3 + sin\theta_W B_\mu \tag{9.11}$$

with:

$$cos\theta_W = \frac{m_W}{m_Z} = \frac{g'}{\sqrt{g^2 + g'^2}} \tag{9.12}$$

$$sin\theta_W = \frac{g}{\sqrt{g^2 + g'^2}} \tag{9.13}$$

The mass of the Z boson is then defined as:

$$m_Z = \frac{\nu}{2}\sqrt{g^2 + g'^2} \tag{9.14}$$

The Higgs couples to himself and his mass is defined as:

$$m_h^2 = 2\mu^2 = 2\lambda\nu^2 \tag{9.15}$$

Finally, in order to generate masses for fermions, a additional terms is added to the Lagrangian to couple fermions to the scalar Higgs field. It is the so-called Yukawa coupling. The Yukawa Lagrangian in the SM electroweak Lagrangian is:

$$\mathcal{L}_Y = -\lambda_Y^f(\overline{\psi_L}\psi_R + \overline{\psi_R}\psi_L) \tag{9.16}$$

with λ_Y^f the Yukawa coupling of the fermion f. The couplings constant between the fields are, however, arbitrary, in contrast to what happens for the gauge bosons,

and therefore the model can't predict fermion masses. Nonetheless, as in the gauge boson case, the couplings to the fermions are still proportional to their masses, which allows for these predictions to be tested experimentally. The coupling between the fermion and the Higgs field yields fermion mass m_f :

$$m_f \approx \lambda_Y^f \nu \tag{9.17}$$

9.3 Higgs boson production and decay predictions at the LHC

The existence of a Higgs field, discussed in the previous section, can be proved by the detection of its carrier, the Higgs boson. The search for the Higgs boson was one of the main motivations for the construction of the LHC and was also a key component of the physics programs at other colliders, such as LEP and the Tevatron. At a proton-proton collider, the Higgs boson can be produced through four different production mechanisms. Moreover, the Higgs boson has no appreciable lifetime, and decays immediately into final state fermions or bosons. In this section, I discuss the different production and decay modes of of the Higgs boson in the context of a proton-proton hadronic collider such as the LHC.

9.3.1 Higgs production mechanisms

At the LHC, proton collisions allow for a large variety of interactions. Indeed, through the sea (with quarks and gluons) of the proton, important at this energy, one can consider virtually all type of quarks and gluon as initial states of processes. Therefore, several processes leading to the creation of a Higgs boson are accessible. Figure 9.4 presents the Higgs boson cross section (as a function of its mass) of the main production processes for protons colliding at a center of mass energy of $\sqrt{s}$= 14 TeV.

The SM Higgs boson can be produced in several ways. Four production processes are considered to give a measurable contribution to the total cross-section. The main production mechanisms are the gluon fusion (ggH) which is the dominant production mode, the vector boson fusion (VBF), the associated production with a gauge boson (WH and ZH) and the associated production with top quarks (ttH). The corresponding Feynman diagrams are shown in Figure 9.5. These processes differ by the partons required in the initial state but also of the particle content present in the final state along with the Higgs boson. It is then possible to infer the process which produced a Higgs boson by the study of the rest of the event.

Gluon fusion production mode (ggF): The dominant production mode for the SM Higgs boson at the LHC is the fusion of gluons (ggH). Gluons are masseless

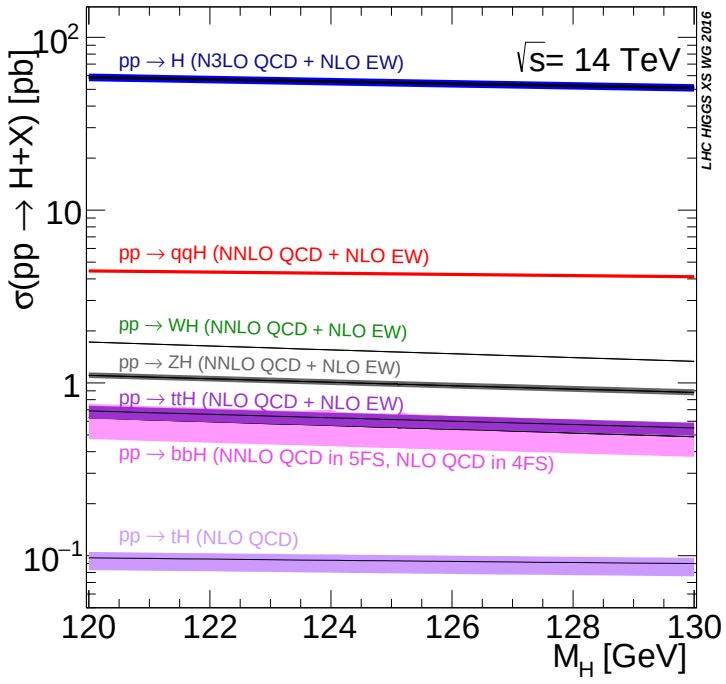

Figure 9.4: Inclusive Higgs boson production cross-section as a function of its mass at $\sqrt{s}$= 14 TeV at the LHC. [156]

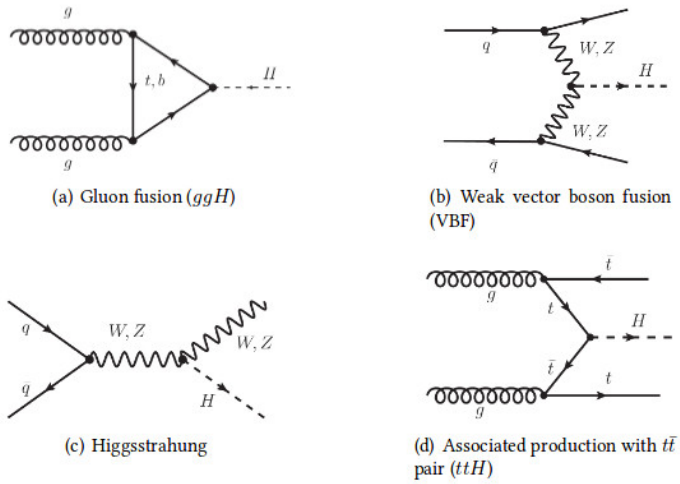

Figure 9.5: SM Higgs boson leading order production processes at the LHC.[157]

particels, so they do not couple directly to the Higgs boson, hence at the lowest order the production is mediated by heavy quark loop, as illustrated in Figure 9.5. From the first glance on the final state of this process, it seems to us that this can provide and easy and clear environment to search the Higgs boson, since no other particle appears at the final state along with the Higgs boson in this production mode, but this dominant production mechanism that have the largest cross section suffers from various overwhelming QCD background that affect the signal over background ratio.

Vector boson fusion (VBF): The second most important production mode is the vector boson fusion (VBF) which is initiated by quarks radiating weak bosons which fuse into a Higgs boson. This process has a cross section which is about 10 times smaller than the one of the ggF. This production mode accounts for about 10% of the total cross-section. It is particularly interesting as it probes the coupling of the Higgs boson to the gauge bosons. Furthermore, this production process can be differentiated from the main ggH production by the two quarks in the final state which will create two forward jets. Tagging those jets is the core concept of VBF coupling measurement.

Associated production to a vector boson (VH): This production mode also probes the coupling of the Higgs boson with electroweak bosons : WH and ZH, also called Higgs-strahlung, both result from a production of a weak boson which will radiate a Higgs boson. The weak boson which remains in the final state can also be tagged. The cross section of this process is approximately 3 times less than the VBF, this production mode provides a relatively clean environment to study the dominant Higgs boson decay to a pair of bottom quark.

Associated production to a a pair of top quarks (ttH): Finally, the Higgs boson can be produced by the interaction of a pair of top quarks. This production process mode has a cross-section that is almost two order of magnitude smaller than the direct production (ggH). An important feature of this mechanism is that it gives informations about the Higgs Yukawa coupling to fermions and can provide access to the Higgs decay into bottom quarks.

The production cross section of the SM Higgs boson depends on the centre of mass energy $\sqrt{s}$. The production cross section as a function of $\sqrt{s}$ is shown in Figure 9.6. It is clear that with the increase of the energy of the LHC in 2015 up to 13 TeV in Run-2, the production cross-sections of Higgs boson production processes increase. Compared to Run-1, the production cross section is increased by a factor $\approx$ 2-4 for the different processes. Therefore, this increase of energy plays a major role in the improvement of measurement of the Higgs boson properties.

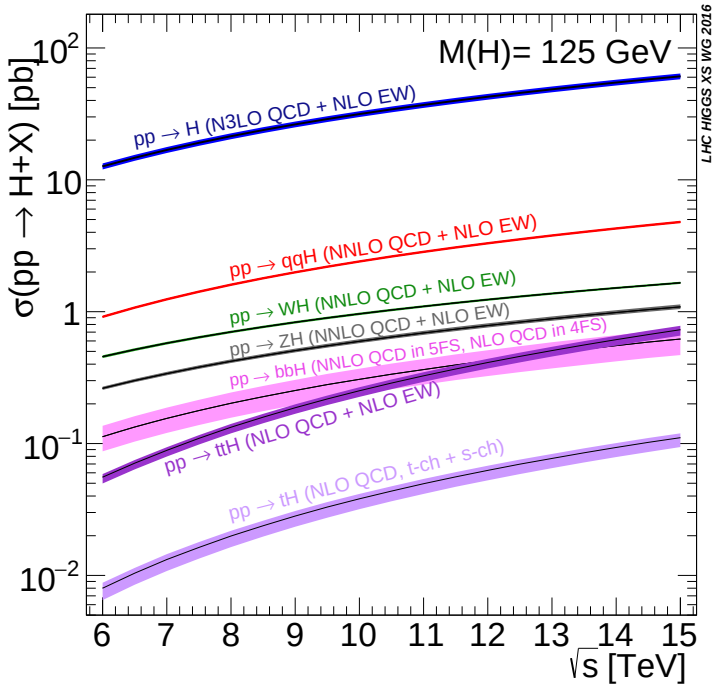

Figure 9.6: SM Higgs boson production cross section as a function of the center-of-mass energy $\sqrt{s}$ at $m_H = 125$ GeV. [156]

9.3.2 Higgs boson decay

The experimental confirmation of the Brout-Englert-Higgs mechanism, and more generally the investigation of the electroweak symmetry breaking origin, was one of the main goals of the physics program at the Large Hadron Collider (LHC) at CERN. With the discovery of a new particle with a mass of 125 GeV by the ATLAS [158] and CMS [159] collaborations, this goal was achieved. This particle has been observed to decay into a pair of bosons,$\gamma\gamma$, ZZ and WW , and further studies confirmed the observed particle's properties are consistent with the SM predictions for a Higgs boson with mass $m_H = 125$ GeV. The decay into bosons includes two, three and four body bosonic decays, photons pair decay, gluons pair decay or Zγ associated decay. Decays to fermions can be divided in leptonic decay modes ($\tau^+\tau^-, \mu^+\mu^-$and e^+e^- pairs) and hadronic decay modes (mainly $b\bar{b}$ and $c\bar{c}$).

The branching ratio to any single decay mode is defined as the ratio of the partial width to the total width, where the total width is the sum of all possible partial widths.

The SM Higgs boson branching ratios for the different decay modes as a function of the Higgs mass is shown in Figure 9.7. This Figure shows that the observation of the Higgs particle at $m_H = 125$ GeV gives access to many possible decay modes

to search compared to higher masses. Moreover, for the Higgs boson with mass 125 GeV, the dominant branching fraction is to bottom quarks pairs at $\approx 58\%$, covering more than half of the Higgs decay width. This thesis focuses indeed on this specific decay mode, hence more details are given later.

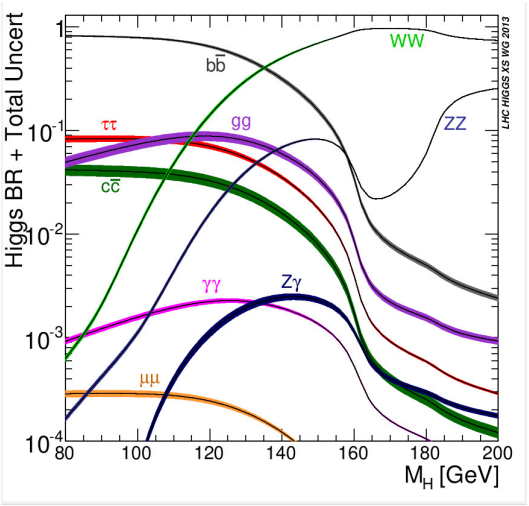

Figure 9.7: Standard Model Higgs boson branching ratio as a function of its mass. The theoretical uncertainties in the branching ratios include the higher order corrections on the theoretical calculations and also the errors in the SM input parameters in particular gauge couplings and fermions masses. [156]

9.3.2.1 Bosonic decay modes

The discovery channel of the Higgs boson, the H$\rightarrow \gamma\gamma$ channel, has peculiar characteristics. It suffers from a very low branching ratio ($\approx 2 \times 10^{-3}$) which makes it rare. However the final state, two isolated photons, can be efficiently detected by an electromagnetic calorimeter. Given that the background has a monotonous shape, the Higgs signal can be observed above the background. This particular decay is described by the diagrams in Figure 9.8. Even at the leading order, it consists in a loop of t and b quarks and of W boson. This allows to probe the couplings to these particles and brings additional complementary information to other dedicated channels. Finally, since the decay is done through a loop, this process is sensitive to the contribution of heavy BSM particles inside the loop so contributes to indirect BSM searches. A similar process, with even lower branching fraction, is the H$\rightarrow Z\gamma$ production.

The decay of the Higgs boson into a pair of weak bosons has a large branching ratio. However, the bosons will themselves decay into various stable particles. The most promising channel in term of identification is a decay into a pair of Z bosons which themselves decay into a pair of leptons. This channel is extremely rare due to

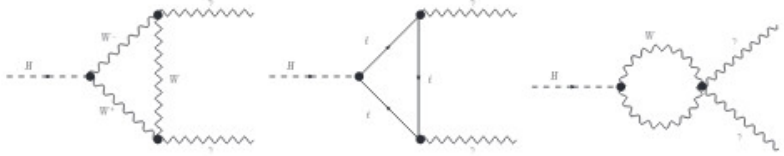

Figure 9.8: Leading order Feynman diagrams of SM Higgs boson decay to a photon pair. [157]

the leptonic branching ratio of the Z boson but this is compensated by a low level of background. The decay into a W boson pair have the second largest branching ratio after the $b\bar{b}$ decay. This decay channel is studied at the LHC considering all Higgs production modes, and presents different challenges: the hadronic W decay channels show similar issues to the $b\bar{b}$ case, with large hadronic activity in the detector, while for the leptonic W decay channels we have to treat the presence of neutrinos in the final state. This channel contributed to the discovery of the Higgs boson and remains a leading one for measurement of its properties.

The decay to gluon pairs takes the third largest branching fraction but it's not distinguishable from the SM background, and it's not studied at the LHC. The experimental signature of these decays is only a pair of jets, which is widely produced in an hadronic collider. However, the diagram of the gluon decay is the same as the gluon fusion production process but inverted.

9.3.2.2 The fermionic decay channels

Besides the bosonic decay modes, the SM predicts that the Higgs boson decays to fermions as well. Moreover, the mass generation mechanism for fermions, as implemented in the SM, can only be established by measuring the direct coupling of the Higgs boson to fermions. The fermionic decays with the highest branching ratios are decays to a pair of b-quarks, H$\rightarrow b\bar{b}$ and to a pair of τ leptons, H$\rightarrow \tau\tau$, since the Yukawa couplings of the Higgs boson to fermions are proportional to fermions' masses.

At 125 GeV, the leading decay channel is $b\bar{b}$. This channel is a priori the most promising as the leading one with about 58% of branching fraction. However, the search for H$\rightarrow b\bar{b}$ decays is challenging due to the fact that its final signature is a pair of jets which suffers a high irreducible QCD background in an hadronic collider, even when identifying b jets. More details is coming later.

The $\tau\tau$ decay channel is first observation of the Higgs field coupling to leptons at the hadron colliders, since, for a Higgs boson of $m_H \approx 125$ GeV, the branching fraction to $\tau^+\tau^-$ is $\approx 6\%$, the fourth after the gluon pair decay. However, the presence of a very large background for this channel make its rate really small

and their detections a challenging search. The main difficulties come from the reconstruction of a final state with undetectable neutrinos from the τ lepton decays, and the discrimination between hadronically decaying τ leptons and light-quark jets. The ATLAS experiment reported that the Higgs boson decay to a pair of τ leptons has been observed with observed (expected) significance of 4.5 σ (3.4 σ) [160]. The combination of the results from ATLAS and CMS yields an observed (expected) significance of 5.5 σ (5.0 σ) [161].

The charm quarks pair production has a very low branching ratio and overwhelming background contributions from QCD SM processes (dominated by gluon-splitting g$c\bar{c}$ production), with the additional experimental challenge of tagging hadronic jets from charm quarks. For these reasons this channel is very challenging to be exploited at the LHC. The Standard Model (SM) Higgs boson is expected to decay to a charm quark pair in around 3% of cases. While this number seems small, the success of the LHC Higgs boson measurement programme is such that this contribution represents one of the largest expected contributions to the total Higgs boson decay width for which we have no experimental evidence. Furthermore, all experimental evidence for Yukawa couplings is limited to the third generation fermions and the smallness of the SM charm quark Yukawa coupling makes it particularly sensitive to modifications from potential physics beyond the SM. Recently, a novel charm jet tagging algorithm commissioned by the ATLAS experiment to perform the first direct search for Higgs boson decays to charm quark pairs with the ATLAS experiment, see ref. [162] which helped to set an upper limit on the production cross section of the Higgs decaying into pair of charm quarks in association with Z bosons.

Finally the $\mu\mu$ decay channel presents a very clean experimental signature: a dimuon pair with invariant mass peaking at m_H. The extremely suppressed branching fraction makes it a challenging channel for Higgs boson searches, but it's a prime candidate to probe the nature of the Higgs boson couplings with leptons of the second family. Only upper limits exist on its coupling to muons [163] [164].

9.3.3 VH$\rightarrow b\bar{b}$ Channel

The research work documented in this thesis focuses on the search for a SM Higgs boson with a mass of 125 GeV, produced in association with a vector boson V ($W^{\pm}$ and Z) and decaying into a pair of $b\bar{b}$ quarks with more details comes later in Chapter 10.

As described in section 9.3.2, the $b\bar{b}$ decay channel is particularly appealing since it allows us to consider more than half of the Higgs total width, with a branching ratio of BR(H$\rightarrow b\bar{b}$) = 0.5809. In addition, this decay channel is a unique probe to study the direct coupling of the Higgs boson to fermions.

The main production mechanism at the LHC, gluon fusion Higgs production, cannot be exploited since the SM $b\bar{b}$ pair production constitutes an irreducible and overwhelming background with cross section several orders of magnitude larger than the gg→H$b\bar{b}$ one. We have to consider other production modes, with lower cross section but cleaner experimental signatures which allow for triggering, identifying and discriminating signal events with more peculiar features. VBF, VH and $t\bar{t}H$ mechanisms have been studied at the LHC in conjunction with H→ $b\bar{b}$ decays: the most significant results and the ones considered in this work are obtained from the VH associated production mode, exploiting the leptonic decays of the V boson to achieve good triggering conditions and strong background rejection.

VH($b\bar{b}$) signal: The pp→ VH,H→ $b\bar{b}$ processes, henceforth referred to as VH($b\bar{b}$) , have three possible final states according to the leptonic decays of the vector bosons: the '1-lepton' channel for W→ $l\nu$ decays, the '2-lepton' channel for Z → l^+l^- and the '0-lepton' channel for Z → $\nu\bar{\nu}$, represented as LO diagrams in Figure 9.9. The signature of these processes consists of a pair of hadronic jets originated from the bottom quarks (b-jets) from the Higgs decay, produced in association with charged lepton(s) (electrons, muons and possibly leptonically decaying τ's) and/or large missing transverse energy from undetected neutrino(s) in the detector.

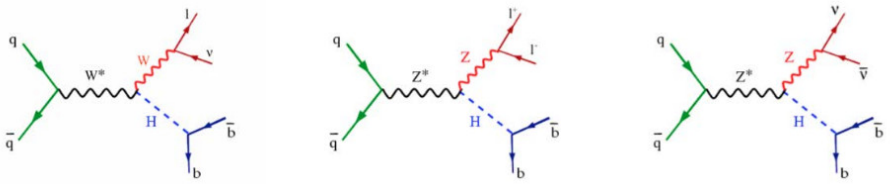

Figure 9.9: Feynman diagrams for the three leptonic decay channels of VH($b\bar{b}$).

SM backgrounds: These signal processes have large background from numerous SM processes in large part common, but contributing in different proportions, across the three lepton channels. In this section, I give a general overview of these backgrounds, while a more detailed description of their modelling is left to the following Chapters. The dominant SM backgrounds arise from vector boson production in association with hadronic jets (in particular jets originated by heavy flavour quarks) and top-antitop ($t\bar{t}$) pair production. Albeit with lower rates, also semi-leptonic diboson production VV (with one boson decaying leptonically and the other decaying hadronically), single-top production and QCD multi-jet, give significant background contributions.

- **V+jets background:** the production of a vector boson decaying to leptons in association with two b-jets (W$b\bar{b}$, Z$b\bar{b}$) is an irreducible background. For quark-induced initial states the main contribution comes from V boson production in association with gluon-splitting to $b\bar{b}$, while gluon-induced processes (allowed

only for Z+jets production) contributes as bbZ associated production: both sets of processes are shown schematically in Figure 9.10. Other combinations of quark flavours in the final state can become a background for the VH($b\bar{b}$) signal due to the misidentification of jets from charm or lighter quarks (c-jets and light-jets respectively) as b-jets.We note that given the proton-proton nature of the LHC hadronic collision, the flavour composition of Z+jets and W+jets events is not identical and it is driven by the composition of the proton's PDFs: for instance W production in association with a single b-jet plus additional c- or light(l)-jets (W+bl or W+bc) has a lower rate than the corresponding Z+bl or Z+bc production.

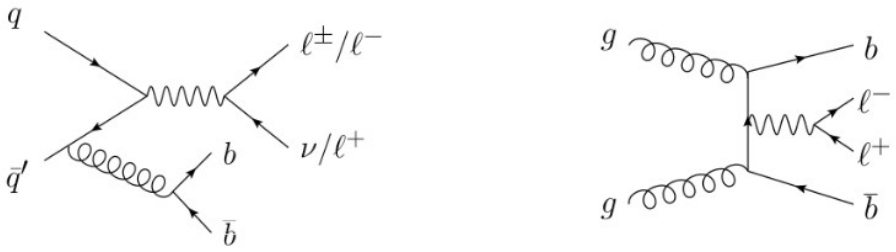

Figure 9.10: Lowest order Feynman diagrams for quark-induced W$b\bar{b}$ or Z$b\bar{b}$ production (left) and gluon-induced Z$b\bar{b}$ production.

- **top-antitop pair production:** the production of $t\bar{t}$ pairs has a quite large rate, however it is a reducible background which can be suppressed with specific analysis cuts (described in full details in the next Chapters). The top quark decays to Wb as shown by the diagram in Figure 9.11, thus the final state signature of a $t\bar{t}$ decay can vary considerably.

  In di-leptonic decays both W bosons decay leptonically to $l\nu$ pairs, resulting in a final state with two b-jets, large missing transverse energy and two leptons with opposite charge.

  In semi-leptonic decays one W boson decays to leptons, while the second to hadrons, providing a final state with a single charged lepton, significant missing transverse energy and four hadronic jets, two of which are b-jets.

  In fully-hadronic decays both W bosons decay hadronically, producing a final state with six jets, two of which are b-jets.

  For the VH($b\bar{b}$) signal the di-leptonic and semi-leptonic contributions are the main backgrounds, and can be rejected by vetoing events with multiple additional jets in addition to the two b-jets from the Higgs decay. Since the b-jets are produced from recoiling top quarks, they tend to be less collimated, and the p_T spectrum of the selected b-jets pair is softer than in the VH($b\bar{b}$) case (in fact, for high $p_T(b\bar{b})$ the main $t\bar{t}$ contribution comes from events with a

misidentified c-jet from the W decay, close-by to the b-jet from the same top decay).

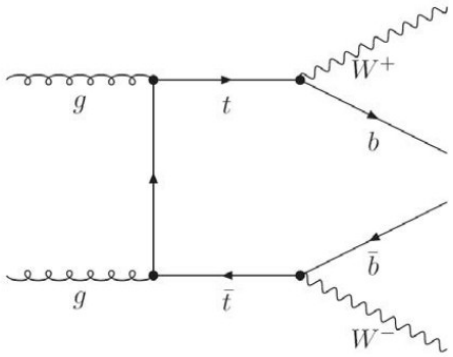

Figure 9.11: Lowest order Feynman diagram for top-antitop pair production and decay.

- **semileptonic VV production:** diboson processes with semileptonic decays have much smaller rates than V+jets or $t\bar{t}$, but constitute a very important background for the VH($b\bar{b}$) search as they can mimic very closely the signal signature, as shown by the diagrams in Figure 9.12.

  The main contributions come from ZZ→ $l^+l^-b\bar{b}$, ZZ→ $\nu\bar{\nu}b\bar{b}$ and WZ→ $l\nu b\bar{b}$ processes in which the Z boson plays the role of the Higgs decaying to a $b\bar{b}$ pair with invariant mass lower than the Higgs one ($m_Z < m_H$), but with a cross section approximately 5 times larger than the VH($b\bar{b}$) one. Considering the relatively poor m_H resolution for H→ $b\bar{b}$ events, this background can bring significant contamination in the region of the Higgs invariant mass peak.

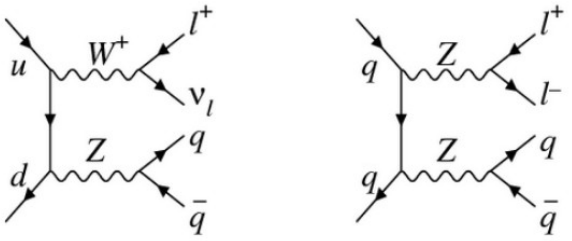

Figure 9.12: LO Feynman diagrams for semileptonic diboson production in WZ and ZZ channels.

- **single-top production:** three main sets of single-top processes contribute as background in these searches: s-channel production, t-channel production and Wt-channel production, shown schematically in Figure 9.13. In all cases the final state contains at least one W boson and at least one b-jet, and can thus reproduce the signal experimental signature. Similarly to the $t\bar{t}$ production

case the angular separation between b-jets can be a good quantity to reject the background.

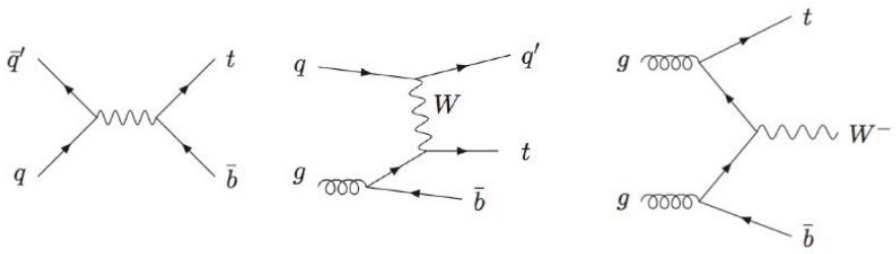

Figure 9.13: Feynman diagrams for single-top production: (from left to right) (a) LO s-channel diagram, (b) NLO t-channel diagram and (c) NLO Wt-channel diagram.

- **QCD multi-jet production:** these processes are strongly suppressed when selecting leptonic final states, but they can still produce a small background due to the extremely large production rate at the LHC.

  Their main contribution arises from the misidentification of hadronic jets as charged leptons, and the genuine production of b-jets (possibly containing semileptonic decays to muons, and resulting in missing transverse energy). Isolation criteria for the selected leptons are crucial to reject this background, which is mostly relevant for the WH$\rightarrow l\nu b\bar{b}$ decay mode for low transverse momenta of the W boson.

  This background can be sizeable in the ZH$\rightarrow \nu\bar{\nu}b\bar{b}$ channel as well, mostly due to multi-jet events with poorly reconstructed hadronic jets faking a genuine missing transverse energy contribution from neutrinos. In this case the background is suppressed with cuts on angular variables, defined from the reconstructed jets, the Higgs candidate dijet-pair, and the missing transverse energy.

9.4 LHC Higgs results

The major highlight of the Run-1 of the LHC was the discovery by ATLAS and CMS collaborations of the Higgs boson. This observation was driven by three decay channels : H $\rightarrow \gamma\gamma$, H $\rightarrow ZZ^* \rightarrow 4l$ and H $\rightarrow WW^* \rightarrow l\nu l\nu$. Since then, the measurement of the mass of the resonance has been performed for each decay channel available as well as a combined one [166] [167]. ATLAS and CMS decided to combine [168] their results in order to get a single LHC mass measurement. This combination of four measurements (diphoton and four leptons for each experiment) took place with approximately 25 fb^{-1} in each experiment. The final LHC Run-1 Higgs boson mass measurement is $m_H = 125.09 \pm 0.21(stat.) \pm 0.11(syst.)$. Since

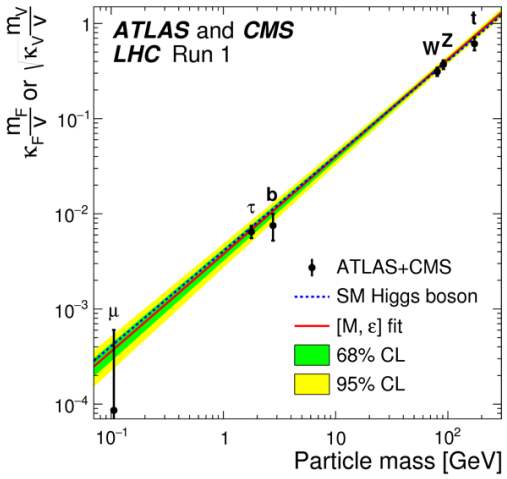

Figure 9.14: The measured interaction strength of the SM Higgs boson as a function of the mass of different particles in the Standard Model [165].

then, a compatible measurement by CMS of the Higgs boson mass in the $4l$ channel of $m_H = 125.26 \pm 0.21 = 125.26 \pm 0.20(stat.) \pm 0.08(syst.)$ GeV occurred [169].

The discovery of the Higgs boson relied on measurements of its decay to vector bosons. In the SM, different couplings determine its interactions to fermions and bosons, so new physics might impact them differently. Therefore, it is important to measure both. The first direct probe of fermionic couplings was to tau particles, which was observed in the combination of ATLAS and CMS results performed at the end of Run-1, with a signal significance of 5.5 σ [160] [161].

During Run-2, the increase in the center-of-mass energy to 13 TeV and the larger dataset allowed further channels to be probed. Over the past year, the evidence has been obtained for the Higgs decay to bottom quarks and the production of the Higgs boson together with top quarks has been observed with an observed (expected) significance of 6.3 σ (5.1 σ) [170] [171]. This means that the interaction of the Higgs boson to fermions has been clearly established.

On 9 July at the 2018 International Conference on High-Energy Physics (ICHEP) in Seoul, the observation of the challenging Higgs boson decaying into a pair of b-quarks has been announced. The ATLAS results, for the combined Run-2 and Run-1 data, yields an observed (expected) significance of 5.4 σ (5.5 σ) [172]. The combination of this result with searches by the CMS experiment for Higgs decay to bottom quarks yields an observed (expected) significance of 5.6 σ (5.5 σ) [173].

Additionally, a combination of Run-2 results searching for the Higgs boson produced in association with a vector boson with ATLAS yields an observed (expected) significance of 5.3 σ (4.8 σ) [172]. More results concerning the $b\bar{b}$ decay mode are

described in details in Chapter 10.

Figure 9.14 summarises what we currently know about the interaction of the Higgs boson with other SM particles by comparing the interaction strength to the mass of each particle. This clearly shows that the interaction strength depends on the particle mass: the heavier the particle, the stronger its interaction with the Higgs field. This is one of the main predictions of the BEH mechanism in the SM.

The couplings of the Higgs to various particles is related to the masses of the decay particles. As these measurements have already been performed, the SM is in principle complete. However, the newly discovered Higgs sector can probe BSM effects. It is then of major importance to try and measure all these couplings, including the effective ones containing loops, so as to spot any possible deviation from the theory.

The global signal strength μ, defined as the ratio of the observed Higgs boson rate to the SM expectation, can be extracted experimentally. It is measured to be

$$\mu_{VH} = 1.13^{+0.09}_{-0.08} = 1.13 \pm 0.05(\text{stat.})^{+0.05}_{-0.04}(\text{sig. th.}) \pm 0.03(\text{bgk. th.})$$

where the total uncertainty is decomposed into components for statistical uncertainties, experimental systematic uncertainties, and theory uncertainties on signal and background modelling. Figure 9.15 shows the combined production cross-section times branching fraction results for ggF, VBF, VH and tH+$t\bar{t}$H production in each relevant decay mode, normalized to their SM predictions.

We don't only do tests to verify that the properties of the Higgs boson agree with those predicted by the SM - we specifically look for properties that would provide evidence for new physics. For example, constraining the rate that the Higgs boson decays to invisible or unobserved particles provides stringent limits on the existence of new particles with masses below that of the Higgs boson. We also look for decays to combinations of particles forbidden in the SM. So far, none of these searches have found anything unexpected, but that doesn't mean that we're going to stop looking anytime soon!

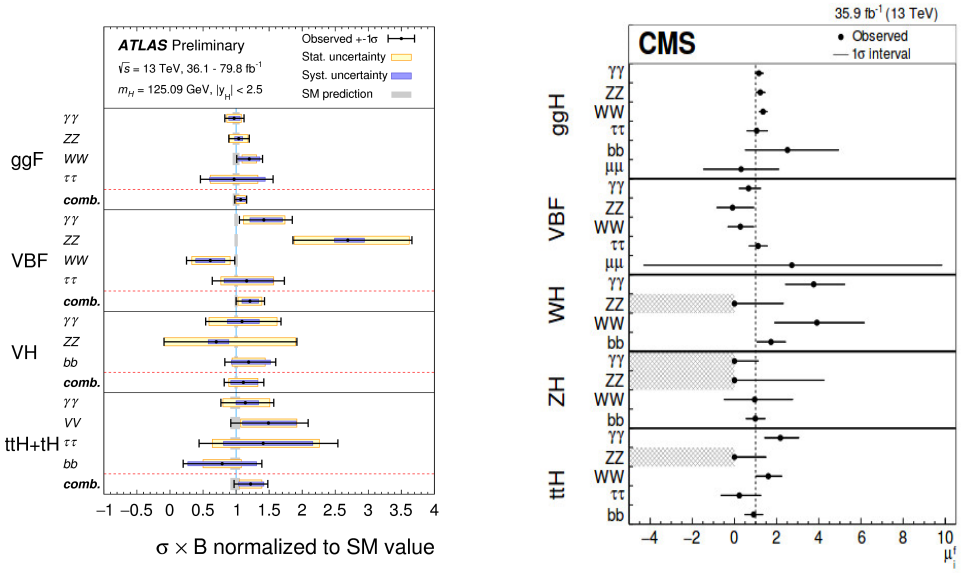

(a) (b)

Figure 9.15: (a) Cross-sections times branching fraction for ggF, VBF, VH and tH+$t\bar{t}$H production in each relevant decay modes, normalized to their SM predictions with (a) ATLAS expirement [174] and (b) CMS experiment [175].

Chapter 10

Search for standard model Higgs boson decay into b-quark pair in the VH($b\bar{b}$) mode

Contents

10.1 Introduction . . . 190
10.2 Data and simulated event samples . . . 193
10.3 Object and event selection . . . 196
10.3.1 Analysis specific object definition . . . 196
10.3.2 Trigger selection . . . 200
10.3.3 Event selection and categorization . . . 201
10.3.4 Additional selections for dijet-mass analysis . . . 205
10.3.5 Analysis regions . . . 206
10.4 Systematic Uncertainties . . . 207
10.4.1 Experimental uncertainties . . . 207
10.4.2 Uncertainties on the MC modelling of signal and backgrounds 208
10.4.3 Uncertainties of the multi-jet background . . . 213
10.5 Statistical Analysis . . . 214
10.5.1 Multivariate analysis . . . 215
10.5.2 Dijet-mass analysis . . . 216
10.5.3 Diboson analysis . . . 218
10.6 Results . . . 218
10.6.1 Results of the Multivariate analysis . . . 218
10.6.2 Results of the dijet-mass analysis . . . 219
10.6.3 Results of the diboson analysis . . . 225
10.7 Results of combinations . . . 225
10.7.1 Run-1 and Run-2 combination for VH,H$\to b\bar{b}$ . . . 225
10.7.2 Observation of H$\to b\bar{b}$ decays: combination of all production modes . . . 225
10.7.3 Observation of VH production: combination of all decay modes 228

10.1 Introduction

The Brout-Englert-Higgs mechanism [152] solves the apparent theoretical impossibility of weak vector bosons (W and Z) to acquire mass. The discovery of the Higgs boson in 2012 via its decays into photon, Z and W pairs was a triumph of the SM built upon this mechanism. After the discovery, the observation of many of the Higgs production modes and decay channels predicted by the SM have been established. The bosonic decay channels have entered an era of precision measurements. the Higgs boson mass was measured by ATLAS as m_H = 124.97±0.24 GeV from the combination of H→ $\gamma\gamma$ and H→ $ZZ^* \rightarrow 4l$ analyses with Run-2 2015-2016 data [176].

The Higgs field can also be used in an elegant way to provide mass to charged fermions (quarks and leptons) through interactions involving "Yukawa couplings", with strength proportional to the particle mass. The observation of the Higgs boson decaying into pairs of τ leptons provided the first direct evidence of this type of interaction [177].

Six years after its discovery, ATLAS has observed about 30% of the Higgs boson decays predicted in the SM. However, the favoured decay of the Higgs boson into a pair of b quarks (H→ bb), which is expected to account for almost 58% of all possible decays, had remained elusive up to last July. On 9 July 2018, the ATLAS experiment reported a preliminary result establishing the observation of the Higgs boson decaying into pairs of b quarks [178]. Furthermore at a rate consistent with the SM prediction. Observing this decay mode and measuring its rate is a mandatory step to confirm the mass generation for fermions via Yukawa interactions, as predicted in the SM, as well as, it is very important to constrain the overall Higgs boson decay width.

Despite the ggF production mode has largest cross section at LHC, the overwhelming multi-jet backgrounds make the search in this production mode very challenging. The most sensitive production modes for probing H→ $b\bar{b}$ decays are the associated production of a Higgs and a W or Z boson (denoted as V), the leptonic decay modes of the vector boson lead to clean signatures that can be efficiently triggered on, while rejecting most of the multi-jet backgrounds.

Evidence [1] of the H→ bb decay was first provided at the Tevatron in 2012, the CDF and D0 Collaborations at Tevatron reported an excess of events in VH associated production in the mass range of 120 GeV to 135 GeV, with a global significance of 3.1 σ, and a local significance of 2.8 σ at a mass of 125 GeV [179].

[1] In the community of particle physics (and beyond), for the detection of a process to be qualified as an "observation", it is necessary to exclude at a level of one in three million the probability that it arises from a fluctuation of the background that could mimic the process in question. When such a probability is at the level of only one in a thousand, the detection is qualified as an "evidence".

The analysis of 13 TeV data collected by ATLAS during Run-2 of the LHC in 2015, 2016 and 2017, which correspond to an integrated luminosity of 79.8 fb^{-1} leads to a significance of 4.9 σ - alone almost sufficient to claim observation. This result was combined with those from a similar analysis of Run-1 data and from other searches by ATLAS for the H$\rightarrow b\bar{b}$ decay mode, namely where the Higgs boson is produced in association with a top quark pair or via a process known as vector boson fusion (VBF). The significance achieved by this combination is 5.4 σ [178].

All four primary Higgs boson production modes at hadron colliders have now been observed, of which two only this year. In order of discovery, the observed Higgs production modes are: (1) fusion of gluons to a Higgs boson, (2) fusion of weak bosons to a Higgs boson, (3) associated production of a Higgs boson with two top quarks, and (4) associated production of a Higgs boson with a weak boson. The last two have been observed in 2018.

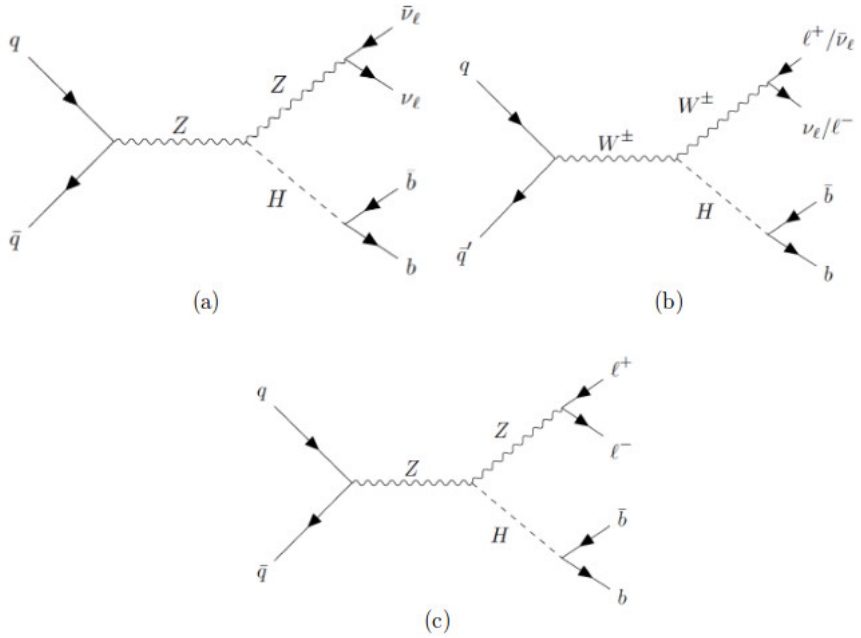

Figure 10.1: Feynman diagrams for the quark initiated SM VH($b\bar{b}$) process in the 0-lepton (a),1-lepton (b) and 2-lepton (c) channels.

Section 9.3.3, in the previous chapter, has introduced as a brief onset for the VH(bb) mode. In this chapter, I describe in details the search for the SM Higgs boson decaying into a $b\bar{b}$ pair in the VH production mode performed with data collected by the ATLAS detector during the LHC Run-2 at a centre-of-mass energy of 13 TeV. This is corresponding to an integrated luminosity of 79.8 fb^{-1} with 2015, 2016 and 2017 data.

Based on the paper published by the ATLAS collaboration in Physics Letters B

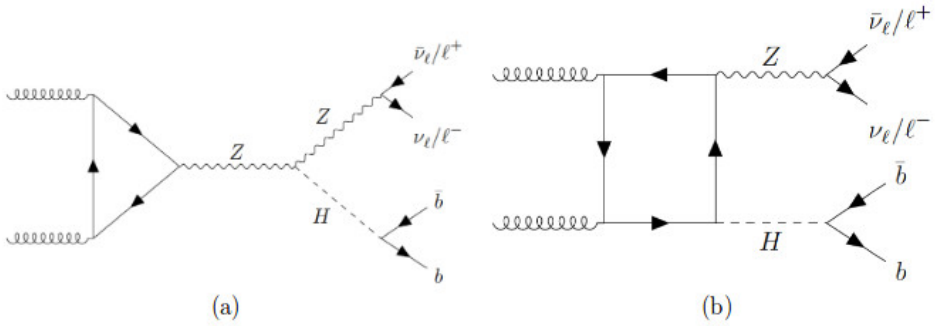

Figure 10.2: Feynman diagrams for the gluon initiated SM VH($b\bar{b}$) process in the 0-lepton (a) and 2-lepton (b) channels.

journal [178], three lepton channels are considered in the VH(bb) analysis. Based on the number of charged leptons, l (electrons or muons), the three channels are referred to as 0-, 1-, 2- lepton channels, to explore signatures of ZH$\rightarrow \nu\nu b\bar{b}$, WH$\rightarrow l\nu b\bar{b}$ and ZH$\rightarrow llb\bar{b}$, respectively. Feynman diagrams for quark induced and gluon induced VH($b\bar{b}$) productions are presented in Figure 10.1 and Figure 10.2, respectively.

There are a number of backgrounds remaining in this search channel, and have much larger yields than signal events. A detailed discussion of the multi-jet background will be given later in chapter 12. The main backgrounds are $t\bar{t}$ (for all three lepton channels), W+jets (for 0- and 1- lepton channel), Z+jets (for 0- and 2- lepton channel), and single top-quark (for 1-lepton channel), are already explained in details in Section 9.3.3.

To maximize the sensitivity to the Higgs boson signal a multivariate analysis [180] using the Boosted Decision Tree (BDT) has been used. The BDT [181] output discriminant is built from variables that describe the kinematics of the selected events, and used as the main fit observable in a binned maximum-likelihood fit, referred to as global likelihood fit. The likelihood fit is performed to data simultaneously across the three channels in multiple analysis regions, in order to extract the signal yield and the main background normalizations.

Two other analyses are used to validate this signal extraction method : the usual cut-based analysis using the dijet-mass as the main fit observable to extract the signal yield, and the diboson analysis, where the nominal multivariate analysis is modified to extract the VZ,Z$\rightarrow b\bar{b}$ diboson process. The result of the main multivariate analysis is also combined with the Run-1 VH($b\bar{b}$) result, as well as with other searches for H$\rightarrow b\bar{b}$ decay and with the other searches in the VH production mode.

10.2 Data and simulated event samples

The datasets used in this analysis include data recorded with the ATLAS detector during the Run-2 of the LHC (i.e. the 2015, 2016 and 2017 running periods).

Only data recorded with stable beam and in optimal functional conditions of the ATLAS detector are used in the analysis, ensuring all essential elements of the ATLAS detector were operational with good efficiency. These runs are summarized in the ATLAS Good Run Lists (GRL) of runs and luminosity blocks whose high quality has been assessed by the Data Quality ATLAS group, taking into account the status and performance of each sub-detector, beam conditions and objects reconstruction performance. Events are selected for the analysis only if they pass the GRL filter requirement. These events correspond to a total integrated luminosity of $79.8 \pm 1.6\ fb^{-1}$.

Simulated Monte Carlo Samples

Monte Carlo samples are used to simulate the VH,H $\rightarrow b\bar{b}$ signal and most background processes. All simulated processes are normalised using the most accurate theoretical cross-section predictions currently available and were generated at least to next-to-leading-order (NLO) accuracy. All samples of simulated events were passed through the ATLAS detector full simulation based on GEANT4 [182] and were reconstructed with the same reconstruction software as for the data. The effects of multiple interactions in the same and nearby bunch crossings (pile-up) were modelled by overlaying minimum-bias events, simulated using the soft QCD processes of Pythia8.186 [183] with the A2 [184] set of tuned parameters (tune) and MSTW2008LO [185] parton distribution functions (PDF). The background processes involving W or Z boson decays into leptons (including those in which the W boson arises from a top-quark decay), which are often referred to as electroweak (EW) backgrounds, were simulated as described above. In contrast, the multi-jet background is estimated in all three channels using data-driven method.

MC simulated signal samples: The quark initiated SM VH($b\bar{b}$) signal samples were generated using Powheg [186] MiNLO + Pythia8 applying the AZNLO tune with NNPDF3 parton distribution functions (PDF). Gluon induced signal samples were simulated using Powheg matrix element generator interfaced with Pythia8 applying AZNLO tune with NNPDF3 PDFs. The SM Higgs boson mass is fixed to 125 GeV, the $b\bar{b}$ branching fraction is fixed to 58%. WH signal samples are normalised to the production cross section at NNLO (QCD) and NLO (EW). The inclusive cross section of ZH production is calculated at NNLO (QCD) and NLO (EW), the cross section of gluon induced ZH production is then calculated at NLO (QCD), and quark induced production is taken as the difference of the two in order to avoid double counting.

MC simulated background samples:

The **V+jets** events samples are obtained using SHERPA2.2.1 [187]. Samples are normalised using cross sections calculated at NNLO accuracy. The (W/Z) + jets samples are sliced in several exclusive sub-sample according to max(H_T,p_T^V), where H_T is the sum of jets momentum, in order to generate sufficient high V(p_T) statistics. Additionally, in order to obtain a good statistical size for the (W/Z) + jets MC samples, even in regions with heavy flavour production or boosted vector bosons, dedicated filters are employed for the generation of this simulation. These filters allows to select events containing b-, c- or light-flavoured hadrons (to enhance the statistics of V production in association with heavy hadrons). These filters are:

- BFilter: requires at least 1 b-hadron with $p_T > 0$ GeV and $|\eta| < 4$.

- CFilterBVeto: requires at least 1 c-hadron with $p_T > 4$ GeV and $|\eta| < 3$ and veto events that pass the BFilter.

- CVetoBVeto: veto all the events that pass the BFilter or the CFilterBVeto.

The generated V+jets events are labelled according to the flavour of the reconstructed jets which is defined based on a ΔR match between truth level hadrons and reconstructed jets. For each jet, all generated hadrons with $p_T > 5$ and within $\Delta R < 0.3$ of the jet axis are considered. Each hadron is matched to only one jet, selecting the closest jet in ΔR space:

- If a truth b-hadron is matched to the jet, the jet is labelled a b-jet.
- If not, and if a truth c-hadron is matched to the jet, the jet is then labelled a c-jet.
- if none of the above, the jet is labelled as a light-jet.

Then, the W + jets and Z + jets simulated background samples are decomposed according to the true flavour of the dijet pair used to reconstruct the Higgs candidate, leading to the twelve sub-samples: Zbb, Wbb, Zcc, Wcc, Zl, Wl, Zbc, Wbc, Zbl, Wbl, Zcl, and Wcl. For each of these samples, the label indicate which the label of each jet in the sample, for example, the Zbc sample means that the one of the two jets is labelled as b-jet and the others as c-jet, and so on.

Top quark pair production events are simulated with the POWHEG generator and interfaced with PYTHIA8. The generated samples are normalised using cross sections calculated at NNLO+NNLL. A filter to require that at least one of the W bosons decays leptonically is used to generate the $t\bar{t}$ samples used for the 0 and 1 lep channels. This filter is called the "non-all-had filter". For the 2-lepton channel, the $t\bar{t}$ samples are generated using the "dilepton" filter which requires that both of the W bosons decays leptonically.

Process	ME generator	ME PDF	PS & Hadronisation	UE model tune	Cross-section order
Signal, mass set to 125 GeV and $b\bar{b}$ branching fraction to 58%					
qq→WH → $l\nu b\bar{b}$	Powheg-Box v2 + GoSam + MiNLO	$NNPDF3.0NLO^{(*)}$	Pythia8.212	AZNLO	NNLO(QCD)+ NLO(EW)
qq→ZH → $\nu\nu b\bar{b}$	Powheg-Box v2 + GoSam + MiNLO	$NNPDF3.0NLO^{(*)}$	Pythia8.212	AZNLO	$NNLO(QCD)^{(\dagger)}$+ NLO(EW)
gg→ZH → $\nu\nu b\bar{b}/llb\bar{b}$	Powheg-Box v2 +	$NNPDF3.0NLO^{(*)}$	Pythia8.212	AZNLO	NLO+ NLL
Top quark, mass set to 172.5 GeV					
$t\bar{t}$	Powheg-Box v2 +	NNPDF3.0NLO	Pythia8.212	A14	NNLO+NNLL
s-channel	Powheg-Box v2 +	NNPDF3.0NLO	Pythia8.212	A14	NLO
t-channel	Powheg-Box v2 +	NNPDF3.0NLO	Pythia8.212	A14	NLO
Wt-channel	Powheg-Box v2 +	NNPDF3.0NLO	Pythia8.212	A14	NLO
Vector boson + jets					
W→ $l\nu$	Sherpa 2.2.1	NNPDF3.0NNLO	Sherpa 2.2.1	Default	NNLO
Zγ^* → ll	Sherpa 2.2.1	NNPDF3.0NNLO	Sherpa 2.2.1	Default	NNLO
Z→ $\nu\nu$	Sherpa 2.2.1	NNPDF3.0NNLO	Sherpa 2.2.1	Default	NNLO
Diboson					
qq→WW	Sherpa 2.1.1	NNPDF3.0NNLO	Sherpa 2.1.1	Default	NLO
qq→WZ	Sherpa 2.1.1	NNPDF3.0NNLO	Sherpa 2.1.1	Default	NLO
qq→ZZ	Sherpa 2.1.1	NNPDF3.0NNLO	Sherpa 2.1.1	Default	NLO
gg→ZZ	Sherpa 2.1.1	NNPDF3.0NNLO	Sherpa 2.1.1	Default	NLO

Table 10.1: The generators used for the simulation of the signal and background processes. If not specified, the order of the cross-section calculation refers to the expansion in the strong coupling constant (αs). The acronyms ME, PS and UE stand for matrix element, parton shower and underlying event, respectively. (*) The events were generated using the first PDF in the NNPDF3.0NLO set and subsequently reweighted to PDF4LHC15NLO set using the internal algorithm in Powheg-Box v2 . (†) The NNLO(QCD)+NLO(EW) cross-section calculation for the pp→ZH process already includes the gg→ZH contribution. The qq→ZH process is normalised using the NNLO(QCD)+NLO(EW) cross-section for the pp→ZH process, after subtracting the gg→ZH contribution. An additional scale factor is applied to the qq→VH processes as a function of the vector boson's transverse momentum to account for electroweak (EW) corrections at NLO. This makes use of the VH differential cross-section computed with Hawk.

For the **single top quark** production, the samples (t-channel,s-channel and Wt-channel) are all simulated using Powheg, interfaced with Pythia8. Samples are normalised using cross sections calculated at NLO.

For the **diboson** samples, the quark induced diboson samples are generated using Sherpa 2.2.1 interfaced with NNPDF 3.0 NNLO PDFs in, while the semi-leptonic loop-induced gg→VV samples are generated using Sherpa 2.2.2 interfaced with NNPDF 3.0 NNLO PDFs.

A complete list of all the MC generators used in this analysis for the simulation of the signal and background processes are reported in Table 10.1.

Generally, MC samples are generated to reflect the different data running conditions and total integrated luminosity between 2015-2016 and 2017 data but with

same generator settings. Two set of statistically independent MC samples has been simulated, referred to as "mc16a" and "mc16d". The "mc16a" MC samples are simulated and reconstructed using the 2015-2016 data running conditions. While the "mc16d" corresponds to the 2017 data. The number of events simulated in mc16d is approximately 1.2 times larger than the events simulated in mc16a to account for the larger integrated luminosity collected in 2017 compared with 2015-2016.

10.3 Object and event selection

The event topologies characteristic of VH, H $\rightarrow b\bar{b}$ processes considered contain zero, one or two charged leptons (e, μ), and two 'b -jets' from b -hadron decays. In this section the object and event selection criteria that define this analysis.

10.3.1 Analysis specific object definition

The section will be dedicated to the detailed definition of the objects (leptons, jets, E_T^{miss}) used in the analysis to reconstruct the event used for this analysis. Considering the analysis specific requirements for the electrons, muons and jets, different categories are defined for these objects.

Electrons

Depending on the electrons selection criteria in the analysis, there are three electron categories, referred to as VH-*loose*, ZH-Signal and WH-Signal.

- VH-loose electrons are required to have $p_T > 7$ and $|\eta| < 2.47$ to allow for the maximum electron selection efficiency for the signal processes. They have to fulfil loose likelihood identification criteria, which encodes information on the electron shower-shape, track-quality criteria, quality of the matching between the track and its associated energy cluster in the calorimeter (direction and momentum/energy), TRT information, and an identification criterion for electrons originated by photon conversions. Loose-TrackOnly isolation is applied to reduce the non-prompt electrons. The isolation selection is chosen to keep 99% efficiency for real electrons. Furthermore the lepton track has to satisfy impact parameter criteria to reject tracks from pile-up events, based on the transverse impact parameter significance and the longitudinal impact parameter difference between the track and the primary vertex [188].

- ZH-Signal electrons are required to satisfy the loose criteria with a tighter selection $p_T > 27$ GeV.

Electron Selection	p_T	Identification Quality	Isolation
Loose	> 7 GeV	Loose	LooseTrackOnly
ZH-Signal	> 27 GeV	Loose	LooseTrackOnly
WH-Signal	> 27 GeV	Tight	FixedCutHighPtCaloOnly

Table 10.2: Summary of electron selection requirements.

Muon Selection	p_T	Identification Quality	Isolation
Loose	> 7 GeV	Loose	LooseTrackOnly
ZH-Signal	> 27 GeV	Loose	LooseTrackOnly
WH-Signal	> 27 GeV	Medium	FixedCutHighPtCaloOnly

Table 10.3: Summary of muon selection requirements.

- WH-Signal electrons are required to satisfy a tighter likelihood identification since these electrons are used in the 1-lepton analysis where it needed to suppress the multi-jet background. The "FixedCutHighPtCaloOnly" isolation selection are required to define the WH-signal electron.

The definitions of the requirements for each category are summarised in Table 10.2.

Muons

Similar with electrons, three categories are defined for muons, and referred to as VH-Loose, ZH-Signal and WH-Signal.

- ZH-signal muons are required to have $p_T > 27$ and $|\eta| < 2.5$ in addition to the VH-loose muon criteria for the 2-lepton channel.
- WH-Signal muons requires tighter lepton selection in order to suppress the multi-jet background. Therefore medium muon quality and FixedCutHighPt-TrackOnly isolation selection are required to define the WH-signal muon.

The definitions of the requirements for each category are summarised in Table 10.3.

Jets

Hadronic jets used in this analysis are classified as either "Signal" jets or "Forward" jets. Signal jets, which are eligible for b-tagging and used in reconstructing the Higgs boson, are defined with the requirements: $p_T > 20$ and $|\eta| < 2.5$. An additional requirement is applied is the jet has $p_T < 60$ and $|\eta| < 2.4$, this additional requirement is the "JetVertexFraction" (JVT) > 0.59. The Forward jets are defined as: $p_T > 30$ and $2.5 < |\eta| < 4.5$. A summary of jets selection requirements is given in Table 10.4.

Jet Category	Selection Criteria
Signal jets	$p_T > 20$ and $\|\eta\| < 2.5$ JVT> 0.59 if the jet with $p_T < 60$ and $\|\eta\| < 2.4$
Forward jets	$p_T > 30$ and $2.5 < \|\eta\| < 4.5$

Table 10.4: Summary of jets selection requirements.

b-jets

In these analyses 'b-jets' are hadronic jets reconstructed as small-R or track jets which pass some identification criteria based on dedicated b-tagging algorithms developed by the ATLAS Collaboration. These algorithms are built to identify jets originated from the fragmentation of b-quarks by using information from the long b-quark lifetime. the b-tagging algorithms provide as output a weight w for each tested jet, related to the likelihood of it being a b-jet: several operating points, corresponding to different b-tagging efficiencies and calibration scale factors, are provided for each algorithm.

For the analysis described in this chapter, the b-tagging algorithm is the'MV2c10' discriminant [189]. This algorithm is a multivariate function, which combines together various b-tagging algorithms built to exploit the information of the track impact-parameter significance, and explicit reconstruction of b- and c-hadron decay vertices and b→c hadron decay chain. The MV2c10 includes also the information from the improved tracking capabilities achieved by ATLAS in particular with the insertion of the additional pixel layer IBL.

Among the different available b-tagging efficiencies for the MV2c10 algorithm described in details in [190], the analysis presented in this chapter uses the 70% fixed cut working point. This working point corresponding to an improved c-rejection factor of 8 and smaller light-jets rejection factor which corresponds to 313.

For both instances of the MV2c algorithm the tagging efficiencies are corrected by data measurements in specific control regions. No MC-to-MC Scale Factors (SFs) are needed for the MV2c algorithms, since the MC simulated samples produced for the analysis of LHC Run-2 data have been generated with consistent setup for the heavy-flavour simulation and the b-quark decays through the EvtGen1.2.0 software.

Missing Transverse Energy

The (E_T^{miss}) is a crucial quantity to identify final states with undetectable neutrinos (as the 0- and 1-lepton process where the vector boson that decays either to two neutrinos or one lepton plus a neutrino), whose presence can be inferred by an apparent momentum imbalance in the transverse plane, and to suppress the background contribution in signal topologies where all the particles in the final state can

be identified in the detector (as the 2-lepton ZH$\rightarrow l^+l^-b\bar{b}$ process). Since the E_T^{miss} quantify the transverse momentum imbalance, it is really an 'event quantity' whose definition relies on all other objects reconstructed for a given event.

E_T^{miss} is comprised of the negative vector sum of p_T of physics objects (leptons, jets, etc.) and a so-called soft term. In Run-2, E_T^{miss} soft term (ST) is reconstructed using well-reconstructed tracks originating from the primary vertex, which are not already included in any of the physics objects [191]. Building the E_T^{miss} (ST) from tracks rather than from energy deposits in the calorimeters, makes this quantity more robust with respect to the pile-up contribution.

In addition to the E_T^{miss}, a track-based missing transverse momentum vector p_T^{miss} is built from the negative vector sum of the transverse momenta of all well-reconstructed tracks associated with the primary vertex. This quantity is mainly used to suppress non-collision and multi-jet backgrounds.

Overlap removal

The 'overlap removal' procedure takes into account all reconstructed objects and applies specific criteria to avoid double-counting, treating objects which are reconstructed from the same detector signature (for instance an electron, which is also reconstructed as fake-jet). The overlap removal procedure is applied in the following steps [190]:

- tau-electron: If $\Delta R(\tau, e) < 0.2$, the τ lepton is removed.
- tau-muon: If $\Delta R(\tau, \mu) < 0.2$, the τ lepton is removed, with the exception that if the τ lepton has $p_T > 50$ GeV and the muon is not a combined muon (i.e. muon of low quality), then the τ lepton is not removed.
- electron-muon: If a combined muon shares an ID track with an electron, the electron is removed. If a calo-tagged muon shares an ID track with an electron, the muon is removed.
- electron-jet: If $\Delta R(jet, e) < 0.2$, the jet is removed. For any surviving jets, if $\Delta R(jet, e) < min(0.4, 0.04 + 10 \text{ GeV}/p_T^e$, the electron is removed. Such electrons are likely to originate from semileptonic b- or c-hadron decays.
- muon-jet: If $\Delta R(jet, \mu) < 0.2$ and the jet has less than three associated tracks or the muon ID track is ghost associated to the jet (i.e. the muon energy constitutes most of the jet energy), the jet is removed. For any surviving jets, if $\Delta R(jet, \mu) < min(0.4, 0.04 + 10 \text{ GeV}/p_T^\mu$, the muon is removed.
- τ-jet: If $\Delta R(\tau, jet) < 0.2$, the jet is removed.

Trigger Name	Period	Threshold (GeV)	Description
HLT_xe70_mht_L1XE50	2015	70 GeV	Seeded using the level L1_XE50 LAr and Tile calorimeter triggers, calibrated at the EM scale, with a threshold of 50 GeV.
HLT_xe90_mht_L1XE50	2016(A-D3)	90 GeV	
HLT_xe110_mht_L1XE50	2016(≥D4)	110 GeV	
HLT_xe110_pufit_L1XE50	2017	110 GeV	

Table 10.5: E_T^{miss} triggers used during the 2015, 2016 and 2017 data collection period. The notation, (A, D3, D4,...) refer to the ATLAS collection periods in the year of 2016.

Trigger Name	Period	Threshold (GeV)	Description
HLT_e24_lhmedium_L1EM20VH	2015	24 GeV	Seeded using L1EM20VH level 1 trigger calibrated at the EM scale with a threshold of 20 GeV, and require medium ID quality.
HLT_e60_lhmedium_L1EM20VH	2015	60 GeV	Seeded using L1EM20VH level 1 trigger calibrated at the EM scale with a threshold of 20 GeV, and require medium ID quality.
HLT_e120_lhmedium_L1EM20VH	2015	120 GeV	Seeded using L1EM20VH level 1 trigger calibrated at the EM scale with a threshold of 20 GeV, and require loose ID quality.
HLT_e26_lhtight_nod0_ivarloose	2016&2017	26 GeV	Tight likelihood ID required, and variable loose isolation required.
HLT_e60_lhmedium(nod0)	2016&2017	60 GeV	Medium ID likelihood required.
HLT_e140_lhloose(nod0)	2016&2017	140 GeV	Loose ID likelihood required.
HLT_e300_etcu	2017	300 GeV	No ID requirements.

Table 10.6: Single electron triggers used during the 2015, 2016 and 2017 data collection period.

10.3.2 Trigger selection

The 0-lepton data events are recorded using lowest un-prescaled E_T^{miss} triggers with online thresholds of 70 GeV for the data recorded in 2015, of 90 and 110 GeV for the data recorded in 2016 and of 110 GeV for the data recorded in 2017, depending on the data-taking period and the different trigger rates. Their efficiency was measured in W+jets, Z+jets and $t\bar{t}$ events in data using single-muon triggers, resulting in correction factors that are applied to the simulated events, ranging from 1.05 at the offline E_T^{miss} threshold of 150 GeV to a negligible deviation from unity at an E_T^{miss} above 200 GeV. The details of these E_T^{miss} triggers are shown in Table 10.5.

Events in the 1-lepton electron sub-channel are recorded by at least one lowest un-prescaled single electron triggers in each data collection period and p_T thresholds started at 24 GeV in 2015 and increased to 26 GeV in 2016 and 2017. The lowest-threshold trigger in 2016 and 2017 includes isolation and identification requirements which are looser than any of the isolation and identification requirements applied in the offline analysis. These requirements are relaxed or removed for the higher-threshold triggers. Table 10.6 shows the details for these single electron triggers.

In the 1-lepton muon sub-channel, events are recorded using the same E_T^{miss} trigger as those used in the 0-lepton channel. The E_T^{miss} calculation at trigger level

Trigger Name	Period	Threshold (GeV)	Description
HLT_mu20_iloose_L1MU15	2015	20 GeV	Seeded using L1MU15 level 1 trigger with a threshold of 15 GeV, and requiring loose isolation requirements.
HLT_mu40	2015 & 2016 (A)	40 GeV	No isolation requirements.
HLT_mu50	2015 & 2016 & 2017 (A)	50 GeV	No isolation requirements.
HLT_mu24_iloose(L1MU15)	2016(A,MC)	24 GeV	Variable and Fixed cone Loose isolation requirements.
HLT_mu24_ivarmedium	2016(A-D3)	24 GeV	Variable cone medium isolation requirements.
HLT_mu26_ivarmedium	2016($\geq$D4) & 2017	26 GeV	Variable cone medium isolation requirements.

Table 10.7: Single muon triggers used during the 2015, 2016 and 2017 data collection period.

is relied on the calorimeter information, therefore muons are not included for this calculation. In events where a muon is present, the E_T^{miss} trigger is actually selecting events based on p_T^W, and is fully efficient for events with p_T^W >180 GeV. The overall signal efficiency for E_T^{miss} trigger in muon sub-channel is $\approx 98\%$, compared to $\approx 80\%$ efficiency for the combination of single-muon triggers, therefore E_T^{miss} trigger is used. Only $\approx 2\%$ more signal events can be recovered by using the combination triggers. To simplify the analysis, only E_T^{miss} trigger is used in the muon sub-channel.

In the 2-lepton channel, events in electron sub-channel are triggered by the same lowest un-prescaled single electron triggers as in the 1-lepton channel. For muon sub-channel, events are recorded using the lowest un-prescaled single muon triggers in each data collection period and p_T thresholds started at 20 GeV in 2015 and increased to 26 GeV in 2017. Table 10.7 shows the details for these single muon triggers.

10.3.3 Event selection and categorization

This section is outlining the event selection criteria that define the VH(bb) analysis. The selection cuts employed to reject the backgrounds and are optimized to disentangle the signal from VH(bb) Higgs production (with $m_H = 125$ GeV) from the SM backgrounds. The various categories and regions, defined in the following, is meant to increase the sensitivity of the analysis.

- **Lepton categories**: Both data and MC simulation events, that pass the GRL selection, are categorized into three sub-channels. The 0-, 1- and 2-lepton channels are defined by requiring respectively exactly 0 VH-loose lepton, exactly 1 WH-signal lepton and exactly 2 VH-loose leptons with at least one ZH-signal lepton.
- **Jets categories**: In all the three lepton channels, events are required to

contain at least two signal jets. In order to maximize the signal significance, exclusive categories of events, depending on the number of selected jets they contain, are defined:

- events containing two jets comprise the 2-jet category,

- events with exactly three jets form the 3-jet category

- and events with three or more jets form the 3+-jet category.

In the 0- and 1-lepton channels, the 2- and 3-jet categories are used, and events with four or more jets are rejected due to the high $t\bar{t}$ background contamination. In the 2-lepton channel, where the high jet multiplicity regions result in some additional sensitivity, the 2-jet and 3+-jet categories are used.

Moreover, events are categorized according to the number of b-tagged signal jets and only the 2-tag region is considered in this analysis, as this is the region that has the largest signal sensitivity. The leading b-tagged jet in the 2-tag category is required to have $p_T > 45$ GeV. In all three lepton channels, b-tagging is applied to all signal jets selected using the MV2c10 algorithm at the 70% efficiency working point. The b-tagging strategy, and efficiency working point have been optimized to maximize the expected signal significance [192].

- **Vector boson transverse momentum p_T^V regions**: The p_T^V categorization has the goal of separating high-sensitivity regions (at high p_T^V) from lower-sensitivity categories which are mainly used to constrain the background modelling, thanks to their larger statistical power. In the 0-lepton channel the p_T^Z is defined as the reconstructed E_T^{miss}; in 1-lepton events p_T^W is equal to the vector sum of the selected p_T and the E_T^{miss} contribution; in the 2-lepton channel p_T^Z corresponds to the vector sum of the transverse momenta of the two selected leptons.

  In the 0- and 1-lepton channels a single p_T^V region is included, requiring events with vector boson transverse momentum above 150 GeV. Events in the 2-lepton channel are divided into low- and high-p_T^V, with boundary at 150 GeV. While in the 0-lepton channel the p_T^V cut at 150 GeV is justified by the threshold of the E_T^{miss} trigger, in the 1-lepton channel we could in principle include events with lower p_T^W: the low-p_T^W region is not considered in this search to avoid the harsh difficulties related to the modelling and estimate of the multi-jet background, which contributes significantly in this region, in view of a moderate impact on the analysis sensitivity (of the order of 5-10%) [190].

- **Analysis sub-channels selections**: After the event categorization just described, an additional set of criteria specific to each lepton channel is applied, in order to reduce the background contribution.

  - **0-lepton channel**: The reconstructed transverse momentum of the Z boson, p_T^Z, corresponds to E_T^{miss} in the 0-lepton channel, is required to be greater than 150 GeV, due to the slow turn-on curve of the E_T^{miss}

trigger. Further requirements are applied on the scalar sum of the p_T of the jets in the event (H_T), to remove a region which is mis-modelled in simulation due to a non-trivial dependence of the trigger efficiency on the jet multiplicity. H_T >120 GeV is applied to the 2-jets events, and H_T >150 GeV is applied to the 3-jets events. The multi-jet background in 0-lepton channel is mainly due to the jet energy mis-measurements in the calorimeters, as a result, the fake missing transverse energy and momentum tend to be aligned with the mis-measured jet. In order to reduce the multi-jet background, four angular selection criteria (referred to as anti-QCD cuts) are required:
- $\Delta\phi(E_T^{miss}, P_{miss}^T) < 90°$
- $\Delta\phi(b_1, b_2) < 140°$
- $\Delta\phi(E_T^{miss}, bb) > 120°$
- $min[\Delta\phi(E_T^{miss}, jets)] > 20°$ for 2 jets and $> 30°$ for 3 jets.

Where ϕ is the azimuthal angle, p_T^{miss} is defined as the missing transverse momentum calculated using only tracks reconstructed in the inner tracking detector and matched to the primary vertex. b_1 and b_2 are the two b-tagged jets forming the Higgs boson candidate's dijet system. The last cut, $min[\Delta\phi]$ is the minimum azimuthal angle between the p_T^{miss} vector and the closest jet. These anti-QCD cuts are the reason behind the fact that the multi-jet background in 0-lepton channel is found to be negligible.

- **1-lepton channel**: The transverse momentum of the W boson, p_T^W is reconstructed as vectorial sum of E_T^{miss} and the charged lepton's transverse momentum and required to be greater than 150 GeV in 1-lepton channel, due to the much increased sensitivity and the reduced multi-jet background contamination in such high p_T^W region compare to the relative low p_T^W region. Although not used in this iteration of the analysis, an effort to include the 75 GeV $< p_T^W <$ 150 GeV region (referred to as medium p_T^W region) in the 1-lepton channel has been studied. For this study, the details about the multi-jet reduction and estimation in medium p_T^W region can be found in Chapter 12.

  In the electron sub-channel, an additional selection of $E_T^{miss} > 30$ GeV is applied to further reduce the multi-jet background.

  In the 1-lepton channel, events are categorized into the signal region (SR) or into a W + HF events enriched control region (W +HF CR), based on the selections on the invariant mass of the two b-tagged jets (m_{bb}), and on the reconstructed mass of a semi-leptonically decaying top-quark candidate (m_{top}). The W + HF CR is obtained by applying two additional selection requirements: m_{bb} <75 GeV and $m_{top} > 225$ GeV.

- **2-lepton channel**: The transverse momentum of the Z boson, p_T^Z, is reconstructed as vectorial sum of transverse momentum of two leptons,

Common Selection	
Jets	$\geq$ 2 signal jets
b-jets	2 b-tagged signal jets
Leading jet p_T	>45 GeV
0-lepton Channel	
Trigger	E_T^{miss} shown in Table 10.5
Jets	Exactly 2 or 3 jets
Leptons	Exactly 0 VH-loose lepton
E_T^{miss}	>150 GeV
H_T	>120 GeV(2jets), >150 GeV(3jets)
$\Delta\phi(E_T^{miss}, P_{miss}^T)$	$< 90°$
$\Delta\phi(b_1, b_2)$	$< 140°$
$\Delta\phi(E_T^{miss}, bb)$	$> 120°$
$min[\Delta\phi(E_T^{miss}, jets)]$	$> 20°$ for 2 jets and $> 30°$ for 3 jets
p_T^V regions	>150 GeV
1-lepton Channel	
Trigger	e-channel: un-prescaled single electron as show Table 10.6 μ channel: E_T^{miss} as shown in Table 10.5
Jets	Exactly 2 or 3 jets
Leptons	Exactly 1 WH-signal lepton
E_T^{miss}	>30 GeV
m_{top} and m_{bb}	m_{bb} <75 GeV and m_{top} >225 GeV
p_T^V regions	>150 GeV
2-lepton Channel	
Trigger	e-channel: un-prescaled single electron as show Table 10.6 μ-channel: un-prescaled single muon as show Table 10.7
Jets	Exactly 2 or 3 jets
Leptons	Exactly 2 VH-loose lepton, at least one ZH-signal lepton Same flavour, opposite-charge for $\mu\mu$
m_{ll}	$81GeV < m_{ll} < 101GeV$
p_T^V regions	75 GeV $< p_T^V <$150 GeV, >150 GeV

Table 10.8: Summary of the event selection and categorization in the 0-, 1- and 2-lepton channels.

with a $p_T^Z > 75$ GeV cut applied due to low signal sensitivity in the lower p_T^Z regions. The 2-lepton channel is then split into two regions, 75 GeV $< p_T^Z <$ 150 GeV and $p_T^Z >$ 150 GeV. The invariant mass of the di-lepton system must be consistent with the Z boson mass: 81 GeV $< m_{ll} <$ 101 GeV, in order to suppresses backgrounds have a non-resonant lepton-pair, such as $t\bar{t}$ and multi-jet productions. For the selected di-muon events the two muons are further required to be of opposite charge; the requirement is not applied to di-electron events due to higher rate of charge misidentification. A top $e\mu$ control region is defined by applying the nominal selection but requiring an $e\mu$ lepton flavour combination instead of ee or $\mu\mu$, and requiring the two leptons to have opposite-sign charges.

All the above signal events selection which are applied in each of the three sub-channels in the VH(bb) analysis are summarized in Table 10.8.

	Channel		
Selection	0-lepton	1-lepton	2-lepton
m_T^W	-	<120 GeV	-
$E_T^{miss}/\sqrt{S_T}$	-	-	$< 3.5\sqrt{\text{GeV}}$
	p_T^V Regions		
p_T^V	75 GeV< p_T^V ≤150 GeV (2-lepton channel only)	150 GeV< p_T^V ≤200 GeV	$p_T^V > 200$ GeV
$\Delta R(b1, b2)$	<3.0	<1.8	<1.2

Table 10.9: Summary of the additional event selections in the 0-, 1- and 2-lepton channels of the dijet mass analysis.

10.3.4 Additional selections for dijet-mass analysis

Two versions of the analysis are carried out, one using a multivariate approach, called MVA analysis (more details in Section 10.5.1), and the other using the dijet-mass as the final discriminant, referred as cut-based analysis. The cut-based analysis, where the m_{bb} variable is used as a discriminant to separate signal from background, is performed as a cross-check to the main multivariate analysis. The event selection shown in Table 10.8 is applied to both versions, with a number of additional selection criteria are applied for the dijet-mass analysis to further reduce the background contamination. These additional selections, shown in Table 10.9, increase the purity of the signal regions and are necessary to increase the sensitivity for the dijet-mass analysis.

The high-p_T^V region is split into two region: 150 GeV $< p_T^V <$ 200 GeV and$p_T^V >$ 200 GeV, with further different requirements on the $\Delta R(b1, b2)$ cut applied in different regions as shown in Table 10.9.

In the 1-lepton channel, an additional cut on W boson's transverse mass $m_T^W <$ 120 GeV is applied to further reduce the $t\bar{t}$ background. The W boson's transverse mass, m_T^W, is defined as

$$m_T^W = \sqrt{2p_T^l E_T^{miss}(1 - cos(\Delta\phi(l, E_T^{miss})))} \tag{10.1}$$

where the p_T^l is the lepton's transverse momentum.

In the 2-lepton channel, in order to suppress the $t\bar{t}$ background, an additional cut is applied, with requiring $E_T^{miss}/\sqrt{S_T} < 3.5\sqrt{\text{GeV}}$ where S_T is defined as the scalar sum of the transverse momenta of all jets and leptons in the event.

Channel	SR/CR	Categories			
		75 GeV< p_T^V <150 GeV		p_T^V > 150 GeV	
		2Jet	3Jet	2Jet	3Jet
0 lepton	SR	-	-	BDT	BDT
1 lepton	SR	-	-	BDT	BDT
2 lepton	SR	BDT	BDT	BDT	BDT
1 lepton	W+HF CR	-	-	Yield	Yield
2 lepton	top eμ CR	m_{bb}	m_{bb}	Yield	BDT

Table 10.10: The distributions used in the global likelihood fit for the signal regions (SR) and control regions (CR) for all the categories in each channel, for the nominal multivariate analysis.

10.3.5 Analysis regions

Based on the event selection criteria listed in Table 10.8, events are categorised into the signal region (SR) or into a control region (CR). A total of eight signal regions (SR) and six control regions (CR) are defined for the VH(bb) analysis, separately for 0-, 1-, and 2-lepton channels, 2-Jet and 3-Jet categories, low- and high-p_T^V regimes.

The eight 2-tag SR, considered here, are corresponding to two jet categories for the three lepton channels in the high-p_T^V region, in addition to the two jet categories for the 2-lepton medium-p_T^V region. Table 10.10 outlines schematically the set of categories included in the analysis with for the nominal multivariate analysis.

In addition, six CR are defined to help better constrain the modelling of background processes. These control regions are designed to be highly pure in one background process, and are defined using a series of selection cuts. These control regions are then orthogonal to the signal region, with negligible level of signal contamination.

In the 1-lepton channel, the normalization uncertainty on the W + HF background is one of the largest systematic uncertainties. Therefore, a dedicated 1-lepton W+HF CR is defined to better constrain the normalization of W + HF background. To achieve a high W + HF background purity in this CR, a cut on the reconstructed leptonically decaying top mass, m_{top} is introduced, with $m_{top} > 225$ GeV to reduced the dominated $t\bar{t}$ background in 1-lepton channel and keep a significant number of W + HF events. m_{top} is calculated as the invariant mass of the lepton, the reconstructed neutrino and the b-tagged jet that yields the lowest mass value. To make sure the signal contribution in this CR is negligible, a cut on the invariant mass, $m_{bb} < 75$ GeV, is applied. Performing these two selection resulting in a purity around 75% of the W+HF CR [178].

In the 2-lepton channel, the $t\bar{t}$ background is known as a flavour symmetric process. Therefore, the high purity $t\bar{t}$ control region can be obtained by requiring dif-

ferent flavour of a pair of dilepton ($e\mu$ or μe), instead of requiring the same flavour as in SR. This defines the 2-lepton top $e\mu$ CR. The purity of the $e\mu$ CR is over 99% [178]. This means that more than 99% events in this CR are from $t\bar{t}$ and single top processes with almost 0 signal events contamination.

In the dijet-mass analysis, the fitting regions are modified in order to improve the analysis sensitivity. In the dijet-mass analysis, the number of signal regions is increased to fourteen as a consequence of splitting the event regions with $p_T^V >$ 150 GeV in two. An additional division at $p_T^V = 200$ GeV is made in all channels (except in the top $e\mu$ CR in order to maintain a sufficient number of data events) to exploit the larger signal sensitivity in the higher p_T^V regions. In the 1-lepton channel, the W+HF CR is merged into the signal region as the low m_{bb} region sufficiently constrains the W+HF background. The corresponding analysis regions for the dijet-mass analysis are summarised in Table 10.10 as well.

10.4 Systematic Uncertainties

In this Section, I give a description of the different sources of systematic uncertainties included in this analysis, from the experimental systematics related to the performance of the detector and the object identification and reconstruction, to the uncertainties on the data-driven multi-jet estimate, to the systematics on the MC modelling of the simulated EW backgrounds and the Higgs boson signal simulation.

10.4.1 Experimental uncertainties

This set of systematics includes uncertainties affecting the trigger selection, the object reconstruction and identification, the object energy, momentum and mass calibrations and resolutions, for the different objects used in this analysis (charged leptons, hadronic jets, missing transverse momentum). The main details of these uncertainties are here summarized:

- **integrated luminosity and pile-up**: the uncertainty on the integrated luminosity amounts to 2.0%. It is derived, following a methodology similar to that detailed in ref. [193] using the LUCID-2 detector [194]. An uncertainty on the average number of interactions per bunch crossing is rescaled by 1.03 based on the measurement of the visible cross-section in minimum-bias events [195].

- **leptons**: systematic uncertainties affecting the leptons triggers, lepton reconstruction, identification and isolation efficiencies and the energy and resolution

corrections are included, for both electrons and muons, are estimated using 13 TeV data, with very low impact on the analysis performance.

- $\boldsymbol{E_T^{miss}}$ **trigger**: the trigger efficiency is corrected with scale factors (SFs) obtained from data-to-MC comparison. Uncertainties on these scale factors account for statistical fluctuations in its determination, and differences in its measurement with alternative physics processes (comparing SFs obtained from W+jets, Z+jets and $t\bar{t}$ events.

- **Jet Energy Scale (JES) and Energy Resolution (JER)**: the systematic uncertainty on the JES is fully documented in [196] and includes several sources, estimated from data collected at 13 TeV. It is divided into several components covering in-situ analyses, η inter-calibration, high-p_T jets, pile-up effects, flavour composition, flavour response, b-jets specific effects and impact of punch-through jets. These sources are decomposed into 23 uncorrelated components that are treated as independent.

- **Flavour-tagging**: the uncertainties related to the flavour-tagging algorithm applied to small-R and track jets cover different systematic effects. Uncertainties originate from the b-tagging correction factors (or alternatively scale factors) are dominant. It is determined from the difference between the efficiency measured in data and simulation, from the jet energy scale corrections and from the modelling of the jet energy resolution. The b-tagging correction factors are derived separately for b-jets, c-jets and light-flavour jets [197] [198] [199]. The uncertainties in these three correction factors have estimated from multiple measurements, resulting in three separated uncertainties for b-jets and c-jets, and five for light-flavour jets. The uncertainty in the tagging efficiency is approximately 2% for b-jets, 10% for c-jets and 40% for light-flavour jets. Two additional uncertainties are included, related to the extrapolation of the b-jet efficiency calibration to jets with $p_T > 300$ GeV and to the misidentification of hadronically decaying τ-leptons as b-jets.

- $\boldsymbol{E_T^{miss}}$: the uncertainties in the jets and lepton energy scale and resolution are propagated to the calculation of E_T^{miss}. Furthermore uncertainties on the determination of the E_T^{miss} soft term included, covering its scale, resolution and reconstruction efficiency of the tracks, along with the modelling of the underlying event.

10.4.2 Uncertainties on the MC modelling of signal and backgrounds

The analysis of the VH(bb) strongly relies on MC simulation to estimate the several sources of SM background: the proper assessment of systematic uncertainties on the MC modelling of the backgrounds is therefore crucial as it reflects our degree of

confidence in the theoretical prediction for these processes, and the level of accuracy that can be expected from the simulation. The estimate of the background however is also driven by the data sample analyzed, in the sense that all backgrounds enter in a combined Profile Likelihood Fit, and their shape and normalization can be adjusted by the fit to properly the data distributions. The size of the systematic uncertainties on the background prediction, and the correlations among them, are two crucial elements of the Likelihood fit model that determine how and to what extent the fit to data is able to change and modify the MC estimate of background and signal.

For these reasons extensive studies have been performed to assess modelling systematic uncertainties for the main and the smaller backgrounds after the VH($b\bar{b}$) analysis selection, as well as for the VH signal processes.

10.4.2.1 Signal uncertainties

Systematics on the signal model may be categorized in uncertainties on the total NNLO(QCD)+NLO(EW) cross section used for the normalization of the signals and the Higgs branching ratio BR(H$\rightarrow b\bar{b}$), and shape and acceptance uncertainties from the MC simulation.

Uncertainties on the total cross section and the branching ratio affect only the overall normalization of the signal prediction [200]. The systematic uncertainties in the calculations of the VH production cross-sections and the H$\rightarrow b\bar{b}$ branching fraction are assigned following the recommendations of the LHC Higgs Cross Section Working Group [201], and it is applied directly in the analysis.

The second set of systematic uncertainties on the signal prediction covers effects on the acceptance and the shape of the baseline MC simulation after the analysis selection. Using alternative samples generated with a larger number of events, and using a parameter tune optimized more recently for the evaluation of the parton shower uncertainty, two types of systematic uncertainties have been studied. These are the relative acceptance variations across the different analysis categories, and variations in the shape of two of the most discriminating variables used in the MVA analysis, the vector boson transverse momentum p_T^V and the invariant mass of the Higgs candidate m_{bb}.

Table 10.11 shows a schematic summary of the systematic uncertainties that affect the modelling of the signal.

Signal Uncertainties	
Cross-section (scale)	0.7% (qq), 27% (gg)
Cross-section (PDF)	1.9% (qq→WH), 1.6% (qq→ZH), 5% (gg)
H→ $b\bar{b}$ branching fraction	1.7%
Acceptance from scale variations	2.5 - 8.8%
Acceptance from PS/UE variations for 2 or more jets	2.9 - 6.2% (depending on lepton channel)
Acceptance from PS/UE variations for 3 jets	1.8 - 11%
Acceptance from PDF+α_S variations	0.5 - 1.3%
m_{bb},p_T^V, from scale variations	S
m_{bb},p_T^V, from PS/UE variations	S
m_{bb},p_T^V, from PDF+α_S variations	S
p_T^V from NLO EW correction	S

Table 10.11: Summary of the systematic uncertainties in the signal modelling. An 'S' symbol is used when only a shape uncertainty is assessed and 'PS/UE' indicates parton shower / underlying event. Where the size of an acceptance systematic uncertainty varies between regions, a range is displayed.

10.4.2.2 Background uncertainties

For the three dominant backgrounds, $t\bar{t}$, Z+jets and W+jets, unconstrained floating normalisations are applied, such that the overall normalisation of these processes can be constrained using data where possible. Acceptance uncertainties within the fit model then allow for the normalisations of these processes to vary between each region. The general model for these processes is as follows:

- **Z+jets**: Z+HF is a dominant background in the 0- and 2-lepton channels. Two floating normalisation factors for the overall Z+HF background are used for the 2-jet and 3-jet regions ($Z + bb$ normalisation). The 2-lepton channel has the best constraining power on the Z+HF background, with extrapolation uncertainties applied to the normalisation in the 0-lepton region (0-to-2-lepton ratio). Additional uncertainties on the Z+HF composition(ratio of bb-to-$bc/bl/cc$ events) are also derived and implemented ($Z+bc$-to-$Z+bb$ ratio, $Z+cc$-to-$Z+bb$ ratio, $Z+bl$-to-$Z+bb$ ratio). Due to the small contribution of the $Z+cl$ and $Z+ll$ backgrounds, only a single prior normalisation uncertainty is considered for each process ($Z + cl$ normalisation, $Z + ll$ normalisation).

- **W+jets**: W+HF is a dominant background in the 0- and 1-lepton channels. Two floating normalisation factors for the overall W+HF background are used for the 2-jet and 3-jet regions ($W + bb$ normalisation). The 1-lepton channel W+HF CR has the best constraining power on the W+HF background, with extrapolation uncertainties applied to the normalisation in the 1-lepton signal region (W+HF CR to SR ratio), and to the normalisation in the 0-lepton region (0-to-1-lepton ratio). Additional uncertainties on the W+HF composition (ratio of bb-to-$bc/bl/cc$ events) are also derived and implemented implemented ($W + bc$-to-$W + bb$ ratio, $W + cc$-to-$W + bb$ ratio, $W + bl$-to-$W + bb$ ratio). Due to the small contribution of the $W + cl$ and $W + ll$ backgrounds, only a

single prior normalisation uncertainty is considered for each process ($W + cl$ normalisation, $W + ll$ normalisation).

- $\boldsymbol{t\bar{t}}$: $t\bar{t}$ is a dominant background in all three channels. The characteristics of the contribution of $t\bar{t}$ to the 0- and 1-lepton regions is very different to that in the 2-lepton channel. Generally, in 0- and 1-lepton events, there needs to be an object which has been missed or not reconstructed from the $t\bar{t}$ decay. In the 2-lepton channel, di-leptonic $t\bar{t}$ is the main contribution, with the event being fully reconstructed. For this reason, in 0- and 1-lepton, a single common floating $t\bar{t}$ normalisation is implemented, with extrapolation uncertainties applied to the normalisation in the 0-lepton region (0-to-1-lepton ratio). As the 3-jet region has the best constraining power on the $t\bar{t}$ normalisation, an extrapolation uncertainty is applied to the normalisation in the 2-jet region (2-to-3-jet ratio). In the 2-lepton channel, two floating normalisations are used for the 2-jet and 3+-jet regions, as each region has a corresponding top $e\mu$ CR, which can strongly constrain the tt normalisation.

- **Single top-quark**: As a sub-dominant background, single top-quark production is treated using a slightly simpler scheme compared to the $t\bar{t}$ and V+jets backgrounds. The single top-quark background is composed of 3 processes, t-channel, s-channel and Wt production. In the Wt- and t-channels, uncertainties are derived for the normalisation, acceptance and shapes of the m_{bb} and p_T^V distributions. For the Wt-channel, the estimated modelling uncertainties are based on the flavour of the two b-tagged jets (mentioned as Wt(bb) in Table 10.12. In the same table, this Wt(bb) uncertainty is compared with Wt(other) which are events where there are fewer b-jets present. The s-channel is sufficiently sub-dominant in all channels that no further acceptance or shape uncertainties are considered. Only a normalisation uncertainty is derived for the s-channel.

  The systematic uncertainties affecting the modelling of all the above mentioned background samples are summarised in Tables 10.12.

- **Diboson**: As diboson events are considered as signal events in the $VZ \to Vb\bar{b}$ analysis, a more complete model of the modelling systematic uncertainties is implemented. Shape variations are calculated for the scale variations, parton shower/underlying event (PS/UE), in both m_{bb} and p_T^V. The WW background is sub-dominant, and contributes $< 0.1\%$ of the total background in all channels, and so is only treated with a normalisation uncertainty. The most important contribution comes from the WZ and ZZ processes. for these, uncertainties associated to the overall normalization and the relative acceptance between the regions have been derived. Shape uncertainty is only considered for m_{bb} for both WZ and ZZ background, as the uncertainty was found to have a negligible impact on the p_T^V shape. The systematic uncertainties on diboson production are summarised in Table 10.13.

Z+Jets Uncertainties	
Z+ll normalisation	18%
Z+cl normalisation	23%
Z+HF normalisation	Floating (2-jet, 3-jet)
Z+bc-to-Z+bb ratio	30 - 40%
Z+cc-to-Z+bb ratio	13 - 15%
Z+bl-to-Z+bb ratio	20 - 25%
0-to-2 lepton ratio	7%
m_{bb}, p_T^V	S
W+Jets Uncertainties	
W+ll normalisation	32%
W+cl normalisation	37%
W+HF normalisation	Floating (2-jet, 3-jet)
W+bl-to-W+bb ratio	26% (0-lepton) and 23% (1-lepton)
W+bc-to-W+bb ratio	15% (0-lepton) and 30% (1-lepton)
W+cc-to-W+bb ratio	10% (0-lepton) and 30% (1-lepton)
0-to-1 lepton ratio	5%
W+ HF CR to SR ratio	10% (1-lepton)
m_{bb}, p_T^V	S
$t\bar{t}$(all are uncorrelated between the 0+1- and 2-lepton channels)	
$t\bar{t}$ normalisation	Floating (0+1-lepton, 2-lepton 2-jet, 2-lepton 3-jet)
0-to-1 lepton ratio	8%
2-to-3-jet ratio	9% (0+1-lepton only)
W+HF CR to SR ratio	25%
m_{bb}, p_T^V	S
Single top-quark)	
Cross-section	4.6% (s-channel), 4.4% (t-channel), 6.2% (Wt)
Acceptance 2-jet	17% (t-channel), 55% (Wt(bb)), 24% (Wt(other))
Acceptance 3-jet	20% (t-channel), 51% (Wt(bb)), 21% (Wt(other))
m_{bb}, p_T^V	S (t-channel, Wt(bb), Wt(other))
Multi-jet (Only 1-lepton))	
Normalisation	60 - 100% (2-jet), 90 - 140% (3-jet)
BDT template	S

Table 10.12: Summary of the systematic uncertainties in the background modelling for Z + jets, W + jets, $t\bar{t}$, single top-quark and multi-jet production. An 'S' symbol is used when only a shape uncertainty is assessed. The regions for which the normalisations float independently are listed in brackets. Where the size of an acceptance systematic uncertainty varies between regions, a range is displayed.

ZZ	
Normalisation	20%
0-to-2 lepton ratio	6%
Acceptance from scale variations	10 - 18%
Acceptance from PS/UE variations for 2 or more jets	6%
Acceptance from PS/UE variations for 3 jets	7% (0-lepton), 3% (2-lepton)
m_{bb}, p_T^V, from scale variations	S (correlated with WZ uncertainties)
m_{bb}, p_T^V, from PS/UE variations	S (correlated with WZ uncertainties)
m_{bb}, from matrix-element variations	S (correlated with WZ uncertainties)
WZ	
Normalisation	26%
0-to-1 lepton ratio	11%
Acceptance from scale variations	13 - 21%
Acceptance from PS/UE variations for 2 or more jets	4%
Acceptance from PS/UE variations for 3 jets	11%
m_{bb}, p_T^V, from scale variations	S (correlated with ZZ uncertainties)
m_{bb}, p_T^V, from PS/UE variations	S (correlated with ZZ uncertainties)
m_{bb}, from matrix-element variations	S (correlated with ZZ uncertainties)
WW)	
Normalisation	25%

Table 10.13: Summary of the systematic uncertainties in the background modelling for diboson production. An 'S' symbol is used when only a shape uncertainty is assessed and 'PS/UE' indicates parton shower/underlying event. When extracting the (W/Z)Z diboson production signal yield, as the normalisations are unconstrained, the normalisation uncertainties are removed. Where the size of an acceptance systematic uncertainty varies between regions, a range is displayed.

10.4.3 Uncertainties of the multi-jet background

Since this background is neglected in the 0- and 2-lepton channel, as will be shown later in Section 12.5, the systematic uncertainties on its estimate only affect the 1-lepton channel and are separately considered for the electron and muon sub-channels. Multi-jet estimation in the 1-lepton channel is obtained using data-driven method.

Systematic uncertainties impact the multi-jet estimation in two ways: either changing the m_T^W distributions used in the multi-jet template fits, thus impacting the extracted multi-jet normalisations, or directly changing the multi-jet BDT distributions used in the global likelihood fit.

The different variations are obtained by changing the definition of the multi-jet control region (more stringent isolation requirements, a different single-electron trigger to probe a potential trigger bias in the isolation requirements), and varying the normalisation of the contamination from the top ($t\bar{t}$ and Wt) and V+jets processes in the multi-jet control region. Then these respective variations in both sub-channels are added in quadrature for the normalisations, or considered as separate shape uncertainties.

Another systematic uncertainties can be considered that have an impact only on the multi-jet normalisation. The first results from the use of another discriminant variable instead of m_T^W for the template fit (the azimuthal separation between the directions of the lepton transverse momentum and the vectorial sum of the momenta

of the two or three jets) and. The second, for the electron sub-channel only, is the inclusion of the $E_T^{miss} < 30$ GeV region, which significantly enhances the multi-jet contribution in the template fit. More details will be given later in Chapter 12.

10.5 Statistical Analysis

This Section contains a brief summary of the statistical procedures implemented in the analyse described in this thesis in order to extract the final results. The main statistical model used to perform the analyses is the binned Likelihood. The likelihood function $\mathcal{L}(\mu, \theta)$ is built as the product of Poisson probability terms over the bins of the input distributions. Although extracting the signal significance is one of the main aims of the analysis, it is interesting to measure the compatibility of the signal strength with the SM. In this model, the likelihood function is taking into account the scaling factor for the expected signal rate (signal strength μ) as the parameter of interest under study. The signal strength, in the searches for the SM Higgs boson presented in this work, is defined as the ratio of the measured Higgs rate to its SM prediction:

$$\mu = \frac{\sigma.BR}{\sigma_{SM}.BR_{SM}} \tag{10.2}$$

The signal strength μ is extracted by maximising the likelihood.

All the systematic uncertainties introduced in the previous section enter the liklihood as nuisance parameters (NPs), θ. Most of the uncertainties discussed in Section 10.4 are constrained with Gaussian or log-normal probability density functions [172]. The normalisations of the largest backgrounds, $t\bar{t}$, W+HF and Z+HF, can be reliably determined by the fit, so they are left unconstrained in the likelihood.

In addition, the uncertainties due to the limited number of events in the simulated samples used for the background predictions are included using the Beeston-Barlow technique [202]. The systematic variations that are subject to large statistical fluctuations are smoothed, and systematic uncertainties that have a negligible impact on the final results are pruned away region-by-region.

In this model, the profile-likelihood test statistic, q_0, is defined as logarithmic ration of the profile-likelihood ratio. In the search for the VH($b\bar{b}$), one can use the probability value or p-value, p_0, to determine the significance of discovery of a signal, and the compatibility of the observed data with the background-only model. A small p_0 therefore corresponds to a low false positive probability, and can be converted into standard deviations (σ) of the Gaussian distribution using the normal inverse cumulative distribution function. A p_0 value of 1.35 $\times 10^{-2}$ % corresponds to a 3 σ

deviation from the background-only model. A p_0 value of 2.87 $\times 10^{-5}$ % corresponds to a 5 σ deviation from the background-only model, and is generally used as the benchmark deviation required for discovery in high energy physics.

10.5.1 Multivariate analysis

Multivariate analyses (MVAs) are used in a variety of high energy physics analyses to offer increased signal purity and background rejection. This is achieved through the combination of a well-chosen set of discriminating input variables which the multivariate algorithm is trained on, to construct a one dimensional discriminant.

When searching for the SM VH$\rightarrow V b\bar{b}$ signal, the dijet mass, m_{bb}, is the variable which provides the single largest sensitivity to the signal. However, a number of other variables exist, which are only partially correlated with m_{bb}, and can be used to increase the sensitivity of the analysis, such as $\Delta R(b,b)$ or p_T^V. A number of these variables can be combined using a boosted decision tree (BDT) to boost the sensitivity of the analysis. In the SM VH$\rightarrow V b\bar{b}$ analysis, eight to thirteen input variables describing the kinematics of the events are used depending on the channels, of which m_{bb}, p_T^V and $\Delta R(b_1,b_2)$ (where b_1 and b_2 refer to the two b-tagged jets) are the most discriminating.

An iterative procedure is used to select the input variables for the BDT. Starting with m_{bb}, one variable is tested at a time, selecting the variable which yields the largest improvement in sensitivity. The procedure is repeated, adding one variable at a time, until no further improvement in the sensitivity is observed. Eight BDTs are trained in total, one for each signal region in each channel. For each signal region of the analysis a separated "2-fold cross-validation" training is performed. The 2-fold procedure is done by performing one training using even (odd) event-numbered MC events, and then the training is applied to odd (even) events, thereby ensuring orthogonality between the samples the algorithm is trained on and evaluated on. The final discriminant is then build by summing the multivariate discriminant of the even and odd events since no difference in the physics is expected between them. Due to varying kinematics and background compositions separate trainings increase the sensitivity of the analysis. The nominal one ($\mathrm{BDT_{VH}}$) is designed to separate Higgs boson events from the sum of expected backgrounds. The $\mathrm{BDT_{VH}}$ multivariate discriminant output distributions in these regions are input to the fit [190].

The post-fit normalisation factors of the unconstrained backgrounds in the global likelihood fit to the 13 TeV data are shown in Table 10.14. In the two W+HF control regions of the 1-lepton channel the event yields are used. In the four $e\mu$ control regions of the 2-lepton channel, the m_{bb} distributions are input to the fit, except for the 2-jet category of the high-p_T^V region, where the event yield is used.

Process	Normalisation factor
$t\bar{t}$ 0- and 1-lepton	0.98 ± 0.08
$t\bar{t}$ 2-lepton 2-jet	1.06± 0.09
$t\bar{t}$ 2-lepton 3-jet	0.95± 0.06
W+HF 2jet	1.19 ± 0.12
W+HF 3jet	1.05±0.12
Z+HF 2jet	1.37±0.11
Z+HF 3jet	1.09±0.09

Table 10.14: Factors applied to the nominal normalisations of the t t , W + HF and Z + HF backgrounds, as obtained from the global likelihood fit to the 13 TeV data for the nominal multivariate analysis, used to extract the Higgs boson signal. The errors represent the combined statistical and systematic uncertainties.

In the MVA approach, the total statistical uncertainty is defined as the uncertainty in μ when all the NPs are fixed to their best-fit values. The total systematic uncertainty is then defined as the difference in quadrature between the total uncertainty in μ and the total statistical uncertainty. Table 10.15 shows the breakdown of the error on μ in the different sources of uncertainty. The impact of a category of systematic uncertainties is defined as the difference in quadrature between the uncertainty in μ computed when all NPs are fitted and that when the NPs in the category are fixed to their best-fit values. Furthermore, it is worth noting that among the systematic uncertainties, the uncertainties due to the modelling of the signal play a dominant role, followed by the statistical fluctuations in the MC simulation due to the limited size of the simulated samples. This uncertainty in particular could be directly improved by increasing the size of the simulated samples (in principle a simple task, but often technically demanding). Among the experimental systematics, the flavour-tagging uncertainties play the stronger role, specially the b-tagging uncertainty. This type of uncertainties could also largely benefit from the increased statistics collected by the LHC data-taking, since they are extracted from data measurements. The largest single experimental systematic contribution arises from the b-jet scale factor can be improved as the b-tagging efficiency improves.

10.5.2 Dijet-mass analysis

In the dijet-mass analysis, fourteen signal regions are considered due to the extra splitting at $p_T^V = 200$ GeV in all channels. The dijet-mass analysis is performed as cross-check of the MVA approach. In the dijet-mass analysis, the m_{bb} distributions are input to the fit in all categories, except for the 2-jet medium- and high-p_T^V categories of the 2-lepton $e\mu$ control region, where the event yield is used.

Source of uncertainty		σ_μ
Total		0.259
Statistical		0.161
Systematic		0.203
Experimental uncertainties		
Jets		0.035
E_T^{miss}		0.014
Leptons		0.009
b-tagging	b-jets	0.061
	c-jets	0.042
	light-flavour jets	0.009
	extrapolation	0.008
Pile-up		0.007
Luminosity		0.023
Theoretical and modelling uncertainties		
Signal		0.094
Floating normalisations		0.035
Z+jets		0.055
W+jets		0.060
$t\bar{t}$		0.050
Single top quark		0.028
Diboson		0.054
Multi-jet		0.005
MC statistical		0.070

Table 10.15: Breakdown of the contributions to the uncertainty in μ. The sum in quadrature of the systematic uncertainties attached to the categories differs from the total systematic uncertainty due to correlations.

10.5.3 Diboson analysis

The main MVA analysis has been validated by measuring the diboson VZ signal strength parameter μ_{VZ}. In this diboson anlysis, the $\mathrm{BDT_{VZ}}$ output distributions are used as inputs to the fit, instead of $\mathrm{BDT_{VH}}$ defined for the nominal MVA analysis. The parameter of interest, μ_{VZ}, is defined as the signal strength of the combined WZ and ZZ diboson processes. The SM Higgs boson is included in the diboson analysis as a background process normalised to the predicted SM cross-section with an uncertainty of 50% [203].

10.6 Results

In this Section, results from the the SM Higgs boson search in the mode VH$\rightarrow V b\bar{b}$ at $\sqrt{s}$ = 13 TeV are presented.

10.6.1 Results of the Multivariate analysis

Post-fit BDT output distributions in the 0-, 1-, and 2-lepton channels in the most sensitive, high-p_T^V, region are presented in Figure 10.3. The background prediction in all post-fit distributions is obtained by normalising the backgrounds and setting the nuisance parameters according to the results of the signal extraction fit. Good post-fit agreement between data and MC is achieved for all these variables in all regions. Table 10.16 presents the post-fit signal and background yields for all signal regions.

The Higgs signal strength extracted from the fit, p_0 and significance values from the combined fit with a single signal strength, and from a fit where the lepton channels each have their own signal strength are quoted in Table 10.17. The probability p_0 of obtaining a signal at least as strong as the observation from background alone is 5.3×10^{-7}, whilst the expected value is 7.3×10^{-6}. The probability that the signal strengths measured in the three lepton channels are compatible is 80%. The observation corresponds to an excess with a significance of 4.9 σ, to be compared with an expectation of 4.3 σ. The fitted value of the signal strength is:

$$\mu_{VH}^{bb} = 1.16^{+0.27}_{-0.25} = 1.16 \pm 0.16(stat.)^{+0.21}_{-0.19}(syst.)$$

Figure 10.4 shows the data, background and signal yields, where final-discriminant bins in all analysis regions are combined into bins of log_{10}(S/B), with S(B) the signal (background) yield in each bin. The VH(bb) signal contribution is scaled to the fitted signal strength, μ = 1.16. The pull, in this plot, corresponds to the

difference between data and the background-only model, divided by the statistical uncertainty. The full line indicates the pull of the prediction for signal and background with respect to the background-only prediction. Good agreement between data and simulation is observed over the full range of S/B bins.

A combined fit is also performed separating the Higgs signal strength in WH and ZH production modes (still including all regions in the combined fit mode). The signal strength parameter is floated independently for each signal process (WH/ZH) in the fit to data, and without changes in the background fit model. The results of this fit are shown in Figure 10.5. Good agreement between the signal strengths in the WH and ZH channels is observed, with a compatibility of 84%. The WH and ZH production modes have observed (expected) significances of 2.5 σ (2.3 σ) and 4.0 σ (3.5 σ), respectively, with a linear correlation between the two signal strengths of-1%.

10.6.2 Results of the dijet-mass analysis

Although the dijet-mass analysis sensitivity is lower than that of the MVA analysis, consistency between the background model and fit results can provide further validation of the MVA results shown in the previous section. In this section, results from the dijet-mass m_{bb} fit to data are presented.

Figure 10.6 shows the m_{bb} distribution for the 13 TeV data after subtraction of all backgrounds except for VH diboson production. In this figure, the contribution of all signal regions from all lepton channels is combined, weighted by their respective ratios of fitted Higgs boson signal to background yields (S/B) for that region. The Higgs boson signal contribution can be visually seen as a shoulder on the side of the diboson peak, in good agreement with the data points.

From the fit to all analysis regions, the observed (expected) significance is 3.6 σ (3.5 σ), this to be compared to the 4.9 σ (4.3 σ) for the MVA analysis, which is thus the main analysis. In the dijet-mass analysis, the observed signal strength combined from all channels is:

$$\mu_{VH}^{bb} = 1.16^{+0.36}_{-0.33} = 1.16 \pm 0.20(stat.)^{+0.30}_{-0.26}(syst.),$$

which is in good agreement with the result of the MVA analysis. The signal strengths in the individual channels from the dijet-mass analysis is found to be compatible with those from the multivariate analysis.

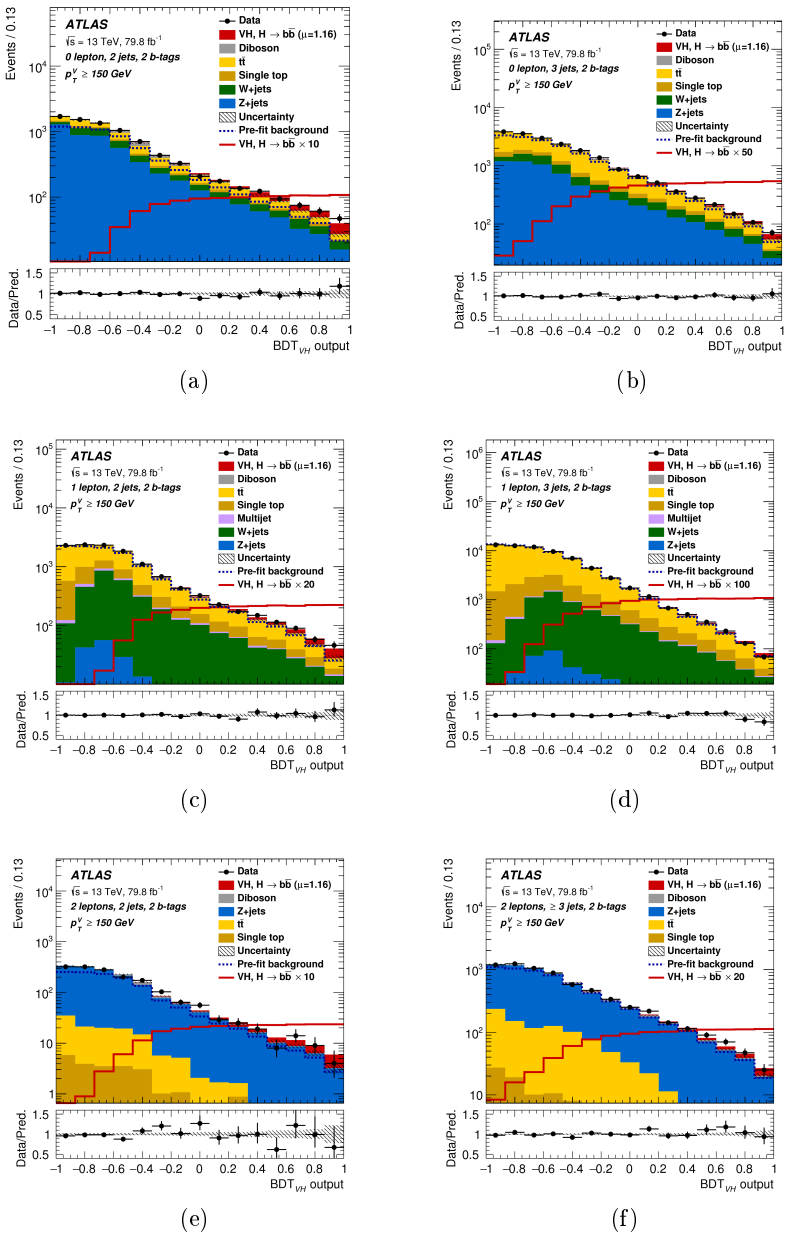

Figure 10.3: The $\mathrm{BDT_{VH}}$ output post-fit distributions in the 0-lepton (top), 1-lepton (middle) and 2-lepton (bottom) channels for 2-b-tag events, in the 2-jet (left) and exactly 3-jet (or ≥ 3 jets for the 2-lepton case) (right) categories in the high-p_T^V region. The background contributions after the global likelihood fit are shown as filled histograms. The Higgs boson signal ($m_H = 125$ GeV) is shown as a filled histogram on top of the fitted backgrounds normalised to the signal yield extracted from data ($\mu = 1.16$), and unstacked as an unfilled histogram, scaled by the factor indicated in the legend. The dashed histogram shows the total pre-fit background. The size of the combined statistical and systematic uncertainty for the sum of the fitted signal and background is indicated by the hatched band. The ratio of the data to the sum of the fitted signal ($\mu = 1.16$) and background is shown in the lower panel. The $\mathrm{BDT_{VH}}$ output distributions are shown with the binning used in the global likelihood fit.

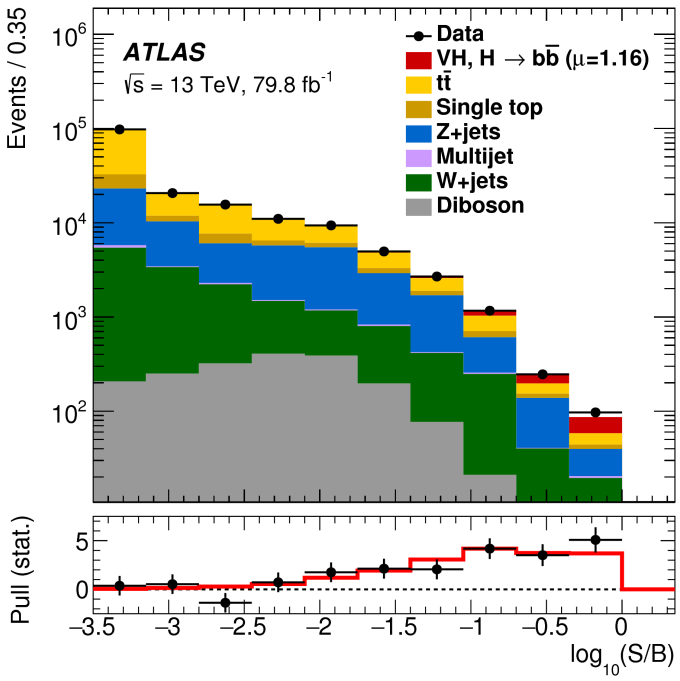

Figure 10.4: Event yields as a function of log_{10}(S/B) for data, background and a Higgs boson signal with $m_H = 125$ GeV. Final-discriminant bins in all regions are combined into bins of log_{10}(S/B) , with S being the fitted signal and B the fitted background yields. The Higgs boson signal contribution is shown after rescaling the SM cross-section according to the value of the signal strength extracted from data ($\mu = 1.16$). In the lower panel, the pull of the data relative to the background (the statistical significance of the difference between data and fitted background) is shown with statistical uncertainties only. The full line indicates the pull expected from the sum of fitted signal and background relative to the fitted background.

	0-lepton		1-lepton		2-lepton		75 GeV< p_T^V > 150 GeV, 2-b-tag	
	p_T^V > 150 GeV, 2-b-tag		p_T^V > 150 GeV, 2-b-tag		p_T^V > 150 GeV, 2-b-tag			
Process	2-jet	3-jet	2-jet	3-jet	2-jet	≥3-jet	2-jet	≥3-jet
Z+ll	17±11	27±18	2±1	3±2	14±9	49±32	4±3	30±19
Z+cl	45 ± 18	76 ± 30	3±1	7± 3	43±17	170±67	12±5	88±35
Z+HF	4770±140	5940±300	180±9	348±21	7400±120	14160±220	1421±34	5370±100
W+ll	20± 13	32±22	31±23	65±48	< 1	< 1	< 1	< 1
W+cl	43±20	83±38	139±67	250±120	< 1	< 1	< 1	< 1
W+HF	1000±87	1990±200	2660±270	5400±670	2±0	13±2	1±0	4±1
Single top quark	368±53	1410±210	2080±290	9400±1400	188±89	440±200	23±7	93±26
$t\bar{t}$	1333±82	9150±400	6600±320	50200±1400	3170±100	8880±220	104±6	839±40
Diboson	254±49	318±90	178±47	330 ±110	152±32	355±68	52±11	196±35
Multi-jet e sub-ch	-	-	100±100	41±35	-	-	-	-
Multi-jet μ sub-ch	-	-	138±92	260±270	-	-	-	-
Total bkg.	7850±90	19020±140	12110±120	66230±270	10960±100	24070±150	1620±30	6620±80
Signal (post-fit)	128±28	128±29	131±30	125±30	51±11	86±22	28±6	67±17
Data	8003	19143	12242	66348	11014	24197	1626	6686

Table 10.16: The Higgs boson signal, background and data yields for each signal region category in each channel after the full selection of the multivariate analysis. The signal and background yields are normalised to the results of the global likelihood fit. All systematic uncertainties are included in the indicated uncertainties. An entry of "-" indicates that a specific background component is negligible in a certain region, or that no simulated events are left after the analysis selection.

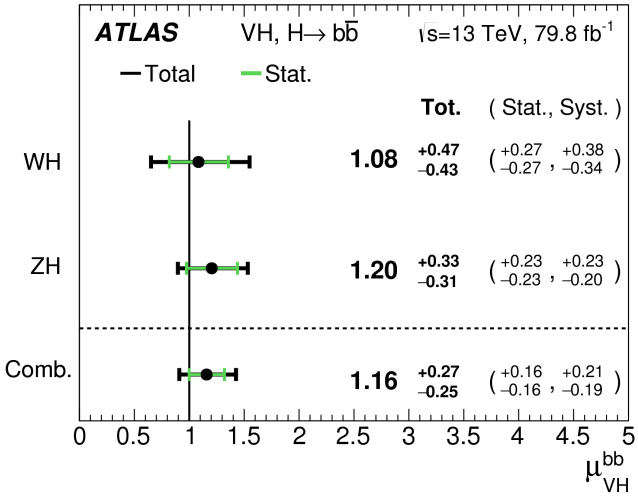

Figure 10.5: The fitted values of the Higgs boson signal strength μ_{VH}^{bb} for $m_H = 125$ GeV for the WH and ZH processes and their combination. The individual μ_{VH}^{bb} values for the (W/Z)H processes are obtained from a simultaneous fit with the signal strength for each of the WH and ZH processes floating independently. The probability of compatibility of the individual signal strengths is 84%.

Channel	Signal strength	p_0		Significance	
		Exp.	Obs.	Exp.	Obs.
0-lepton	$1.04^{+0.34}_{-0.32}$	9.5×10^{-4}	5.1×10^{-4}	3.1	3.3
1-lepton	$1.09^{+0.46}_{-0.42}$	8.7×10^{-3}	4.9×10^{-3}	2.4	2.6
2-lepton	$1.38^{+0.46}_{-0.42}$	4.0×10^{-3}	3.3×10^{-4}	2.6	3.4
VH, H $\to b\bar{b}$ combination	$1.16^{+0.27}_{-0.25}$	7.3×10^{-6}	5.3×10^{-7}	4.3	4.9

Table 10.17: Measured signal strengths with their combined statistical and systematic uncertainties, expected and observed p_0 and significance values (in standard deviations) from the combined fit with a single signal strength, and from a combined fit where each of the lepton channels has its own signal strength, using 13 TeV data.

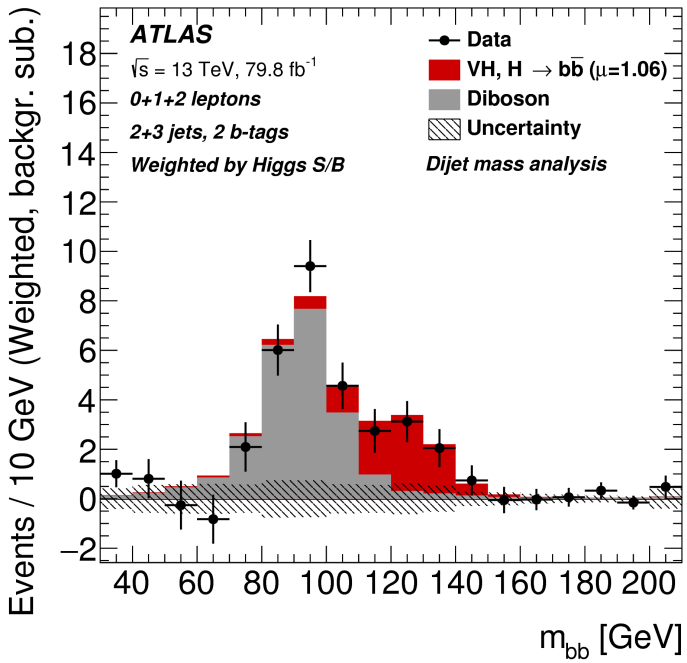

Figure 10.6: The distribution of m_{bb} in data after subtraction of all backgrounds except for the WZ and ZZ diboson processes, as obtained with the dijet-mass analysis. The contributions from all lepton channels, p_T^V regions and number-of-jets categories are summed and weighted by their respective S / B , with S being the total fitted signal and B the total fitted background in each region. The expected contribution of the associated WH and ZH production of a SM Higgs boson with $m_H = 125$ GeV is shown scaled by the measured signal strength ($\mu = 1.06$). The size of the combined statistical and systematic uncertainty for the fitted background is indicated by the hatched band.

10.6.3 Results of the diboson analysis

The MVA analysis has been validated by the measuring the diboson VZ production based on the multivariate analysis described in Section 10.5.3.

The signal strength for the 13 TeV dataset, which is consistent with the SM prediction, is found to be:

$$\mu_{VZ}^{bb} = 1.20^{+0.20}_{-0.18} = 1.20 \pm 0.08(stat.)^{+0.19}_{-0.16}(syst.)$$

10.7 Results of combinations

10.7.1 Run-1 and Run-2 combination for VH,H$\to b\bar{b}$

The result of the Run-2 analysis is combined with the Run-1 VH,H$\to b\bar{b}$ result [204]. The Run-1 result includes 4.7 fb^{-1} of data collected at $\sqrt{s} = 7$ TeV, and 20.3 fb^{-1} collected at $\sqrt{s} = 8$ TeV between 2011 and 2012.

The observed p_0 value is 5.5 $\times 10^{-7}$, corresponding to an excess with a significance of 4.9 σ, compared with an expectation of 5.1 σ. This corresponds to a measured signal strength:

$$\mu_{VH}^{bb} = 0.98^{+0.22}_{-0.21} = 0.98 \pm 0.14(stat.)^{+0.17}_{-0.16}(syst.),$$

Fits are also performed with the signal strengths floated independently for the WH and ZH production processes. Consistent signal strengths between the WH and ZH channels are observed, with the level of compatibility at 72%, and the results of this fit are shown in Figure 10.7.

10.7.2 Observation of H$\to b\bar{b}$ decays: combination of all production modes

A search for the H$\to b\bar{b}$ decay has been performed by combining the results from all the Higgs production modes. The final results for the H$\to b\bar{b}$ decay has been found by combing the VH result, presented in the previous section, along with results from the SM Higgs boson decaying into a $b\bar{b}$ pair produced in association with a $t\bar{t}$ pair as well as in vector-boson fusion for both Run-1 and Run-2.

An observed significance for the H$\to b\bar{b}$ decay of 5.4 σ has been measured, to be compared with an expectation of 5.5 σ. For all channels combined and assuming the

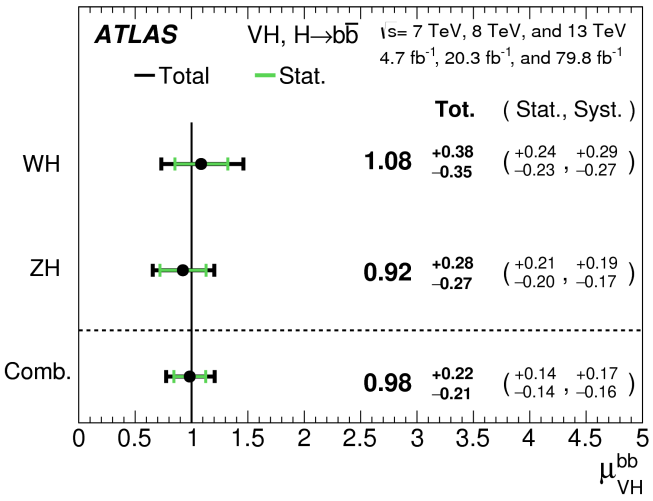

Figure 10.7: The fitted values of the Higgs boson signal strength μ_{VH}^{bb} for $m_H = 125$ GeV for the WH and ZH processes and their combination, using the 7 TeV, 8 TeV and 13 TeV data. The individual μ_{VH}^{bb} values for the (W / Z) H processes are obtained from a simultaneous fit with the signal strengths for each of the WH and ZH processes floating independently.

branching fractions are as predicted by the SM, this is corresponding to the fitted value of the signal strength :

$$\mu_{H\to b\bar{b}} = 1.01 \pm 0.20 = 1.01 \pm 0.12(stat.)^{+0.16}_{-0.15}(syst.),$$

Table 10.18 shows the significance values independently for the VBF+ggF, $t\bar{t}$H and VH channels in the combination of the Run-1 and Run-2 data, and for the combined global likelihood fit [172]. One can notice that the VH production modes is the most significance compared to other production modes. This experimental result confirms the aforementioned fact in the previous chapter that the VH production mode is the most sensitive channel.

Moreover, Figure 10.8 displays the signal strengths separately for all the production modes along with their combination for the combined Run-1 and Run-2. The individual signal strength in this plot has been obtained from a fit where the signal strengths are fitted simultaneously for the three production modes. Fits are also performed with the signal strengths floated independently for each of the production processes in both Run-1 and Run-2. The probability of compatibility of the six individual measurements, for the three production modes from Run-1 and Run-2, is 54%.

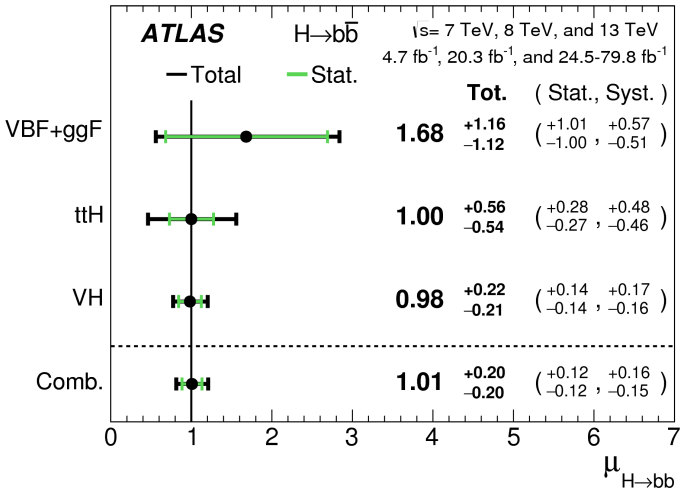

Figure 10.8: The fitted values of the Higgs boson signal strength $\mu_{H\to b\bar{b}}$ for $m_H = 125$ GeV separately for the VH, $t\bar{t}$H and VBF+ggF analyses along with their combination, using the 7 TeV, 8 TeV and 13 TeV data. The individual $\mu_{H\to b\bar{b}}$ values for the different production modes are obtained from a simultaneous fit with the signal strengths for each of the processes floating independently. The probability of compatibility of the individual signal strengths is 83%.

Channel	Significance	
	Exp.	Obs.
VBF+ggF	0.9	1.5
$t\bar{t}$H	1.9	1.9
VH	5.1	4.9
H→ $b\bar{b}$ combination	5.5	5.4

Table 10.18: Expected and observed significance values (in σ) for the H→ $b\bar{b}$ channels fitted independently and their combination using the 7 TeV, 8 TeV and 13 TeV data.

Channel	Significance	
	Exp.	Obs.
H$\to ZZ^* \to 4l$	1.1	1.1
H$\to \gamma\gamma$	1.9	1.9
H$\to b\bar{b}$	4.3	4.9
VH combined	4.8	5.3

Table 10.19: Expected and observed significance values (in standard deviations) for the VH production channels from the combined fit and from a combined fit where each of the lepton channels has its own signal strength, using 13 TeV data.

10.7.3 Observation of VH production: combination of all decay modes

Results of other Run-2 search for the Higgs boson produced in the VH production mode, but decaying into either two photons or four leptons via ZZ^* decays is combined with the Run-2 VH,H$\to b\bar{b}$ result to preform a search of the VH production mode.

The observed significance for the combined VH production from all decay modes is 5.3 σ, to be compared with an expectation of 4.8 σ.

Table 10.19 shows the significance values for the combined fit, as well as for a fit where the four-lepton (H$\to ZZ^* \to 4l$), diphoton (H$\to \gamma\gamma$) and H$\to b\bar{b}$ decay modes each have their own signal strength for the Run-2 data [172]. It is worth to note here that the H$\to b\bar{b}$ decay mode is the dominant one.

Assuming the branching fractions are as predicted by the SM, the fitted value of the VH signal strength for all channels combined is:

$$\mu_{VH} = 1.13^{+0.24}_{-0.23} = 1.13 \pm 0.15(stat.)^{+0.18}_{-0.17}(syst.),$$

The signal strengths obtained from the fit where individual signal strengths are fitted for the three decay modes are displayed in Figure 10.9, along with their combination.

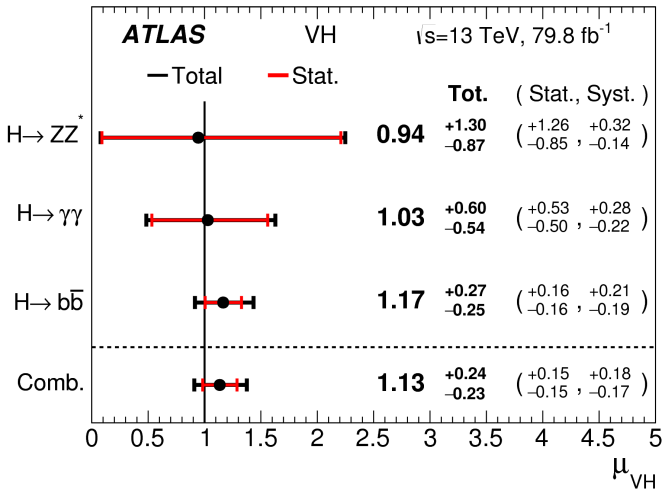

Figure 10.9: The fitted values of the Higgs boson signal strength μ_{VH} for $m_H = 125$ GeV separately for the H$\to b\bar{b}$, H$\to \gamma\gamma$ and H$\to ZZ^* \to 4l$ decay modes, along with their combination. The individual μ_{VH} values for the different decay modes are obtained from a simultaneous fit with the signal strengths for each of the processes floating independently. The probability of compatibility of the individual signal strengths is 96%.

Chapter 11

Feasibility study of using taus in VH(bb) analysis

Contents

11.1 Motivation . . . 231
11.2 Methodology of the feasibility study . . . 232
11.2.1 Event Samples . . . 232
11.2.2 Analysis chain . . . 233
11.2.3 CxAOD Framework . . . 234
11.3 Tau identification and selection . . . 235
11.4 Z($\tau\tau$)H(bb) channel . . . 238
11.4.1 The hadronic channel, $\tau_{had}\tau_{had}$ . . . 239
11.4.2 The semi-leptonic channel, $\tau_{lep}\tau_{had}$ . . . 243
11.4.3 Optimizing the p_T^Z cut in the semi-leptonic channel . . . 247
11.5 W($\tau\nu$)H(bb) channel . . . 248
11.6 Conclusion . . . 249

11.1 Motivation

As introduced in chapter 10, the VH(bb) analysis splits in 3 channels: 0, 1,and 2 lepton(s) in the final state. While the electrons and muons are usually chosen in the cases where the leptons are selected by the analysis, We don't have any channel in the VH(bb) analysis that consider the tau leptons in the final state. More precisely, we don't have a dedicated W($\tau\nu$)H(bb) or Z($\tau\tau$)H(bb) in the current VH(bb) analysis. The Feynman diagram of the WH/ZH channel with taus in the final state is shown in Figure 11.1. About 35% τ lepton undergo leptonic decay and present an electron or muon in the final state, the default 1-lepton channel selections can already cover such events efficiently. In the other hand, about 65% τ lepton undergo hadronic decay, and a hadronic τ jet presents in the final state. The default 0-lepton channel actually has some sensitivities for such events since no hadronic τ veto selection presents in this channel.

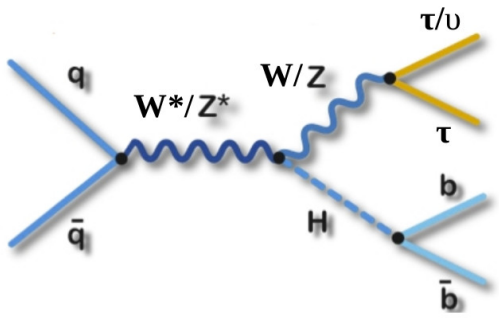

Figure 11.1: Tree-level Faynman diagram representing quark-initiated WH/ZH process with the tau leptons in the final state. The ZH process is the signal Feynman diagram searched for in this feasibility study.

Process	Sample ID	MC Generator	ME PDF	UE model
$qq \to ZH \to llbb$	345055	PowhegPythia8	NNPDF3	AZNLO
$gg \to ZH \to llbb$	345057	PowhegPythia8	NNPDF3	AZNLO

Table 11.1: Specification of event sample used in this study. The acronyms ME and UE stand for matrix element and underlying event, respectively.

In this chapter, I review the studies concerning using the tau leptons in the final state specifically in the Z($\tau\tau$)H(bb) channel in order to examine and decide if channels explicitly selecting tau decays could bring additional sensitivity for the VH(bb) analysis or not. In this study the two taus decay either hadronically into mainly charged and neutral pions (i.e. $\tau_{had}\tau_{had}$ channel) or semi-leptonically where one tau decays hadronically and the other decays leptonically into an electron or muon and neutrinos (i.e. $\tau_{lep}\tau_{had}$ channel). A summary of a similar study in the W($\tau\nu$)H(bb) channel is given in section 11.5.

11.2 Methodology of the feasibility study

In the following, the framework and method used to select events in this study are illustrated.

11.2.1 Event Samples

This study was performed using Monte Carlo (MC) simulated unskimmed (qqZH and ggZH) signal samples derivations. These samples generated at a center of mass 13 TeV subject to the full GEANT 4 ATLAS detector simulation. Details about the used MC samples are in Table 11.1.

The MC events used in this study are normalized to luminosity value of 36.8 fb^{-1}. The output from this step of the analysis is a set of nTuples root files which is used afterwards for further analysis.

11.2.2 Analysis chain

Any data analysis needs special processing steps to manipulate data toward the final results. In ATLAS experiment, after collecting the Raw data, "Athena"[205] framework processes these raw data to produce Analysis Object Data or xAOD input files. Then a "derivation" step comes to produce the so called Derived-xAOD (DxAOD). Each DxAOD is produced from the xAOD applying any/all of [206]:

- Skimming: is the removal of whole events, based on some criteria related to the features of the event.

- Thinning: is the removal of individual objects within an event, based on some criteria related to the features of the object.

- Slimming: is the removal of variables within a given object type, uniformly across all objects of that type and all events. Unlike the other operations, slimming does not vary depending on any event/object properties: the same variables are removed for every event and object.

The DxAOD files are then used as an input to a tool in a dedicated analysis framework to produce the final root files that is called "nTuples" used for the analysis. The ATLAS analysis model for Run-2 is shown in Figure 11.2

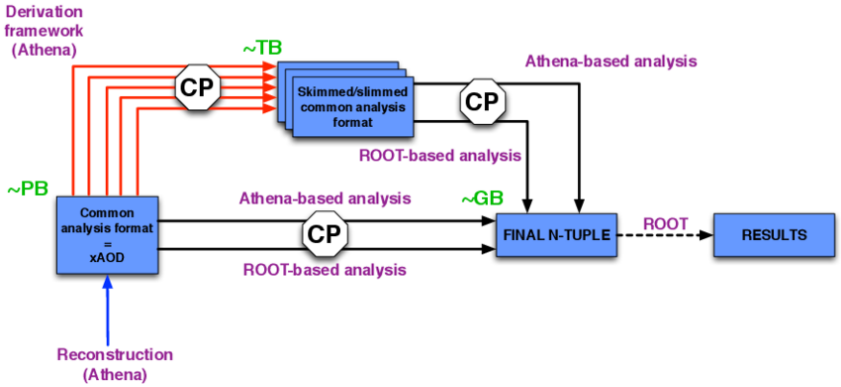

Figure 11.2: The ATLAS analysis model for Run-2. [206]

The samples used for this study, listed in the previous section, are unskimmed ZH signal sample. This is done on purpose in order to gain as much as we can at the end of even selection for this specific analysis.

11.2.3 CxAOD Framework

The "CxAOD Framework" is used to perform the analysis in this study. The CxAOD Framework is a general and common framework officially used by the VH(bb) analysis groups. It is developed for all sub-channels and contains many packages and tools related to the specificity of each of them. Depending on the sub-channel final state topology, selections are applied in the framework.

There is two level of selection, the first is done within the "CxAODMaker" tool and the other within the "CxAODReader" tool. The workflow of the CxAOD Framework is illustrated in Figure 11.3.

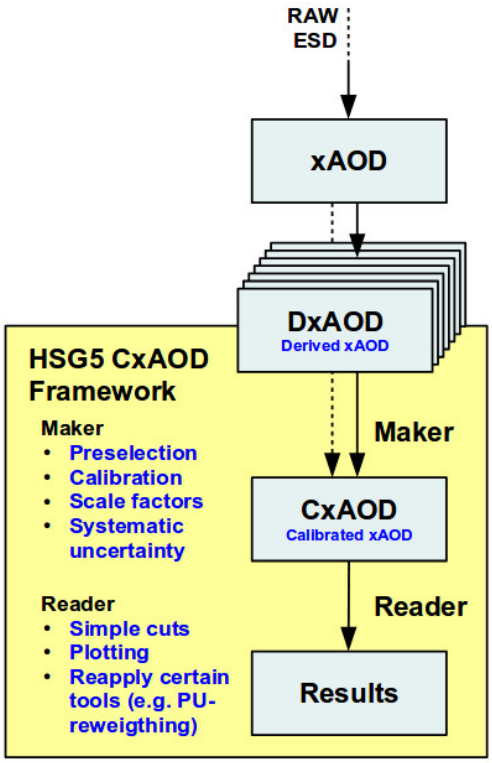

Figure 11.3: Overview of the CxAOD Framework workflow. The framework made of two key algorithm: CxAODMaker and CxAODReader. At each level, basic object and event selections are applied to serve the specific analysis.

The CxAODMaker is the tool that runs on DxAOD inputs to produce the Calibrated xAOD (CxAOD) by applying a series of object selections and low level event selections (pre-selections). Some of the preselection that could be applied at the maker level are listed in Table 11.2.

Using CxAOD files produced from the CxAODMaker, the CxAODReader accesses the pre-computed physics objects and applies analysis level event selection.

CxAODMaker Preselection		
	Standard 0-lep analysis	Standard 1-lep analysis
Lepton preslection	lepton veto (0loose lepton)	1 tight lepton and 2^{nd} lepton veto
Lepton p_T	$>$ 7 GeV	
Jet preselection	nSignalJet$\geq$2	
Jet p_T	$>$ 20 GeV	
E^T_{miss}	$>$ 140 GeV	-

Table 11.2: CxAODMaker preselection applied to DxAOD events to produce CxAOD. For this specific study, the CxAODMaker preselection were not applied. [207]

The standard analysis event selection in each sub-channel (0-, 1- and 2-lepton) are mentioned in section 10.3.3. In addition, different corrections ranging from luminosity to b-tagging scale factor are applied in the CxAODReader.

In this study, no selections have been used at the CxAODMaker level (i.e. all the default selection such as 0loose lep, nJet$\geq$2, and E_T^{miss} >140 GeV have been removed) so we can keep the maximum possible number of events to be further analysed by the CxAODReader. Cuts are applied at the CxAODReader level or in the analysis step that is carried later on. In the CxAOdReader, I have implemented certain selections for each channel ($\tau_{had}\tau_{had}$ and $\tau_{lep}\tau_{had}$) that will be discussed in the next section.

After the CxAODReader selection, the last analysis step used a cut-based selection method. First, find among the physical quantities of each event those that are more "discriminant" and then apply cuts on these variables or on combinations of these variables. The selection procedure is a sequence of cuts, and is typically described by plots or table that are called "Cut-Flows". A cutflow diagram displays the events yield as a function of a series of applied cuts. The additional selection for each channel are optimized and examined with the help of "cutflow" diagrams. Using the cutflow diagrams we can understand the role each cut play in the event selection, how it affects the event yield and try to optimize the selection criteria.

11.3 Tau identification and selection

The tau lepton is the heaviest lepton with a mass of 1.77 GeV. The tau lepton mainly decays:

- leptonically into an electron or muon and neutrinos (Figure 11.4 (a)) with branching ratio (BR) $\approx$ 35%

- hadronically into mainly charged and neutral pions (Figure 11.4 (b)) with branching ratio (BR) $\approx$ 65%

The tau dominating decay modes and their corresponding branching ration(BR) are shown in Figure 11.5.

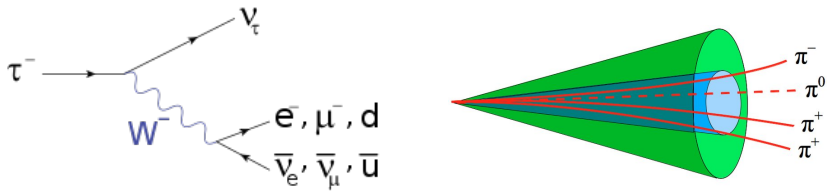

(a) (b)

Figure 11.4: (a) Feynman diagram of the tau leptonic decay by the emission of an off-shell W boson. (b) Typical signature of a hadronic tau decay.

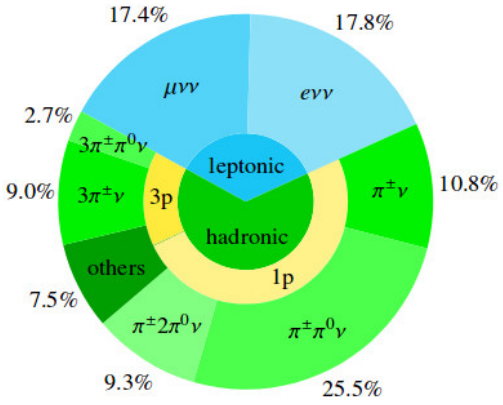

Figure 11.5: Overview of the dominating tau lepton decay modes. The category "others" contains decays with other charged or neutral mesons (mainly kaons), and higher number of neutral or charged pions.

The mean lifetime of the tau lepton is 290×10^{-15}s. As a consequence, a typical 50 GeV tau lepton travels ≈2 mm and decays before it reaches the first layer of the ATLAS detector. Hence, the tau lepton can not be detected directly and is identified by its decay products. A final state tau lepton is then regarded with all decay components: a lepton or hadronic jet and missing transverse energy from the neutrino(s).

In the object reconstruction based on detector hits, only the detectable decay components are of interest. Since neutrinos leave the detector unseen, the visible decay products are the lepton or the hadronic jet only. The electron or muon from the leptonic decay is nearly indistinguishable from primary (prompt) electrons or muons. In the object reconstruction these are thus treated as electron or muon candidates.

In the majority of hadronic tau decays, the hadrons are one or three charged pions and up to two neutral pions. The neutral pions immediately decay into two photons and are seen in the electromagnetic calorimeter. The charged pions leave a track in the inner detector and are stopped mainly in the hadronic calorimeter. The detector signature resembles jets in multi-jet events (QCD-jets). It is known that the multi-jet events occur at very high rates at the LHC and consequently QCD-jets represent the highest background to tau identification. The fact that hadronic tau decays consist of one or three charged hadrons is a starting point for the rejection of such jets. The decays are then referred to as 1-prong and 3-prong.

The tau leptons emerging from a collision event are mostly boosted and the decay products appear in a narrow cone in the direction of flight. The decay products are reconstructed as a jet. Also the fact that the tau lepton travels a small distance before it decays can be used for tau identification. This leads to a larger transverse impact parameter of the tracks and the possibility to reconstruct a secondary vertex in the case of a 3-prong decay.

A good identification of tau leptons is of great importance for this study. Equally important is a good rejection of objects with a similar detector signature, so that it is possible to select a sample that is dominated by genuine tau leptons. Many different algorithms are available to identify tau leptons. The BDT method is used for tau identification in this study [208].

The tau identification efficiency is the fraction of 1-prong (3-prong) taus reconstructed correctly as 1-track (3-track) τ_{had} candidates that passes the BDT identification cuts. And three working points (Tight, Medium and Loose) are defined. For each point corresponds an identification efficiency value. The combined efficiency is the product of the reconstruction and identification efficiency. Figure 11.6 shows the combined efficiency as function of tau p_T.

In this study the working point used for tau identification is "BDTMedium" which corresponding to a combined (reconstruction and identification) efficiency of about 50%. In addition to the requirement on the tau identification, some cuts were applied to select tau lepton. These cuts are often used only for overlap removal in the standard VH(bb) analysis. The tau lepton has to fulfil the following criteria:

- $p_T > 20$ GeV

- $|\eta| < 2.5$

- 1 or 3 tracks.

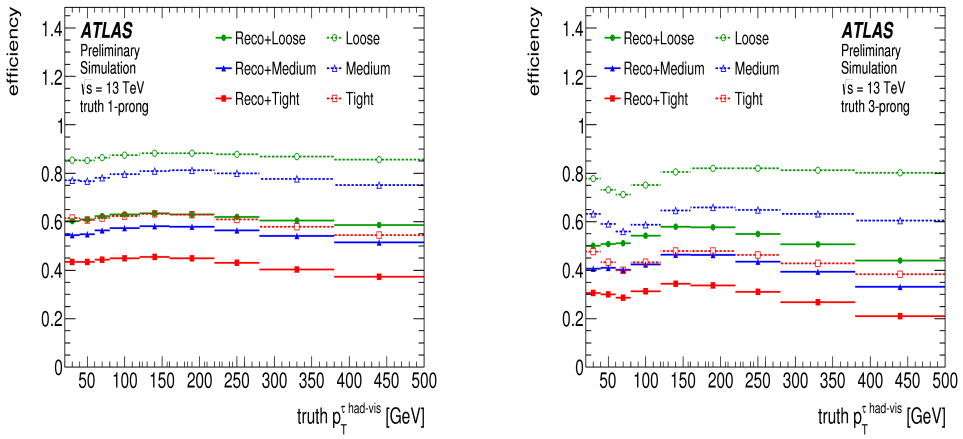

(a) (b)

Figure 11.6: Efficiency for hadronic tau identification (open symbols) and combined reconstruction and identification efficiency (full symbols) as a function of the hadronic tau p_T, for 1-track (a) and 3-track (b) hadronic tau candidates. [208]

11.4 Z($\tau\tau$)H(bb) channel

In this section, I will discuss in details my contribution to investigate the search in the Z($\tau\tau$)H(bb) channel. As mentioned before, we are trying to answer two questions: if adding a new channel to the current VH(bb) analysis that is involving the tau decays would be worth the effort or not? how much it would be possible to add to the current ZH yields?

Referring to the actual W/ZH(bb) analysis, the current ZH yields in the different channels: 0,1 and 2 leptons and for two jets categories: 2-jet and 3-jet can be found in Table 11.3. These yields are taken from the (Z$\rightarrow ee + \mu\mu + \tau\tau$)H($bb$) in the standard VH(bb) inputs. The 2 lepton channel is splitt into two regions according to p_T^Z range used, these regions are : high p_T^Z region with $p_T^Z > 150$ GeV and low p_T^Z region with $75 < p_T^Z < 150$ GeV. The total numbers in this table will be the reference value to compare with for all results found in this section.

As indicated earlier in section 11.3, there are two tau main decay modes, leptonic and hadronic. This leads to three $Z \rightarrow \tau\tau$ final states:

- $\tau_{had}\tau_{had}$: where both taus decays into hadronic jets. The BR $\approx$ 42.0% but the high branching ratio is affected by the difficulty to reconstruct efficiently the hadronic jets.

- $\tau_{lep}\tau_{had}$: where one tau decays leptonically and the other one decays hadronically. It has the highest branching ratio of $\approx$ 45.6%.

Sub-channel	2 Jets	3 Jets
0-lep	0.31	0.37
1-lep	0.98	1.65
2-lep ($p_T^Z > 150$ GeV)	11.27	30.12
2-lep ($75 < p_T^Z < 150$ GeV)	21.47	40.35
Total (Without/With 2-lep low p_T^Z region)	**12.56/34.04**	**32.14/72.49**

Table 11.3: The current ZH yields in the different channels: 0,1 and 2 leptons and for two jets categories: 2-jet and 3-jet. The 2 lepton channel is divided into: high-p_T^Z region with $p_T^Z > 150$ GeV and low-p_T^Z region with $75 < p_T^Z < 150$ GeV. The total yields is calculated with and without the low-p_T^Z region.

- $\tau_{lep}\tau_{lep}$: where both taus decay into leptons (e or μ) with BR $\approx 12.4\%$. Despite the clean signature of leptons, this decay channel is the less sensitive due to the presence of four neutrinos in the final state as well as low statistics.

In this study, only the first two configuration have been inspected. For each of these channels a specific selection criteria has been performed. The event selection criteria are explained in the following separately for each channel.

11.4.1 The hadronic channel, $\tau_{had}\tau_{had}$

11.4.1.1 Event selection criteria

For this channel, the standard 0-lepton analysis selection has been used. As stated before, No CxAODMaker selection has been applied. The default 0-lepton CxAODReader selections has been applied. In addition to the 0-lepton selections, additional selection are chosen to see how many signal events can be extracted and recuperated (i.e. collected and added to the standard analysis). Since at this level no background evaluation is done (e.g. no QCD rejection is applied), the event yield found by this study will represent the maximum obtainable yield.

The event selected for this channel are the events that do not pass the 0-lepton standard selection. Then they are required to satisfy the following criteria:

- No leptons (lepton veto is applied).

- nSignalJet ≥ 2.

- pass at least one of the tau triggers: single tau, di-tau, tau+MET. All the tau triggers used in this study are listed in Table 11.4 for 2015 and 2016 periods.

- pass the cuts listed in Table 11.5 and in the same order.

Trigger Name	Threshold [GeV]
Period 2015	
Single Tau Triggers	
HLT_tau80_medium1_tracktwo	80 GeV
HLT_tau80_medium1_tracktwo_L1TAU60	80 GeV
Di-Tau Triggers	
HLT_tau35_loose1_tracktwo_tau25_loose1_tracktwo_L1TAU20IM_2TAU12IM	35 GeV, 25 GeV
HLT_tau35_medium1_tracktwo_tau25_medium1_tracktwo_L1TAU20IM_2TAU12IM	35 GeV, 25 GeV
Tau+MET Triggers	
HLT_tau35_medium1_tracktwo_L1TAU20_tau25_medium1_tracktwo_L1TAU12_xe50	35 GeV, 25 GeV
HLT_tau35_medium1_tracktwo_L1TAU20_xe70_L1XE45	35 GeV
HLT_tau35_medium1_tracktwo_L1TAU20_tau25_medium1_tracktwo_L1TAU12_xe50w	35 GeV, 25 GeV
HLT_tau35_medium1_tracktwo_xe70_L1XE45 (w/J20)	35 GeV
Period 2016	
Single Tau Triggers	
HLT_tau80_medium1_tracktwo_L1TAU60	80 GeV
HLT_tau125_medium1_tracktwo	125 GeV
HLT_tau160_medium1_tracktwo	160 GeV
Di-Tau Triggers	
HLT_tau35_loose1_tracktwo_tau25_loose1_tracktwo	35 GeV, 25 GeV
HLT_tau80_medium1_TAU60_tau50_medium1_L1TAU12	80 GeV, 50 GeV
Tau+MET Triggers	
HLT_tau35_medium1_tracktwo_xe70_L1XE45	35 GeV
HLT_tau35_medium1_tracktwo_L1TAU20_tau25_medium1_tracktwo_L1TAU12_xe50	35 GeV, 25 GeV
HLT_tau35_medium1_tracktwo_tau25_medium1_tracktwo_xe50	35 GeV, 25 GeV

Table 11.4: Tau trigger list for 2015 and 2016 periods used for this study.

Cuts Applied in the $\tau_h\tau_h$ Channel	
nTags	$= 2$
pTB1	$> 45GeV$
nTaus	$>= 2$
p_T^Z	$> 150GeV$
nJets	$2or3$

Table 11.5: Additional event selections applied for events that don't pass the standard 0-lepton CxAODReader selection in the $\tau_{had}\tau_{had}$ channel. pTB1 is the transverse momentum of the leading b-jet. p_T^Z is calculated as shown in equation 11.1.

The combination of triggers used in this selection was chosen based on the fact that it gives the maximum event yield as shown in Figure 11.7 and Figure 11.8 for the ggZH and qqZH samples, respectively. The two figures show how the events that do not pass the default 0-lepton selection are distributed over the different trigger configuration. Three main triggers were investigated: Tau trigger (which is the OR of the single tau and di-tau trigger), Tau+MET trigger and MET-Only trigger. These triggers provide eleven trigger configuration, all have been considered here. One can notice that, for both samples (i.e ggZH and qqZH), *for events that do not pass the 0-lepton selection, no events pass MET-Only trigger.* According to this conclusion, any additional selection based on MET-Only trigger, which is the trigger used in the standard 0-lepton selections, is useless.

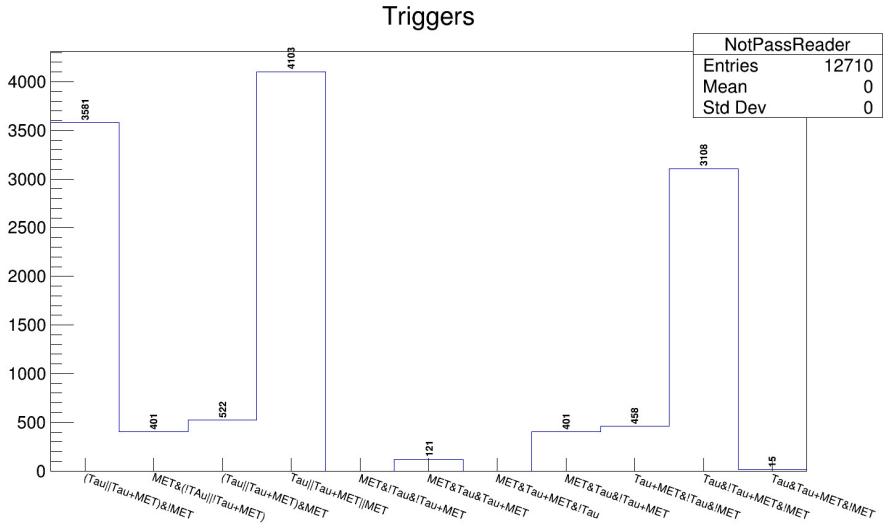

Figure 11.7: Number of events in different trigger configuration for the ggZH sample in the $\tau_{had}\tau_{had}$ channel. No events pass the MET Only trigger.

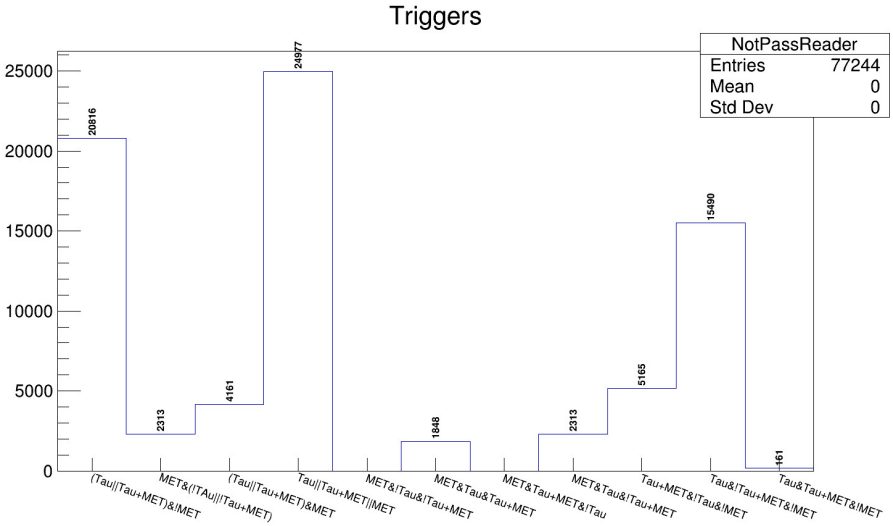

Figure 11.8: Number of events in different trigger configuration for the qqZH sample in the $\tau_{had}\tau_{had}$ channel. No events pass the MET Only trigger.

11.4.1.2 Results

After applying the previous selection, and normalizing the MC samples to $\mathcal{L} = 36.8\ fb^{-1}$, the event yield results from applying the aforementioned sequence of cuts is displayed in a weighted cutflow plot shown in Figure 11.9. Two large drops are observed in the cutflow. As seen from the cutflow, about 72% of events are eliminated after requiring the event to have a 2 b-tagged jets. That shows that most of these events are not originated from Z($\tau\tau$)H(bb) events. The second drop in the event yields is after the ntaus = 2 cut, about 95% of events were rejected. This can be improved by improving the reconstruction efficiency of the tau jets. the rest of the cuts does not have a large impact on the event yield.

As seen in the last bin of this cutflow, after the nJets = 2 or 3 cut, the event yield is 0.4 events. Out of these, about 0.17 events in the 2-Jet category which is equivalent to 1.4% of the high-p_T^Z reference above-mentioned in Table 11.3. On the other hand, the 3-Jet category yield is 0.23 events which is corresponding to 0.7% of the high-p_T^Z reference value specified in Table 11.3. The transverse momentum distribution of the Z boson (p_T^Z) for the selected events in the hadronic tau channel is shown in Figure 11.10. The p_T^Z in this channel is calculated as:

$$(\vec{p_T})_Z = (\vec{p_T})_{\tau_1} + (\vec{p_T})_{\tau_2} + (\vec{p_T})_{MET} \tag{11.1}$$

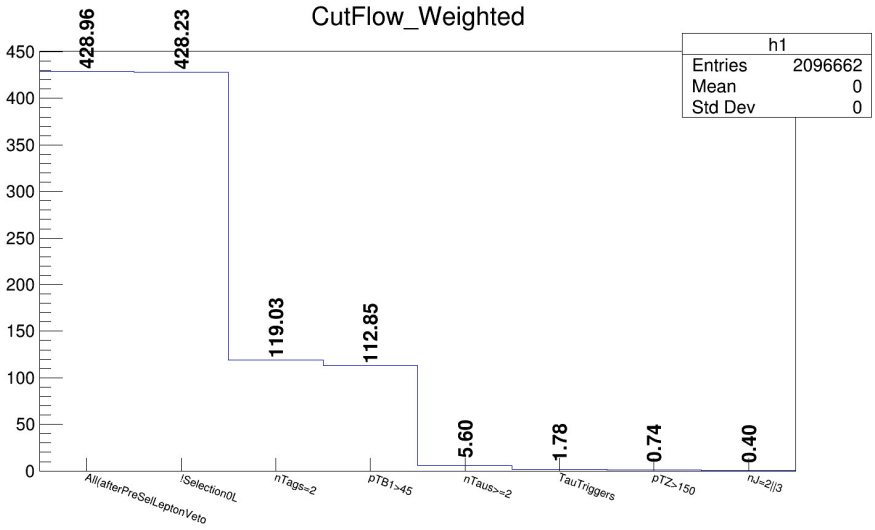

Figure 11.9: Weighted Cutflow for the event selected in the $\tau_{had}\tau_{had}$ channel.

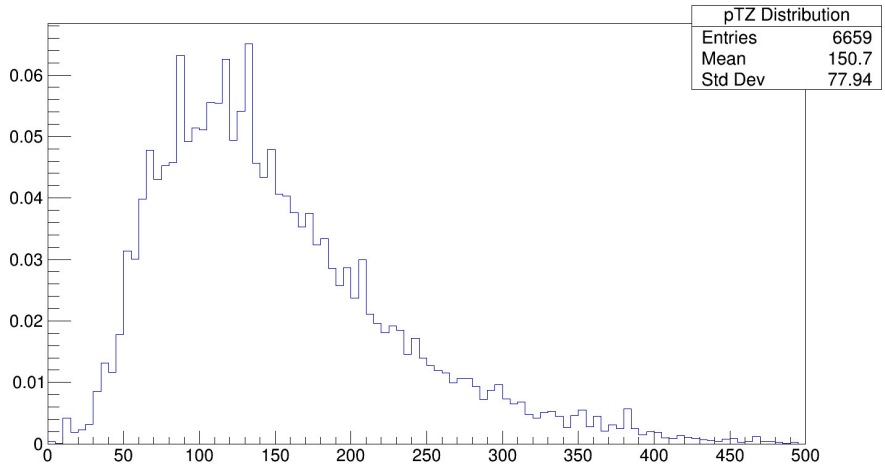

Figure 11.10: The transverse momentum distribution of the Z boson (p_T^Z) in the selected events in the $\tau_{had}\tau_{had}$ channel.

11.4.2 The semi-leptonic channel, $\tau_{lep}\tau_{had}$

11.4.2.1 Event selection criteria

In the semi-leptonic channel, after applying the standard 1-lepton selection at the CxAODReader level, some additional selections has been used. Events that do not pass the standard 1-lepton selection were selected, then some additional cuts has been applied:

- 2^{nd} lepton veto.

- nSignalJet≥ 2.

- pass at least one of the following triggers: MET (see Table 10.5), single lepton (see Table 10.6 and Table 10.7), single tau, tau+MET+(X) in Table 11.4.

- pass the cuts listed in Table 11.6 in the same order. Notice that, among these cuts, the $E_T^{miss} > 30$ GeV cut is only applied in the electron sub-channel and p_T^Z is calculated as:

$$(\vec{p_T})_Z = (\vec{p_T})_l + (\vec{p_T})_{\tau_{had}} + (\vec{p_T})_{MET} \tag{11.2}$$

Cuts Applied in the $\tau_l\tau_h$ Channel	
nJets	$2, 3, >= 4$
nTags	$= 2$
pTB1	$> 45GeV$
nTaus	$>= 1$
MET	$> 30GeV (only for Electron channel)$
p_T^Z	$> 75\ GeV,\ \ > 150\ GeV$

Table 11.6: Additional event selections applied for events that don't pass the standard 1-lepton CxAODReader selection in the $\tau_{lep}\tau_{had}$ channel. pTB1 is the transverse momentum of the leading b-jet. p_T^Z is calculated as shown in equation 11.2.

11.4.2.2 Results

As a result of the previous selection in the semi-leptonic channel, the resulting weighted cutflow showing the applied cuts is shown in Figure 11.11. Again, two large drops in the event yield is observed. A round 78% of the selected events are eliminated after requiring 2 b-tagged jets. Then, by applying the nTaus=2 cut, 94% of the events were discarded.

The total event yield after the last cut, $p_T^Z > 150$ GeV cut, is 0.89. These events are distributed over three orthogonal nJet selection, nJets=2 or 3 or ≥4. The cutflow in these three nJet configuration are displayed in Figure 11.12, 11.13 and 11.14, respectively.

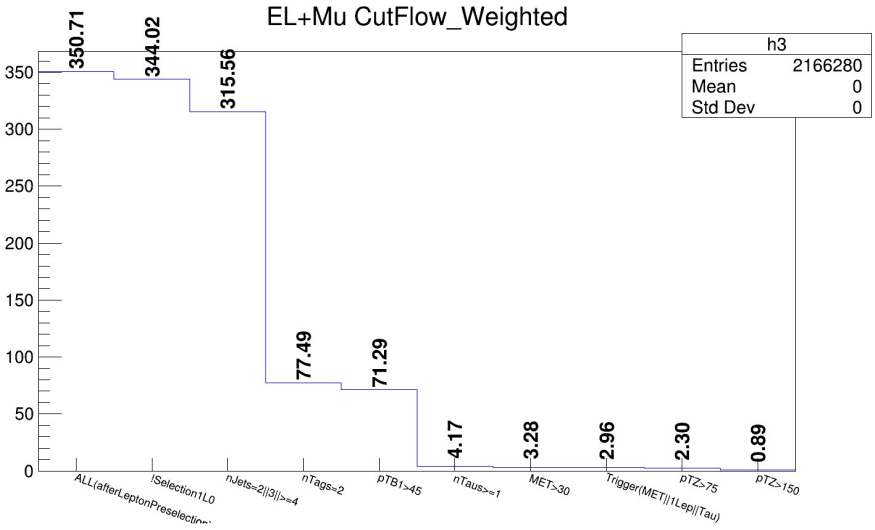

Figure 11.11: Weighted Cutflow for the event selected in the $\tau_{lep}\tau_{had}$ channel.

In the 2-Jet category, the event yield is 0.24 after the $p_T^Z > 150$ GeV cut. This is comparable to about 1.9% of the high-p_T^Z reference indicated in Table 11.3. The

corresponding p_T^Z distribution is shown in Figure 11.15.

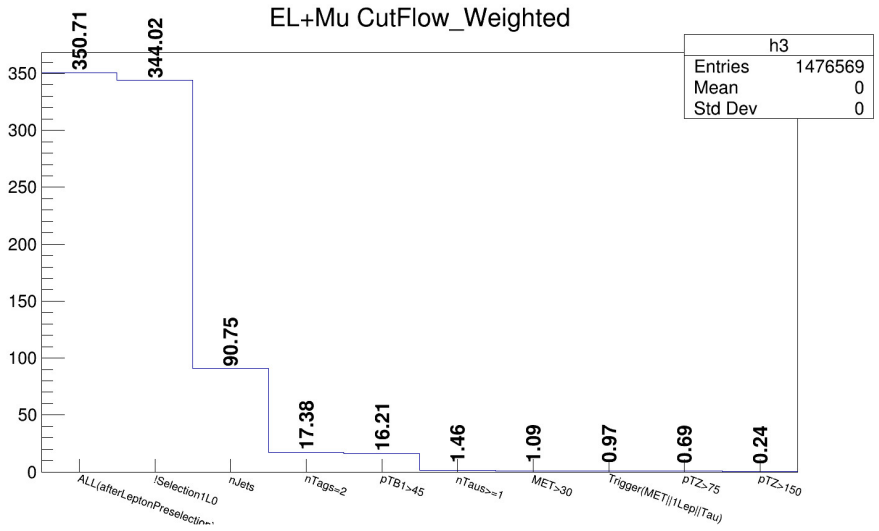

Figure 11.12: Weighted Cutflow for the event selected in the $\tau_{lep}\tau_{had}$ channel for nJets=2.

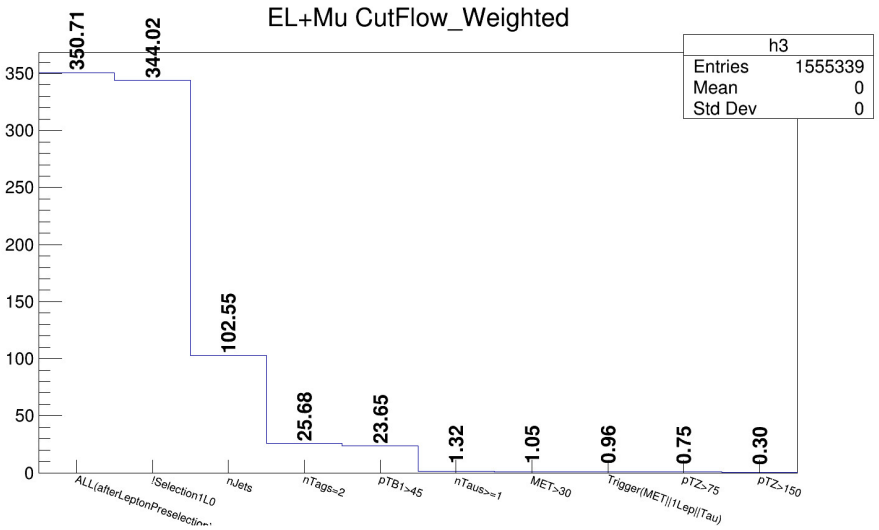

Figure 11.13: Weighted Cutflow for the event selected in the $\tau_{lep}\tau_{had}$ channel for nJets=3.

While in the other category, the 3-Jet category, shown in Figure 11.13, after the $p_T^Z > 150$ GeV cut, the event yield is 0.3. This is result is corresponding to 0.9% of the high-p_T^Z reference determined in Table 11.3. The relevant p_T^Z distribution for the 3-Jet category can be found in Figure 11.16.

As seen in Figure 11.14, 0.35 weighted events have nJet ≥ 4. This is equivalent to 1.1% of the high-p_T^Z reference.

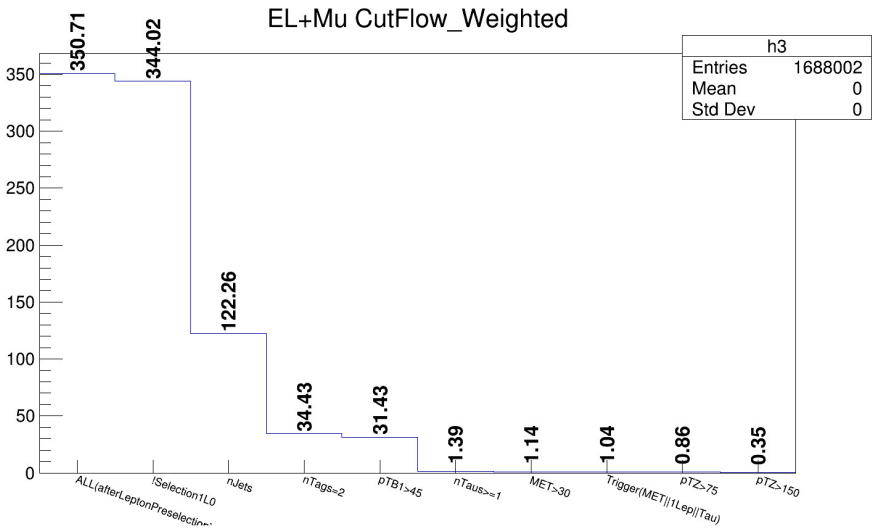

Figure 11.14: Weighted Cutflow for the event selected in the $\tau_{lep}\tau_{had}$ channel for nJets$\geq$4.

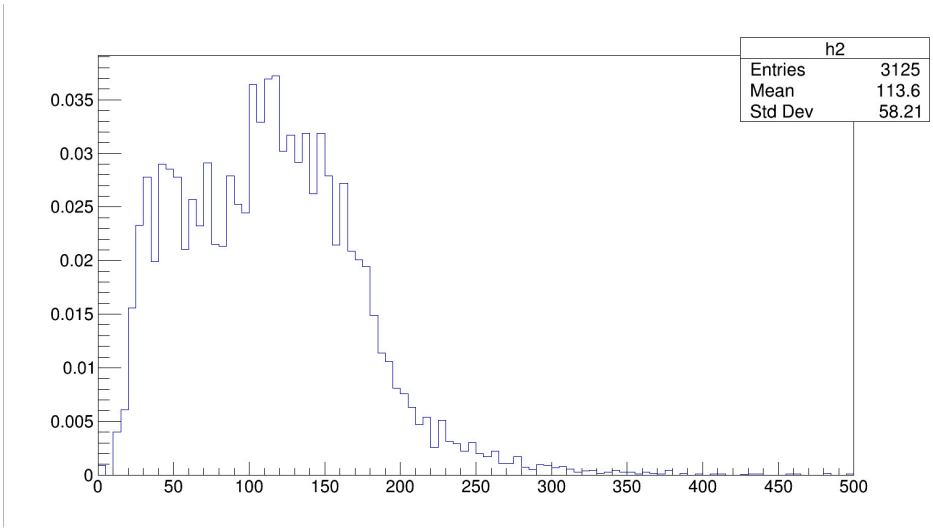

Figure 11.15: The transverse momentum distribution of the Z boson (p_T^Z) in the selected events in the $\tau_{lep}\tau_{had}$ channel for nJets=2

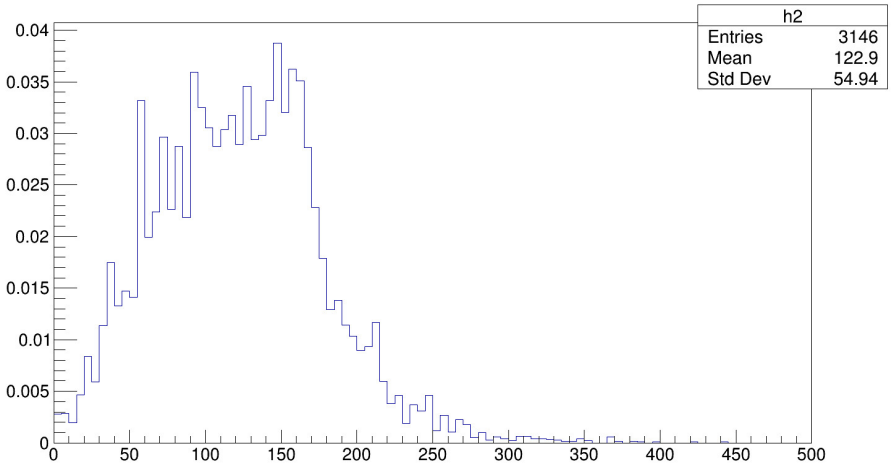

Figure 11.16: The transverse momentum distribution of the Z boson (p_T^Z) in the selected events in the $\tau_{lep}\tau_{had}$ channel for nJets=3

nJet	$p_T^Z > 150$ GeV	$p_T^Z > 75$ GeV
2-Jet	0.24	0.69
3-Jet	0.30	0.75
4p-Jet	0.35	0.86

Table 11.7: Event yield in the different jet categories: 2,3 and ≥4 jets for the two p_T^Z cut: >150 GeV and >75 GeV. The event yield after reducing the p_T^Z cut is increased but the relative increase to the reference value is almost the same for the two cuts which is 2%.

11.4.3 Optimizing the p_T^Z cut in the semi-leptonic channel

The previous results show the event yield up to the $p_T^Z > 150$ GeV cut. With this cut, the events yields in the different nJet categories is summarized in Table 11.7. This leads to about 2% of the high-p_T^Z reference yields for each of the 2 and ≥3 jets categories.

Then, what is the yield if we reduce the p_T^Z cut to 75 GeV instead? This condition has been tested for each of the three jet categories and this leads to the yield shown in Table 11.7. The corresponding yield for each channel is shown Figures 11.12, 11.13 and 11.14 in the bin before the last labeled as "$p_T^Z > 75$". The total yield in this case is increased and gives 2.3 weighted events. But this increase is again about 2% of the (low+high) p_T^Z reference yields for each of the 2-jet and ≥ 3-jet categories. So relaxing the p_T^Z cut does not effectively change the conclusion.

	2 Jets	3 Jets
0-lep	8.77	10.06
1-lep	50.38	54.85
2-lep ($p_T^W > 150$ GeV)	0.0022	0.0083
2-lep ($75 < p_T^W < 150$ GeV)	0.0063	0.0167
Total (Without/With 2-lep low p_T^W region)	**59.15/59.16**	**64.92/64.94**

Table 11.8: The current WH yields in the different channels: 0,1 and 2 leptons and for two jets categories: 2-jet and 3-jet. The 2 lepton channel is divided into: high-p_T^W region with $p_T^W > 150$ GeV and low-p_T^W region with $75 < p_T^W < 150$ GeV. The total yields is calculated with and without the low-p_T^W region.

11.5 W($\tau\nu$)H(bb) channel

In the default 1-lepton channel analysis, only electron and muon sub-channels are considered and a dedicated channel W$\rightarrow \tau\nu$ is not included. For tau leptonic decays, the current 1-lepton channel can cover the signal events. For the tau hadronic decays, the current 0-lepton channel has some sensitivity (No hadronic tau-veto). In this study, we want to test if a channel explicitly selecting hadronic τ decays could bring additional sensitivity for this analysis.

The current WH yields in all sub-channels and for 2-jet and 3-jet categories can be found in Table 11.8. These yields are taken from the (W$\rightarrow e\nu + \mu\nu + \tau\nu$)H($bb$) in the standard inputs. The 2 lepton channel is splitted into two regions according to p_T^W range used, these regions are : high p_T^W region with $p_T^W > 150$ GeV and low p_T^W region with $75 < p_T^W < 150$ GeV.

This study is based on the unskimmed WH signal MC samples which are simulated and reconstructed using the 2015-2016 data running conditions, and normalized to 36.1 fb^{-1}. The methodology used in the previous Z($\tau\tau$)H(bb) study was also employed in this study. The first step is to apply the default 0-lepton selections (with no selection at the CxAODMaker level) on these WH signal events, then for events do not pass the selections, a dedicated requirement to select the signal events with W decays to hadronic τ and neutrino (referred as hadronic τ selection) is considered to check how many events can be recovered. The possible triggers can be used in the hadronic τ selection are: the signal tau triggers, tau+MET triggers and MET triggers. Then additional cuts was applied, see Table 11.9. The $E_T^{miss} > 150$ GeV cut was applied for events triggered only by MET Trigger. The transverse momentum of the W boson, p_T^W was calculated as:

$$(\vec{p_T})_W = (\vec{p_T})_{\tau_{had}} + (\vec{p_T})_{MET} \tag{11.3}$$

For all events that do not pass the standard 0-lepton selection, the event yield

Cuts Applied in the $\tau_h\nu$ Channel	
nJets	2 or 3
nTags	$= 2$
nTaus	$= 1$
p_T^W	$> 150\ GeV$
MET	$> 150\ GeV$

Table 11.9: Additional event selections applied for events that don't pass the standard 0-lepton CxAODReader selection in the $W \to \tau\nu$ channel. p_T^W is calculated as shown in equation 11.1.

Cuts Applied in the $\tau_h\nu$ Channel	Yields
All	470.76
pass Trigger(MET or Tau+MET or Single Tau)	44.13
nTaus=1	10.25
$p_T^W > 150$ GeV	6.83
$MET > 150$ GeV(MET-Only Trigger)	5.28

Table 11.10: Summary of event yield after applying a sequence of additional cuts in $W \to \tau\nu$ channel.

cutflow is described in Table 11.10. After the p_T^W >150 GeV cut, the event yield is 6.83 (5.6% of the reference for the 2-jet and 3-jet categories combined). The additional cut, E_T^{miss} >150 GeV, applied for events that pass the MET trigger only reduces the yield to 5.28 (4.3% of the reference for the 2-jet and 3-jet categories combined).

11.6 Conclusion

In this chapter, the impact of using the tau lepton in the final state in the VH(bb) analysis has been investigated. This study is meant to show if the dedicated Z($\tau\tau$)H(bb) channel in the context of the current VH(bb) analysis with the additional optimized selection to explicitly selecting tau decays could bring additional

sub-channel	2-jet	3-jet	$>= 4J$
$\tau_h\tau_h$ channel	0.17	0.23	–
$\tau_l\tau_h$ channel (High-p_T^Z)	0.24	0.30	0.35
$\tau_l\tau_h$ channel ((low+High)-p_T^Z)	0.69	0.75	0.86
$\tau_h\nu$ channel (combined (2-jet,3-jet))	5.28		

Table 11.11: Possible maximum increase of signal yield in the different channels:$\tau_{had}\tau_{had}$, $\tau_{lep}\tau_{had}$ and $\tau_{had}\nu$ in the different nJet categories: 2, 3 and $\geq$4 jets. The $\tau_{lep}\tau_{had}$ channel is studied in the high-p_T^Z region as well as (low+high)-p_T^Z.

sensitivity to the analysis. It would be possible to add at most 2% of the current ZH yield. The maximum possible increase to the event yield is shown in Table 11.11. This table gives in details the event yields in the different channels: $\tau_{had}\tau_{had}$, $\tau_{lep}\tau_{had}$ for the different nJet categories: 2, 3 and $\geq$4 jets with the $\tau_{lep}\tau_{had}$ channel is studied in the high-p_T^Z region as well as (low+high)-p_T^Z. This study shows that the possibility to use taus to split the analysis further would results in an increase in the sensitivity but even though this increase is relatively small and so probably useless. Regarding the W($\tau\nu$)H(bb) channel, in total, only 4.3% of WH signal events can be recovered by additional selections. This makes this channel also helpless for increasing the analysis sensitivity and therefore not considered in the analysis. The yields found by this study are the signal yields only, hence a proper handling of backgrounds processes will further reduce this tiny extra yield.

Chapter 12

Multi-jet background estimation in the 1-lepton channel

Contents

12.1 Template method 252

12.2 Defining control region for the multi-jet template 252

12.3 1-lepton channel: MVA analysis 253

12.3.1 Shape uncertainties 260

12.3.2 Normalisation uncertainties 261

12.4 1-lepton channel: dijet-mass analysis 263

12.4.1 Systematics uncertainties 269

12.5 Multi-jet estimation in the 0- and 2-lepton channel 270

12.5.1 0-lepton channel 270

12.5.2 2-lepton channel 272

The process involved the W or Z boson decay into leptons are usually defined as electroweak backgrounds. These processes are modelled using the background MC samples summarized in Table 10.1. The multi-jets background provides no real leptonic signatures, but still have the potential to contribute as a non-negligible background component due to the large cross-sections. The QCD multi-jet background involving final state jets can directly fake lepton signatures by either replicating electron electromagnetic calorimeter signatures, or by producing electrons/muons via non-prompt weak decays. Such processes often result in a miss-calibrated physics object, thereby yielding a fake non-negligible E_T^{miss} signature. Due to the difficulty to properly model this background using MC methods, data driven approaches are used instead. In this chapter, the estimation of this background in the 0-, 1- and 2-lepton sub-channels is discussed with emphasis on the 1-lepton channel where I have mostly contributed.

12.1 Template method

When measuring a physics process with data collected by ATLAS it is imperative to be able to model the background processes which have the same final state products recorded by the detector. This accurate description of background events will enable us to measure the signal process and from this the cross-section can be extracted and compared to the theoretical predictions.

To separate the signal and background events MC simulations are often used. However, not all the backgrounds can be simulated using MC. The multi-jet background is a notoriously difficult background to simulate and there is currently no adequate existing MC technique. This is a fairly significant background in the VH($b\bar{b}$) search as it has a very large cross section. Given the complexity in modelling the multi-jet background, data-driven techniques is one of the primary methods used for estimating the multi-jet background.

In order to build a data-driven template, one needs to carefully select a Control Region (CR) where the majority of events that originate from the multi-jet background and does not have a high contamination of signal events. The shape of the multi-jet background is determined in the CR. Theoretically, the shape of the multi-jet background for the chosen discriminating variable should be the same in both regions. Therefore the shape of the multi-jet background can be extrapolated to the signal region using events from the control region. In the following sections, methodology of the data-driven multi-jet template method used to estimate the multi-jet background in the 1-lepton channel is detailed.

In this study, two tools were used to estimate the contribution of each template, RooFit [209] and TFractionFitter [210] which are classes within the data analysis framework ROOT. Template fit to some distribution that showed good discrimination between EWK and MJ backgrounds was performed.

12.2 Defining control region for the multi-jet template

Two important cuts which are used for the SR to reduce multi-jet background contamination are:

- The loose isolation (IsLooseTrackIso) is used for the loose lepton definition that separates events between the 0-, 1- and 2-lepton channels, and thus also for the object overlap removal. It has a flat signal efficiency versus lepton p_T of around 99%

- The tight isolation applied by the tight absolute cut on either calorimeter iso-

	Isolated Region	Inverted Isolation Region
Electron	IsLooseTrackOnlyIso	IsLooseTrackOnlyIso
	TopoEtCone20<3.5 GeV	TopoEtCone20>3.5 GeV
Muon	IsLooseTrackOnlyIso	IsLooseTrackOnlyIso
	PtCone20<1.25 GeV	PtCone20>1.25 GeV

Table 12.1: Summary of differences in lepton isolation between the isolated and inverted isolation regions used for the template method. In each region the AND of the two isolation criteria listed in the table is used.

lation "TopoEtCone20" (for the electron channel) or on the track isolation "PtCone20" (for the muon channel). These tighter isolation are applied in addition for the tight lepton definition (exclusively for the signal lepton in the 1-lepton channel). The additional cut corresponds to a signal efficiency of around 95%.

The isolation requirement is the most discriminating feature for selecting multi-jet events. It is important to chose the cuts in such a way as to minimise the contamination of signal events in the template, while having sufficient statistics. The CR is selected by rejecting events which pass the isolation requirements, in other words, the isolation requirement is inverted.

The multi-jet enriched control region is defined using inverted lepton isolation cuts. Table 12.1 summarises both the isolation cuts applied in the signal region and the inverted selection used for the multi-jet enhanced control region.

12.3 1-lepton channel: MVA analysis

In the 0- and 2-lepton channels, studies have shown that the multi-jet contamination is negligible [211]. However, in the 1-lepton channel, there is a non-negligible contribution from multi-jet events, which pass the event selection due to the reconstruction of a fake lepton.

In the 1-lepton channel, the multi-jet background contributes to both the electron and muon sub-channels. The dominant contribution to this background comes from the real electrons or muons from semileptonic decay of the heavy flavour hadrons. A second contribution in the electron sub-channel arises from the $\gamma \to e^+e^-$ conversions where photons are produced in the decays of neutral pions or from π^0 Dalitz decay. These non-prompt leptons are not expected to be isolated, but still a non-negligible fraction passes the isolation requirements.

In this channel, the contribution of the multi-jet background is greatly reduced in the high-p_T^V region compared to the fraction in the medium-p_T^V region. In order to further reduce the multi-jet background in medium p_T^V region, an additional cut

on the transverse W-candidate mass (m_T^W) is applied only in this region, to remove the events with $m_T^W < 20$ GeV. However, the multi-jet background still contributes a significant fraction of the background events. A robust procedure is necessary to estimate the contributions of this background both in the electron and muon W decay modes. This background is estimated separately not only in high and medium p_T^V regions, but also in the electron and muon sub-channels, and in the 2- and 3-jets categories, using the similar procedures. In both sub-channels, the template method is employed.

The transverse W-candidate mass (m_T^W) is chosen as the variable offering the best discrimination between pure strong multi-jet production and electroweak induced processes. A multi-jet template for this variable is obtained in the inverted isolation region.

The contribution from electroweak background processes in the inverted isolation region is subtracted based on MC predictions. A fit to the transverse W-candidate mass distribution is then applied in the signal region to extract simultaneously the normalization factors for both the multi-jet and the electroweak components.

Separate templates for the multi-jet contributions are obtained depending on lepton flavour (e/μ), jet multiplicity (2/3-jet regions) and p_T^V category (high and medium p_T^V regions). For each of these eight signal regions a corresponding multi-jet control region is thus defined.

In this study, instead of requiring 2 b-tag as in the signal region, only 1 b-tag is required in the control region. This was decided in order to reduce the impact of statistical fluctuations when deriving the template, since the statistics in the multi-jet enhanced control region is limited: it is expected to be around 9 (2) times the signal region statistics for the electron (muon) channel. Figure 12.1 show the m_T^W distributions for the data and electroweak processes in the inverted isolation e/μ, 2/3-jet regions with requiring exactly 1 b-tag, in high p_T^V region. The same set of distributions for the medium p_T^V region is shown in Figure 12.2.

The multi-jet shapes are derived, analogously to the m_T^W distribution used as template in the fit, from the inverted isolation regions, after subtracting the electroweak backgrounds.

The $t\bar{t}$ and W+jets background processes are dominant in the signal region, and their normalization can have a significant impact on the multi-jet estimate. While the m_T^W variable provides discrimination mainly between processes with and without a W boson, the distributions of m_T^W for the $t\bar{t}$ and W+jets processes are not identical. This is due to the fact that the di-leptonic $t\bar{t}$ events induce a tail at high values of m_T^W. Separate normalization factors are extracted for the top ($t\bar{t}$+single top) and W+jet contributions to avoid a bias onto the multi-jet estimate.

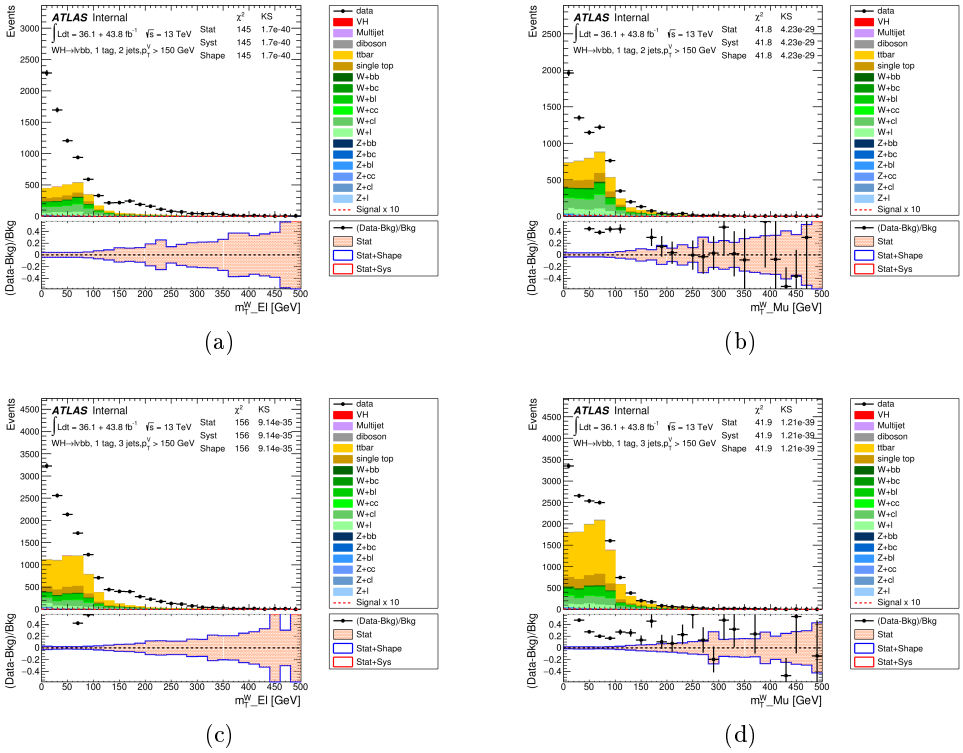

(a) (b)

(c) (d)

Figure 12.1: The m_T^W distribution in the inverted isolation 1-lepton $p_T^W > 150$ GeV region, requiring exactly 1 b-tag with 2 signal jets in e channel(a), 2 signal jets in μ channel(b), 3 signal jets in e channel(c), 3 signal jets μ channel(d).

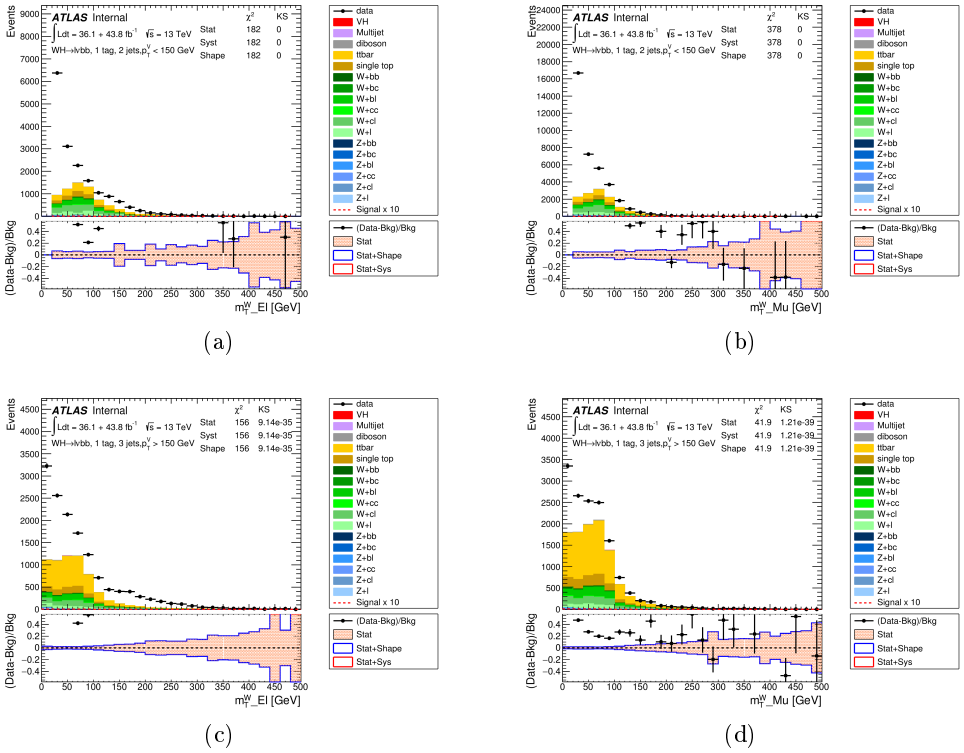

Figure 12.2: The m_T^W distribution in the inverted isolation 1-lepton 75 GeV $< p_T^W <$ 150 GeV region, requiring exactly 1 b-tag with 2 signal jets in e channel(a), 2 signal jets in μ channel(b), 3 signal jets in e channel(c), 3 signal jets μ channel(d).

To determine the respective contribution of the W+jet and the top background, a simultaneous fit is applied to the signal region and the W+HF control region. The simultaneous fit to the two regions allows the extraction of the two separate normalizations with decent precision since the relative W+jet / top purity is very different in these two regions. Afterwards, the m_T^W distribution is used in the fit basically only to disentangle the multi-jet contribution from both the top and W+jets backgrounds.

To increase the statistical precision in the determination of the top and W+jet normalization factors, the fit is also applied simultaneously in the electron and muon channel, extracting simultaneously the normalizations for the electron multi-jet, muon multi-jet, top and W+jets components.

In this study, separated templates are used for the electron multi-jet, muon multi-jet, top and W+jets components. The normalization factor extracted for each contribution is presented in Table 12.2.

Post-fit plots for the distribution exploited in the fit are shown in Figure 12.3 and Figure 12.4, for high and medium p_T^V region, respectively. Apart from the m_T^W distribution which is directly used in the multi-jet fit, Figure 12.5 and Figure 12.6 also show some other post-fit distributions for other variables in both electron and muon channels, and in both high-p_T^V regions. In these distributions, the normalization is fixed to the result of the multi-jet fit. It is seen that over all, there is a fair agreement between data and MC and the data-driven multi-jet background estimate.

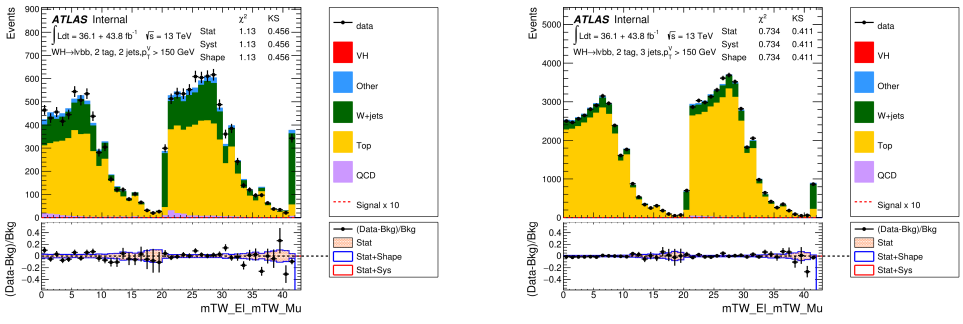

(a) (b)

Figure 12.3: The m_T^W distribution in the isolated 1-lepton $p_T^W > 150$ GeV region, requiring exactly 2 b-tag with 2 signal jets (a), 3 signal jets (b), after applying top ($t\bar{t}$+ single top) and W+jets normalisation factors. Bins 1-21 correspond to the e only channel, bins 22 to 42 correspond to the mu only channel, and bins 21 and 42 represent the W+HF control region.

Many sources of systematic uncertainty impact the normalization and shape of the multi-jet background in the electron and muon sub-channels. Both shape and normalization uncertainties are discussed in the next section.

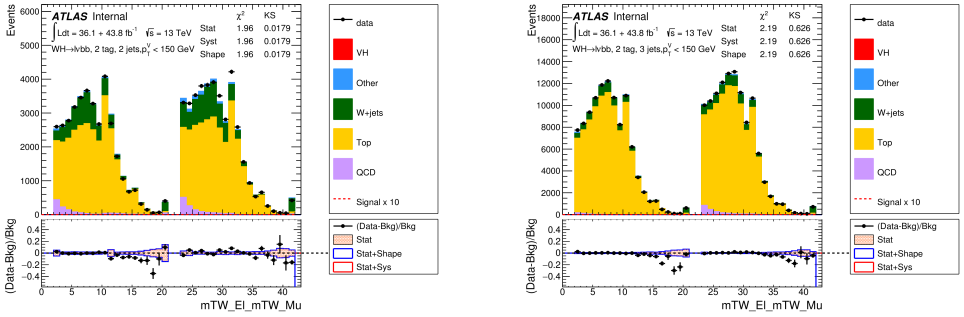

(a) (b)

Figure 12.4: The m_T^W distribution in the isolated 1-lepton 75 GeV $< p_T^W <$ 150 GeV region, requiring exactly 2 b-tag with 2 signal jets (a), 3 signal jets (b), after applying top ($t\bar{t}$+ single top) and W+jets normalisation factors. Bins 1-21 correspond to the e only channel, bins 22 to 42 correspond to the mu only channel, and bins 21 and 42 represent the W+HF control region.

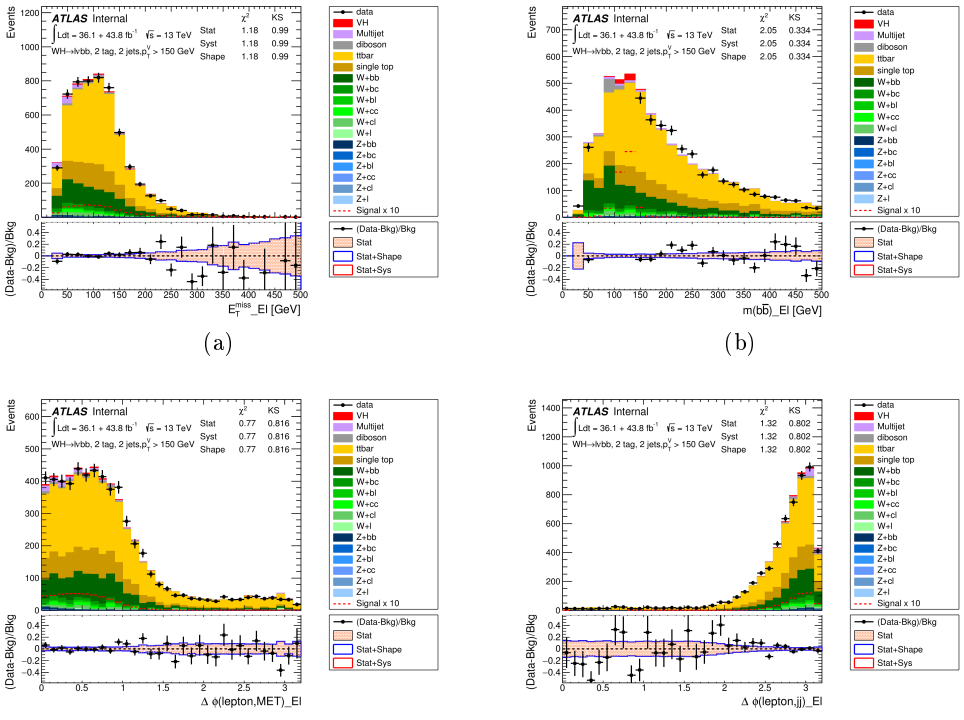

(a) (b)

(c) (d)

Figure 12.5: The distributions, for the 2-tag 2-jet p_T^W >150 GeV category in electron channel W+HF signal region, of (a) E_T^{miss} (b) m_{bb} (c) $\Delta\phi(lepton, E_T^{miss})$ and (d) $\Delta\phi(lepton, bb)$ are shown.

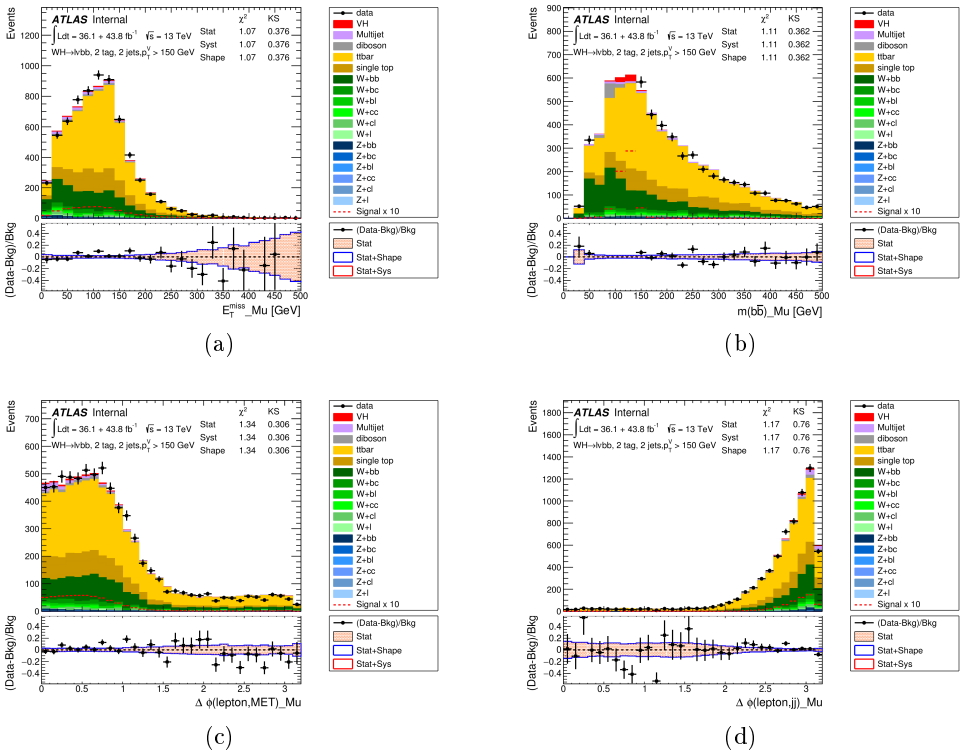

(a) (b)

(c) (d)

Figure 12.6: The distributions, for the 2-tag 2-jet $< p_T^W >$150 GeV category in muon channel W+HF signal region, of (a) E_T^{miss} (b) m_{bb} (c) $\Delta\phi(lepton, E_T^{miss})$ and (d) $\Delta\phi(lepton, bb)$ are shown.

Region	top ($t\bar{t}$ + single top)	W+jets
high-p_T^V 2-tag, 2-jet	1.02	1.27
high-p_T^V 2-tag, 3-jet	0.99	1.13
medium-p_T^V 2-tag, 2-jet	1.05	1.49
medium-p_T^V 2-tag, 3-jet	1.07	1.10

Table 12.2: Summary of normalisation scale factors for Top ($t\bar{t}$ + single top) and W+jets derived in the isolated lepton region.

Dataset	Single e Trigger	Single μ Trigger
2015	e24_lhmedium_L1EM20VH	mu20_iloose_L1MU15
2016-2017	e26_lhtight_nod0_ivarloose	mu26_ivarmedium

Table 12.3: Reduced triggers used to evaluate possible trigger bias in inverted isolation region.

Sub-channel	high-p_T^V	medium-p_T^V region
e-channel	$E_T^{cone0.2}$ <12 GeV	$E_T^{cone0.2}$ <6 GeV
μ-channel	$p_T^{cone0.2} < 2.9$ GeV	$p_T^{cone0.2} < 2.1$ GeV

Table 12.4: Additional isolation cuts defined for the electron and muon sub-channel, in the high- and medium-p_T^V regions to evaluate possible bias results from the extrapolation from the full inverted isolation region to the signal region.

12.3.1 Shape uncertainties

Shape systematic uncertainty, studied in this context, are the systematic uncertainty that have an impact on the multi-jet shape. There are three type of shape systematic uncertainties that have been considered in the evaluation of the shape uncertainty of the multi-jet background estimate:

- Lepton trigger: This systematic affects only the electron sub-channel channel and medium p_T^V muon sub-channel, since in the high p_T^V muon sub-channel the p_T^{miss} trigger is used rather than the single muon trigger. To evaluate this the impact of the choice of the trigger on the multi-jet estimation, the lowest p_T trigger was used instead of using the combination of triggers, listed in Section 10.3.3. The reduced single lepton triggers used are listed in Table 12.4.

- Extrapolation from the full inverted isolation region to the signal region: To evaluate this systematic, a reduced inverted-isolation region is defined, with additional isolation cuts applied to the inverted isolation region previously defined in Table 12.1. These additional cuts are optimized to keep about half of data events in the full inverted regions for both electron and muon sub-channels.

- top and W+jets normalization factors: To evaluate the effect of using the normalization factors extracted from the template fit on the electroweak background subtraction procedure, the nominal multi-jet template shape is evaluated with and without applying the normalization factors, and the difference in shape taken as the systematic uncertainty.

These systematic uncertainties are implemented as shape only systematic uncertainties by normalizing the variation to the nominal multi-jet yield. Plots in Figure 12.7 and Figure 12.8 show the shape comparison for the nominal BDT and the main

shape systematics variations in the high and medium p_T^V region for both electron and muon sub-channels.

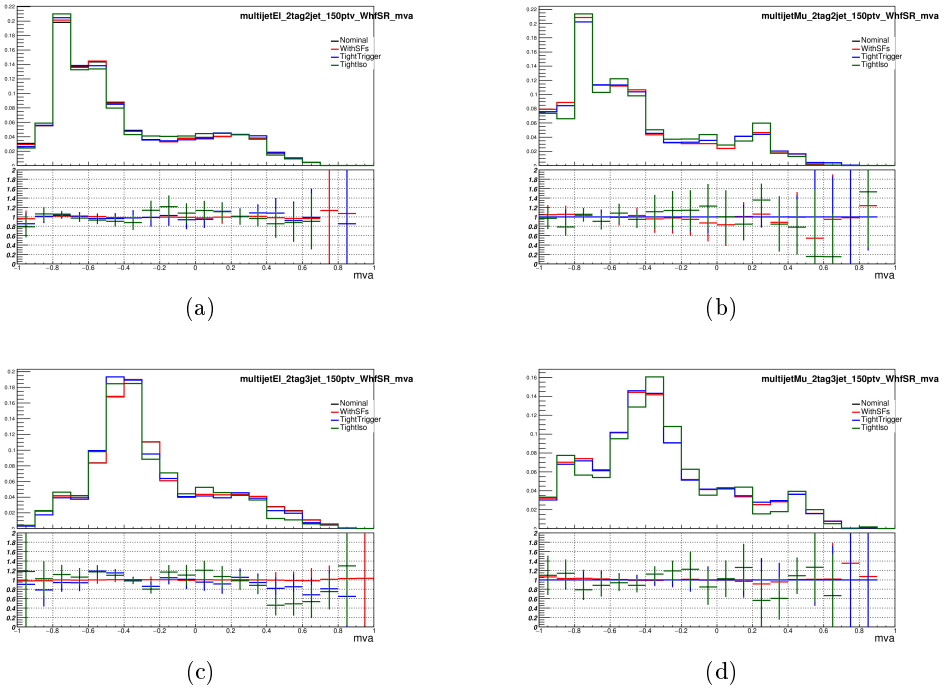

(a) (b) (c) (d)

Figure 12.7: The MJ BDT shape comparison for the nominal (in black) and some main shape variations in the high-p_T^V region, 2 jet e channel (a), 2 jet μ channel (b), 3 jet e channel (c), and 3 jet μ channel (d). The green histograms indicate the impact of using the reduced inverted isolation region, the red histograms indicate the impact of using the top and W+jets normalization factors in the inverted isolation region, and the histograms in blue indicate the impact of using the lowest lepton p_T trigger.

12.3.2 Normalisation uncertainties

Most of the shape uncertainties discussed in the previous section also contribute to the normalization uncertainties which affect the estimated multi-jet normalization. The impact on the multi-jet normalization is indirectly driven by changes to the m_T^W template distributions, and to the relative yield in the signal and W+HF control regions. The individual contributions to the normalization uncertainty are added in quadrature to give the overall normalization uncertainty, separately in the high and medium p_T^V region, in the 2 and 3 jet regions, and for the electron and muon modes. Few of the normalization uncertainties encountered are listed below :

- E_T^{miss} cut in electron sub-channel: the $E_T^{miss} < 30$ GeV cut implemented in the template fit ,in the high p_T^V region, induces a significant change to the m_T^W

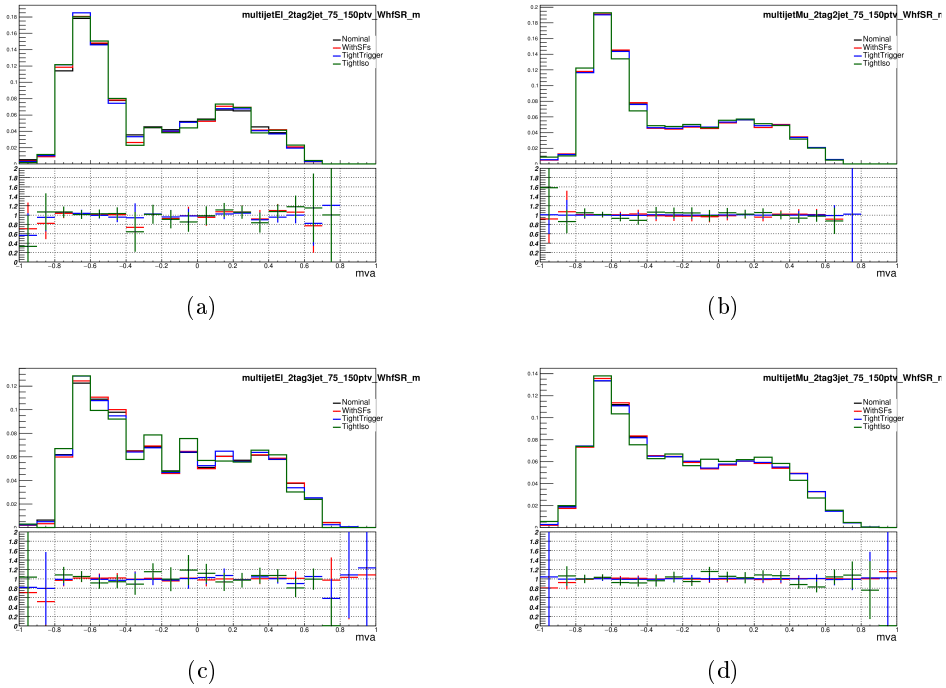

Figure 12.8: The MJ BDT shape comparison for the nominal (in black) and some main shape variations in the medium-p_T^V region, 2 jet e channel (a), 2 jet μ channel (b), 3 jet e channel (c), and 3 jet μ channel (d). The green histograms indicate the impact of using the reduced inverted isolation region, the red histograms indicate the impact of using the top and W+jets normalization factors in the inverted isolation region, and the histograms in blue indicate the impact of using the lowest lepton p_T trigger.

Region	MJ Fraction(%)	MJ norm. uncertainity
2-tag, 2-jet, e	$1.91^{+1.96}_{-1.91}$	-100% / +105%
2-tag, 2-jet, μ	$2.76^{+2.06}_{-1.65}$	-60% / +75%
2-tag, 3-jet, e	$0.15^{+0.24}_{-0.15}$	-100% / +160%
2-tag, 3-jet, μ	$0.43^{+1.10}_{-0.43}$	-100% / +260%

Table 12.5: Summary of MJ fractions, along with their associated uncertainty in the 2-jets and 3-jets high p_T^V regions (W+HF and SR are combined) separately.

Region	MJ Fraction(%)	MJ norm. uncertainity
2-tag, 2-jet, e	$3.57^{+0.44}_{-0.79}$	-12% / +22%
2-tag, 2-jet, μ	$2.76^{+1.19}_{-0.64}$	-25% / +40%
2-tag, 3-jet, e	$0.85^{+0.37}_{-0.31}$	-40% / +45%
2-tag, 3-jet, μ	$2.14^{+0.26}_{-1.03}$	-50% / +12%

Table 12.6: Summary of MJ fractions, along with their associated uncertainty in the 2-jets and 3-jets medium p_T^V regions (W+HF and SR are combined) separately.

distribution. This affects the multi-jet component derived from the inverted isolation region in data as well as the electroweak background components estimated using simulations.

- m_T^W cut in the medium p_T^V region: similarly, including the $m_T^W < 20$ GeV in the template fit, to evaluate the impact of the additional m_T^W cut on the estimated multi-jet normalization.

- Choice of the fitting variable: Traditionally this variable is m_T^W. Alternatively, the $\Delta\phi(lepton, b\bar{b})$ variable was used in the template fit, for both high and medium p_T^V region, in 2 jets category. While, in 3 jets category, $\Delta\phi(lepton, b\bar{b}j)$ is selected due to the good discrimination between multi-jet and electroweak background.

The combination of all the systematic uncertainties gives rise to the fractions of the multi-jet contribution compared to the total background. The multi-jet fractions and their uncertainties are presented in Table 12.5 and Table 12.6 for high and medium p_T^V region, respectively.

12.4 1-lepton channel: dijet-mass analysis

In the dijet-mass analysis, due to the additional cuts and the different analysis categories compared to multivariate analysis, independent multi-jet estimation is needed. The general strategy is very similar to what was used for the multivariate analysis presented in the previous subsection. The relevant differences are presented

in here. As in the MVA analysis, all the results refer to the full (2015-2016-2017) dataset.

Briefly, the multi-jet background is estimated with the same template method as in the MVA. However, the template fits to the m_T^W distributions do not have as good a performance in terms of discrimination between the top and W backgrounds. This is because the latter is obtained in the MVA thanks to the distinction between signal and W+HF control regions, which is not applied in the dijet-mass analysis.

Therefore, a preliminary fit is performed in each analysis region to a variable showing good discrimination between these two backgrounds. The variable showing the best performance in this respect was found to be $\Delta R(b,\bar{b})$, defined as the distance between the center of the two b-jets. The fit is performed over the combined electron-muon $\Delta R(b,\bar{b})$ distribution with two free normalization factors. The multi-jet background, known to be small, is neglected at this stage, but the fitted normalization factors are used to provide only the relative fractions of top and W backgrounds, from which the global shape of the electroweak (EWK) background that is used in the subsequent template fit involving the multi-jet background is obtained. An example of such a preliminary fit to the $\Delta R(b,\bar{b})$ distribution is shown in Figure 12.9.

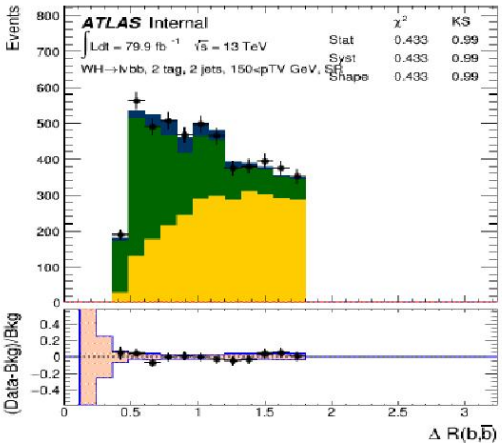

Figure 12.9: The distribution of $\Delta R(b,\bar{b})$ in the dijet-mass analysis for all regions with $p_T^W > 150$ GeV combined, in the 2-jet category. The electron and muon contributions are summed. The top (yellow) and W (green) contributions are normalized according to the results of the fit to this distribution. The fitted normalization factors are 1.08 and 1.26, respectively.

A template fit is then performed in each analysis region to a variable showing good discrimination between multi-jet and electroweak backgrounds. This variable is traditionally m_T^W, but it was found that other variables could provide a similar or even better discrimination (based on the statistical errors of the fits). Here, the azimuthal angle between the lepton and the missing transverse energy, $\Delta\phi(lepton, E_T^{miss})$, was found to provide the best overall performance, considering the various analysis re-

gions. Fits to the m_T^W distributions are nevertheless used in the assessment of systematic errors. Each template fit is performed simultaneously over the separate electron and muon distributions with three free scale factors (SF), one for the electroweak background, one for the multi-jet background in the electron channel, and similarly one in the muon channel, with all SFs constrained to remain non-negative. An example of such a template fit to the $\Delta\phi(lepton, E_T^{miss})$ distribution is shown in Figure 12.10.

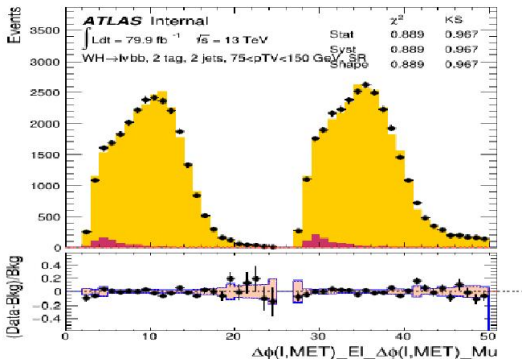

Figure 12.10: Distribution of $\Delta\phi(lepton, E_T^{miss})$ in the dijet-mass analysis in the medium-p_T^V region for electrons (left) and muons (right), in the 2-jet category. The electroweak (yellow) and multi-jet (red) contributions are normalized according to the results of the fit to this distribution. The multi-jet fractions are 2.6% and 3.0% in the electron and muon channels, respectively.

Such multi-jet scale factors should be determined in each of the analysis regions. However, the statistics are quite limited for $p_T^V > 200$ GeV, leading to results extremely sensitive to statistical fluctuations. Therefore, multi-jet SFs are determined for $p_T^V > 150$ GeV (henceforth called high-p_T^V region) and applied in all analysis regions in this p_T^V range, such as 150-200 GeV or > 200 GeV. In total, there are therefore eight multi-jet SFs (two lepton channels, two p_T^V ranges, 2- or 3-jet events).

The resulting multi-jet fractions are given in Table 12.7, separately for electrons and muons as well as for their combination. The uncertainties quoted are discussed further down. The multi-jet fractions are small, less than 1% except in the medium p_T^V region in the 2-jet category where they are at the 3% level. The top, W and multi-jet SFs obtained in the template fits are used in Figure 12.11 and Figure 12.12 to show the agreement of the simulation with the data.

To provide a better appreciation of the quality of the modelling of the multi-jet background, an "extended" medium-p_T^V region is used, where the $m_T^W > 20$ GeV cut has been removed, thus greatly enhancing the multi-jet contribution. Examples of distributions especially sensitive to the shape and normalization of the multi-jet background are shown in Figure 12.13.

Region	MJ Fraction(%) medium-p_T^V	MJ Fraction(%) high-p_T^V
2-tag, 2-jet, e	2.6 (+0.6 -0.4)	0.0 (+2.1 -0.0)
2-tag, 2-jet, μ	3.0 (+1.6 -0.7)	0.6 (+1.1 -0.6)
2-tag, 2-jet, Combined	2.8 (+0.9 -0.4)	0.4 (+1.1 -0.4)
2-tag, 3-jet, e	0.0 (+1.1 -0.0)	0.0 (+0.9 -0.0)
2-tag, 3-jet, μ	1.5 (+1.0 -0.1)	0.0 (+0.7 -0.0)
2-tag, 3-jet, Combined	0.8 (+0.7 -0.0)	0.0 (+0.6 -0.0)

Table 12.7: Summary of multi-jet (MJ) fractions, separately for electrons and muons as well as combined, for 2- and 3-jet events, in the high and medium p_T^V regions . The errors represent the combined statistical and systematic uncertainties.

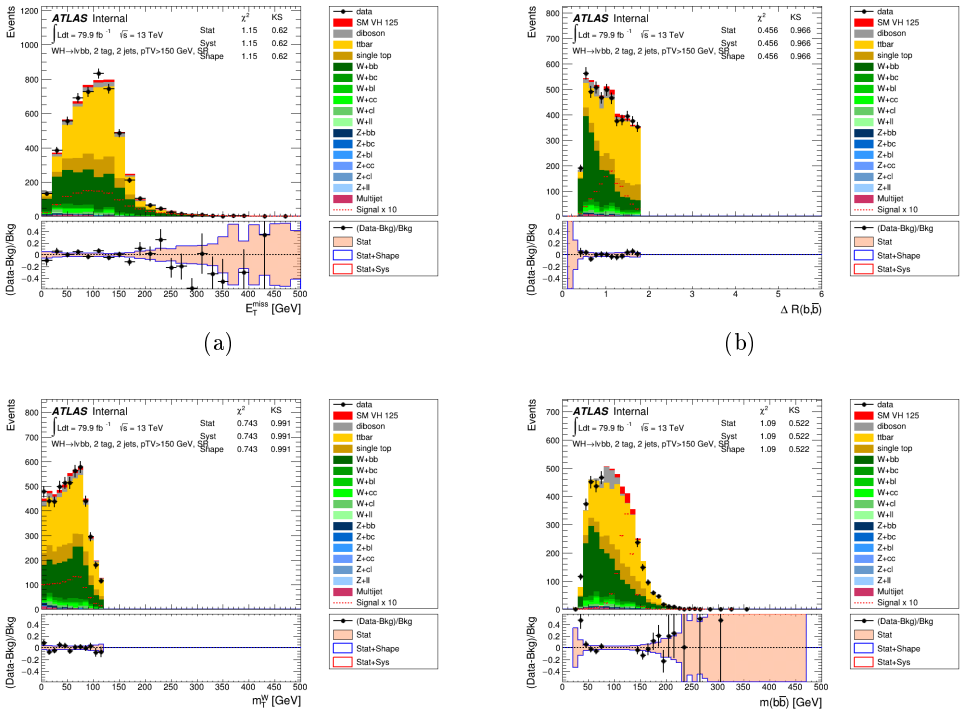

(a) (b) (c) (d)

Figure 12.11: The distributions, for the 2-tag 2-jet p_T^W >150 GeV category, of (a) E_T^{miss} (b) $\Delta R(b\bar{b})$ (c) m_T^W and (d) $m_{b\bar{b}}$ are shown. The electron and muon channels are combined.

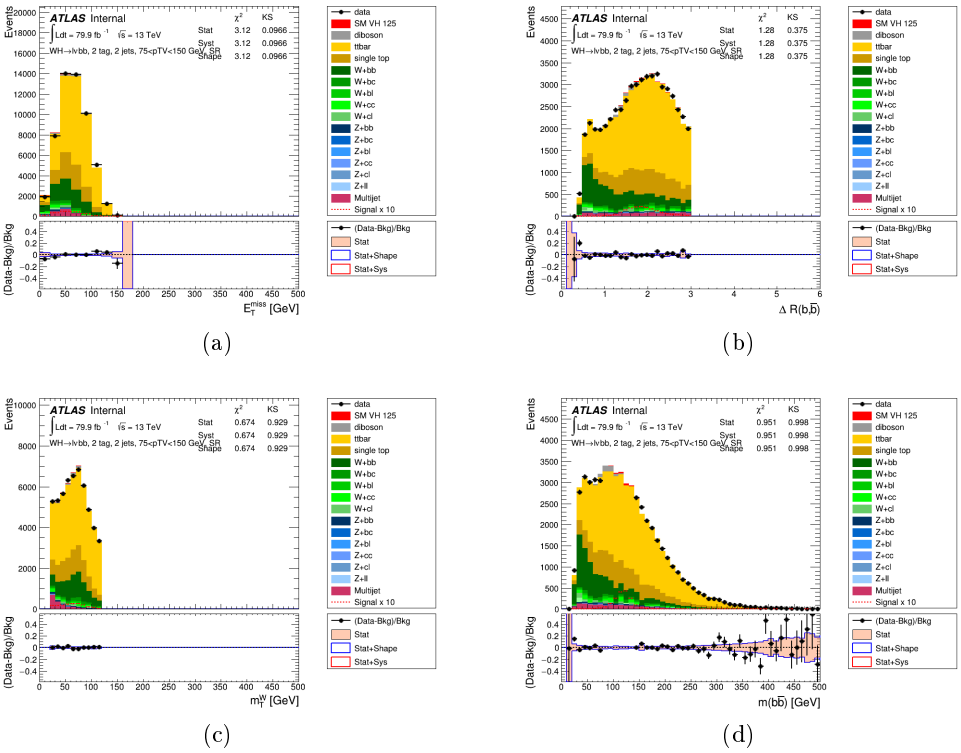

(a) (b)

(c) (d)

Figure 12.12: The distributions, for the 2-tag 2-jet 75 GeV $< p_T^W <$150 GeV category, of (a) E_T^{miss} (b) $\Delta R(b\bar{b})$ (c) m_T^W and (d) $m_{b\bar{b}}$ are shown. The electron and muon channels are combined.

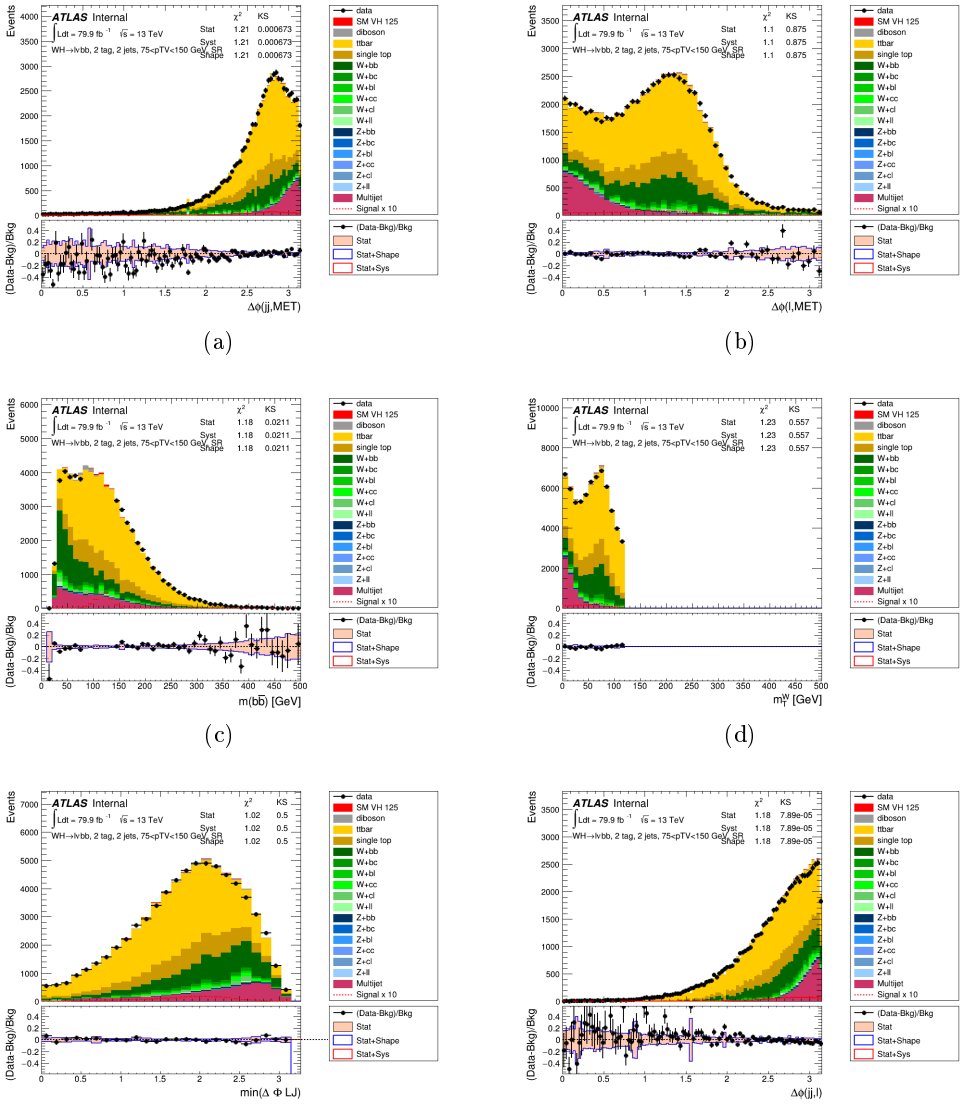

Figure 12.13: Distributions in the "extended" medium-p_T^V region and for 2-jet events of a few multi-jet sensitive variables, for electrons and muons combined. From left to right and from top to bottom: $\Delta\phi(jj, E_T^{miss})$,$\Delta\phi(lepton, E_T^{miss})$, $m_{b\bar{b}}$, m_T^W, $min(\Delta\phi(lepton, j))$, $\Delta\phi(lepton, jj)$.

12.4.1 Systematics uncertainties

Systematic uncertainties can have impacts on the multi-jet estimation. In the following, a number of sources of systematic uncertainty are evaluated, and uncorrelated between electron and muon sub-channels, between 2- and 3- jets regions, and between high and medium p_T^V categories:

- The m_T^W distribution is used in the template fits instead of $\Delta\phi(lepton, E_T^{miss})$.
- The multi-jet templates are obtained from data in the 1-tag control regions after subtraction of the electroweak background. To normalize the electroweak background in a given 1-tag CR, an "ad hoc" scale factor is applied, simply taken to be the ratio of data to simulation in the corresponding 2-tag signal region. This is replaced by a similar ratio calculated in the 1-tag signal region.
- The shape of the electroweak background in a template fit is affected by the relative contributions of the top and W+jets backgrounds. These fractions are obtained from a fit to the $\Delta R(b, \bar{b})$ distribution. The fitted top and W+jets fractions are modified by the corresponding fitted errors, taking into account their anti-correlation.
- Instead of using the full CRs, only the halves of multi-jet events closest to the signal regions in terms of value of the isolation variable are used.
- The 2-tag CRs are directly used instead of the 1-tag CRs (at the expense of reduced statistics).
- In the medium-p_T^V region, the $m_T^W > 20$ GeV cut is removed.
- For $p_T^V > 150$ GeV and in the electron sub-channel, the $E_T^{miss} > 30$ GeV cut is removed.
- Only the lowest unprescaled single-lepton triggers, which involve isolation criteria, are used. (The muon sub-channel is unaffected for $p_T^V > 150$ GeV, where E_T^{miss} triggers are used instead.

For each multi-jet scale factor, the positive and negative differences from the nominal value are separately added in quadrature, and the results are added in quadrature to the statistical uncertainty of the nominal fit. These combined uncertainties, totally dominated by the systematic component, are shown in Table 12.7 in terms of multi-jet fractions. The negative uncertainties are restricted to be at most equal to the nominal values. The main contributors to the systematic uncertainties are: the change of variable used in the template fit and the removal of the m_T^W cut in the medium-p_T^V region; and the replacement of the 1-tag CRs by 2-tag CRs in the

high-p_T^V region. In cases where the fitted nominal value is equal to zero, half of the positive error is used in the global fit as nominal value as well as symmetric error.

The shape of the m_{bb} distribution of the multi-jet background is also affected by some of the aforementioned systematic uncertainties, namely those related to: the choice of "ad-hoc" scale factors; the shape of the electroweak background; the size of the CRs; the choice of 2-tag rather than 1-tag CRs; the single-lepton triggers.

For each of these systematic uncertainty sources, the ratio of the varied to nominal m_{bb} distributions is computed and is found to be significantly different from being uniform in only a few cases: the choice of 2-tag CRs in the medium-p_T^V region in the electron channel and the reduction of the size of the CRs for 2-jet events in the high-p_T^V region. They cover all the other variations and are implemented in the global fit as shape-only systematics. These two variations are shown in Figure 12.14 for 2-jet events in the electron channel.

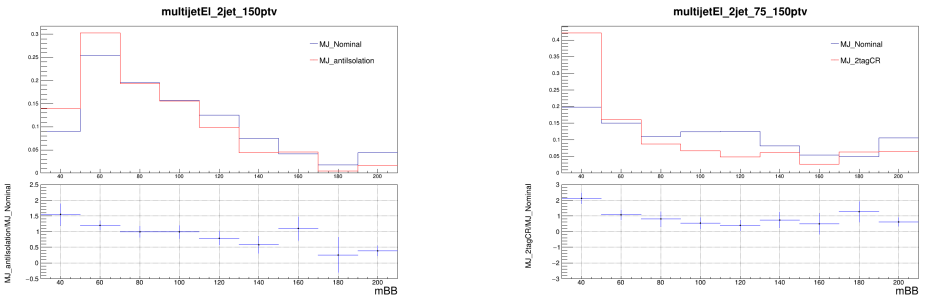

(a) (b)

Figure 12.14: Nominal and systematically varied distributions, with their ratio in the bottom panels. The systematic variations are, for the electron channel: the reduction of the size of the CRs in the high-p_T^V region (a); the choice of 2-tag rather than 1-tag CRs in the medium-p_T^V region (b).

12.5 Multi-jet estimation in the 0- and 2-lepton channel

12.5.1 0-lepton channel

In the 0-lepton channel, the multi-jet background contributes via jet energy mis-measurements. As a result, the fake missing transverse energy tend to be aligned with the mis-measured jet. As already discussed in Section 10.3.3, a set of anti-QCD cuts are applied to reduce the multi-jet background contamination.

In order to estimate the remaining multi-jet contribution, the anti-QCD cuts are loosened by removing the $min[\Delta\phi(E_T^{miss}, jets)]$ cut. A fit to the $min[\Delta\phi(E_T^{miss}, jets)]$

distribution in the 3-jets region is then performed to extract the multi-jets yield. After applying the nominal selection criteria with $min[\Delta\phi(E_T^{miss}, jets)] > 30°$ in 3-jets region, the residual multi-jet contamination is found to be less than 10% of the expected signal contribution and negligible with respect to the total background. Furthermore, the BDT shape of the multi-jet background is studied by selecting the events within the $min[\Delta\phi(E_T^{miss}, jets)] < 20°$ region by subtracting the electroweak backgrounds from data and is found to have the similar shape as the one expected for the sum of all the electroweak backgrounds. The small multi-jet contribution therefore can be absorbed in the floating normalization factors of the electroweak backgrounds in the global likelihood fits. Figure 12.15 shows the post-fit $min[\Delta\phi(E_T^{miss}, jets)]$ distribution in 3-jet region. It is seen that the multi-jet contribution in the 3-jet category occupys the low $min[\Delta\phi(E_T^{miss}, jets)]$ region.

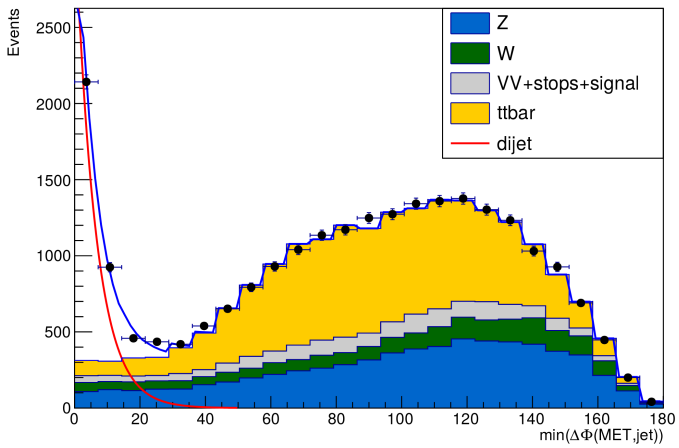

Figure 12.15: Post-fit $min[\Delta\phi(E_T^{miss}, jets)]$ distribution in 2-tag, 3-jet region in 0-lepton channel. The multi-jet is modelled using an exponentially falling distribution of shape $A.e^{-X/c}$, the fitted value of the parameter A is 3264.1 ± 130.4 and the parameter c is 6.27 ± 0.24.

In the 2-jets region, the similar fit cannot be used since the events in the low value of $min[\Delta\phi(E_T^{miss}, jets)]$ region have been already removed by the other anti-QCD cuts. However the multi-jet shape in this region is shown to have the same exponential behaviour as in the 3-jets region, the nominal anti-QCD selections are safe enough to reduce most of multi-jet contribution in the 2-jets region. Therefore the multi-jet background in the 0-lepton channel is found to be a small enough and can be neglected in the global likelihood fit. Figure 12.16 shows the post-fit $min[\Delta\phi(E_T^{miss}, jets)]$ distribution in 2-jet region. As seen in this figure, no multi-jet was observed in this region due to the effect of the remaining event selection applied in the 0-lepton channel.

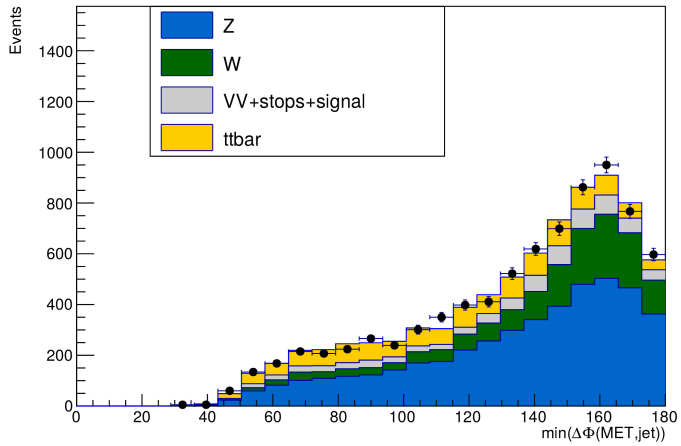

Figure 12.16: Post-fit $min[\Delta\phi(E_T^{miss}, jets)]$ distribution in 2-tag, 2-jet region in 0-lepton channel. No multi-jet was observed in this region.

12.5.2 2-lepton channel

In the 2-lepton channel the multi-jet background is highly suppressed by requiring an event with two isolated leptons, and a dilepton invariant mass close to that of a Z boson. Any residual multi-jet background is estimated using the template method, which fits the expected electroweak background contributions evaluated from MC simulations, and an exponential model for the multi-jet background, to same-sign charged data events. An estimate is then made of the fraction of the background in a mass window around the Z boson peak in the signal region that could be attributed to multi-jet events based on the assumption that the ratio of opposite sign events to same sign events is one for multi-jet background. Inside a dilepton mass window 71 GeV$< m_{ll} <$121 GeV the upper limit of the expected multi-jet contamination as a fraction of the total electroweak background is estimated to be 0.34% and 0.08% for the electron and muon sub-channels, respectively. In the 100 GeV$< m_{b\bar{b}} <$ 140 GeV mass window, the residual multi-jet contamination is found to be less than 10% of the signal contribution, and found to have a BDT shape similar to the one expected for the sum of the remaining backgrounds. This is thus small enough to have a negligible impact on the signal extraction and so is not included in the global likelihood fit.

Chapter 13

Conclusion II

The announcement of the discovery of the Higgs boson in 2012 by the ATLAS and CMS experiments at the LHC was a ground breaking moment in the understanding of the SM. Since the discovery, an extensive work toward the improvement of the accelerator and the detectors for Run-2 has been carried ou. At the end of Run-2, the outstanding performances of the accelerator with higher energy ($\sqrt{s}$ = 13 TeV) and higher luminosity allowed the experiments to collect a large set of high quality data. Among the most challenging analysis in Run-2 is the search for a Higgs boson decaying into b-quark pair. Six years after the 2012 discovery of the Higgs boson, the observation of the $H \to b\bar{b}$ decay has been achieved. Furthermore, for the first time, the production of a Higgs boson in association with a vector boson has been observed.

In the second part of this thesis, the work done towards the observation of the $H \to b\bar{b}$ decay mode and the VH production mode is presented. The search for the SM Higgs boson decaying into b-quark pairs in the associated production mode VH(bb) has been performed using full dataset collected by ATLAS experiment during the LHC Run-2, corresponding to an integrated luminosity of 79.8 fb^{-1} collected at a center-of-mass energy of $\sqrt{s}$ = 13 TeV.

A combined MVA fit of all channels results in a measured VH(bb) signal strength of $\mu_{VH}^{bb} = 1.16 \pm 0.16(stat.)^{+0.21}_{-0.19}(syst.)$. The observation corresponds to an excess with a significance of 4.9 σ, to be compared with an expectation of 4.3 σ.

This result has been cross-checked with a fit to the SM VZ$\to Vb\bar{b}$ signal, and also a cut-based dijet-mass analysis. The VH(bb) signal was observed with a significance of 3.6 σ in the cut-based dijet-mass analysis, compared to 3.5 σ expected. The VZ$\to Vb\bar{b}$ signal was observed with a measured signal strength of $\mu_{VZ}^{bb} = 1.20 \pm 0.08(stat.)^{+0.19}_{-0.16}(syst.)$ which is consistent with the Standard Model prediction.

In a combination with the Run-1 analysis, an observed signal significance of 4.9 σ of the VH(bb) process over the background-only model has been measured, compared to an expectation of 5.1 σ. This corresponds to a measured signal strength of $\mu_{VH}^{bb} = 0.98 \pm 0.14(stat.)^{+0.17}_{-0.16}(syst.)$.

Results from the search for the H$\rightarrow b\bar{b}$ decay from all the Higgs production modes from Run-1 and Run-2 has been combined. An observed significance for the H$\rightarrow b\bar{b}$ decay of 5.4 σ has been measured, to be compared with an expectation of 5.5 σ. Assuming the branching fractions are as predicted by the SM, this is corresponding to a measured signal strength of $\mu_{H\rightarrow b\bar{b}} = 1.01 \pm 0.12(stat.)^{+0.16}_{-0.15}(syst.)$. This result provides direct observation of $H \rightarrow b\bar{b}$ decay mode.

Finally, results of other Run-2 search for the Higgs boson produced in the VH production mode, but decaying into either two photons or four leptons via ZZ^* decays is combined with the Run-2 VH,H$\rightarrow b\bar{b}$ result. The observed significance for the combined VH production from all decay modes is 5.3 σ, to be compared with an expectation of 4.8 σ. Assuming the branching fractions are as predicted by the SM, the measured value of the VH signal strength is $\mu_{VH} = 1.13 \pm 0.15(stat.)^{+0.18}_{-0.17}(syst.)$, providing an observation of the Higgs produced in association with a vector boson.

Within the VH(bb) group, many studies have been carried out to improve the analysis sensitivity and robustness toward the observation. This thesis describes my contribution to two specific studies. The first is a feasibility study to use the taus in the VH(bb) analysis, where the main goal was to verify if a channel explicitly selecting τ decays could bring additional sensitivity for the analysis. Both, the Z($\tau\tau$)H(bb) channel as well as the W($\tau\nu$)H(bb) channel have been investigated. In this study, three different final state have been considered: $\tau_{had}\tau_{had}$, $\tau_{lep}\tau_{had}$ and $\tau_{had}\nu$. The analysis was performed using a cut-based selection method using the data collected by ATLAS during the 2015-2016 running periods, corresponding to total integrated luminosity of 36.8 fb^{-1}. I have been working on defining an additional selection criteria for tau decays events so that additional gain can be increased as much as possible. It was found that a dedicated Z($\tau\tau$)H(bb) channel, in the context of the current VH(bb) analysis, with the additional optimized selections, would add at most 2% of the current ZH yield. Analogously, the additional selections in the W($\tau\nu$)H(bb) channel can recover at most 4% of WH signal events. Compared to the current VH yields, the total increase of the sensitivity, resulting from using taus, is relatively small and so considering a dedicated Z($\tau\tau$)H(bb) channel or W($\tau\nu$)H(bb) channel is probably useless.

When measuring a physics process with data collected by ATLAS it is imperative to be able to model the background processes. This accurate description of background events will enable us to measure accurately the signal process. One of the significant background for the VH(bb) analysis is the multi-jet background, which have the potential to contribute a non-negligible background component due to the large cross-sections. Most of the time, MC simulation is used to describe the background events. However, given the complexity in modelling properly the multi-jet background, data-driven techniques is used for estimating this background. In this thesis, the multi-jet background is estimated using the Template method in a multi-jet enriched control region that is defined using inverted lepton isolation cuts.

The multi-jet background is studied in details for the 1-lepton channel using the MVA and dijet-mass analysis methods. The fraction of the multi-jet events in the signal region was estimated. In the 1-lepton channel, a non-negligible contribution from multi-jet events was found. The different sources of the systematic uncertainty including shape and normalization uncertainties were discussed. A brief summary of the multi-jet background estimation in the 0- and 2-lepton channel is given. Studies have shown that the multi-jet contamination is negligible in these two channels.

Looking to the future, this is just another step in our understanding of the Standard Model, and the recently discovered Higgs boson. Whilst the $H \to b\bar{b}$ branching ratio has been measured to be consistent with the SM, this is still with large ($\approx$ 30%) uncertainties, meaning that couplings of the Higgs boson beyond those predicted by the SM are far from ruled out. As the dataset increases in size with more collected data and our understanding of systematic uncertainties improves, we can now look towards precision measurements of the coupling and decay of the Higgs boson provides an effective way to search for physics beyond the Standard Model, and will be a rapidly developing field for the remainder of LHC-era physics and beyond.

List of Figures

2.1 The LHC Layout 7

2.2 Cumulative luminosity versus time delivered by LHC (green) and recorded by ATLAS (yellow) during stable beams for pp collisions at $\sqrt{s}$= 13 TeV for the year of 2015 (a), 2016 (b), 2017 (c) and 2018 (d).[2] 8

2.3 The CERN Accelerator Complex showing all experiments around the LHC. 10

2.4 Cumulative luminosity versus time delivered to ATLAS (green), recorded by ATLAS (yellow), and certified to be good quality data (blue) during stable beams for pp collisions at 13 TeV centre-of-mass energy in 2015-2017. 10

2.5 Cumulative luminosity versus day delivered to ATLAS during stable beams and for high energy p-p collisions over the years 2011-2018 . . 11

2.6 Mean number of interactions per bunch crossing for the 2015, 2016 and 2017 ATLAS pp datasets [6]. 12

2.7 Cut-away view of the ATLAS detector. 13

2.8 The layout of the current ATLAS inner tracking detector, including the additional IBL detector layer. 15

2.9 View of the Inner Detector, which consists of a set of precision silicon tracking detectors (Pixel and SCT) extending up to a radius of 60 cm surrounded by the TRT gaseous detector. 16

2.10 Layout of the ATLAS inner detector 17

2.11 The ATLAS calorimeters. Image courtesy of the ATLAS Experiment at CERN, http://atlas.ch. 20

2.12 Diagram of principal components of the Trigger/DAQ system and interconnections. 23

2.13 Racks of the first-level calorimeter trigger system installed close to the detector. 25

2.14 Sketch of the flow of tracks through the ambiguity solver. [16] 26

2.15 The efficiency to reconstruct charged primary particles in jets with $|\eta| < 1.2$ as a function of the angular distance of the particle from the jet axis for various jet p_T for simulated dijet MC events.[16] . . . 28

2.16 The track reconstruction efficiency is compared for charged primary particles in jets with $|\eta| < 1.2$ ($|\eta| > 1.2$) for the entire jet-p_T range as a function of the jet p_T for simulated dijet MC events.[16] 28

2.17 Distribution of the average number of reconstructed vertices as a function of μ. The curve represents the result of a fit to the simulation, while dots correspond to the 2016 data.[19] 29

2.18 The track reconstruction efficiency as a function of η (a) and p_T (b).[20] 29

2.19 The transverse impact parameter resolution in 2015 (with IBL) and 2012 (without IBL) as function of p_T (a) and η (b).[21] 30

2.20 Average number of reconstructed tracks in the ATLAS Inner Detector as a function of μ for the Loose and TightPrimary track selections[22]. 30

2.21 Schematic view of a B hadron decay inside a jet. [34]. 34

2.22 Light-flavor rejection (defined as the inverse of the mis-tagging rate) as a function of b-tagging efficiency for the MV1 algorithm, as measured in simulated $t\bar{t}$ jets. [33]. 34

3.1 Forecast for peak luminosity (red dots) and integrated luminosity (blue line) in the HL-LHC era, for the case of ultimate HL-LHC parameters. Note that for the sake of simplicity there is no learning curve for luminosity after LS3.[38] 40

3.2 Plan for LHC operation towards the upgrade for the High-Luminosity LHC. 41

3.3 Insertion of IBL, together with the beam pipe, inside the pixel inner support tube. 45

3.4 Unfolded longitudinal impact parameter resolution measured from data in 2015, at $\sqrt{s}$ 13 T eV , with the Inner Detector including the IBL, as a function of p_T compared to that measured from data in 2012, at $\sqrt{s}$ 8TeV . The data in 2015 is collected with a minimum bias trigger. The data in 2012 is derived from a mixture of jet, tau and missing E_T triggers [41] 47

3.5 The fluence and dose distributions for the ITk (including the strip and pixel detector) layout in 1 MeV neutron equivalent flux using FLUKA [42] simulation. [43] 49

3.6 Schematic layout of the ITk for the HL-LHC phase of ATLAS. Here only one quadrant and only active detector elements are shown. The horizontal axis is the axis along the beam line with zero being the interaction point. The vertical axis is the radius measured from the IP. 50

4.1 Working principle of the pn-junction. The upper images show the energy band structure in the n- and p-type silicon. The lower images visualize the acceptors, donors, electrons, and holes (large blue, large red, small blue, and small red circles, respectively) in the doped silicon materials. The width of the depletion zone is denoted by w. 52

4.2 Representation of an impurity occupying the site of a silicon atom in the lattice. The donor (left) donates an extra electron, creating an n-type semiconductor. The acceptor (right) reduces the density of electrons creating a p-type semiconductor. The missing electron is illustrated by a missing bond line. 54

4.3 Representation of the relative depletion regions for (a) an unbiased pn-junction, (b) a forward biased semiconductor and (c) a reverse biased semiconductor. 55

4.4 A p-n junction in thermal equilibrium with zero-bias voltage applied. Under the junction, plots for the charge density, the electric field, and the voltage are reported. (The log concentration curves should actually be smoother, like the voltage.) [49] 56

4.5 The stopping power for positive muons in copper as a function of the muon momentum [54]. The solid line is the total stopping power of the muon. [55] 61

4.6 The Bethe dE/dx and the Landau most probable energy per unit thickness $\delta p/x$ in silicon. Minimum ionization ($dE/dx|_{min}$) is 1.664 MeV $g^{-1}cm^2$. Radiative losses are excluded. The incident particles are muons.[55] 61

4.7 Straggling functions in silicon for 500 MeV pions, normalized to unity at the most probable value. The width w is the full width at half maximum. [55] 62

4.8 Most probable energy loss in silicon δp per unit thickness (x) , scaled to the mean loss of a minimum ionizing particle, 388 eV/μm (1.66 MeV $g^{-1}cm^2$)[55]. 63

4.9 Illustrations of the three major photon interactions with matter. . . 64

4.10 Monte Carlo simulation of the interaction of a PKA with an initial energy of 50 keV in silicon. The PKA initially travels in the vertical direction upwards, starting from the origin. At the ends of the trajectories of the displaced atoms, clusters of defects are generated [63]. 67

4.11 Schematic representation of some point defects in a square lattice. Silicon atoms are shown in green, other atoms in purple. 68

4.12 The calculated damage functions for protons, neutrons, pions, and electrons over a wide range of energies. The normalization of the ordinate to 95 MeV mb represents the damage equivalent to 1 MeV neutrons [67]. 70

4.13 Relationship between the depletion voltage, U_{dep} , (left) and effective doping, N_{eff} , (right) as a function of the fluence for a 300 μm silicon detector [68]. 71

4.14 Measured change of the effective doping concentration as a function of the time during controlled annealing at 60 °C with fitted contributions of short term beneficial annealing, long term reverse annealing, and stable damage [65]. 72

5.1 Schematic view of a pixel cell in a hybrid pixel detector. This detector is composed of a sensor and a readout chip interconnected via a bump ball in between the under bump metallizations on chip and sensor side [71]. 77

5.2 (a) n^+-in-n sensor design with an n-type bulk and n^+ implants. The guard rings are located on the backside. (b) n^+-in-p sensor design with a p-type bulk and n^+ implants [73]. The guard rings are on the topside. 78

5.3 Layout of a pixel sensor: (a) cut-out of a sensor corner with GRs in the periphery of the active area of the sensor, (b) cut-out of four pixels from the active area of the sensor. A bias rail runs in between the short side of the pixels. It is situated on the same side as the bias dots, implemented either in an opening of the pixel implant (as shown in the figure) or in close proximity. Such design is called standard single punch-through design. On the other side of the pixel cell the bump pad for the interconnection to the readout channels is located [74]. 79

5.4 Schematic view of the ATLAS 4-Layer Pixel Detector for Run-2[76]. 81

5.5 Top: 3D rendering of the IBL detector with its 14 staves (some staves removed to make the module side of staves visible). Bottom: Sketch of the loading scheme of the different module types on the IBL staves. 81

5.6 The present ATLAS module displaying a sensor in the thickness range from 200 μm (FE-I4 sensor) to 250 μm (FE-I3 sensor)[78]. 82

5.7 The FE-I4 readout chip for IBL with the to-scale FE-I3 readout chip used in ATLAS for comparison to[79]. 83

5.8 (top) the current ATLAS sensor design and (bottom) the IBL sensor design [80]. 83

5.9 The two sensor technologies: (a) planar n^+-in-n and (b) 3D n^+-in-p sensors. The n^+ electrodes are illustrated in green, while the p^+ electrode are coloured red. In the IBL, the charge collection distance d_c is 200 μm for the planar sensors and 67 μm for the 3D sensors [74]. 84

5.10 Schematics of the two 3D sensor options presently operational in the ATLAS IBL. The 3D sensor (a) with columns, etched partially through the bulk (CNM design) and (b) with full-through columns (FBK design). Both sensors are processed double-sided. [80] 85

5.11 A possible schematic layout of the pixel detector for Phase-II. It represents the inclined layout with a pseudo-rapidity coverage up to $|\eta| = 4$. The horizontal axis is parallel to the beam line, while the vertical axis is the radius from the center of the beam line, point zero in the diagram. Only the active detector elements of the first quadrant are shown. [43]. 86

5.12 schematic of a HV-CMOS pixel. A CMOS consists of an NMOS and a PMOS. The NMOS is embedded in a shallow p-well inside the deep n-well while the PMOS is located inside the deep n-well in the p-substrate [89]. 89

5.13 A brief representation of the active edge process flow applied on n-in-p detector fabrication [94]. 91

5.14 The four design variations of the active edge production. From left to right: no Guard Ring - no Bias Rail design, no Bias Rail - one Guard Ring design, no Guard Ring - one Bias Rail design and one Guard Ring - one Bias Rail design. 92

5.15 Measured $1/C^2$, where C is the capacitance, as a function of bias voltage for an Advacam active edge structure. CV-measurement is carried out at three operational frequencies (30 kHz, 50 kHz, 100 kHz). The three CV curves are fitted with linear function in two regions. The intersection of the lines determines $V_{fd} \approx 6$ V. 94

5.16 Probe station at LAL-clean-room used for the IV- and CV- measurements. The probe is attached to an optical microscope and a conductive copper chuck. The needle probe and high precision mechanical base is also visible at the left side of the picture. 94

5.17 IV-measurement for different design variations for all the structures with 50 μm thickness and NiAu UBM (a), Pt UBM (b). Semi-logarithmic scale is used. 95

5.18 IV-measurement for the two UBM variations for all the structures with 50 μm thickness and NoGR-NoBR design. Semi-logarithmic scale is used. 95

5.19 IV-measurement for different design variations for all structures with 100 μm thickness and NiAu UBM (a), Pt UBM (b). Semi-logarithmic scale is used. 96

5.20 IV-measurement for different design variations for all structures with 150 μm thickness and NiAu UBM (a), Pt UBM (b). Semi-logarithmic scale is used. 96

5.21 IV-measurement for different thickness variations for all structures with NoGR-NoBR design and NiAu UBM (a), Pt UBM (b). Semi-logarithmic scale is used. 96

5.22 Average breakdown voltage for different wafer thickness, comparing NiAu UBM and Pt UBM. 97

5.23 Average breakdown voltage for different design, comparing NiAu UBM and Pt UBM. 98

5.24 Average depletion voltage for different wafer thickness, comparing NiAu UBM and Pt UBM. 99

6.1 First order derivative of secondary ion intensity for all monitored elements on a typical silicon sensor sample. Abrupt changes are observed in layer interface regions which are marked with different shading colors. Oxygen and silicon curves are scaled to a factor of 10^{-2} and 10^{-5} respectively for representation purposes. 108

6.2 Schematic of the SIMS sputter-then-image method to create separate two-dimensional images. A series of these 2D images can be reconstructed to create a 3D representation of the sample. 110

6.3 Meshing of a disc surface using triangular sub-elements. 114

6.4 The CAMECA IMF 7F System where SIMS measurements were performed at GEMAC laboratory at the university Saint-Quentin-en-Yvelines at Versailles [102]. 115

6.5 Doping profile map (left) and comparison of 1D doping profile from simulation (blue curve) and SIMS measurement (red curve) for Phosphorus implant in the pixel region (right). 116

6.6 Doping profile map (left) and comparison of 1D doping profile from simulation (blue curve) and SIMS measurement (red curve) for Phosphorus implant in the Edge region (right). 117

6.7 Doping profile map (left) and comparison of 1D doping profile from simulation (blue curve) and SIMS measurement (red curve) for Boron implant for p-spray (right). 117

6.8 Doping profile map (left) and comparison of 1D doping profile from simulation (blue curve) and SIMS measurement (red curve) for Boron implant in active edge region (right). 118

6.9 Overall view of the simulated n^+-in-p active edge pixel structure showing dopant concentration profile. Sensor geometrical size is $400\mu m$ in the x-direction and $150\mu m$ in the y-direction. 119

6.10 Doping profile map (left) and comparison of 1D doping profile from simulation (blue curve) and SIMS measurement (red curve) for Boron implant in active edge region (right). 119

6.11 Simulated Leakage current as a function of Bias Voltage for different doses. As the irradiation dose increases the breakdown voltage increases up to 225 V for 2x10^{16} n_{eq}/cm^2. 121

6.12 Leakage current as a function of Bias Voltage, with a comparison of simulation to data, after irradiation. The sensor is 150 μm thick and has a GR and BR at the edge. The breakdown of irradiated sensor increases up to 225 V for a fluence of 2x10^{16} n_{eq}/cm^2. 121

6.13 Leakage current as a function of Bias Voltage, with a comparison of simulation to data, before irradiation. The sensor is 150 μm thick and has a GR and BR at the edge. The breakdown of non-irradiated sensor is about 150 V. 122

6.14 The majority charge carriers contribute to the electric current in n-type and p-type semiconductor 124

6.15 A transmission line method (TLM) test structure. The Blue regions is the doped silicon region. Dark gray region is the array of aluminium contacts which formed with various spacings over the doped region. . 125

6.16 Top view of a two-terminal contact semiconductor structure. 125

6.17 Mask used in the mask-based lithography with direct laser writing used produce the TLM test structure used in this study. 127

6.18 An example of the layout design of one of the contact series in the TLM test structure used in this study, taken from the GDS design file. 128

6.19 A brief process flow to fabricate the TLM test structure. 129

6.20 Schematic cross section of TLM sample illustrating the etching process for n-times of doped layers (blue region) until reaching the silicon substrate (beige region). 130

6.21 The TLM measurement allows assessing the magnitude of the resistance by applying a voltage across the contacts and measuring the resulting current. 130

6.22 Resistance versus contact separation obtained from TLM measurement. Both the sheet resistance as well as the contact resistance can be determined using this technique. 130

6.23 Resistance in-depth measurement used in this study. Repetitively, a small layer of implant is etched, using Reactive Ion Etching (RIE), and the resistance at different depths is measured until reaching the substrate. 131

6.24 (a) The two-point probe station used to measure the resistance using the TLM method. (b) Microscope view of needles placed on two adjacent contacts to perform the IV measurement. 133

6.25 The "Advanced Vacuum-Vision 320" RIE machine used in this study to etch the TLM samples. 134

6.26 Cross section of the RIE chamber where the TLM samples were etched. 134

6.27 Three consecutive profilometer measurement of an irradiated sample obtained after the first, second and third etching was performed. A layer of thickness 200 nm is etched in each step. 135

6.28 Measured Current as function of bias Voltage of a non irradiated Boron doped sample at different spacing between contacts. 135

6.29 Measured resistance as a function of contact spacing distance for non irradiated sample (a) as well as irradiated sample (b) at four different etching steps. The semi-logarithmic scale is used here. 136

6.30 TLM measurement of the active carrier concentration as a function of depth for non irradiated sample (red curve) compared to two irradiated samples of 2×10^{15} n_{eq}/cm^2 (blue curve) 2×10^{16} n_{eq}/cm^2(Violet curve) neutrons irradiation fluences. 137

6.31 TLM measurement (green curve) compared to SIMS measurement (red curve) of the active carrier concentration as a function of depth for non irradiated sample. 138

6.32 TLM measurement (green curve) of the active carrier concentration as a function of depth for non irradiated sample compared to simulated doping profile corresponding to three implantation energies: 240 keV, 130 keV and 60 keV. The sample provided by the manufacturer was implanted with a 60 keV. 139

7.1 A diagram illustrating the process of producing an electron or positron beam for tests at DESY [115]. 142

7.2 Photograph of the DESY beam hall. The beam direction is from right to left. . . . 143

7.3 Illustration of a standard beam test setup [117]. . . . 144

7.4 The cooling box, manufactured by MPP (a) which is situated at CERN, while the Dortmund cooling box (b) is used at CERN and DESY [122]. . . . 146

7.5 The EUDAQ control panel. . . . 147

7.6 Example of EUDET Online Monitoring plots for a non-irradiated Active edge pixel detector. The colorbar in this plot indicate number of hits. As seen here, most of the particle hits are positioned at the edge of the module. The module was placed such that the beam hits the edge in order to study the edge efficiency in this case. . . . 148

7.7 Example of EUDET Online Monitoring correlation plot for a non-irradiated active edge pixel detector with another DUT. The majority of the hits lie on the straight line start at the top left corner and extend to the bottom right corner. This indicates a negative correlation between the two modules. Hence, the fact that the two DUTs are not aligned. This is explained by the fact the two DUTs where mounted back-to-back. . . . 149

7.8 An example of the output from the clusters vs run analysis class written for TBMon, showing the total matched cluster size for a sensor as a function of time (per run). (a) is an example of a good set of runs while (b) is an example of a set of runs with lower statistics and poorer alignment. . . . 152

7.9 Four different sensor types of the Advacam SOI production: the active edge design with $d_e = 50\ \mu m$, one GR and no p-t structure (top left), the slim edge design with $d_e = 100\ \mu m$, one grounded BR and the common p-t structure (top right), the slim edge design with one BR and GR and the single p-t design (bottom left) and the slim edge design with only one BR and the single p-t structure (bottom right) [132]. . . . 155

7.10 Sensor design under study. (a) Active edge design of 150 μm thickness with GR edge structure. (b) Slim Edge design of 100 μm thickness with BR and punch-through edge design. . . . 156

7.11 Comparison of the hit efficiency maps of active edge and slim edge modules. (a) Active edge design of 150 μm thickness with GR edge structure. (b) Slim Edge design of 100 μm thickness with BR and punch-through edge design. The modules were measured at a beam test at CERN-SpS. 156

7.12 Comparison of the in-pixel hit efficiency maps of active edge and slim edge modules with a projection of the pixel cell in each design. Pixel cell size in both designs is 50×250 μm^2. (a) Active edge design of 150 μm thickness with GR edge structure. (b) Slim Edge design of 100 μm thickness with BR and punch-through edge design. The modules were measured at a beam test at CERN-SpS. 157

7.13 In-pixel hit efficiency map (left) at the edge of 150 μm thick sensor with 50 μm active edge module with a projection of the pixel cell (right). Pixel cell size is 50×250 μm^2. The module was measured at a beam test at CERN-SpS. 158

7.14 Hit efficiency at the edge of the 150 μm thick active edge module with the 50 μm edge distance. The module was measured at CERN-SpS. The pixel cell has an FE-I4 cell size of 50×250 μm^2 and the hit efficiency is evaluated as a function of the distance from the last pixel column to the edge region. 158

9.1 The Standard Model of particle physics, with quarks (purple), leptons (green), gauge bosons (red), and Higgs boson (yellow). The first, second, and third columns show the three generations of fermions, the fourth, fifth columns show the vector bosons, and the sixth columns shows the Higgs boson. The gluon is the vector boson of strong nuclear force, the photon is the vector boson of electromagnetism, and the Z and $W^{\pm}$ are the vector bosons of weak interaction. The Higgs boson is linked to the electroweak symmetry breaking. The mass, charge, spin and name of each particle is given in the Figure [147]. 169

9.2 Feynman diagram example: Annihilation of an electron and a positron creating a photon which decays into a new electron positron pair. . . 171

9.3 Shape of the Higgs potential for negative (a) and positive μ^2(b) [153]. 173

9.4 Inclusive Higgs boson production cross-section as a function of its mass at $\sqrt{s}$= 14 TeV at the LHC. [156] 176

9.5 SM Higgs boson leading order production processes at the LHC.[157] 176

9.6 SM Higgs boson production cross section as a function of the center-of-mass energy $\sqrt{s}$ at $m_H = 125$ GeV. [156] 178

9.7 Standard Model Higgs boson branching ratio as a function of its mass. The theoretical uncertainties in the branching ratios include the higher order corrections on the theoretical calculations and also the errors in the SM input parameters in particular gauge couplings and fermions masses. [156] 179

9.8 Leading order Feynman diagrams of SM Higgs boson decay to a photon pair. [157] 180

9.9 Feynman diagrams for the three leptonic decay channels of VH($b\bar{b}$). . 182

9.10 Lowest order Feynman diagrams for quark-induced W$b\bar{b}$ or Z$b\bar{b}$ production (left) and gluon-induced Z$b\bar{b}$ production. 183

9.11 Lowest order Feynman diagram for top-antitop pair production and decay. 184

9.12 LO Feynman diagrams for semileptonic diboson production in WZ and ZZ channels. 184

9.13 Feynman diagrams for single-top production: (from left to right) (a) LO s-channel diagram, (b) NLO t-channel diagram and (c) NLO Wt-channel diagram. 185

9.14 The measured interaction strength of the SM Higgs boson as a function of the mass of different particles in the Standard Model [165]. . 186

9.15 (a) Cross-sections times branching fraction for ggF, VBF, VH and tH+$t\bar{t}$H production in each relevant decay modes, normalized to their SM predictions with (a) ATLAS expirement [174] and (b) CMS experiment [175]. 188

10.1 Feynman diagrams for the quark initiated SM VH($b\bar{b}$) process in the 0-lepton (a),1-lepton (b) and 2-lepton (c) channels. 191

10.2 Feynman diagrams for the gluon initiated SM VH($b\bar{b}$) process in the 0-lepton (a) and 2-lepton (b) channels. 192

10.3 The BDT_{VH} output post-fit distributions in the 0-lepton (top), 1-lepton (middle) and 2-lepton (bottom) channels for 2-b-tag events, in the 2-jet (left) and exactly 3-jet (or ≥ 3 jets for the 2-lepton case) (right) categories in the high-p_T^V region. The background contributions after the global likelihood fit are shown as filled histograms. The Higgs boson signal ($m_H = 125$ GeV) is shown as a filled histogram on top of the fitted backgrounds normalised to the signal yield extracted from data ($\mu = 1.16$), and unstacked as an unfilled histogram, scaled by the factor indicated in the legend. The dashed histogram shows the total pre-fit background. The size of the combined statistical and systematic uncertainty for the sum of the fitted signal and background is indicated by the hatched band. The ratio of the data to the sum of the fitted signal ($\mu = 1.16$) and background is shown in the lower panel. The BDT_{VH} output distributions are shown with the binning used in the global likelihood fit. 220

10.4 Event yields as a function of log_{10}(S/B) for data, background and a Higgs boson signal with $m_H = 125$ GeV. Final-discriminant bins in all regions are combined into bins of log_{10}(S/B) , with S being the fitted signal and B the fitted background yields. The Higgs boson signal contribution is shown after rescaling the SM cross-section according to the value of the signal strength extracted from data ($\mu = 1.16$). In the lower panel, the pull of the data relative to the background (the statistical significance of the difference between data and fitted background) is shown with statistical uncertainties only. The full line indicates the pull expected from the sum of fitted signal and background relative to the fitted background. 221

10.5 The fitted values of the Higgs boson signal strength μ_{VH}^{bb} for $m_H = 125$ GeV for the WH and ZH processes and their combination. The individual μ_{VH}^{bb} values for the (W/Z)H processes are obtained from a simultaneous fit with the signal strength for each of the WH and ZH processes floating independently. The probability of compatibility of the individual signal strengths is 84%. 223

10.6 The distribution of m_{bb} in data after subtraction of all backgrounds except for the WZ and ZZ diboson processes, as obtained with the dijet-mass analysis. The contributions from all lepton channels, p_T^V regions and number-of-jets categories are summed and weighted by their respective S / B , with S being the total fitted signal and B the total fitted background in each region. The expected contribution of the associated WH and ZH production of a SM Higgs boson with $m_H = 125$ GeV is shown scaled by the measured signal strength ($\mu = 1.06$). The size of the combined statistical and systematic uncertainty for the fitted background is indicated by the hatched band. 224

10.7 The fitted values of the Higgs boson signal strength μ_{VH}^{bb} for $m_H = 125$ GeV for the WH and ZH processes and their combination, using the 7 TeV, 8 TeV and 13 TeV data. The individual μ_{VH}^{bb} values for the (W / Z) H processes are obtained from a simultaneous fit with the signal strengths for each of the WH and ZH processes floating independently. 226

10.8 The fitted values of the Higgs boson signal strength $\mu_{H\to b\bar{b}}$ for $m_H = 125$ GeV separately for the VH, $t\bar{t}$H and VBF+ggF analyses along with their combination, using the 7 TeV, 8 TeV and 13 TeV data. The individual $\mu_{H\to b\bar{b}}$ values for the different production modes are obtained from a simultaneous fit with the signal strengths for each of the processes floating independently. The probability of compatibility of the individual signal strengths is 83%. 227

10.9 The fitted values of the Higgs boson signal strength μ_{VH} for $m_H = 125$ GeV separately for the H$\to b\bar{b}$, H$\to \gamma\gamma$ and H$\to ZZ^* \to 4l$ decay modes, along with their combination. The individual μ_{VH} values for the different decay modes are obtained from a simultaneous fit with the signal strengths for each of the processes floating independently. The probability of compatibility of the individual signal strengths is 96%. 229

11.1 Tree-level Faynman diagram representing quark-initiated WH/ZH process with the tau leptons in the final state. The ZH process is the signal Feynman diagram searched for in this feasibility study. 232

11.2 The ATLAS analysis model for Run-2. [206] 233

11.3 Overview of the CxAOD Framework workflow. The framework made of two key algorithm: CxAODMaker and CxAODReader. At each level, basic object and event selections are applied to serve the specific analysis. 234

11.4 (a) Feynman diagram of the tau leptonic decay by the emission of an off-shell W boson. (b) Typical signature of a hadronic tau decay. . . 236

11.5 Overview of the dominating tau lepton decay modes. The category "others" contains decays with other charged or neutral mesons (mainly kaons), and higher number of neutral or charged pions. . . 236

11.6 Efficiency for hadronic tau identification (open symbols) and combined reconstruction and identification efficiency (full symbols) as a function of the hadronic tau p_T, for 1-track (a) and 3-track (b) hadronic tau candidates. [208] 238

11.7 Number of events in different trigger configuration for the ggZH sample in the $\tau_{had}\tau_{had}$ channel. No events pass the MET Only trigger. . 241

11.8 Number of events in different trigger configuration for the qqZH sample in the $\tau_{had}\tau_{had}$ channel. No events pass the MET Only trigger. . 241

11.9 Weighted Cutflow for the event selected in the $\tau_{had}\tau_{had}$ channel. . . 242

11.10 The transverse momentum distribution of the Z boson (p_T^Z) in the selected events in the $\tau_{had}\tau_{had}$ channel. 243

11.11 Weighted Cutflow for the event selected in the $\tau_{lep}\tau_{had}$ channel. . . 244

11.12 Weighted Cutflow for the event selected in the $\tau_{lep}\tau_{had}$ channel for nJets=2. 245

11.13 Weighted Cutflow for the event selected in the $\tau_{lep}\tau_{had}$ channel for nJets=3. 245

11.14 Weighted Cutflow for the event selected in the $\tau_{lep}\tau_{had}$ channel for nJets≥4. 246

11.15 The transverse momentum distribution of the Z boson (p_T^Z) in the selected events in the $\tau_{lep}\tau_{had}$ channel for nJets=2 246

11.16 The transverse momentum distribution of the Z boson (p_T^Z) in the selected events in the $\tau_{lep}\tau_{had}$ channel for nJets=3 247

12.1 The m_T^W distribution in the inverted isolation 1-lepton $p_T^W > 150$ GeV region, requiring exactly 1 b-tag with 2 signal jets in e channel(a), 2 signal jets in μ channel(b), 3 signal jets in e channel(c), 3 signal jets μ channel(d). 255

12.2 The m_T^W distribution in the inverted isolation 1-lepton 75 GeV $< p_T^W <$ 150 GeV region, requiring exactly 1 b-tag with 2 signal jets in e channel(a), 2 signal jets in μ channel(b), 3 signal jets in e channel(c), 3 signal jets μ channel(d). 256

12.3 The m_T^W distribution in the isolated 1-lepton $p_T^W > 150$ GeV region, requiring exactly 2 b-tag with 2 signal jets (a), 3 signal jets (b), after applying top ($t\bar{t}$+ single top) and W+jets normalisation factors. Bins 1-21 correspond to the e only channel, bins 22 to 42 correspond to the mu only channel, and bins 21 and 42 represent the W+HF control region. 257

12.4 The m_T^W distribution in the isolated 1-lepton 75 GeV $< p_T^W <$ 150 GeV region, requiring exactly 2 b-tag with 2 signal jets (a), 3 signal jets (b), after applying top ($t\bar{t}$+ single top) and W+jets normalisation factors. Bins 1-21 correspond to the e only channel, bins 22 to 42 correspond to the mu only channel, and bins 21 and 42 represent the W+HF control region. 258

12.5 The distributions, for the 2-tag 2-jet p_T^W >150 GeV category in electron channel W+HF signal region, of (a) E_T^{miss} (b) m_{bb} (c) $\Delta\phi(lepton, E_T^{miss})$ and (d) $\Delta\phi(lepton, bb)$ are shown. 258

12.6 The distributions, for the 2-tag 2-jet $< p_T^W >$150 GeV category in muon channel W+HF signal region, of (a) E_T^{miss} (b) m_{bb} (c) $\Delta\phi(lepton, E_T^{miss})$ and (d) $\Delta\phi(lepton, bb)$ are shown. 259

12.7 The MJ BDT shape comparison for the nominal (in black) and some main shape variations in the high-p_T^V region, 2 jet e channel (a), 2 jet μ channel (b), 3 jet e channel (c), and 3 jet μ channel (d). The green histograms indicate the impact of using the reduced inverted isolation region, the red histograms indicate the impact of using the top and W+jets normalization factors in the inverted isolation region, and the histograms in blue indicate the impact of using the lowest lepton p_T trigger. 261

12.8 The MJ BDT shape comparison for the nominal (in black) and some main shape variations in the medium-p_T^V region, 2 jet e channel (a), 2 jet μ channel (b), 3 jet e channel (c), and 3 jet μ channel (d). The green histograms indicate the impact of using the reduced inverted isolation region, the red histograms indicate the impact of using the top and W+jets normalization factors in the inverted isolation region, and the histograms in blue indicate the impact of using the lowest lepton p_T trigger. 262

12.9 The distribution of $\Delta R(b,\bar{b})$ in the dijet-mass analysis for all regions with $p_T^W > 150$ GeV combined, in the 2-jet category. The electron and muon contributions are summed. The top (yellow) and W (green) contributions are normalized according to the results of the fit to this distribution. The fitted normalization factors are 1.08 and 1.26, respectively. 264

12.10Distribution of $\Delta\phi(lepton, E_T^{miss})$ in the dijet-mass analysis in the medium-p_T^V region for electrons (left) and muons (right), in the 2-jet category. The electroweak (yellow) and multi-jet (red) contributions are normalized according to the results of the fit to this distribution. The multi-jet fractions are 2.6% and 3.0% in the electron and muon channels, respectively. 265

12.11The distributions, for the 2-tag 2-jet p_T^W >150 GeV category, of (a) E_T^{miss} (b) $\Delta R(b\bar{b})$ (c) m_T^W and (d) $m_{b\bar{b}}$ are shown. The electron and muon channels are combined. 266

12.12The distributions, for the 2-tag 2-jet 75 GeV $< p_T^W <$150 GeV category, of (a) E_T^{miss} (b) $\Delta R(b\bar{b})$ (c) m_T^W and (d) $m_{b\bar{b}}$ are shown. The electron and muon channels are combined. 267

12.13Distributions in the "extended" medium-p_T^V region and for 2-jet events of a few multi-jet sensitive variables, for electrons and muons combined. From left to right and from top to bottom: $\Delta\phi(jj, E_T^{miss})$,$\Delta\phi(lepton, E_T^{miss})$, $m_{b\bar{b}}$, m_T^W , $min(\Delta\phi(lepton, j))$, $\Delta\phi(lepton, jj)$. 268

12.14Nominal and systematically varied distributions, with their ratio in the bottom panels. The systematic variations are, for the electron channel: the reduction of the size of the CRs in the high-p_T^V region (a); the choice of 2-tag rather than 1-tag CRs in the medium-p_T^V region (b). 270

12.15Post-fit $min[\Delta\phi(E_T^{miss}, jets)]$ distribution in 2-tag, 3-jet region in 0-lepton channel. The multi-jet is modelled using an exponentially falling distribution of shape $A.e^{-X/c}$, the fitted value of the parameter A is 3264.1 $\pm$ 130.4 and the parameter c is 6.27 $\pm$ 0.24. 271

12.16Post-fit $min[\Delta\phi(E_T^{miss}, jets)]$ distribution in 2-tag, 2-jet region in 0-lepton channel. No multi-jet was observed in this region. 272

List of Tables

2.1 Beam and machine parameters for collisions in 2012, 2016 and 2017 (projected) Compared to the design.[3] 9

4.1 Parameters for the multiplication rate, defined in Equation 4.9, in high electric fields as listed in [56]. 58

4.2 Parameters for the drift velocity relation in silicon. 59

4.3 Definition and units/values of the variables used in Bethe-Bloch formula, Equation 4.13. 62

5.1 Summary of the RD53A chip specification, that will be used in Phase-II upgrade for the ITk, in comparison with the previous readout: the FE-I3 and the FE-I4.[86]. (**) Note that for the RD53A chip, the chip grid is 50×50 μm^2 but the compatible sensors are either 25×100 μm^2 or 50×50 μm^2. 87

5.2 Summary of the geometrical characteristics of the four active edge sensor designs. 92

5.3 Average breakdown voltage for different design and thickness variations for all structures with Pt UBM. 97

5.4 Average breakdown voltage for different designs and thickness variations for all structures with NiAu UBM. 97

6.1 Typical RSF values calculated in silicon sensors measurements. . . . 106

6.2 The radiation damage model for P-type (up to 7×10^{15} n_{eq}/cm^2) . . 120

6.3 The radiation damage model for P-type (in the range $7 \times 10^{15} n/cm^2 - 2.2 \times 10^{16}$ n_{eq}/cm^2) 120

6.4 Main characterization of the different wafers fabricated for this study. 128

7.1 Summary of the single chip modules from Advacam productions relevant for this thesis. [132] 154

9.1 Gauge bosons in the Standard Model. [148] 169

9.2 The Standard Model leptons and corresponding electric charge and mass. The antiparticles are implicit, with opposite sign electric charges. Neutrino masses are larger than zero for at least two generations. [14] 170

9.3 The Standard Model quarks and corresponding electric charge and mass. The antiparticles are implicit, with opposite sign electric charges.[14] 170

9.4 Interaction and force carriers of the Standard Model. Relative intensity with respect to the strong interaction is given at low energy. . . 171

10.1 The generators used for the simulation of the signal and background processes. If not specified, the order of the cross-section calculation refers to the expansion in the strong coupling constant (αs). The acronyms ME, PS and UE stand for matrix element, parton shower and underlying event, respectively. (*) The events were generated using the first PDF in the NNPDF3.0NLO set and subsequently reweighted to PDF4LHC15NLO set using the internal algorithm in POWHEG-Box v2 . (†) The NNLO(QCD)+NLO(EW) cross-section calculation for the pp→ZH process already includes the gg→ZH contribution. The qq→ZH process is normalised using the NNLO(QCD)+NLO(EW) cross-section for the pp→ZH process, after subtracting the gg→ZH contribution. An additional scale factor is applied to the qq→VH processes as a function of the vector boson's transverse momentum to account for electroweak (EW) corrections at NLO. This makes use of the VH differential cross-section computed with Hawk. 195

10.2 Summary of electron selection requirements. 197

10.3 Summary of muon selection requirements. 197

10.4 Summary of jets selection requirements. 198

10.5 E_T^{miss} triggers used during the 2015, 2016 and 2017 data collection period. The notation, (A, D3, D4,...) refer to the ATLAS collection periods in the year of 2016. 200

10.6 Single electron triggers used during the 2015, 2016 and 2017 data collection period. 200

10.7 Single muon triggers used during the 2015, 2016 and 2017 data collection period. 201

10.8 Summary of the event selection and categorization in the 0-, 1- and 2-lepton channels. 204

10.9 Summary of the additional event selections in the 0-, 1- and 2-lepton channels of the dijet mass analysis. 205

10.10 The distributions used in the global likelihood fit for the signal regions (SR) and control regions (CR) for all the categories in each channel, for the nominal multivariate analysis. 206

10.11 Summary of the systematic uncertainties in the signal modelling. An 'S' symbol is used when only a shape uncertainty is assessed and 'PS/UE' indicates parton shower / underlying event. Where the size of an acceptance systematic uncertainty varies between regions, a range is displayed. 210

10.12 Summary of the systematic uncertainties in the background modelling for Z + jets, W + jets, $t\bar{t}$, single top-quark and multi-jet production. An 'S' symbol is used when only a shape uncertainty is assessed. The regions for which the normalisations float independently are listed in brackets. Where the size of an acceptance systematic uncertainty varies between regions, a range is displayed. 212

10.13 Summary of the systematic uncertainties in the background modelling for diboson production. An 'S' symbol is used when only a shape uncertainty is assessed and 'PS/UE' indicates parton shower/underlying event. When extracting the (W/Z)Z diboson production signal yield, as the normalisations are unconstrained, the normalisation uncertainties are removed. Where the size of an acceptance systematic uncertainty varies between regions, a range is displayed. 213

10.14 Factors applied to the nominal normalisations of the t t , W + HF and Z + HF backgrounds, as obtained from the global likelihood fit to the 13 TeV data for the nominal multivariate analysis, used to extract the Higgs boson signal. The errors represent the combined statistical and systematic uncertainties. 216

10.15 Breakdown of the contributions to the uncertainty in μ. The sum in quadrature of the systematic uncertainties attached to the categories differs from the total systematic uncertainty due to correlations. . . . 217

10.16 The Higgs boson signal, background and data yields for each signal region category in each channel after the full selection of the multivariate analysis. The signal and background yields are normalised to the results of the global likelihood fit. All systematic uncertainties are included in the indicated uncertainties. An entry of "-" indicates that a specific background component is negligible in a certain region, or that no simulated events are left after the analysis selection. . . . 222

10.17 Measured signal strengths with their combined statistical and systematic uncertainties, expected and observed p_0 and significance values (in standard deviations) from the combined fit with a single signal strength, and from a combined fit where each of the lepton channels has its own signal strength, using 13 TeV data. 223

10.18 Expected and observed significance values (in σ) for the H$\to b\bar{b}$ channels fitted independently and their combination using the 7 TeV, 8 TeV and 13 TeV data. 227

10.19 Expected and observed significance values (in standard deviations) for the VH production channels from the combined fit and from a combined fit where each of the lepton channels has its own signal strength, using 13 TeV data. 228

11.1 Specification of event sample used in this study. The acronyms ME and UE stand for matrix element and underlying event, respectively. 232

11.2 CxAODMaker preselection applied to DxAOD events to produce CxAOD. For this specific study, the CxAODMaker preselection were not applied. [207] 235

11.3 The current ZH yields in the different channels: 0,1 and 2 leptons and for two jets categories: 2-jet and 3-jet. The 2 lepton channel is divided into: high-p_T^Z region with $p_T^Z > 150$ GeV and low-p_T^Z region with $75 < p_T^Z < 150$ GeV. The total yields is calculated with and without the low-p_T^Z region. 239

11.4 Tau trigger list for 2015 and 2016 periods used for this study. 240

11.5 Additional event selections applied for events that don't pass the standard 0-lepton CxAODReader selection in the $\tau_{had}\tau_{had}$ channel. pTB1 is the transverse momentum of the leading b-jet. p_T^Z is calculated as shown in equation 11.1. 240

11.6 Additional event selections applied for events that don't pass the standard 1-lepton CxAODReader selection in the $\tau_{lep}\tau_{had}$ channel. pTB1 is the transverse momentum of the leading b-jet. p_T^Z is calculated as shown in equation 11.2. 244

11.7 Event yield in the different jet categories: 2,3 and ≥4 jets for the two p_T^Z cut: >150 GeV and >75 GeV. The event yield after reducing the p_T^Z cut is increased but the relative increase to the reference value is almost the same for the two cuts which is 2%. 247

11.8 The current WH yields in the different channels: 0,1 and 2 leptons and for two jets categories: 2-jet and 3-jet. The 2 lepton channel is divided into: high-p_T^W region with $p_T^W > 150$ GeV and low-p_T^W region with $75 < p_T^W < 150$ GeV. The total yields is calculated with and without the low-p_T^W region. 248

11.9 Additional event selections applied for events that don't pass the standard 0-lepton CxAODReader selection in the $W \to \tau\nu$ channel. p_T^W is calculated as shown in equation 11.1. 249

11.10 Summary of event yield after applying a sequence of additional cuts in $W \to \tau\nu$ channel. 249

11.11 Possible maximum increase of signal yield in the different channels: $\tau_{had}\tau_{had}$, $\tau_{lep}\tau_{had}$ and $\tau_{had}\nu$ in the different nJet categories: 2, 3 and ≥4 jets. The $\tau_{lep}\tau_{had}$ channel is studied in the high-p_T^Z region as well as (low+high)-p_T^Z. 249

12.1 Summary of differences in lepton isolation between the isolated and inverted isolation regions used for the template method. In each region the AND of the two isolation criteria listed in the table is used. 253

12.2 Summary of normalisation scale factors for Top ($t\bar{t}$ + single top) and W+jets derived in the isolated lepton region. 259

12.3 Reduced triggers used to evaluate possible trigger bias in inverted isolation region. 260

12.4 Additional isolation cuts defined for the electron and muon subchannel, in the high- and medium-p_T^V regions to evaluate possible bias results from the extrapolation from the full inverted isolation region to the signal region. 260

12.5 Summary of MJ fractions, along with their associated uncertainty in the 2-jets and 3-jets high p_T^V regions (W+HF and SR are combined) separately. 263

12.6 Summary of MJ fractions, along with their associated uncertainty in the 2-jets and 3-jets medium p_T^V regions (W+HF and SR are combined) separately. 263

12.7 Summary of multi-jet (MJ) fractions, separately for electrons and muons as well as combined, for 2- and 3-jet events, in the high and medium p_T^V regions . The errors represent the combined statistical and systematic uncertainties. 266

Bibliography

[1] J. P. Blewett. "200 GeV Intersecting Storage Accelerators". *eConf C*, (710920 501), 1971. (Cited on page 6.)

[2] The ATLAS Collaboration. "Luminosity public results". https://twiki.cern.ch/twiki/bin/view/AtlasPublic/LuminosityPublicResultsRun2, 2018. (Cited on pages 8 and 277.)

[3] J. Wenninger. "Approaching nominal performance at LHC". In *Proceedings of IPAC2017, Copenhagen, Denmark*, ISBN 978-3-95450-182-3 http://accelconf.web.cern.ch/AccelConf/ipac2017/papers/moyaa1.pdf. MOYAA1, 2017. (Cited on pages 9 and 295.)

[4] L. Evans and P. Bryant. "LHC Machine". *JINST*, 3(08):S08001, 2008. (Cited on page 11.)

[5] The ATLAS Collaboration. "The ATLAS Experiment at the CERN Large Hadron Collider". *JINST*, 3(08):S08003, 2008. (Cited on page 11.)

[6] The ATLAS Collaboration. "ATLAS public results". https://twiki.cern.ch/twiki/bin/view/AtlasPublic/LuminosityPublicResultsRun2#Pileup%20Interactions%20and%20Data_AN1, 2018. (Cited on pages 12 and 277.)

[7] The ATLAS Collaboration. "Observation of a new particle in the search for the Standard Model Higgs boson with the ATLAS detector at the LHC". *Phys. Lett. B*, 716(30), 2012. (Cited on page 13.)

[8] The CMS Collaboration. "Observation of a new boson at a mass of 125 GeV with the CMS experiment at the LHC". *Phys. Lett. B*, 716(30), 2012. (Cited on page 13.)

[9] The ATLAS Collaboration. "Measurements of Higgs boson production and couplings in diboson final states with the ATLAS detector at the LHC". *Phys. Lett. B*, 726(88), 2013. (Cited on page 13.)

[10] R. J. Dankers. PhD thesis, University of Amsterdam, 1998. (Cited on page 14.)

[11] The ATLAS Collaboration. "ATLAS liquid argon calorimeter: Technical design report". *CERN-LHCC-96-41*, . (Cited on page 19.)

[12] The ATLAS Collaboration. "ATLAS tile calorimeter: Technical design report". *CERN-LHCC-96-42*, . (Cited on page 20.)

[13] The ATLAS Collaboration. "atlas muon spectrometer: Technical design report". *CERN-LHCC-97-22*, . (Cited on page 21.)

[14] The ATLAS Collaboration. "Improved luminosity determination in pp collisions at $\sqrt{s}$ = 7 TeV using the ATLAS detector at the LHC". *Eur. Phys. J.*, C 73(2518), 2013. (Cited on page 22.)

[15] The ATLAS Collaboration. "Performance of the ATLAS Inner Detector Track and Vertex Reconstruction in the High Pile-Up LHC Environment". *InspireHEP*, https://inspirehep.net/record/1204277, 2012. (Cited on page 26.)

[16] The ATLAS Collaboration. "Performance of the ATLAS Track Reconstruction Algorithms in Dense Environments in LHC run 2". *arXiv*, https://arxiv.org/abs/1704.07983, 2017. (Cited on pages 26, 28, 277 and 278.)

[17] The ATLAS Collaboration. "Vertex Reconstruction Performance of the ATLAS Detector at $\sqrt{s}$=13 TeV. Technical Report". *ATL-PHYS-PUB-2015-026*, http://cds.cern.ch/record/2037717, 2015. (Cited on page 27.)

[18] V. Lacuesta. "Track and vertex reconstruction in the atlas experiment". *JINST*, 8(02, http://stacks.iop.org/1748-0221/8/i=02/a=C02035):C02035, 2013. (Cited on page 27.)

[19] The ATLAS Collaboration. "Public Results - Approved Plots of the Tracking Combined Performance Group". https://atlas.web.cern.ch/Atlas/GROUPS/PHYSICS/PLOTS/IDTR-2016-013/, 2016. (Cited on pages 29 and 278.)

[20] The ATLAS Collaboration. "Charged-particle distributions in $\sqrt{s}$=13 TeV pp interactions measured with the ATLAS detector at the LHC". *ATLAS-CONF-2015-028*, 2015. (Cited on pages 29 and 278.)

[21] The ATLAS Collaboration. ATLAS Public Plots. https://atlas.web.cern.ch/Atlas/GROUPS/PHYSICS/PLOTS/IDTR-2015-007/, 2015. (Cited on pages 30 and 278.)

[22] The ATLAS Collaboration. ATLAS Public Plots. https://atlas.web.cern.ch/Atlas/GROUPS/PHYSICS/PLOTS/IDTR-2017-007/, 2017. (Cited on pages 30 and 278.)

[23] The ATLAS Collaboration. "Electron and photon energy calibration with the ATLAS detector using LHC Run 1 data". *Eur. Phys. J. C*, 74(3071), 2014. (Cited on page 31.)

[24] The ATLAS Collaboration. "Measurement of the muon reconstruction performance of the ATLAS detector using 2011 and 2012 LHC proton-proton collision data". *Eur. Phys. J. C*, 74(3130), 2014. (Cited on page 32.)

[25] The ATLAS Collaboration. "Calorimeter Clustering algorithms: Description and Performance, Tech.Rep.". *ATLAS-LARG-PUB-2008-002*, 2008. (Cited on page 32.)

[26] The ATLAS Collaboration. "Local Hadronic Calibration, Tech.Rep.". *ATL-LARG-PUB-2009-001-2. ATL-COM-LARG-2008-006. ATL-LARG-PUB-2009-001*, 2008,2009. (Cited on page 32.)

[27] The ATLAS Collaboration. "Pile-up subtraction and suppression for jets in ATLAS,Tech.Rep.". *ATLAS-CONF-2013-083*, 2013. (Cited on page 33.)

[28] The ATLAS Collaboration. "Tagging and suppression of pileup jets, Tech. Rep.". *ATL-PHYS-PUB-2014-001*, 2014. (Cited on page 33.)

[29] The ATLAS Collaboration. "Jet energy scale measurements and their systematic uncertainties in proton-proton collisions at $\sqrt{s}$ = 13 TeV with the ATLAS detector. Tech. rep.". *ATL-COM-PHYS-2016-213*, https://cds.cern.ch/record/2136864, 2016. (Cited on page 33.)

[30] The ATLAS Collaboration. "Performance of b-Jet Identification in the ATLAS Experiment". *CERN-PH-EP-2015-216*, https://cds.cern.ch/record/2110203, 2015. (Cited on page 33.)

[31] The ATLAS Collaboration. "Optimisation and performance studies of the ATLAS b-tagging algorithms for the 2017-18 LHC run. Tech. Rep.". *ATL-PHYS-PUB-2017-013*, http://cds.cern.ch/record/2273281, 2017. (Cited on page 33.)

[32] The ATLAS Collaboration. "Commissioning of the ATLAS high-performance b-tagging algorithms in the 7 TeV collision data ,Tech.Rep.". *ATLAS-CONF-2011-102*, 2011. (Cited on page 33.)

[33] The ATLAS Collaboration. "Calibration of the performance of b-tagging for c and light-flavour jets in the 2012 ATLAS data ,Tech.Rep.". *ATLAS-CONF-2014-046*, 2014. (Cited on pages 33, 34 and 278.)

[34] The ATLAS Collaboration. "b-tagging in dense environments,Tech.Rep.". *ATL-PHYS-PUB-2014-014*, 2014. (Cited on pages 34, 35 and 278.)

[35] The ATLAS Collaboration. "Calibration of b-tagging using dileptonic top pair events in a combinatorial likelihood approach with the ATLAS experiment, Tech. Rep.". *ATLAS-CONF-2014-004*, 2014. (Cited on page 34.)

[36] The ATLAS Collaboration. "flavor tagging with track jets in boosted topologies with the atlas detector , tech. rep.". *ATLAS-CONF-2014-013*, 2014. (Cited on page 35.)

[37] G. Apollinari et al. "High-Luminosity Large Hadron Collider (HL-LHC), Preliminary Design Report". *CERN*, http://inspirehep.net/record/1418897/files/CERN-2015-005.pdf, 2015. (Cited on page 40.)

[38] G. Apollinari et al. "High-Luminosity Large Hadron Collider (HL-LHC)". *CERN*, http://lss.fnal.gov/archive/design/fermilab-design-2015-02.pdf, 2015. (Cited on pages 40 and 278.)

[39] Ahmed Bassalat. *"Contribution to the construction of the Insertable B-Layer of ATLAS for high luminosity upgrade and Research for invisible Higgs"*. PhD thesis, University Paris-Saclay, 2015. (Cited on page 45.)

[40] The ATLAS Collaboration. "ATLAS Insertable B-Layer Technical Design Report". *CERN-LHCC-2010-013*, 2010. (Cited on page 46.)

[41] The ATLAS Collaboration. ATLAS public plots: "Impact Parameter Resolution". https://atlas.web.cern.ch/Atlas/GROUPS/PHYSICS/PLOTS/IDTR-2015-007/, 2015. (Cited on pages 46, 47 and 278.)

[42] A. Fasso et al. A. Ferrari, P. R. Sala. "FLUKA: A multi-particle transport code (Program version 2005), Tech. Rep.". *CERN-2005-010, SLAC-R-773, INFN-TC-05-11*, 2005. (Cited on pages 49 and 279.)

[43] The ATLAS Collaboration. "Technical Design Report for the ATLAS Inner Tracker Strip Detector". *ATLAS-TDR-025*, https://cds.cern.ch/record/2257755/files/ATLAS-TDR-025.pdf, 2017. (Cited on pages 49, 85, 86, 279 and 281.)

[44] R. Dyck et al. "Integrated arrays of silicon photodetectors for image sensing". *IEEE Trans. Electron Devices*, ED-15(4):196 – 201, 1968. (Cited on page 51.)

[45] P. J. W. Noble. "Self-Scanned Silicon Image Detector Arrays". *IEEE Trans. Electron Devices*, ED-15:202 – 209, 1968. (Cited on page 51.)

[46] G. Hallewel et al. "Pixel Detector Technical Design Report". *CERN*, http://atlas.web.cern.ch/Atlas/GROUPS/INNER_DETECTOR/PIXELS/tdr.html, 1998. (Cited on page 51.)

[47] C. Kittel. "Introduction to Solid State Physics". *John Wiley & Sons*, 2005. (Cited on page 52.)

[48] L. Ma et al. "Holes in Hall Effect". *Lat. Am. J. Phys. Educ.*, 3(1):48 – 51, 2009. (Cited on page 53.)

[49] P. Kuiper. *Wikimedia*, https://commons.wikimedia.org/wiki/File:Pn-junction-equilibrium-graphs.png#file, 2007. (Cited on pages 56 and 279.)

[50] H. Moser. "Silicon Detector Szstems in high energy physics". *Nucl. Instrum. Methods Phys. Res., Sect. A*, 63:186 – 237, 2009. (Cited on page 58.)

[51] R. van Overstraeten et al. "Measurement of the ionization rates in diffused silicon p-n junctions". *Solid-State Electron*, 13:583 – 608, 1970. (Cited on page 58.)

[52] S. Ramo. "Currents Induced by Electron Motion". In *Proceedings of the I.R.E*, volume 27, pages 584 – 585. MOYAA1, 1939. (Cited on page 58.)

[53] C. Jacoboni et al. "A review of some charge transport properties of silicon". *Solid-State Electron*, 20(2):77 – 89, 1977. (Cited on page 59.)

[54] S. Striganov D.E. Groom, N.V.Mokhov. "Muon Stopping Power and Range". *Atomic Data and Nuclear Data Tables*, 76(2):http://pdg.lbl.gov/2017/AtomicNuclearProperties/adndt.pdf, 2001. (Cited on pages 60, 61 and 279.)

[55] D.E. Groom and S.R. Klein. "Passage of particles through matter". *The European Physical Journal*, C15, 1999. (Cited on pages 61, 62, 63, 279 and 280.)

[56] C. Grupen and B. Swartz. "Particle Detectors". *Cambridge University Press*, 2008. (Cited on page 60.)

[57] K.A. Olive et al. "Review of particle physics". *Chin. Phys.*, C 38(090001), 2014. (Cited on page 60.)

[58] Arthur H. Compton. "A Quantum Theory of the Scattering of X-rays by Light Elements". *Phys. Rev*, 21(483), 1923. (Cited on page 64.)

[59] G. F. Knoll. *"Radiation Detection and Measurement"*. Wiley, 4th edition, 2010. (Cited on page 65.)

[60] J. Wustenfeld. *"Characterization of Ionization-Induced Surface Effects for the Optimization of Silicon-Detectors for Particle Physics Applications"*. PhD thesis, Universitat Dortmund, 2001. (Cited on page 66.)

[61] K. L. Brower. "Kinetics of H2 passivation of Pb centers at the Si-SiO2 interface". *Phys. Rev. B*, 38:9657 – 9666, 1988. (Cited on page 66.)

[62] R. H. Richter et al. "Strip detector design for ATLAS and HERA-B using two-dimensional device simulation". *Nucl. Instrum. Methods Phys. Res.*, Sect. A 377:412 – 421, 1996. (Cited on page 66.)

[63] V. van Lint et al. "Mechanisms of Radiation Effects in Electronic Materials". *John Wiley & Sons*, 1980. (Cited on pages 67 and 280.)

[64] J. R. Srour et al. "Review of Displacement Damage Effects in Silicon Devices". *IEEE Trans. Nucl. Sci.*, 50:653 – 670, 2003. (Cited on page 67.)

[65] M. Moll. *"Radiation damage in silicon particle detectors: Microscopic defects and macroscopic properties"*. PhD thesis, University of Hamburg, 1999. https://mmoll.web.cern.ch/mmoll/thesis/. (Cited on pages 67, 72, 73 and 280.)

[66] J. Frenkel. "On Pre-Breakdown Phenomena in Insulators and Electronic Semi-Conductors". *Phys. Rev.*, 54:647 – 648, 1938. (Cited on page 69.)

[67] E. Fretwurst et al. "Radiation Damage in Silicon Detectors Caused by Hadronic and Electromagnetic Irradiation". *arXiv*, 2002. (Cited on pages 70 and 280.)

[68] R. Wunstorf. *"Systematische Untersuchungen zur Strahlenresistenz von Silizium-Detektoren fur die Verwendung in Hochenergiephysik-Experimenten"*. PhD thesis, University of Hamburg, 1992. (Cited on pages 71 and 280.)

[69] J. Lange. *"Radiation Damage in Proton - Irradiated Epitaxial Silicon Detectors"*. PhD thesis, University of Hamburg, 2008. (Cited on page 72.)

[70] F. Hartmann. *"Evolution of silicon sensor technology in particle physics"*. Springer, 2009. (Cited on page 76.)

[71] L. Rossi et al. *"Pixel detectors: From fundamentals to applications"*. Springer Science & Business Media, 2006. (Cited on pages 77, 78 and 280.)

[72] J. Kemmer. "Improvement of detector fabrication by the planar process". *Nucl. Instr. Meth. A*, 226(1):89–93, 1984. (Cited on page 77.)

[73] P. Weigell. *"Investigation of Properties of Novel Silicon Pixel Assemblies Emploiynh Thin n-in-p Sensors and 3D-Integration"*. PhD thesis, Technische Universitat Munchen, 2013. https://publications.mppmu.mpg.de/2013/MPP-2013-5/FullText.pdf. (Cited on pages 78 and 280.)

[74] S. Terzo. *"Development of radiation hard pixel modules employing planar n-in-p planar silicon sensors with active edges for the ATLAS detector at HL-LHC"*. PhD thesis, Technische Universitat Munchen, 2015. https://publications.mppmu.mpg.de/2015/MPP-2015-291/FullText.pdf. (Cited on pages 79, 80, 84, 154 and 281.)

[75] The ATLAS Collaboration. "The ATLAS Insertable B-Layer Technical Design Report". *ATLAS-TDR-019*, 2010. (Cited on page 80.)

[76] The ATLAS Collaboration. "Technical Design Report for the ATLAS Inner Tracker Pixel Detector". *ATLAS-TDR-030*, 2018. (Cited on pages 81 and 281.)

[77] M. Karagounis. "Development of the ATLAS FE-I4 pixel readout IC for b-layer Upgrade and Super-LHC". *CERN-2008-008*, https://cds.cern.ch/record/1158505, 2008. (Cited on page 81.)

[78] M. Beimforde. *"Development of thin sensors and a novel interconnection technology for the upgrade of the atlas pixel system"*. PhD thesis, Technische Universitat Munchen, 2010. https://publications.mppmu.mpg.de/2010/MPP-2010-115/FullText.pdf. (Cited on pages 82 and 281.)

[79] The ATLAS collaboration. " prototype atlas ibl modules using the fe-i4a front-end readout chip ". *JINST*, 7:P11010, 2012. (Cited on pages 83 and 281.)

[80] The ATLAS collaboration. "Prototype ATLAS IBL modules using the FE-I4A front-end readout chip". *JINST*, 7(11):P11010, 2012. (Cited on pages 83, 85 and 281.)

[81] A. Micelli. *"3D sensors for the Insertable B-Layer of the ATLAS experiment at the CERN LHC"*. PhD thesis, Udine University, 2012. https://cds.cern.ch/record/2094621/files/Thesis-2012-Micelli.pdf. (Cited on page 84.)

[82] G. Pellegrini et al. "First double-sided 3-D detectors fabricated at CNM-IMB". *Nucl. Instr. Meth. A*, 592(1):38 – 43, 2008. (Cited on page 84.)

[83] E. Vianello et al. "Optimization of double-side 3D detector technology for first productions at FBK". *Nuclear Science Symposium and Medical Imaging Conference (NSS/MIC)*, pages 523 – 528, 2011. (Cited on page 84.)

[84] C. Da Via et al. "3D active edge silicon sensors: Device processing, yield and QA for the ATLAS-IBL production". *Nucl. Instr. Meth. A*, 699:18 – 21, 2013. (Cited on page 85.)

[85] RD-53 Collaboration. http://rd53.web.cern.ch/RD53/, . (Cited on page 86.)

[86] Garcia-Sciveres and Mauricio. "RD53A Integrated Circuit Specifications". *RD53 Collaboration, CERN*, CERN-RD53-PUB-15-001, 2015. (Cited on pages 87 and 295.)

[87] J. Lange et al. "3D silicon pixel detectors for the High-Luminosity LHC". *JINST*, 11:C11024, 2016. (Cited on page 88.)

[88] J. Lange et al. "Radiation hardness of small-pitch 3D pixel sensors up to HL-LHC fluences". In *International conference on Technology and Instrumentation in Particle Physics'17 (TIPP2017), Beijing, China*, arXiv:1707.01045, 2017. (Cited on page 89.)

[89] Bompard et al. "Radiation-hard active pixel detectors for tracking of charged particles based on HV-CMOS technology". In *Proc. Int. Image Sensors Workshop*, pages 273–276, 2013. (Cited on pages 89 and 281.)

[90] ADVACAM. http://www.advacam.com. (Cited on page 90.)

[91] The ATLAS Collaboration. "ATLAS Phase-II, Upgrade Scoping Document". *CERN*, 2015. (Cited on page 90.)

[92] G. Aaad et al. "ATLAS pixel detector electronics and sensors". *JINST*, 3: P07007, 2008. (Cited on page 90.)

[93] T. Wittig. PhD thesis, Technishe Universitt Dortmund, 2013. (Cited on page 90.)

[94] J. Kalliopuska et al. X. Wu. "Recent advances in processing and characterization of edgeless detectors". *IOP Science*, 2012. (Cited on pages 90, 91 and 282.)

[95] VTT. http://www.vttresearch.com/. (Cited on page 90.)

[96] Audrey Ducourthial. *"Upgrade of the ATLAS Experiment Inner Tracker and related physics perspectives of the Higgs boson decay into two b quarks"*. PhD thesis, Sorbonne paris university, 2018. (Cited on page 92.)

[97] G. Stingeder et al. "Quantitative Distribution Analysis of Phosphorus with Sims in the Layer System SiO2/Si". In *MRS Spring Meeting*, 1986. (Cited on page 103.)

[98] J.W. McDonald et al. "Surface charge compensation for a highly charged ion emission microscope". *Ultramicroscopy*, 101:225 – 229, 2004. (Cited on page 103.)

[99] C. W. Magee et al. "Secondary ion quadrupole mass spectrometer for depth profiling design and performance evaluation". *Rev. Scient. Instrum.*, 94(4): 477 – 485, 1978. (Cited on page 104.)

[100] SYNOPSYS Inc. http://www.synopsys.com/tools/tcad/Pages/default.aspx, . (Cited on page 111.)

[101] SILVACO Inc. http://www.silvaco.com/products/tcad.html, . (Cited on page 111.)

[102] CAMECA Science and Metrology Solutions. France. https://www.cameca.com/products/sims/ims7f-geo. (Cited on pages 115 and 283.)

[103] R. Singiresu. *"The Finite Element Method in Engineering"*. 4th edition, 2004. ISBN 9780750678285. (Cited on page 115.)

[104] W. Shockley and W.T Read. "Statistics of the Recombinations of Holes and Electrons". *Phys. Rev*, 87:835–842, 1952. (Cited on page 115.)

[105] D. Passeri et al. "Comprehensive modeling of bulk-damage effects in silicon radiation detectors". *IEEE Trans. Nucl. Sci.*, 48(5):1688 – 1693, 2001. (Cited on page 120.)

[106] D. Passeri et al. "Numerical simulation of radiation damage effects in p-type and n-type FZ silicon detectors". *IEEE Trans. Nucl. Sci.*, 53(5):2971–2976, 2006. (Cited on page 120.)

[107] J. F. Ziegler. "Ion Implantation - Science and Technology". *Ion Implantation Technology Co.*, 1996. (Cited on page 123.)

[108] Y. Nishi and R. Doering. *"Handbook of Semiconductor Manufacturing Technology"*. Marcel Dekker Inc., 2000. (Cited on page 123.)

[109] D. K. Schroder. *"Semiconductor Material and Device Characterization"*. Wiley Interscience, 3th edition, 2005. (Cited on page 124.)

[110] H. Murrman and D. Widmann. "Current crowding on metal contacts to planar devices". *IEEE Transactions*, 16(12):1022 – 1024, 1969. (Cited on page 124.)

[111] W. Shockley. "Research and investigation of inverse epitaxial UHF power transistors". *Wright-Patterson AFB*, 1964. (Cited on page 124.)

[112] D. K. Schroder. *"Semiconductor Material and Device Characterization"*. John Wiley & Sons, 1990. (Cited on page 125.)

[113] A.F. Gerodolle and J. Pelletier. "Two-Dimensional Implications of a Purely Reactive Model for Plasma Etching". *IEEE Trans.Electron Devices*, 38(9): 2025–2032, 1991. (Cited on page 131.)

[114] Avinash P. Nayak et al. "Wet and Dry Etching". `http://web.ece.ucdavis.edu/~anayakpr/Papers/Wet%20and%20Dry%20Etching_submitted.pdf`. (Cited on page 131.)

[115] Lubjana irradiation facility. Slovania. `https://rd50.web.cern.ch/rd50/irradiation/Irradiation_ljubljana.html`. (Cited on page 136.)

[116] D. Autiero et al. "Characterization of the T24 electron beam line available at DESY". *OPERA Note*, 2004. (Cited on page 142.)

[117] S. Tsiskaridze. *"Beam Test Performance of 3D Pixel Detectors for the IBL Upgrade"*. PhD thesis, Universitat Autonoma de Barcelona, 2012. (Cited on pages 144 and 286.)

[118] J. Baudot et al. "First Test Results Of MIMOSA-26, A Fast CMOS Sensor With Integrated Zero Suppression And Digitized Output". In *2009 IEEE NSS Conference Record*, page 1169, 2009. (Cited on pages 144 and 145.)

[119] I. Rubinskiy et al. "An EUDET/AIDA pixel beam telescope for detector development". *Physics Procedia*, 37:923–931, 2012. (Cited on pages 144 and 145.)

[120] R. Turchetta. "Spatial resolution of silicon microstrip detectors". *Nucl. Instr. Meth. A*, 335:1–2 44–58, 1993. (Cited on page 145.)

[121] J. Weingarten et al. "Planar pixel sensors for the ATLAS upgrade: beam tests results". *JINST*, 7(10):P10028, 2012. (Cited on page 145.)

[122] G. Troska. *"Development and operation of a testbeam setup for qualification studies of ATLAS pixel sensors"*. PhD thesis, Technische Universitat Dortmund, 2012. `https://eldorado.tu-dortmund.de/handle/2003/29351`. (Cited on pages 146 and 286.)

[123] E. Corrin. "EUDAQ Software User Manual". 2010. (Cited on page 147.)

[124] T. Bisanz et al. "EUTelescope 1.0: Reconstruction Software for the AIDA Testbeam Telescope". *AIDA-NOTE-2015-009*, http://cds.cern.ch/record/2000969, 2015. (Cited on page 148.)

[125] K. N. Sjobaek. *"Full simulation of a testbeam experiment including modeling of the Bonn ATLAS Telescope and ATLAS 3D pixel silicon sensors"*. PhD thesis, University of Oslo, 2010. (Cited on page 148.)

[126] V. Blobel. "Software alignment for tracking detectors". *Nucl. Instr. Meth. A*, 566(1):5–13, 2006. (Cited on page 150.)

[127] S. Fleischmann. *"Track Reconstruction in the ATLAS Experiment: The deterministic annealing filter"*. PhD thesis, Universitat Wuppertal. (Cited on page 151.)

[128] Kalman et al. "A new approach to linear filtering and prediction problems". *Journal of basic Engineering*, 82(1):35–45, 1960. (Cited on page 151.)

[129] C. Kleinwort. "General Broken Lines as advanced track fitting method". *Nucl. Instr. Meth. A*, 673:107–110, 2012. (Cited on page 151.)

[130] AIDA-2020 project. Advanced European Infrastructure for Detectors and Accelerators. http://aida2020.web.cern.ch. (Cited on page 154.)

[131] ITk Pixel Group. https://twiki.cern.ch/twiki/bin/view/Atlas/ITkPixel, . (Cited on page 154.)

[132] Natascha Savic. *"Development of Pixel Detectors for the Inner Tracker Upgrade of the ATLAS Experiment"*. PhD thesis, Universitat Munchen, 2017. https://www.mpp.mpg.de/~savicn/talks/main.pdf. (Cited on pages 154, 155, 157, 159, 286 and 295.)

[133] J. Weingarten et al. "Planar pixel sensors for the ATLAS upgrade: beam tests results". *JINST*, 7(10):P10028, 2012. (Cited on page 159.)

[134] T. Rashid et al. "new 3d doping profile measurement and tcad simulation of radiation damage in advacam active edge pixel detector for high energy physics experiments". *IEEE*, https://ieeexplore.ieee.org/document/8069766, DOI:10.1109/NSSMIC.2016.8069766(17262867), 2017. (Cited on page 163.)

[135] S. Glashow. "Partial Symmetries of Weak Interactions". *Nucl.Phys.22*, pages 579–588, 1961. (Cited on page 167.)

[136] S. Weinberg. "A Model of Leptons". *Phys.Rev.Lett.*, 19:1264–1266, 1967. (Cited on page 167.)

[137] A. Salam. "Weak and Electromagnetic Interactions". *Conf.Proc.*, C680519: 367–377, 1968. (Cited on page 167.)

[138] D. J. Gross and F. Wilczek. "Ultraviolet Behavior of Nonabelian Gauge Theories". *Phys.Rev.Lett.*, 30:1343–1346, 1973. (Cited on page 167.)

[139] H. D. Politzer. "Reliable Perturbative Results for Strong Interactions". *Phys.Rev.Lett.*, 30:1346–1349, 1973. (Cited on page 167.)

[140] D. Gross and F. Wilczek. "Asymptotically Free Gauge Theories. 1". *Phys.Rev.*, D8:3633–3652, 1973. (Cited on page 167.)

[141] H. D. Politzer. "Asymptotic Freedom: An Approach to Strong Interactions". *Phys.Rept.*, 14:129–180, 1974. (Cited on page 167.)

[142] M. Veltman G. Hooft. "Regularization and Renormalization of Gauge Fields". http://www.sciencedirect.com/science/article/pii/0550321372902799?via%3Dihub., 1968. (Cited on page 168.)

[143] The ATLAS Collaboration. "Observation of a new particle in the search for the Standard Model Higgs boson with the ATLAS detector at the LHC.". *Phys. Lett.*, B716:1–29, 2012. (Cited on page 168.)

[144] The CMS Collaboration. "Observation of a new boson at a mass of 125 GeV with the CMS experiment at the LHC.". *Phys. Lett.*, B716:30–61, 2012. (Cited on page 168.)

[145] M. E. Peskin and D. V. Schroeder. "An Introduction to quantum field theory". 1995. (Cited on page 168.)

[146] E. Noether. "Invariante Variations probleme". *Mathematisch-Physikalische Klasse*, B716:235–257, 1918. (Cited on page 168.)

[147] Lubej Matic. "Standard Model". http://www.physik.uzh.ch/groups/serra/StandardModel.html. (Cited on pages 169 and 287.)

[148] Particle Data Group Collaboration. "Review of Particle Physics (RPP)". *Phys.Rev.*, D86:010001, 2012. (Cited on pages 169 and 296.)

[149] Chen-Ning Yang and Robert L. Mills. "Conservation of Isotopic Spin and Isotopic Gauge Invariance". *Phys.Rev.*, D86:191–195, 1954. (Cited on page 172.)

[150] J. Goldstone. "Field theories with sup erconductor solutions". *Phys.Rev.*, 19: 154–164, 1961. (Cited on page 172.)

[151] J. Goldstone et al. "Broken symmetries". *Phys.Rev.*, 127:965–970, 1962. (Cited on page 172.)

[152] F. Englert and R. Brout. "Broken Symmetry and the Mass of Gauge Vector Mesons". *Phys. Rev. Lett.*, 13:321–323, 1964. (Cited on pages 172 and 190.)

[153] R. Barbier et al. "R-parity violating supersymmetry". *Phys. Rept.*, 420:1–202, 2005. (Cited on pages 173 and 287.)

[154] Morad Aaboud et al. "Measurement of the W-boson mass in pp collisions at $\sqrt{s} = 7$ TeV with the ATLAS detector". *arXive*, https://arxiv.org/pdf/1701.07240.pdf., 2017. (Cited on page 174.)

[155] C. Patrignani et al. "Review of Particle Physics". *Chin. Phys.*, C40(10): 100001, 2016. (Cited on page 174.)

[156] LHC Higgs cross-section Working Group. *https://twiki.cern.ch/twiki/bin/view/\LHCPhysics/LHCHXSWG/Latestplots*, 2017. (Cited on pages 176, 178, 179, 287 and 288.)

[157] Estelle Scifo. *"Measurement of the Brout-Englert-Higgs boson couplings in its diphoton decay channel with the ATLAS detector at the LHC"*. PhD thesis, U. Paris-Sud 11, Orsay, 2014. https://cds.cern.ch/record/1756391. (Cited on pages 176, 180, 287 and 288.)

[158] The ATLAS Collaboration. "Observation of a new particle in the search for the Standard Model Higgs boson with the ATLAS detector at the LHC". *Phys. Lett. B*, 716(1), 2012. (Cited on page 178.)

[159] The CMS Collaboration. "Observation of a new new boson at a mass of 125 GeV with the CMS experiment at the LHC". *Phys. Lett. B*, 716(30), 2012. (Cited on page 178.)

[160] The ATLAS Collaboration. "Evidence for the Higgs-boson Yukawa coupling to tau leptons with the ATLAS detector". *JHEP*, 04:117, 2015. (Cited on pages 181 and 186.)

[161] The CMS Collaboration. "Evidence for the direct decay of the 125 GeV Higgs boson to fermions". *Nature Phys.*, 10:557, 2014. (Cited on pages 181 and 186.)

[162] The ATLAS Collaboration. "Search for the Decay of the Higgs Boson to Charm Quarks with the ATLAS Experiment". *Phys. Rev. Lett.*, 120 (1802.04329):211802, 2018. (Cited on page 181.)

[163] The ATLAS Collaboration. "Search for the Dimuon Decay of the Higgs Boson in pp Collisions at $\sqrt{s} = 13$ TeV with the ATLAS Detector". *Phys. Rev. Lett.*, 119:051802, 2017. (Cited on page 181.)

[164] The CMS Collaboration. "Search for the Standard Model Higgs Boson Decaying to $\mu^+\mu^-$ in pp Collisions at $\sqrt{s} = 7$ and 8 TeV with the CMS Detector". *arXiv:1409.0839 [hep-ex]*, 2014. (Cited on page 181.)

[165] The ATLAS Collaboration. "ATLAS Feature: The Higgs boson". *ATLAS-PHOTO-2018-020, CERN*, https://cds.cern.ch/record/2627611, 2018. (Cited on pages 186 and 288.)

[166] The CMS Collaboration. "Precise determination of the mass of the Higgs boson and tests of compatibility of its couplings with the standard model predictions using proton collisions at 7 and 8 TeV". *Eur. Phys. J.*, C75, 2014. (Cited on page 185.)

[167] The ATLAS Collaboration. "Measurement of the Higgs boson mass from the H to $\gamma\gamma$ and H$\rightarrow ZZ^* \rightarrow 4l$ channels with the ATLAS detector using 25 fb^{-1} of pp collision data". *Phys. Rev.*, D90, 2014. (Cited on page 185.)

[168] ATLAS and CMS Collaboration. "Combined Measurement of the Higgs Boson Mass in pp Collisions at $\sqrt{s} = 7$ and 8 TeV with the ATLAS and CMS Experiments". *Phys. Rev. Lett.*, 114, 2015. (Cited on page 185.)

[169] The ATLAS Collaboration. "Measurements of properties of the Higgs boson decaying into four leptons in pp collisions at $\sqrt{s} = 13$ TeV". *Tech. rep. CMS-PAS-HIG-16-041, CERN*, http://cds.cern.ch/record/2256357, 2017. (Cited on page 186.)

[170] The ATLAS Collaboration. "Evidence for the associated production of the Higgs boson and a top quark pair with the ATLAS detector". *Phys. Rev.*, D97:072003, 2018. (Cited on page 186.)

[171] The CMS Collaboration. "Observation of ttH production". *arXiv*, (1804.02610):072003, 2018. (Cited on page 186.)

[172] The ATLAS Collaboration. "Observation of H$\rightarrow b\bar{b}$ decays and VH production with the ATLAS detector". *Phys. Lett. B*, (1808.08238), 2018. (Cited on pages 186, 214, 226 and 228.)

[173] The CMS Collaboration. "Observation of Higgs boson decay to bottom quarks with CMS". *CMS-HIG-18-016, CERN*, https://arxiv.org/pdf/1808.08242.pdf, 2018. (Cited on page 186.)

[174] The ATLAS Collaboration. "Combined measurements of Higgs boson production and decay using up to 80 fb^{-1} of proton-proton collision data at $\sqrt{s} = 13$ TeV collected with the ATLAS experiment". *ATLAS-CONF-2018-31, CERN*, http://cdsweb.cern.ch/record/2629412/files/ATLAS-CONF-2018-031.pdf, 2018. (Cited on pages 188 and 288.)

[175] The CMS Collaboration. "Combined measurements of Higgs boson couplings in proton-proton collisions at $\sqrt{s} = 13$ TeV". *CMS-HIG-17-031, CERN*, https://arxiv.org/pdf/1809.10733.pdf, 2018. (Cited on pages 188 and 288.)

[176] The ATLAS Collaboration. "Measurement of the Higgs boson mass in the H$\rightarrow ZZ^* \rightarrow 4l$ and H$\rightarrow \gamma\gamma$ channels with $\sqrt{s}$=13 TeV pp collisions using the ATLAS detector ". *Phys. Lett. B*, 784:345, 2018. (Cited on page 190.)

[177] ATLAS and CMS Collaborations. "Measurements of the Higgs boson production and decay rates and constraints on its couplings from a combined ATLAS and CMS analysis of the LHC pp collision data at $\sqrt{s} = 7$ and 8 TeV ". *JHEP*, 08:045, 2016. (Cited on page 190.)

[178] The ATLAS Collaboration. "Observation of H$\rightarrow b\bar{b}$ decays and VH production with the ATLAS detector ". *Phys. Lett. B*, arXiv:1808.08238, 2018. (Cited on pages 190, 191, 192, 206 and 207.)

[179] CDF and D0 Collaborations. "Evidence for a particle produced in association with weak bosons and decaying to a bottom-antibottom quark pair in Higgs boson searches at the Tevatron". *Phys. Rev. Lett*, 109:071804, 2012. (Cited on page 190.)

[180] A. Hoecker et al. "TMVA - Toolkit for Multivariate Data Analysis". *arXiv:physics/0703039*, https://arxiv.org/pdf/1809.10733.pdf, 2007. (Cited on page 192.)

[181] Freund and R. E. Schapire. "Experiments with a new boosting algorithm". In *ICML'96 Proceedings of the Thirteenth International Conference on International Conference on Machine Learning*, pages 148–156, 1996. (Cited on page 192.)

[182] S. Agostinelli et al. "GEANT4". *Nucl. Instrum. Meth. A*, 506:250, 2003. (Cited on page 193.)

[183] T. Sjostrand et al. "A brief introduction to PYTHIA 8.1". *Comput. Phys. Commun.*, 178:852, 2008. (Cited on page 193.)

[184] The ATLAS Collaboration. "Summary of ATLAS Pythia 8 tunes". *ATL-PHYS-PUB-2012-003*, https://cds.cern.ch/record/1474107, 2012. (Cited on page 193.)

[185] A. Martin et al. "Parton distributions for the LHC". *Eur. Phys. J. C*, 63:189, 2009. (Cited on page 193.)

[186] S. Alioli et al. "A general framework for implementing NLO calculations in shower Monte Carlo programs: the POWHEG BOX". *JHEP*, 06:043, 2010. (Cited on page 193.)

[187] T. Gleisberg et al. "Event generation with SHERPA 1.1". *JHEP*, 02:007, 2009. (Cited on page 194.)

[188] The ATLAS Collaboration. "Electron efficiency measurements with the ATLAS detector using the 2015 LHC proton-proton collision data". *ATLAS-CONF-2016-024*, https://cds.cern.ch/record/2157687, 2016. (Cited on page 196.)

[189] The ATLAS Collaboration. "Expected performance of the ATLAS b-tagging algorithms in Run-2". *tech. rep. ATL-PHYS-PUB-2015-022, CERN*, https://cds.cern.ch/record/2037697, 2015. (Cited on page 198.)

[190] The ATLAS Collaboration. "Object selections for SM Higgs boson produced in association with a vector boson in which H decay to bb and V decays leptonically with Run-2 data". *ATL-COM-PHYS-2018-517, CERN*, https://cds.cern.ch/record/2317182/files/ATL-COM-PHYS-2018-517.pdf?version=4, 2018. (Cited on pages 198, 199, 202 and 215.)

[191] The ATLAS Collaboration. "Expected performance of missing transverse momentum reconstruction for the ATLAS detector at $\sqrt{s} = 13$ TeV". *Technical Report ATL-PHYS-PUB-2015-023, CERN*, 2015. (Cited on page 199.)

[192] The ATLAS Collaboration. "Optimisation of the ATLAS b-tagging performance for the 2016 LHC Run". *Technical Report ATL-PHYS-PUB-2016-012, CERN*, 2016. (Cited on page 202.)

[193] The ATLAS Collaboration. "Luminosity Determination in pp Collisions at sqrt(s) = 8 TeV using the ATLAS Detector at the LHC". *Eur. Phys. J. C*, 76:653, 2016. (Cited on page 207.)

[194] The ATLAS Collaboration. "The new LUCID-2 detector for luminosity measurement and monitoring in ATLAS". *JINST*, 13:P07017, 2018. (Cited on page 207.)

[195] The ATLAS Collaboration. "Measurement of the Inelastic Proton-Proton Cross Section at $\sqrt{s} = 13$ TeV with the ATLAS Detector at the LHC". *Phys. Rev. Lett*, 117:182002, 2016. (Cited on page 207.)

[196] The ATLAS Collaboration. "Jet energy scale measurements and their systematic uncertainties in proton-proton collisions at $\sqrt{s} = 13$ TeV with the ATLAS detector". *Phys. Rev. D*, 96:072002, 2017. (Cited on page 208.)

[197] The ATLAS Collaboration. "Measurements of b-jet tagging efficiency with the ATLAS detector using $t\bar{t}$ events at $\sqrt{s} = 13$ TeV". *JHEP*, 08:089, 2018. (Cited on page 208.)

[198] The ATLAS Collaboration. "Measurement of b-tagging efficiency of c-jets in $t\bar{t}$ events using a likelihood approach with the ATLAS detector". *ATLAS-CONF-2018-001, CERN*, https://cds.cern.ch/record/2306649, 2018. (Cited on page 208.)

[199] The ATLAS Collaboration. "Calibration of light-flavour b-jet mistagging rates using ATLAS proton-proton collision data at $\sqrt{s} = 13$ TeV". *ATLAS-CONF-2018-006, CERN*, https://cds.cern.ch/record/2314418, 2018. (Cited on page 208.)

[200] J R Andersen et al. *"Handbook of LHC Higgs Cross Sections: 3. Higgs Properties"*. 2013. (Cited on page 209.)

[201] LHC Higgs Cross Section Working Group. "CERN Yellow Report 4". *CERN*, . (Cited on page 209.)

[202] J. Barlow and C. Beeston. "Fitting using finite Monte Carlo samples". *Comput. Phys. Commun.*, 77:219, 1993. (Cited on page 214.)

[203] The ATLAS Collaboration. "Evidence for the H→ $b\bar{b}$ decay with the ATLAS detector". *JHEP*, 12:024, 2017. (Cited on page 218.)

[204] The ATLAS Collaboration. "Search for the H→ $b\bar{b}$ decay of the Standard Model Higgs boson in associated (W/Z)H production with the ATLAS detector". *JHEP*, 01:069, 2015. (Cited on page 225.)

[205] The ATLAS Collaboration. "ATLAS Athena Guide". https://atlassoftwaredocs.web.cern.ch/athena/, 2017. (Cited on page 233.)

[206] James Catmore et al. "A new petabyte-scale data derivation framework for ATLAS". *iopscience*, http://iopscience.iop.org/1742-6596/664/7/072007:P11010, 2015. (Cited on pages 233 and 290.)

[207] VHbb group. https://twiki.cern.ch/twiki/bin/viewauth/AtlasProtected/HSG5VHCxAODMakerPreSelection, 2016. (Cited on pages 235 and 298.)

[208] The ATLAS Collaboration. "Reconstruction, Energy Calibration, and Identification of Hadronically Decaying Tau Leptons in the ATLAS Experiment for Run-2 of the LHC". *ATL-PHYS-PUB-2015-045, CERN*, https://cds.cern.ch/record/2064383/files/ATL-PHYS-PUB-2015-045.pdf, 2015. (Cited on pages 237, 238 and 291.)

[209] W. Verkerke and D. Kirkby. "The RooFit toolkit for data modeling". *arXive*, 2013. (Cited on page 252.)

[210] R. Barlow. "TFraction fitter, a root class". https://root.cern.ch/doc/master/classTFractionFitter.html, 2015. (Cited on page 252.)

[211] The ATLAS Collaboration. "Evidence for the H(bb) decay with the ATLAS detector". *arXive*, (1708.03299), 2017. (Cited on page 253.)